

### 许淑妮评选材料清单

- 附件 1: 中科院 2 区文章 SCI 论文一作 (共一)
- 附件 2: 中科院 EI 论文一作
- 附件 3: 中科院 2 区文章 SCI 论文二作
- 附件 4: 中科院 3 区文章 SCI 论文二作
- 附件 5: 软件著作“浒苔基生物炭制备精准控制系统”第四位次
- 附件 6: 软件著作“基于腐熟堆肥产品的碳基有机肥造粒工艺控制系统 V1.0”第三位次
- 附件 7: 三类竞赛, 国家级, 全国农科研究生乡村振兴志愿服务成果, 一等奖 (第五位次)
- 附件 8: 二类竞赛, 国家级, “建行杯”第十六届全国大学生节能减排社会实践与科技竞赛, 三等奖 (首位)
- 附件 9: 四类竞赛, 校级, 第五届青岛农业大学节能减排社会实践与科技竞赛, 一等奖 (首位)
- 附件 10: 参与导师科研项目
- 附件 11: 参编专业相关书籍著作, 编写者
- 附件 12: 参加国家级, 2022 年第十六届全国堆肥技术与工程研讨会
- 附件 13: 参加校级, 第一届青岛农业大学青年虹扬学术论坛
- 附件 14: 参加校级, 青岛农业大学第二届青年人才高峰论坛
- 附件 15: 参加校级, 青岛农业大学第十一届研究生学术论坛 (资环学院分论坛)
- 附件 16: 参加院级, 资源与环境学术论坛
- 附件 17: 参加院级, 资源与环境学院学科发展与专业建设座谈会
- 附件 18: 校级, 2021 年度“优秀共青团员”
- 附件 19: 院级, 心理发展部部长, 优秀
- 附件 20: 参加学校和学院组织的社会实践活动, 志愿者
- 附件 21: 参加省级, 山东省大学生就业创业知识竞赛, 参与奖
- 附件 22: 参加省级, 山东省首届大学生英语口语大赛, 参与奖
- 附件 23: 参加校级, 青岛农业大学第四届“虹创杯”大学生创新创业计划大赛, 参与奖
- 附件 24: 校级, 知网杯竞赛, 参与奖
- 附件 25: 参加院级, 山东省产教融合基地摄影大赛, 二等奖
- 附件 26: 参加院级, 山东省产教融合基地摄影大赛, 三等奖
- 附件 27: 参加院级, 山东省产教融合基地暨科技小院 2021 年度学术报告, 三等奖
- 附件 28: 2022 年获得优秀宿舍 1 次



Contents lists available at ScienceDirect

Environmental Technology &amp; Innovation

journal homepage: [www.elsevier.com/locate/eti](http://www.elsevier.com/locate/eti)

## Effects of aeration rate on the cornstalks used for filtration of anaerobically digested manure centrate direct composting process: Maturity and gas emissions

Yun Li<sup>a,1</sup>, Shuni Xu<sup>a,1</sup>, Yanling Chen<sup>a</sup>, Xiaohan Zhang<sup>b</sup>, Xiaomin Xie<sup>a,b,\*</sup><sup>a</sup> College of Resources and Environmental Sciences, Qingdao Agricultural University, Qingdao 266109, China<sup>b</sup> School of Environmental Science and Engineering, Shandong University, Qingdao 266237, China

### ARTICLE INFO

#### Article history:

Received 29 April 2023

Received in revised form 10 July 2023

Accepted 20 July 2023

Available online 26 July 2023

#### Keywords:

Compost

Aeration rate

Maturity

Gas Emission

### ABSTRACT

This study aimed to clarify the effect of the aeration rate on the maturity and gas emission during the direct composting process of the cornstalks for ADMC filtration under three aeration rates of 0.05 (R1 0.05), 0.1 (R2 0.10), and 0.15 (R3 0.15) m<sup>3</sup>/m<sup>3</sup> min for the 21-day composting experiment. The results showed that the temperature of R3(0.15) treatment was lower than the others during composting. All treatments could maintain high temperatures (>50 °C) for more than 5 days, meeting the Chinese national standard for organic fertilizer production. The cumulative CO<sub>2</sub> emission of the R1(0.05) treatment was the highest, which was 36.59% and 33.04% higher than the R2(0.10) treatment and R3(0.15) treatment, respectively. R1(0.05) treatment is not conducive to N<sub>2</sub>O emissions, and R3(0.15) treatment is not conducive to CH<sub>4</sub> emissions. The cumulative emissions of NH<sub>3</sub> and sulfur-containing odor in the R1(0.05) treatment were the lowest, and the cumulative emissions of H<sub>2</sub>S, C<sub>2</sub>H<sub>6</sub>S, and COS in the R3(0.15) treatment were the highest. Based on the comprehensive comparison, the recommended aeration rate for the cornstalks after the ADMC filtration direct composting is 0.05 m<sup>3</sup>/m<sup>3</sup> min. The results can provide a theoretical basis and measures for the process parameters of the cornstalks for ADMC filtration direct composting.

© 2023 The Authors. Published by Elsevier B.V. This is an open access article under the CC BY-NC-ND license (<http://creativecommons.org/licenses/by-nc-nd/4.0/>).

### 1. Introduction

Global solid waste production will reach 6 million tons daily by 2025 (Wang et al., 2021). The Chinese government has issued relevant policies on the resource utilization of solid waste and improved treatment technology and equipment to promote the green development of agriculture. At present, the yield of corn straw in China is 2.64 billion tons per year (Ren et al., 2020). Corn straw is often used as a filter medium because of its low cost, large yield, and fibrous structure. Moreover, it has been recorded that 3800 large-scale anaerobic digestion plants with an adequate reactor volume of more than 500 m<sup>3</sup> were in China by the end of 2007 (Du et al., 2019). Therefore, a large number of the Cornstalks for filtering anaerobically digested manure centrate (ADMC) need to be reused to reduce environmental pollution. Cornstalks for filtering ADMC is a kind of solid waste (Li et al., 2023). It is rich in various nutrients and is a degradable organic matter. After filtering ADMC, cornstalks can be reused by composting (Li et al., 2022b). Currently, the composting treatment of

\* Corresponding author at: College of Resources and Environmental Sciences, Qingdao Agricultural University, Qingdao 266109, China.

E-mail address: [xiexiaomin@sdu.edu.cn](mailto:xiexiaomin@sdu.edu.cn) (X. Xie).

<sup>1</sup> These authors contributed equally to this work.

## 添加玉米秸秆对胡萝卜尾菜堆肥过程的影响

许淑妮, 冯晓璐, 陈延玲, 李 贇\*

(青岛农业大学资源与环境学院, 青岛, 266109)

**摘要:**为解决规模化胡萝卜种植过程尾菜处理难的问题,在通风速率为 $0.05\text{ m}^3/\text{min}$ 的条件下,探讨不同添加比例的玉米秸秆对胡萝卜尾菜堆肥过程中腐熟度、气体排放和酶活性的影响。通过分析腐熟度、气体排放和酶活性之间的响应关系,确定最优辅料添加比例,以期实现胡萝卜尾菜无害化、资源化利用。结果表明:不同胡萝卜尾菜好氧堆肥产品均能满足种子发芽率指数 $\geq 70\%$ 的无害化标准; $\text{NH}_3$ 和 $\text{CO}_2$ 排放集中在前7d,排放速率主要受温度、pH值等理化性质影响,同时鸡粪的添加导致 $\text{NH}_3$ 累积排放量增加,不添加任何辅料的胡萝卜尾菜单独堆肥处理(CK)其 $\text{CO}_2$ 排放速率最高;胡萝卜尾菜单独堆肥处理(CK)及7.5%秸秆添加处理(T1)在堆肥期间含水率较高,易产生渗滤液;通过相关性热图、冗余分析对5个处理的气体排放、腐熟度、酶活性进行显著性、相关性分析,进一步证实 $\text{NH}_3$ 、 $\text{CO}_2$ 的排放与温度呈正相关,与pH值呈负相关关系;同时过氧化氢酶与腐熟度指标有显著正相关关系,纤维素酶活性影响堆肥产品的腐熟度。因此,胡萝卜尾菜好氧堆肥过程中,添加15%玉米秸秆辅料(T2)可以提高C/N比、孔隙度,降低渗滤液产出,同时 $\text{CO}_2$ 排放量较胡萝卜尾菜单独堆肥(CK)降低6.63%。该研究可为胡萝卜尾菜无害化和资源化利用提供技术支持。

**关键词:**堆肥;胡萝卜尾菜;气体排放;酶活性

doi: 10.11975/j.issn.1002-6819.202302115

中图分类号: X713

文献标志码: A

文章编号: 1002-6819(2023)-11-0230-08

许淑妮,冯晓璐,陈延玲,等.添加玉米秸秆对胡萝卜尾菜堆肥过程的影响[J].农业工程学报,2023,39(11):230-237.

doi: 10.11975/j.issn.1002-6819.202302115 <http://www.tcsae.org>

XU Shuni, FENG Xiaolu, CHEN Yanling, et al. Effects of adding maize stover on the process of carrot waste composting[J].

Transactions of the Chinese Society of Agricultural Engineering (Transactions of the CSAE), 2023, 39(11): 230-237. (in Chinese

with English abstract) doi: 10.11975/j.issn.1002-6819.202302115 <http://www.tcsae.org>

## 0 引言

近年来,中国蔬菜年产量呈不断增加的趋势,2021年中国蔬菜产量高达 $7.75 \times 10^8\text{ t}^{[1]}$ 。与此同时,蔬菜在收获后残留的尾菜产量也随之不断增加,每年年产废弃物达3t左右<sup>[2]</sup>,其中超过60%的尾菜未经处理丢弃在田间大棚中、河流及道路两旁、农贸市场。随意丢弃的尾菜不仅释放污染气体,还存在潜在的病原体传播,对环境造成严重的影响<sup>[3-4]</sup>。胡萝卜尾菜的产量较大,其富含植物所需的营养物质,但易腐烂变质,散发病原菌。目前,对于尾菜的处理方式大多为生成饲料、生成能源、直接还田、生成肥料、厌氧消化生物质回收。虽然饲料化、能源化可有效解决尾菜的资源化再利用,但其生产设备投资大,技术复杂,难以推广;就地还田虽然简单且成本低,但无法控制病虫害的传播,同时该方式渗滤液产生较多,污染环境风险大<sup>[5-6]</sup>。厌氧消化、生物质回收在作为液肥和能源回收领域有所潜力,但存在技术经济因素、生产效率较低和运行控制条件难等问题<sup>[7]</sup>。肥料化

是利用高温好氧堆肥生产有机肥料,其所需设备简单,腐熟周期短,且被广泛应用于固体有机废物处理<sup>[8]</sup>。

高温好氧堆肥是废弃物肥料化的重要方法之一,可以将尾菜转化为稳定和有价值的有机肥料,可以改善土壤质量和促进植物生长<sup>[9]</sup>。而尾菜单独进行堆肥受限于其C/N比低、含水率高等问题<sup>[10]</sup>,难以进行高质量的好氧发酵<sup>[11]</sup>,且在堆肥期间易产生渗滤液,后期难以进行管理。目前,对于尾菜堆肥的研究已有在添加剂对堆肥生产效率和堆肥质量领域的探索<sup>[12]</sup>,堆肥辅料的添加可以调节物料的物理化学性质,从而进行更有效的堆肥<sup>[13]</sup>,如废弃的蘑菇种植基质和农林废弃物<sup>[14]</sup>。农林废弃物玉米秸秆是一种常用的堆肥辅料,与胡萝卜尾菜在同一区域产生,其年产量在中国达 $26.4 \times 10^8\text{ t}^{[15]}$ ,亟需进行资源化利用。

此外,堆肥过程中二氧化碳( $\text{CO}_2$ )、氨气( $\text{NH}_3$ )等气体的排放会对环境造成二次影响<sup>[16]</sup>,碳、氮元素的损失会降低堆肥品质<sup>[17]</sup>。而堆肥初期主要由水解酶(脲酶、蔗糖酶、纤维素酶等)促进矿质化作用;后期主要由氧化还原酶(过氧化氢酶、多酚氧化酶等)发生腐殖化反应<sup>[18-19]</sup>。酶的活性直接受温度、水分、pH值、养分利用率以及堆肥物料的理化性质影响<sup>[20]</sup>。因此,酶活性不仅决定堆肥的速度,还会影响堆肥产品的质量。阐明与胡萝卜尾菜同源产生的农林废弃物作为辅料对堆肥过程中的腐熟度、气体排放和酶活性的响应关系及调控作

收稿日期: 2023-02-21 修订日期: 2023-06-01

基金项目: 山东省自然科学基金项目(ZR2022QD038); 中央引导地方科技发展专项(22-1-3-7-zyyd-nsh); 山东特色作物种植区肥料施用性能研究(20220045)

作者简介: 许淑妮,研究方向为有机肥高值化。

Email: xushuni2021@163.com

※通信作者: 李贇, 博士, 副教授, 研究方向为有机肥高值化。

Email: liyun@qu.edu.cn



## High-Value Processing and Utilization for Digested Manure Effluent Treatment: Advances and Challenges

Yun Li<sup>1</sup> · Shuni Xu<sup>1</sup> · Jiuzhou Li<sup>1</sup> · Shanshan Li<sup>1</sup> · Xiaohan Zhang<sup>2</sup> · Xiaomin Xie<sup>2</sup>

Accepted: 13 August 2022  
© The Author(s), under exclusive licence to Springer Nature Switzerland AG 2022

### Abstract

**Purpose of Review** Digested manure effluent is a potential resource for the production of liquid organic fertilizer and reused water. The purpose of this review is to provide a comprehensive understanding on the advances and challenges to high-value processing and utilization for digested manure effluent treatment.

**Recent Findings** The main problem that restricts the utilization of digested manure effluent is that there is not enough land for consumption. Reasonable and efficient treatment of digested manure effluent is the key to promoting healthy development and sustainable operation. Digested manure effluent can increase yield, improve quality, and enhance the stress resistance of crops. In addition, digested manure effluent can also be used in seed soaking and feed applications. Membrane treatment techniques for the concentration of digested manure effluent can recover water and produce liquid fertilizer. It mainly includes pressure-driven membrane, osmotic-driven membrane, membrane distillation, and their combined technologies. However, membrane concentration of digested manure effluent still has challenges such as high cost and membrane fouling that restrict development. Thus, several potential approaches have been proposed to address these challenges. These approaches can be largely classified as pretreatment, process optimization, and government-guided source control.

**Summary** In this paper, we critically reviewed the properties and utilization of digested manure effluent. Meanwhile, the performance of different membrane concentration processes was provided. Furthermore, key technical challenges of high-value processing and their potential countermeasures were delineated.

**Keywords** Digested manure effluent · Resource recovery · Utilization · Membrane treatment

### Introduction

With rapid economic development, intensive and large-scale livestock and poultry breeding have become an important part of agricultural production. The total output of manure in China exceeds 4.2 billion tons each year. However, the related pollution prevention and treatment is relatively lagging. In addition, manure contains heavy metals, antibiotics,

and other substances, which may cause serious pollution to ecological health.

At present, anaerobic fermentation technology is widely used in the field of manure treatment. In a closed anaerobic environment, anaerobic fermentation is the process of producing methane from organic matter through the metabolic activities of various anaerobic microorganisms [1]. Anaerobic fermentation can not only reduce the amount of manure but also generate clean biogas energy, which is of great significance for solving manure pollution and protecting the ecological environment [2]. There are nearly 5000 large- and medium-sized biogas plants in China, and the number of rural biogas projects is nearly 100,000. In addition, the Chinese government has formulated a series of policies and regulations to promote the utilization of biomass energy. At the same time, traditional energy sources such as coal and oil are becoming increasingly depleted and accompanied by pollution. Therefore, the use of biogas projects to develop biomass energy is a necessary way to adjust the energy structure.

This article is part of the Topical Collection on *Water Pollution*

✉ Yun Li  
liyun@qau.edu.cn

✉ Xiaomin Xie  
xiexiaomin@sdu.edu.cn

<sup>1</sup> College of Resources and Environmental Sciences, Qingdao Agricultural University, Qingdao 266109, China

<sup>2</sup> School of Environmental Science and Engineering, Shandong University, Qingdao 266237, China



Cite this: *Environ. Sci.: Water Res. Technol.*, 2022, 8, 1011

## Filtration with cornstalks as a pre-treatment process to control membrane fouling in the concentration of biogas slurry: performance, mechanism and economic analysis†

Yun Li,<sup>a,b</sup> Shuni Xu,<sup>a</sup> Mingcan Zhao,<sup>a</sup> Yuan Song,<sup>a</sup> Zhiqi Wang<sup>a</sup> and Xiaomin Xie<sup>\*c</sup>

Anaerobic fermentation produces biogas slurry as a by-product of clean energy, which poses a severe challenge for the sustainable management of livestock farms. Clean water can be obtained and nutrients can be enriched through membrane treatment of biogas slurry. Membrane processes without pre-treatment cause serious membrane fouling. In this study, three different densities of cornstalk filling were selected to filter biogas slurry and the impact of the pre-treatment on the subsequent membrane process was studied. The results demonstrate the techno-economic feasibility of filtration with cornstalks as a pre-treatment for membrane concentration. Control of membrane fouling after cornstalk filtration was achieved by intercepting suspended solids in the biogas slurry. Filtration through the high density (150 kg m<sup>-3</sup>) packing material had the best filtering effect. In particular, the best removal rates of TP, turbidity, and COD in the biogas slurry after filtration with cornstalk were more than 60%, 50%, and 25%, respectively. Resistance of the mud cake layer accounted for more than 80% of the total membrane resistance during the membrane treatment. The adsorption of pollutants inside the membrane pores is the main mechanism of membrane pore blockage. Membrane treatment after filtration would be more economically favorable than direct membrane treatment in practical applications despite the increased cost of using cornstalks. This study provides a technical reference for the high-value utilization of biogas slurry.

Received 19th January 2022,  
Accepted 25th February 2022

DOI: 10.1039/d2ew00051b

rsc.li/es-water

### Water impact

Membrane treatment holds promise for agricultural wastewater treatment and reuse. However, the membrane process without pretreatment causes serious membrane fouling. In this study, we demonstrate the techno-economic feasibility of concentrating biogas slurry via filter pretreatment by highlighting the outperformance of pretreatment over direct membrane processing. This study provides a low-cost technique to manage biogas slurry for sustainable agriculture.

## 1. Introduction

Anaerobic fermentation is an effective means for the treatment of livestock and poultry manure,<sup>1</sup> and it produces by-products such as biogas residue and biogas slurry while producing clean energy.<sup>2,3</sup> The solid part, *i.e.* the biogas residue, can be easily used as an organic fertilizer, while the liquid part, *i.e.* the biogas

slurry, poses a severe challenge for the sustainable management of livestock farms.<sup>4</sup> The utilization methods of biogas slurry are numerous and mainly include natural purification, factory processing, and high-value utilization.<sup>5,6</sup> As a form of high-value utilization, membrane treatment has become a wide public concern over the recent years.<sup>7–9</sup> Clean water can be obtained and nutrients in biogas slurry can be enriched through membrane treatment. However, the composition of biogas slurry is complex and the content of suspended solids is too high.<sup>10,11</sup> Membrane treatment without pre-treatment can cause serious membrane fouling. Therefore, it is necessary to remove large particles in biogas slurry in an appropriate way to reduce subsequent membrane fouling.

There have been a few studies on using sand filtration or bag filtration as a form of pre-treatment before membrane treatment.<sup>3,12–14</sup> However, this pre-treatment necessitates

<sup>a</sup> College of Resources and Environmental Sciences, Qingdao Agricultural University, Qingdao 266109, China

<sup>b</sup> Guangdong Provincial Key Laboratory of Agricultural & Rural Pollution Abatement and Environmental Safety, Guangzhou 510642, China

<sup>c</sup> School of Environmental Science and Engineering, Shandong University, Qingdao 266237, China. E-mail: xieziaomin@sdu.edu.cn

† Electronic supplementary information (ESI) available. See DOI: 10.1039/d2ew00051b

附件 5：软件著作权“浒苔基生物炭制备精准控制系统”第四位次

**中华人民共和国国家版权局**  
**计算机软件著作权登记证书**

证书号： 软著登字第10891391号

软件名称： 浒苔基生物炭制备精准控制系统  
V1.0

著作权人： 王格格;李赟;谢秉辰;许淑妮;冯晓璐;解晓敏

开发完成日期： 2022年11月18日

首次发表日期： 2022年11月18日

权利取得方式： 原始取得

权利范围： 全部权利

登记号： 2023SR0304220

根据《计算机软件保护条例》和《计算机软件著作权登记办法》的规定，经中国版权保护中心审核，对以上事项予以登记。


No. 12349635

  
2023年03月07日

附件 6：软件著作“基于腐熟堆肥产品的碳基有机肥造粒工艺控制系统 V1.0”  
第三位次



附件 7：三类竞赛，国家级，全国农科研究生乡村振兴志愿服务成果，一等奖（第五位次）





附件 8：二类竞赛，国家级，“建行杯”第十六届全国大学生节能减排社会实践与科技竞赛，三等奖（首位）



## 附件 9：四类竞赛，校级，第五届青岛农业大学节能减排社会实践与科技竞赛，一等奖（首位）

### 关于公布第五届青岛农业大学节能减排社会实践与科技竞赛获奖名单的通知

2023-06-06 12:31:49 浏览数: 107

节能减排是深入贯彻落实科学发展观，助力伟大中国梦的实现，构建社会主义和谐社会的重大举措。5月10日，由创新创业学院主办，机电工程学院、资源与环境学院、建筑工程学院承办的《第五届青岛农业大学节能减排社会实践与科技竞赛暨2023年“建行杯”第十六届全国大学生节能减排社会实践与科技竞赛选拔赛》汇报答辩在线上顺利举行。资源与环境学院、机电工程学院、建筑工程学院、化学与药学院、巴瑟斯未来农业科技学院等6个学院多支队伍参加了现场汇报答辩。

在校赛汇报答辩环节，选手充分利用PPT、视频、动画等方式对参赛作品进行了全方位讲解。专家评委们从作品科学性、创新性、节能性、环保性和应用效果等方面对作品申报材料进行了严格审阅和现场打分。经专家评委综合评议后，评选出一等奖6项、二等奖9项、三等奖10项。拟推荐一等奖、二等奖获奖作品参加“建行杯”第十六届全国大学生节能减排社会实践与科技竞赛国赛角逐。

具体获奖名单公布如下：

序号	团队或作品名称	团队队长	获奖等级
1	阳光小队	董雅楠	一等奖
2	电驱助农—面向丘陵山区的新能源动力装备	吕延士	一等奖
3	“热电节能”—微环境制冷调温新势力	杨鑫航	一等奖
4	尾菜高温堆肥化处理技术与装置设计	许淑妮	一等奖
5	浮萍碳微球多功能水处理吸附剂“环萍”小队	王玉婷	一等奖

## 参与项目证明

项目“绿色智慧药肥技术服务与应用”，研究生许淑妮，学号 20212108022 参与本项目调研工作及技术报告撰写工作，特此证明！

项目负责人（签字）：



附件 11：参编专业相关书籍著作，编写者

《科技小院：课堂在田间  
青岛农业大学科技小院人才培养之路》

编委会

主 编：陈延玲 辛言君 崔德杰

副 主 编：张妮妮 朱少叶 宁 刚 黄有松

李 赞 陈东杰

参编人员：郭梦瑶 唐文慧 仇恒浩 姜晓芹

李久洲 蒋 伟 孔忠良 赵 颖

张培强 许淑妮 张翠悦 刘晓宇

刘子瑄 卢瑞芸 马艺纯 孟 璐

秦 靖 孙慧婷 范敬文 李 丹

刘腾腾 马胜锡 毛翔荣 王竹雨

徐云耀

附件 12：参加国家级，2022 年第十六届全国堆肥技术与工程研讨会

**双碳创新团队(10)**

李学群老师

李学群(心做良田耕耘百年) 邀请您参加腾讯会议

会议主题: 2022 年第十六届全国堆肥技术与工程研讨会

会议时间: 2022/11/05 07:30-18:30 (GMT+08:00) 中国标准时间 - 北京

重复周期: 2022/11/05-2022/11/06 07:30-18:30, 每天

点击链接入会, 或添加至会议列表:

<https://meeting.tencent.com/dm/HlyNNQFjoGBo>

#腾讯会议: 487-7979-3148

会议直播: <https://meeting.tencent.com//RdoDsUND39fd>

与会地点: 湖北、苏州、北京

复制该信息, 打开手机腾讯会议即可参与

11月5日 上午09:09

路边的草花

7 张国栋老师

中国农业大学 资源与环境学院  
College of Resources and Environmental Sciences, China Agricultural University

**2022年第十六届  
全国堆肥技术与工程研讨会**

直 | 播 | 预 | 告

李季 李国学 彭生平

中国农业大学资源与环境学院 教授 中国农业大学资源与环境学院 教授 北京沃土天地环保科技有限公司 董事长  
中国农业大学农机装备研究院(苏州) 副院长

直播时间 2022年11月5日-11月6日 8:00-18:00

微信扫码参会

特邀单位:  
万科公益基金会  
合作单位:  
荆门法麦克斯农业科技有限公司、维尔利环保科技集团股份有限公司、上海文鑫生物科技有限公司、青岛瑞辰永泰环保科技有限公司

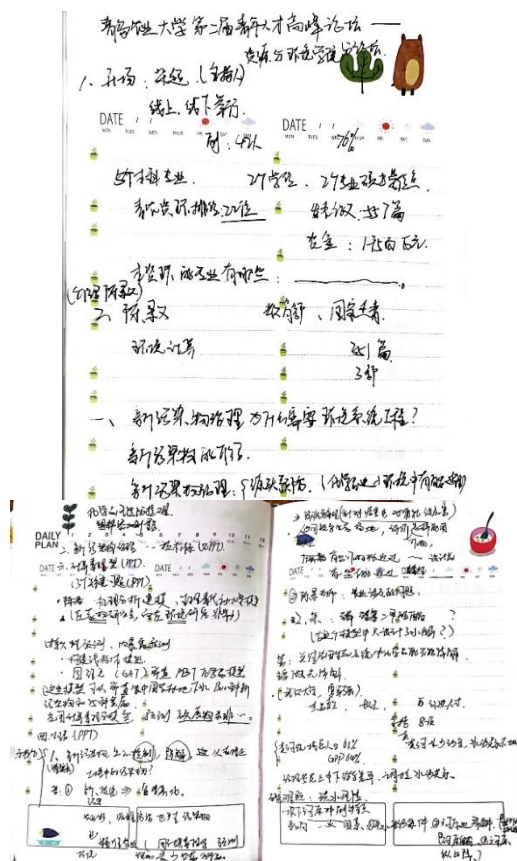
展望

- ✓从技术工艺优化方面, 应考虑农林废弃物的季节性, 一方面充分考虑其他辅料作为替代和备选, 另一方面需考虑辅料存储。
- ✓从一次性设备投资及装备改造方面, 建议增加混料和翻抛装置。对于发酵过程产生的大量冷凝水, 应考虑增加单独的冷凝水收集管道和处理工艺。
- ✓进一步地为解决北京市厨余垃圾资源化利用的迫切需求, 需逐步提升南宫菌肥厂处理量, 从工艺和装备改进、以及发酵车间增容方面不断优化, 可提升处理量至3000吨/天以上。

附件 13: 参加校级, 第一届青岛农业大学青年虹扬学术论坛



附件 14: 参加校级, 青岛农业大学第二届青年人才高峰论坛



附件 15: 参加校级, 青岛农业大学第十一届研究生学术论坛(资环学院分论坛)

青岛农业大学第十一届研究生学术论坛  
(资环学院分论坛) 签到表

206班				207班			
序号	姓名	签到	签退	序号	姓名	签到	签退
1	曹梦寒	曹梦寒	✓	1	陈孟欣	陈孟欣	✓
2	邓文迪	邓文迪	✓	2	程奔	程奔	✓
3	邓艺璇	✓	✓	3	冯芯蕊	冯芯蕊	✓
4	董雅楠	董雅楠	✓	4	高春伟	高春伟	✓
5	高枫舒	高枫舒	✓	5	韩震	韩震	✓
6	高洁	高洁	✓	6	黄丽萍	黄丽萍	✓
7	韩鹏展	韩鹏展	✓	7	姬广庆	姬广庆	✓
8	金岩松	金岩松	✓	8	季泓旭	季泓旭	✓
9	李志	李志	✓	9	李佳欣	李佳欣	✓
10	马俊豪	马俊豪	✓	10	李雪亮	李雪亮	✓
11	元凯霞	元凯霞	✓	11	刘文倩	刘文倩	✓
12	石凤银	石凤银	✓	12	鲁欣彤	鲁欣彤	✓
13	宋佳颖	宋佳颖	✓	13	马佳妮	马佳妮	✓
14	宋昕	宋昕	✓	14	庞忠俊	庞忠俊	✓
15	孙云龙	孙云龙	✓	15	任艳欣	任艳欣	✓
16	王东	王东	✓	16	宋华荣	宋华荣	✓
17	王浩权	王浩权	✓	17	孙伟凯	孙伟凯	✓
18	王舰	王舰	✓	18	孙一鸣	孙一鸣	✓
19	王如云	王如云	✓	19	王国霖	王国霖	✓
20	王一晴	王一晴	✓	20	王娜	王娜	✓
21	王雨欣	王雨欣	✓	21	谢宏伟	谢宏伟	✓
22	王梓瑜	王梓瑜	✓	22	许淑璇	许淑璇	✓
23	魏如雪	魏如雪	✓	23	薛玮	薛玮	✓
24	辛青	辛青	✓	24	杨小春	杨小春	✓
25	徐学磊	徐学磊	✓	25	张翠悦	张翠悦	✓
26	闫多森	闫多森	✓	26	张悦怡	张悦怡	✓
27	闫璐婷	闫璐婷	✓	27	张培强	张培强	✓
28	杨梦达	杨梦达	✓	28	张笑笑	张笑笑	✓
29	尹冰杰	尹冰杰	✓	29	赵梦焱	赵梦焱	✓
30	尹宏亮	尹宏亮	✓	30	赵艺帆	赵艺帆	✓
31	于瑞康	于瑞康	✓	31	赵颖	赵颖	✓
32	张楷悦	张楷悦	✓	32	周欢	周欢	✓
33	张小龙	张小龙	✓	33	朱鑫宇	朱鑫宇	✓
34	张哲宁	张哲宁	✓	34	孙直君	孙直君	✓
35	周明晶	周明晶	✓	35	王鲁军	王鲁军	✓
36	朱晓雪	朱晓雪	✓				
37	朱子晗	朱子晗	✓				

附件 16: 参加院级, 资源与环境学术论坛

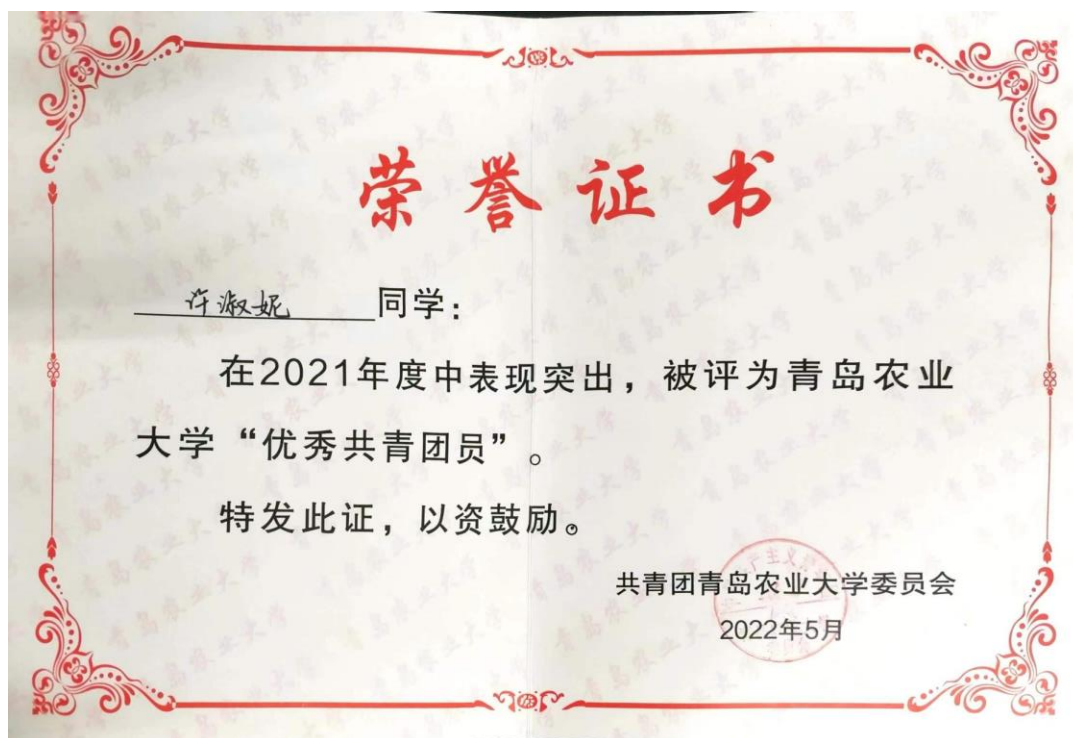


附件 17: 参加院级, 资源与环境学院学科发展与专业建设座谈会





附件 18：校级，2021 年度“优秀共青团员”



附件 19：院级，心理发展部部长，优秀





附件 20: 参加学校和学院组织的社会实践活动, 志愿者

## 青岛农业大学研究生处文件

青农大研发〔2022〕7号

### 关于公布青岛农业大学 2022 年暑期研究生乡村振兴志愿服务队名单的通知

各单位:

根据《关于做好 2022 年研究生乡村振兴志愿者暑期志愿服务活动的通知》, 经学院申报、专家评审、学校审定, 确定“青岛农业大学莱西萝卜科技小院研究生乡村振兴志愿服务队”等六支服务队为青岛农业大学 2022 年暑期研究生乡村振兴志愿服务队。现将名单予以公布。

附件: 青岛农业大学 2022 年暑期研究生乡村振兴志愿服务队名单

研究生处

2022 年 7 月 16 日

附件:

青岛农业大学 2022 年暑期研究生乡村振兴志愿服务队名单

序号	所在学院	团队名称	立项等级	活动主题	团队负责人	团队人数
1	资源与环境学院	青岛农业大学莱西萝卜科技小院研究生乡村振兴志愿服务队	校级	党建引领一赋能乡村振兴新路径: 技术服务、人才培养、环境治理共融共促	赵颖	8
2	海洋科学与工程学院	青岛农业大学黄河入海水产养殖研究生乡村振兴志愿服务队	校级	志愿服务助力乡村振兴, 黄河战略携手美好未来	李兴涛	10
3	资源与环境学院	青岛农业大学乐陵市科技小院研究生乡村振兴志愿服务队	校级	科技小院助力农业技术服务与美丽乡村建设	姜晓芹	7
4	资源与环境学院	青岛农业大学崂山探究农业生产研究生乡村振兴志愿服务队	校级	厚植三农情怀, 助力乡村振兴	安琪	7
5	资源与环境学院	青岛农业大学莱西粮油作物科技小院研究生乡村振兴志愿服务队	校级	科技在农村遍地生根—技术服务、产业帮扶、社会调查	张培强	7
6	草业学院	青岛农业大学沿黄流域草业科技研究生乡村振兴志愿服务队	校级	挖掘乡土草种质, 助力盐碱地开发利用	王洪杰	7

备注:

资助每支校级 2022 年暑期研究生乡村振兴志愿服务队不超过 5000 元的活动经费, 用于报销志愿服务活动相关的支出, 凭借活动立项申请表、活动总结报告、活动成果等报销。主要包括: (1) 服务队志愿者和指导教师的人身意外伤害保险; (2) 服务队志愿者和指导教师的差旅差旅调研费用; (3) 志愿服务活动相关的材料费与资料费等。

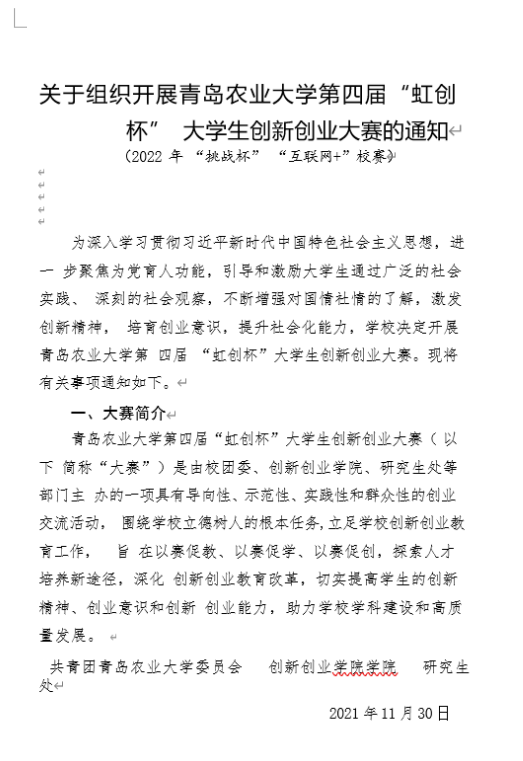
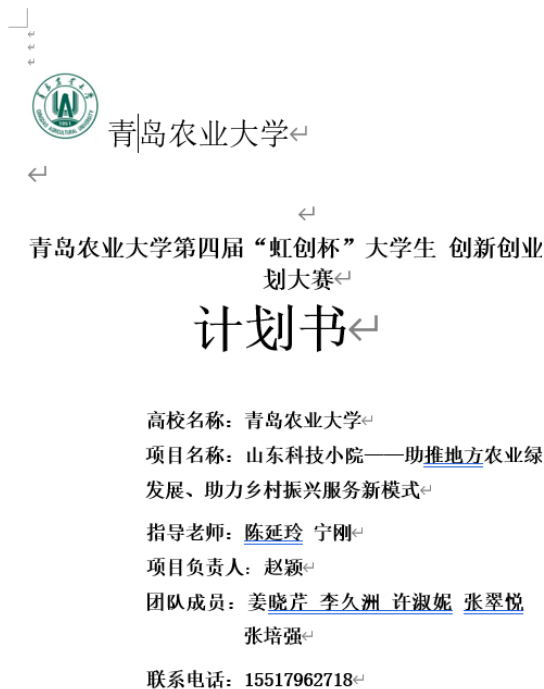
附件 21：参加省级，山东省大学生就业创业知识竞赛，参与奖



附件 22：参加省级，山东省首届大学生英语口语大赛，参与奖



附件 23：参加校级，青岛农业大学第四届“虹创杯”大学生创新创业计划大赛，参与奖



附件 24: 校级, 知网杯竞赛, 参与奖

The image shows a WeChat message from '孟新翔老师' (Mr. Meng Xinxiang) containing a URL: <https://ehall.qau.edu.cn/publicapp/sys/bulletin/bulletinDetail.do?WID=272177742881304359845004439464387#/bulletinDetail>. Below the message is a QR code and a notice about the competition.

The notice, titled '关于举办“知网杯”信息检索技能大赛的通知', provides the following details:

- 为进一步加强广大师生了解并掌握数字资源的使用技巧, 提高大家文献检索、信息获取活动安排如下:
- 一、活动时间: 2022年11月11日-18日
- 二、活动对象: 全校师生
- 三、活动形式: 线上比赛
- 四、参与方式: 读者可通过以下两种方式参加竞赛:  
方式一: 扫描下方二维码进入活动参与答题。

方式二: 关注“青岛农业大学图书馆”微信公众号, 选择“专题活动-阅读推广”栏目  
温馨提示: 首次访问活动平台须使用手机等登录, 首次登录需将个人信息填写完整;

五、活动规则:

1. 竞赛题目内容涉及图书馆数字资源利用、学术资源检索等方面, 答案均可在图书馆;
2. 竞赛题目从题库中随机选取, 共30题, 其中单选题10题、判断题10题, 每题3分, 多分钟。
3. 开始答题后, 每人可答题1次, 中途退出答题页面视为放弃答题, 视为0分并不计入;
4. 本次知识竞赛按答题总分成绩从高到低排序。答题分数相同者以答题时间为排名依据; 排名按查看名次变化。
5. 竞赛活动杜绝任何形式的作弊行为, 一经发现取消获奖资格。严禁同一读者使用多;
6. 所有参赛者均视为阅读并同意遵守相应活动规则, 主办方拥有对活动的最终解释权。

六、奖项设置:

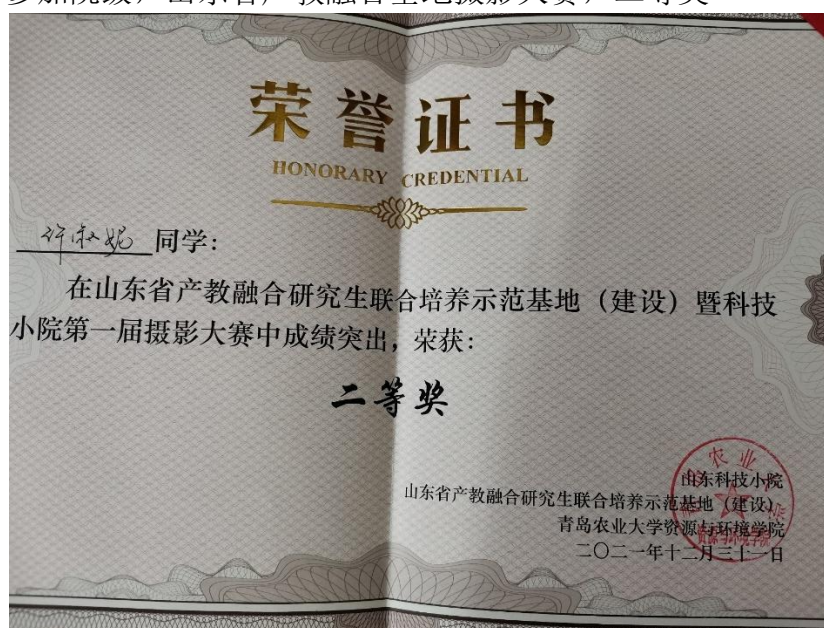
- 一等奖1名, 获奖证书及华为 (HUAWEI) WATCH FIT 2 华为智能手表

二等奖3名, 索尼 (SONY) WH-CH710N 无线降噪立体声耳机

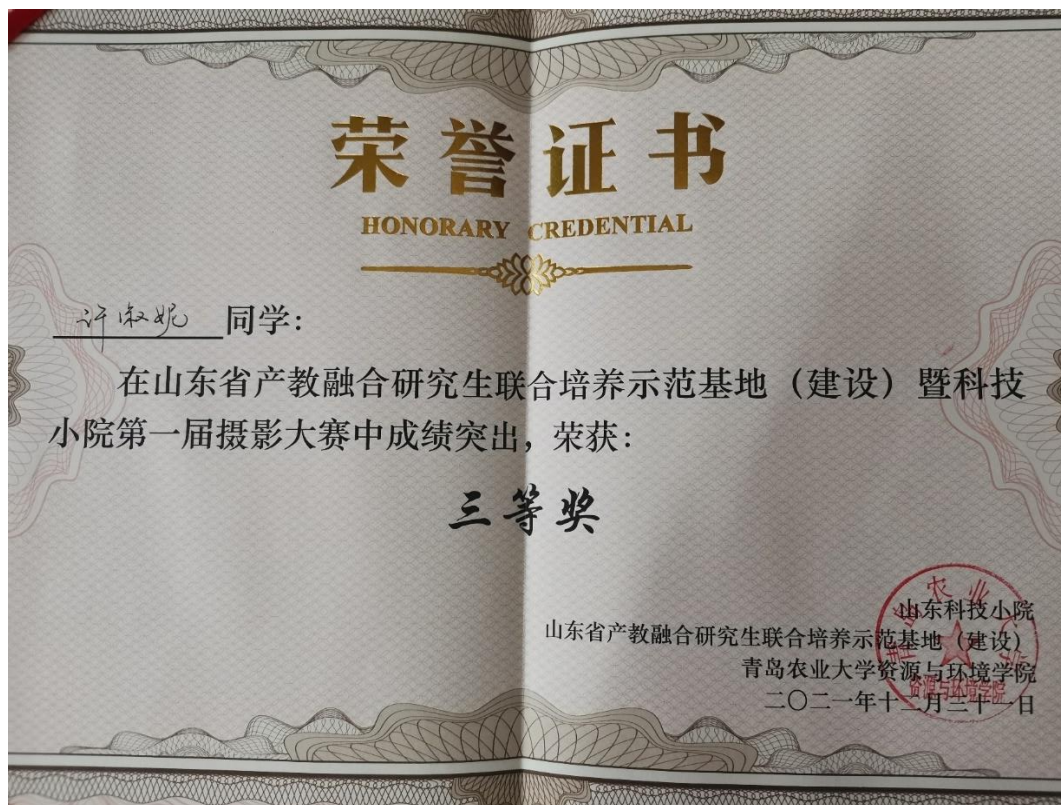
The right side of the image shows the competition results page for the '“知网杯”信息检索技能大赛'. The user's score is 48, with a time of 354 seconds and 0 remaining questions. The current ranking is 193. A list of other participants follows:

Rank	Username	Score	Time
1	用户9207	97分	736.1秒
2	用户0635	94分	135.7秒
3	真的很强	91分	245.7秒
4	用户5213	90分	292.2秒
5	用户5123	90分	324.2秒
6	艺术学院小韩	89分	338.6秒
7	用户4735	88分	256秒
8	用户0501	87分	177.9秒
9	用户6396	87分	400.0秒

附件 25: 参加院级, 山东省产教融合基地摄影大赛, 二等奖



附件 26：参加院级，山东省产教融合基地摄影大赛，三等奖



附件 27：参加院级，山东省产教融合基地暨科技小院 2021 年度学术报告，三等奖



附件 28：2022 年获得优秀宿舍 1 次

2022.10.28宿舍检查情况.xlsx				
文件预览				
Sheet1				
		H	I	J
1				
2	号	学院	优秀宿舍	备注
3		资源与环境学院	17#208	
4		资源与环境学院	17#213	
5		动物医学院	17#229	
6		化学与药学院	19#106	
7				
8				
9				
10				

## 宋佳颖评选材料清单

附件 1: 中科院 1 区 TOP 期刊 SCI 论文, 第一作者

附件 2: 中科院 2 区 TOP 期刊 SCI 论文, 第二作者

附件 3: 中科院 1 区 TOP 期刊 SCI 论文, 第三作者

附件 4: 第十五届山东省大学生环保创意大赛省级三等奖

附件 5: 第五届青岛农业大学节能减排社会实践与科技竞赛校级三等奖

附件 6: 第四届青岛农业大学节能减排社会实践与科技竞赛校级三等奖

附件 7: 参与导师科研项目

附件 8: 参加国家级学术会议并作报告

附件 9: 参加学院组织的学术会议 4 次

附件 10: 2021-2022 学年青岛农业大学优秀研究生干部

附件 11: 学生干部任职

附件 12: 社会实践—青岛农业大学“青春向阳”大学生社区实践计划

附件 13: “知网杯”信息检索技能大赛校级三等奖

附件 14: 山东省产教融合研究生联合培养示范基地(建设)暨科技小院 2021 年度学术报告会院级二等奖

附件 15: 青岛农业大学第一届研究生乡村振兴科技强农+创新大赛科技作品竞赛校级三等奖



报告编号：QAUZJ2023-050

# 检索报告

## 一、检索要求

1. 委托人：刘国成
2. 委托单位：青岛农业大学
3. 检索目的：论文被 SCI-E 收录及所在期刊的影响因子和中科院分区情况

## 二、检索范围

Science Citation Index Expanded (SCI-EXPANDED)	2012-present	网络版
Social Sciences Citation Index (SSCI)	2012-present	网络版
JCR-(Journal of Citation Report)	1997-2022	网络版
中国科学院文献情报中心期刊分区表	2005-2022	网络版

## 三、检索结果

委托人提供的2篇论文被SCI-E收录，论文及其所在期刊的影响因子和中科院分区详细情况见附件一。

特此证明！

青岛农业大学图书馆

(盖章)

检索报告人：张静

2023年9月14日



附件一:

2 record(s) printed from Clarivate Web of Science

**第 1 条, 共 2 条**

**标题:** Highly efficient nanocomposite of Y2O3@biochar for oxytetracycline removal from solution: Adsorption characteristics and mechanisms

**作者:** Song, JY (Song, Jiaying); Lu, L (Lu, Lun); Wang, J (Wang, Jian); Li, X (Li, Xue); Li, JY (Li, Jinying); Wang, QW (Wang, Qianwen); Du, HY (Du, Haiyan); Xin, SS (Xin, Shuaishuai); Xu, LA (Xu, Lina); Yan, QH (Yan, Qinghua); Zhou, CZ (Zhou, Chengzhi); Liu, GC (Liu, Guocheng); Xin, YJ (Xin, Yanjun)

**来源出版物:** BIORESOURCE TECHNOLOGY **卷:** 385 **文献号:** 129380 **DOI:** 10.1016/j.biortech.2023.129380 **提前访问日期:** JUN 2023 **出版年:** OCT 2023

**Web of Science 核心合集中的 "被引频次":** 0

**被引频次合计:** 0

**入藏号:** WOS:001030152400001

**文献类型:** Article

**地址:** [Song, Jiaying; Wang, Jian; Li, Xue; Li, Jinying; Du, Haiyan; Xin, Shuaishuai; Yan, Qinghua; Zhou, Chengzhi; Liu, Guocheng; Xin, Yanjun] Qingdao Agr Univ, Coll Resource & Environm, Qingdao Engn Res Ctr Rural Environm, Qingdao 266109, Peoples R China.

[Lu, Lun] Minist Ecol & Environm, South China Inst Environm Sci, State Environm Protect Key Lab Environ Pollut Hlth, Guangzhou 510655, Peoples R China.

[Wang, Qianwen] Qingdao Agr Univ, Instrumental Anal Ctr, Qingdao 266109, Peoples R China.

[Xu, Lina] Qingdao Agr Univ, Coll Landscape Architecture & Forestry, Qingdao 266109, Peoples R China.

**通讯作者地址:** Liu, GC (通讯作者), Qingdao Agr Univ, Coll Resource & Environm, Qingdao Engn Res Ctr Rural Environm, Qingdao 266109, Peoples R China.

**电子邮件地址:** lg@qau.edu.cn

**Affiliations:** Qingdao Agricultural University; Qingdao Agricultural University; Qingdao Agricultural University

**研究方向:** Agriculture; Biotechnology & Applied Microbiology; Energy & Fuels

**ISSN:** 0960-8524

**eISSN:** 1873-2976

**输出日期:** 2023-09-14

**期刊影响因子 (2022):** 11.4

**中科院分区升级版 (2022):**

BIORESOURCE TECHNOLOGY

刊名	BIORESOURCE TECHNOLOGY
年份	2022
ISSN	0960-8524
Review	否
Open Access	否
Web of Science	SCIE

学科	分区	Top期刊
大类	工程技术	1 是
	AGRICULTURAL ENGINEERING 农业工程	1
小类	BIOTECHNOLOGY & APPLIED MICROBIOLOGY 生物工程与应用微生物	1
	ENERGY & FUELS 能源与燃料	1





# Highly efficient nanocomposite of $Y_2O_3$ @biochar for oxytetracycline removal from solution: Adsorption characteristics and mechanisms

Jiaying Song<sup>a</sup>, Lun Lu<sup>b</sup>, Jian Wang<sup>a</sup>, Xue Li<sup>a</sup>, Jinying Li<sup>a</sup>, Qianwen Wang<sup>c</sup>, Haiyan Du<sup>a</sup>, Shuaishuai Xin<sup>a</sup>, Lina Xu<sup>d</sup>, Qinghua Yan<sup>a</sup>, Chengzhi Zhou<sup>a</sup>, Guocheng Liu<sup>a,\*</sup>, Yanjun Xin<sup>a</sup>

<sup>a</sup> Qingdao Engineering Research Center for Rural Environment, College of Resource and Environment, Qingdao Agricultural University, Qingdao 266109, China

<sup>b</sup> State Environmental Protection Key Laboratory of Environ Pollut Health Risk Assessment, South China Institute of Environmental Sciences, Ministry of Ecology and Environment, Guangzhou 510655, China

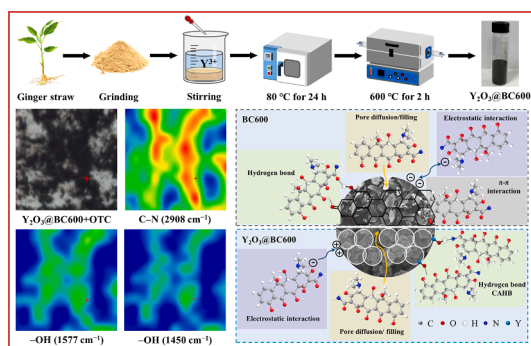
<sup>c</sup> Instrumental Analysis Center of Qingdao Agricultural University, Qingdao 266109, China

<sup>d</sup> College of Landscape Architecture and Forestry, Qingdao Agricultural University, Qingdao 266109, China

## HIGHLIGHTS

- A novel nano  $Y_2O_3$ -modified biochar composite ( $Y_2O_3$ @BC600) was synthesized.
- $Y_2O_3$ @BC600 exhibited excellent adsorption for oxytetracycline of 223.46 mg/g.
- Removal mechanisms of aqueous oxytetracycline by  $Y_2O_3$ @BC600 were clarified.
- $Y_2O_3$ @BC600 showed better anti-interference ability, stability, and reusability.

## GRAPHICAL ABSTRACT



## ARTICLE INFO

### Keywords:

Biochar  
 $Y_2O_3$   
 Antibiotic  
 Removal  
 Charge-assisted hydrogen bond

## ABSTRACT

Nano  $Y_2O_3$ -modified biochar composites ( $Y_2O_3$ @BC600) were fabricated successfully and exhibited great adsorption toward oxytetracycline (OTC). The Langmuir adsorption capacity of  $Y_2O_3$ @BC600-1:4 for OTC reached 223.46 mg/g, 10.52 times greater than that of BC600. The higher dispersion of  $Y_2O_3$  nanoparticles, increased surface area of 175.65 m<sup>2</sup>/g and expanded porosity of 0.27 cm<sup>3</sup>/g accounted for higher OTC adsorption by  $Y_2O_3$ @BC600-1:4.  $Y_2O_3$ @BC600-1:4 could resist the interference of co-existing cations ( $Na^+$ ,  $K^+$ ,  $Mg^{2+}$ ,  $Ca^{2+}$ ) and anions ( $Cl^-$ ,  $NO_3^-$ ,  $SO_4^{2-}$ ) on OTC removal.  $Y_2O_3$  coating changed surface charge property of BC600, favoring the contribution of electrostatic interaction. Synchrotron radiation-based Fourier transform infrared spectroscopy detected obvious peak shift and intensity change of surface -OH when OTC adsorption occurred. Accordingly, stronger H-bonding (charge-assisted hydrogen bond, OTC-H<sub>2</sub>N<sup>+</sup>...HO-Y<sub>2</sub>O<sub>3</sub>@BC600-1:4) was proposed for OTC adsorption.  $Y_2O_3$ @BC600 exhibited renewability and stability in the adsorptive removal of OTC. Therefore,  $Y_2O_3$ @BC600 may be a novel and suitable adsorbent for antibiotic removal.

\* Corresponding author.

E-mail address: [lg@qau.edu.cn](mailto:lg@qau.edu.cn) (G. Liu).

<https://doi.org/10.1016/j.biortech.2023.129380>

Received 18 April 2023; Received in revised form 19 June 2023; Accepted 20 June 2023

Available online 24 June 2023

0960-8524/© 2023 Elsevier Ltd. All rights reserved.

## 1. Introduction

Antibiotics are hailed as human guardians for widespread application in disease prevention and treatment in clinic, livestock, and aquaculture (Kaur Sodhi and Singh, 2022). Increasingly countries are trying to reduce antibiotic use, but the antibiotic market is still expected to reach USD 1.57 trillion by 2024 (Verma et al., 2022). As incomplete metabolism, excessive use and abuse of antibiotics inevitably incur antibiotic residues and metabolites into natural environments (Quaik et al., 2020). Besides, the discharge of sewage and wastes of pharmaceutical enterprises is one of major sources for antibiotic pollution (Xue et al., 2022). To date, antibiotics have been widely distributed in water, soil, sediment and air, regarding as one significant type of emerging pollutants (Okoye et al., 2022). The antibiotics and metabolites can cause several adverse effects on ecosystem and human health, like biotoxicity, intestinal microflora disturbance, and the evolution of drug-resistant bacteria (Leichtweis et al., 2022). Therefore, it is urgently needed to seek simple and efficient technology to eliminate antibiotics in wastewater.

Adsorption is a common method in sewage treatment systems, owing to its numerous advantages including high efficiency, low-cost, and reusability (Cheng et al., 2020). Compared with commercial adsorbents (e.g., activated carbon), biochar attracted great attention as optional carbonaceous adsorbent material and precursor (Xiang et al., 2022). The mechanisms of biochar for adsorptive immobilization of antibiotics primarily involve pore filling, H-bonding, electrostatic effect, and  $\pi$ - $\pi$  interaction (Lu et al., 2020). Its physicochemical properties covering porousness, great surface area, and defective carbonaceous frame favor adsorption capacity (Hamadeen & Elkhatib, 2022). Biomass feedstock for biochar preparation is available in abundance, for instance, rice husk (Li et al., 2020), corn straw (Deng et al., 2022), marine algae waste (Zhao et al., 2022) and groundnut shell (Shakya et al., 2022) were used to prepare biochars, whose had effective adsorption removal for antibiotics. Different from these lignocellulosic biomass, ginger straw contains higher content of alkenes, terpenes, and alcohols, which are unfavorable for direct straw retuning to the field (Zhang et al., 2019b). Furthermore, there is limited research regarding the pyrolysis of ginger straw into biochar for pursuing agronomic and environmental benefits.

In recent years, various modification could be done to enhance adsorption performance and application of biochar materials, including acid/base soaking (Ahsan et al., 2018; Yao et al., 2020), oxidant treatment (Yao et al., 2021), gas activation (Liu et al., 2022), and oxide coating (Qiu et al., 2022). The method of coating metal or metal compounds, like nano iron (Hasan et al., 2020), iron oxide (Xie et al., 2021), zinc oxide (Yang et al., 2022), and layered double hydroxide (Fe/Al) (Tang et al., 2023), was considered a relatively better choice. The improvement of adsorption capacity was primarily attributed to the increase of pore structure and surface area and the change in surface charge. Yttrium oxide ( $Y_2O_3$ ) is widely used in electronic and optical materials because of its physicochemical stability and unique spectroscopy (Guo et al., 2004). Over the lifecycle of  $Y_2O_3$  products, recycling  $Y_2O_3$  waste and the wastewater containing yttrium ions deserves attention greatly. The synthesis of  $Y_2O_3$ @biochar composites using yttrium-containing and biomass wastes may be a feasible strategy for sustainable industry. Point of zero charge (PZC) of  $Y_2O_3$  was  $\sim 7.5$ – $8.0$  (Charisiou et al., 2020; Zhang et al., 2013), higher than that of common crop straw-derived biochars ( $\sim 2$ – $5.5$ ) (Chen et al., 2022; Wang et al., 2007). In aqueous phase,  $Y_2O_3$  modification will alter surface charge properties of biochar, and thus influences electrostatic interaction with targeted contaminant. Besides,  $Y_2O_3$  as metal oxide easily forms ligands with water molecules in solution, leading to hydroxylation of the oxide surface (Lamiri et al., 2015), and  $Y_2O_3$  can provide three hydrogen bond acceptors basing on its chemical formula.  $Y_2O_3$  coating is therefore capable to introduce more adsorption sites onto biochar particles. Overall, nano  $Y_2O_3$ -modified biochar is believed to have good antibiotic adsorption performance, benefitting from complex mechanisms.

The present work therefore developed nano  $Y_2O_3$ -coated biochar composite by one step pyrolysis under oxygen limiting condition to adsorb antibiotic. Oxytetracycline (OTC) is a type of tetracyclines, the global second largest antibiotic in production and use (Leichtweis et al., 2022), and it was selected as target antibiotic contaminant. Batch adsorption kinetic and isotherm were carried out to explore adsorption process and capacity of sorbents toward OTC. The impacts of solution pH and coexisting ions on OTC removal were further investigated. Combined with the characterization of physicochemical properties of  $Y_2O_3$ -modified biochar, possible adsorption mechanisms were analyzed and proposed. Using the biochar-based adsorbent is not only conducive to control antibiotic pollution, but also provides a green and high-added value way for resource utilization of organic wastes.

## 2. Material and methods

### 2.1. Chemicals and materials

The starting feedstock for preparing biochar was ginger straw, which was collected from the farmlands of Shandong province, China. Oxytetracycline hydrochloride (OTC, purity > 98%) was purchased from Shanghai Aladdin Reagent Co. Ltd., China, and other chemical reagents ( $YCl_3$ , NaCl, etc.) were analytical grade.

### 2.2. Preparation and characterization of adsorbents

$Y_2O_3$ -loaded biochars were prepared by the following procedure. The ginger straw was naturally dried, mechanically pulverized, and sieved below 50 mesh (0.28 mm). Then, the powder of ginger straw was soaked in  $YCl_3$  solution with the mass ratio of Y element to biomass feedstock of 1:19, 1:9, and 1:4, and the slurry was desiccated at 80 °C. The pretreated ginger straw was pyrolyzed at 600 °C for 2 h with  $N_2$  protection. After cooling, the carbonized solid was repeatedly washed by deionized water and lastly freeze-dried at  $-60$  °C for gaining  $Y_2O_3$ @BC600 samples, which were labelled as  $Y_2O_3$ @BC600-1:19,  $Y_2O_3$ @BC600-1:9, and  $Y_2O_3$ @BC600-1:4, respectively. For comparison,  $Y_2O_3$  without biomass and the biochar from ginger straw without Y element (BC600) were produced under the same heating condition.

The morphology and microstructure of samples was observed by a scanning electron microscope (SEM, Hitachi Regulus 8100, Japan) coupled with EDAX Genesis apex energy dispersive X-ray spectroscopy and a transmission electron microscope (TEM, FEI Tecnai G2 F20, USA). The as-prepared samples were examined by Raman spectrum (LabRAM HR800, France) with 532 nm wavelength incident laser light. X-ray diffraction (XRD) pattern of adsorbents was conducted using a Bruker D8 ADVANCE (Germany) instrument. The functional group properties of BC600 and  $Y_2O_3$ @BC600 were characterized through an IRTracer-100 Fourier transform infrared spectroscopy (FTIR, Shimadzu, Japan). The adsorbents were treated into 4- $\mu$ m thin sections by a CM1860 microtome (Leica, Germany) for recording the synchrotron radiation-based FTIR (SR-FTIR) in BL01B beamline of Shanghai Synchrotron Radiation Facility (Du et al., 2021).  $N_2$  adsorption-desorption isotherms of the adsorbents were determined by a physisorption system (Builder SSA-7000, China) to analyze surface area and porosity. The specific surface area was calculated by the Brunauer-Emmette-Teller (BET) method basing on the data of  $N_2$  adsorption isotherm. The Barrett-Joyner-Halenda (BJH) model was used to analyze average pore diameter and pore size distribution, and total pore volume was measured at a relative pressure ( $P/P_0$ ) of 0.99. The zeta potential of BC600 and  $Y_2O_3$ @BC600 in water solutions of different pH was measured by a Zetasizer Lab (Malvern, UK) to analyze PZC. Thermogravimetric analysis (TGA) was performed by a Netzsch STA449F5 instrument (German) at temperature range of 30–1000 °C with a heating rate of 10 °C/min under  $N_2$  atmosphere.

### 2.3. Adsorption experiments

Batch experiment system was employed to investigate the adsorption characteristics of OTC on BC600 and Y<sub>2</sub>O<sub>3</sub>@BC600. In brief, the adsorbent samples (10–60 mg) were added into glass bottles containing 36 mL OTC solution, and then shaken at 25 °C, 150 rpm/min in a dark environment. After the centrifugation of suspensions, the supernatants were pipetted and filtered through 0.22-μm membrane to measure residual concentration of OTC in the filtrates. A SIL-20A HPLC (Shimadzu, Japan) was employed to measure OTC concentration with the testing conditions of wavelength 355 nm, C18 column, flow rate 1 mL/min, column thermostat 25 °C and mobile phase 0.1% phosphoric acid solution/acetonitrile (80%/20%) (Zhang et al., 2019a).

The kinetic experiment was performed in 40 mg/L OTC solution at pH 6, and the bottles were routinely taken out from the shaker at 0–72 h for OTC concentration measurement. The experimental conditions for adsorption isotherms were as follows: solution pH 6, OTC concentration range 10–200 mg/L, and equilibrium time 48 h. The environmental conditions (e.g., pH and ions) affect the surface charge of adsorbent and existing-form of adsorbate, thus affecting their contact and interact (Shi et al., 2023). The adsorption systems containing 40 mg/L OTC were therefore set at a series of pH values from 1 to 10 to explore the influence of pH on OTC removal. By adjusting the concentration of Na<sup>+</sup> (0, 0.001, 0.005, 0.01, 0.03, 0.05, 0.1, and 0.2 mol/L) in OTC solution, the impact of ionic strength on OTC sorption was investigated. The effects of coexisting ions on OTC adsorptive removal were conducted by adding cations (K<sup>+</sup>, Na<sup>+</sup>, Mg<sup>2+</sup>, Ca<sup>2+</sup>) and anions (Cl<sup>-</sup>, CO<sub>3</sub><sup>2-</sup>, SO<sub>4</sub><sup>2-</sup>, NO<sub>3</sub><sup>-</sup>, PO<sub>4</sub><sup>3-</sup>) into OTC solutions, respectively. The conditions of this experiment were kept at pH 6, each anion or cation concentration 0.1 mol/L, OTC concentration 40 mg/L, and equilibrium time 48 h.

In addition, the adsorption experiment was conducted in a real wastewater from secondary sedimentation tank of sewage treatment plant. The concentration of OTC in the wastewater was adjusted to 40 mg/L by adding stock OTC solution (1 g/L). After OTC adsorption, Y<sub>2</sub>O<sub>3</sub>@BC600-1:4 was regenerated in 0.3 mol/L NaOH with solid-to-liquid ratio of 1:4. The NaOH-regenerated Y<sub>2</sub>O<sub>3</sub>@BC600-1:4 was washed by deionized water, dried at 80 °C, and subsequently used in the next round of adsorption experiment. The sorbent regeneration was repeated 5 times. Inductively coupled plasma optical emission spectroscopy (ICP-OES, Optima 8000DV, USA) was used to detect free Y ions in the adsorption system. All the samples were repeated three times.

### 2.4. Data analysis

The amounts of antibiotics adsorbed ( $q$ , mg/g) was calculated using following equation (Eq. (1)).

$$q = \frac{(C_0 - C_e)V}{m} \quad (1)$$

where  $C_0$  and  $C_e$  (mg/L) are initial and equilibrium concentration, respectively;  $V$  (L) is solution volume; and  $m$  (g) is adsorbent mass.

The sorption dynamic was fitted by the kinetic models of pseudo first-order and pseudo second-order, Eq. (2) and Eq. (3) respectively, and intra-particle diffusion model (Eq. (4)).

$$\ln(q_e - q_t) = \ln q_e - k_1 t \quad (2)$$

$$\frac{t}{q_t} = \frac{1}{k_2 q_e^2} + \frac{t}{q_e} \quad (3)$$

$$q_t = k_1 t^{1/2} + b \quad (4)$$

where  $q_e$  and  $q_t$  are adsorption capacity at equilibrium time and time  $t$ , respectively;  $k_1$  (min<sup>-1</sup>),  $k_2$  (mg/(g·min)), and  $k_1$  (mg/(g·min<sup>1/2</sup>)) are rate constant of each model, respectively;  $b$  (mg/g) is intercept reflecting the extent of boundary layer thickness.

Langmuir (Eq. (5)), Freundlich (Eq. (6)), and Temkin (Eq. (7)) models were utilized to fit adsorption isotherms.

$$\frac{C_e}{q_e} = \frac{1}{q_m K_L} + \frac{C_e}{q_m} \quad (5)$$

$$\ln q_e = \ln K_F + \frac{1}{n} \ln C_e \quad (6)$$

$$q_e = \frac{RT}{a} \ln(K_T C_e) \quad (7)$$

where  $q_m$  is maximum adsorption amount;  $K_L$  (L/mg),  $K_F$  ((mg/g)/(mg/L)<sup>1/n</sup>), and  $K_T$  (L/g) are Langmuir, Freundlich, and Temkin coefficient, respectively;  $1/n$  is Freundlich constant representing adsorption heterogeneity;  $a$  (J/mol) is Temkin constant representing interaction heat between adsorbent and adsorbate.

Basing on the fitting data of Langmuir model, separation factor ( $R_L$ ) and affinity coefficient ( $K_d$ ) were calculated by Eq. (8) and Eq. (9), respectively.

$$R_L = \frac{1}{1 + K_L C_0} \quad (8)$$

$$K_d = \frac{q_e}{C_e} \quad (9)$$

### 2.5. Statistical analysis

The data were analyzed by SPSS 25.0 with one-way ANOVA, and differences were statistically significant at  $p < 0.05$ .

## 3. Results and discussion

### 3.1. Physicochemical characteristics of adsorbents

The XRD measurement was employed to identify the species of mineral phase in BC600 and Y<sub>2</sub>O<sub>3</sub>@BC600. The ash content of BC600 was 13.22%, and its main mineral crystals were quartz (SiO<sub>2</sub>) and calcite (CaCO<sub>3</sub>), which were detected at  $2\theta$  of 20.9°, 26.7°, 36.6°, 39.5°, 50.2° and 23.0°, 36.0°, 43.2°, 47.6° (see Supplementary material), respectively. These two minerals are common in the biochars from crop straw (Liu et al., 2020). The characteristic diffraction peaks with crystal planes of (211), (222), (400), (440), and (622) were appeared in Y<sub>2</sub>O<sub>3</sub>@BC600, which were well matched with the standard reference of Y<sub>2</sub>O<sub>3</sub> PDF#65-3178 and the XRD pattern of pure Y<sub>2</sub>O<sub>3</sub>. Y<sub>2</sub>O<sub>3</sub>@BC600-1:4 had the strongest XRD peaks of Y<sub>2</sub>O<sub>3</sub> consistent with the mass ratio of Y<sub>2</sub>O<sub>3</sub> to BC600. The diffraction peak for Y<sub>2</sub>O<sub>3</sub> was sharper and stronger at 29.1° than others, suggesting the preferential growth of crystal plane (222).

BC600 had Raman bands for disordered carbon structure at ~1347 cm<sup>-1</sup> and graphitic crystallite at ~1590 cm<sup>-1</sup> (see Supplementary material). Except for these two peaks, there was other Raman peak at 373 cm<sup>-1</sup> in Y<sub>2</sub>O<sub>3</sub>@BC600-1:4, ascribing to phonon energy of Y<sub>2</sub>O<sub>3</sub> (Guo et al., 2004). Guo et al. (2004) also reported that Y<sub>2</sub>O<sub>3</sub> had a FTIR transmittance peak of Y–O at ~460 cm<sup>-1</sup>. For Y<sub>2</sub>O<sub>3</sub>@BC600 samples, Y–O peak overlapped Si–O peak with close FTIR wavelength for SiO<sub>2</sub> of BC600, whereas a weak and sharp peak at ~563 cm<sup>-1</sup> for Y–O could be found in Y<sub>2</sub>O<sub>3</sub>@BC600-1:4 (see Supplementary material). Additionally, the FTIR peaks at 1435 and 1587 cm<sup>-1</sup> for aliphatic and aromatic carbonaceous groups of BC600 were weakened after Y<sub>2</sub>O<sub>3</sub> modification, but an intense and sharp peak was detected at 1443 cm<sup>-1</sup>. The pure Y<sub>2</sub>O<sub>3</sub> possessed sharp FTIR peaks of bonded –OH deformation vibration at 1400, 1520, and 1640 cm<sup>-1</sup> (Aghazadeh et al., 2010), accounting for the complex FTIR peak of Y<sub>2</sub>O<sub>3</sub>@BC600 at this specific region. The results of XRD, Raman, and FTIR demonstrated that crystalline Y<sub>2</sub>O<sub>3</sub> was successfully loaded on ginger straw biochar by direct pyrolysis method.

The zeta potential values of BC600, Y<sub>2</sub>O<sub>3</sub>, and Y<sub>2</sub>O<sub>3</sub>@BC600 were

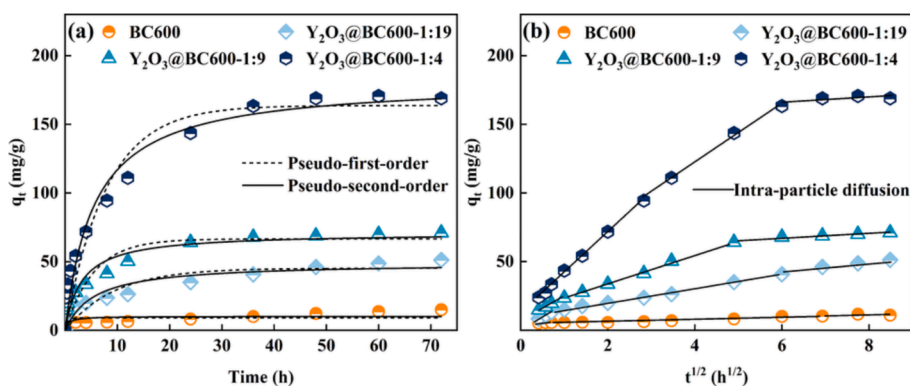


Fig. 1. The kinetics and fitting curves of pseudo first-order and pseudo second-order models (a) and intraparticle diffusion model (b) for OTC adsorption on BC600 and  $Y_2O_3@BC600-1:4$ .

tested in the solutions with various pHs. BC600 surface was positively charged when  $pH < 3$ , while BC600 showed negative zeta potentials at  $pH > 3$  (see Supplementary material). Differently,  $Y_2O_3@BC600-1:4$  had positive charges at  $pH \leq 7.5$  but negative charges at  $pH \geq 8$ . This result suggested that  $Y_2O_3$  modification could alter the surface charge properties of BC600. The point of zero charges ( $pH_{pzc}$ ) of pure  $Y_2O_3$  was about 7.88. The modification of  $Y_2O_3$  increased the  $pH_{pzc}$  from  $\sim 2.69$  for BC600 to  $\sim 7.65$  for  $Y_2O_3@BC600-1:4$ . Similar results were reported regarding the coating modification of biochars by other metallic oxides (e.g.,  $ZrO_2$  and  $MgFe_2O_4$ ) (Deng et al., 2022; Khataee et al., 2017). Consequentially, different  $pH_{pzc}$  of adsorbents signify charge characteristic difference in aqueous solution due to protonation and deprotonation, which may affect the capacity and mechanisms of pollutant adsorption.

The SEM images of BC600 and  $Y_2O_3@BC600-1:4$  are presented in the Supplementary material. BC600 particles were micron-sized rod and slice solids, owing to strong destruction of ginger straw from mechanical pulverization, and the particle surface was relatively flat. In contrast, the surface of  $Y_2O_3@BC600-1:4$  was visibly rough. The enlarged image showed that a large number of solid particles were well deposited and distributed on the carbon wall of BC600. These solid particles had nanoscale sizes, and pore structure formed due to particle–particle bridge and stack. TEM image showed that  $Y_2O_3$  particles on BC600 surface were nanoscale solids ( $\sim 7\text{--}30$  nm) (see Supplementary material). The EDX mapping images depicted the coexistence and distribution of C, O, and Y elements in the same surface region of  $Y_2O_3@BC600-1:4$  (see Supplementary material), confirming uniform coating  $Y_2O_3$  particles onto BC600 surface.

BC600 and  $Y_2O_3@BC600-1:4$  had adsorption–desorption curves of type IV with hysteresis loop (see Supplementary material), revealing the predominance of mesopores (Xiang et al., 2022). For  $Y_2O_3@BC600-1:4$ ,

there was a rapid increase of  $N_2$  adsorption at lower relative pressure, originating from the micropores. The BET surface area of  $Y_2O_3@BC600-1:4$  was  $175.65\text{ m}^2/\text{g}$ , 9.90 times greater than that of BC600 ( $16.12\text{ m}^2/\text{g}$ ). Correspondingly,  $Y_2O_3@BC600-1:4$  also had greater total pore volume compared with BC600 ( $0.27\text{ cm}^3/\text{g}$  vs  $0.08\text{ cm}^3/\text{g}$ ). The diameter of micropores and mesopores of  $Y_2O_3@BC600-1:4$  ranged of  $1.02\text{--}1.95$  nm and  $2.05\text{--}41.7$  nm, respectively.  $Y_2O_3$  coating expanded the micropores and mesopores by  $0.076$  and  $0.136\text{ cm}^3/\text{g}$ . These results can be explained by that the stacking dispersion of  $Y_2O_3$  nanoparticles on the surface of BC600 create more pores and improve surface area. The large surface area of  $Y_2O_3@BC600$  composite can supply more adsorption sites, and the abundant mesopores contributed to the adsorption of pollutants via pore diffusion and filling (Deng et al., 2022).

### 3.2. Adsorption kinetics

As depicted in Fig. 1a, the process of OTC sorption onto  $Y_2O_3@BC600$  could be divided into fast, slow, and balance stages. For example, the adsorption amount of  $Y_2O_3@BC600-1:4$  for OTC increase rapidly before 4 h, accounting for 42.5% of the equilibrium adsorption capacity at 48 h. The fast adsorption in the early stage was associated with unoccupied sorption sites of external surface of adsorbent (Shi et al., 2023). The curves of pseudo first/second-order equations are given in Fig. 1a, and their parameters are listed in Table 1. The slightly higher  $R^2$  values suggested that OTC adsorption onto  $Y_2O_3@BC600$  composites could be better simulated by the pseudo second-order model. This result suggested that there was chemisorption through electron transferring and sharing in the removal of OTC by  $Y_2O_3@BC600$  (Ho & McKay, 1999).

The  $Y_2O_3$  coating-produced improvement of BC600 porosity certainly favors pollutant adsorption via pore diffusion and filling. The

Table 1  
The fitting results of OTC adsorption kinetics on BC600 and  $Y_2O_3@BC600$  samples.

Kinetic models	Parameters	BC600	$Y_2O_3@BC600-1:19$	$Y_2O_3@BC600-1:9$	$Y_2O_3@BC600-1:4$	
Pseudo first-order model	$q_e$ (mg/g)	9.17	45.26	66.57	163.69	
	$k_1$ ( $\text{min}^{-1}$ )	2.01	0.11	0.18	0.13	
	$R^2$	0.4253	0.8205	0.8786	0.9419	
Pseudo second-order model	$q_e$ (mg/g)	10.19	49.15	70.99	181.58	
	$k_2$ ( $\text{mg}/(\text{g}\cdot\text{min})$ )	0.16	0.0037	0.0045	0.0010	
	$R^2$	0.5393	0.8746	0.9282	0.9661	
Intraparticle diffusion model	Phase 1	$k_{i1}$ ( $\text{mg}/(\text{g}\cdot\text{min}^{1/2})$ )	1.26	15.67	15.01	29.39
		$b_1$ (mg/g)	4.70	2.00	8.61	12.30
		$R_1^2$	0.9772	0.9998	0.9944	0.9980
	Phase 2	$k_{i2}$ ( $\text{mg}/(\text{g}\cdot\text{min}^{1/2})$ )	0.83	5.13	10.50	21.72
		$b_2$ (mg/g)	0.45	9.62	12.76	34.71
		$R_2^2$	0.9493	0.9966	0.9978	0.9955
	Phase 2	$k_{i3}$ ( $\text{mg}/(\text{g}\cdot\text{min}^{1/2})$ )	0.49	4.16	1.84	2.35
		$b_3$ (mg/g)	7.26	16.38	55.80	150.77
		$R_3^2$	0.2962	0.9788	0.9303	0.6191

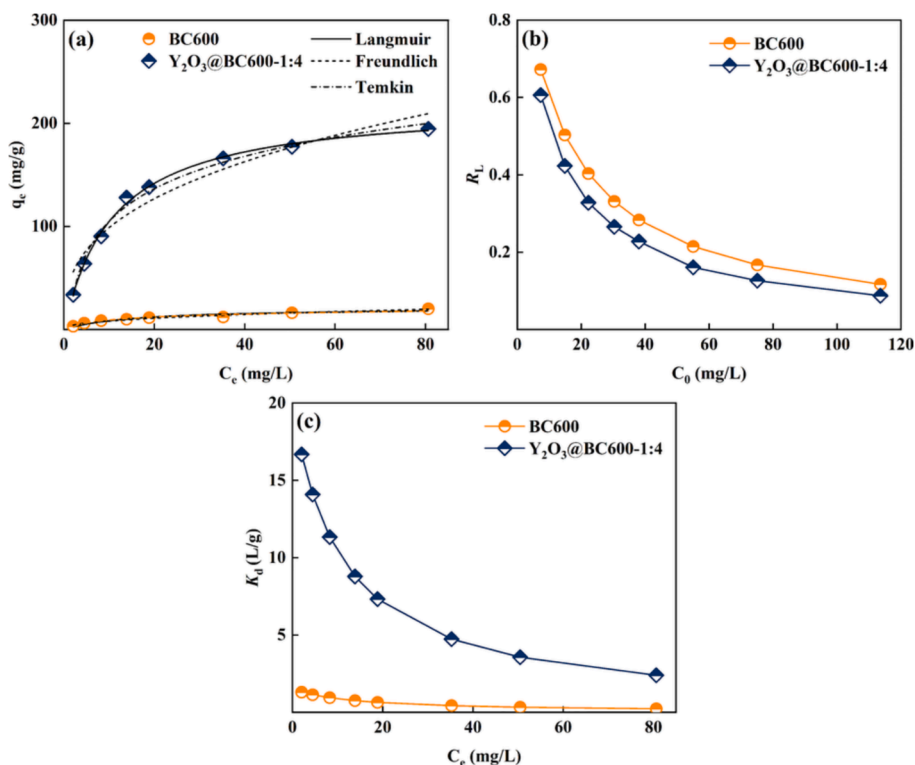


Fig. 2. Adsorption performance of BC600 and Y<sub>2</sub>O<sub>3</sub>@BC600-1:4 for OTC. The adsorption isotherms with the fitting curves of Langmuir and Freundlich models (a), separation factor (R<sub>L</sub>) (b), and adsorption coefficient (K<sub>d</sub>) (c).

intraparticle diffusion model was therefore employed to explore the role of film and pore diffusion in adsorption process (Chen et al., 2022). The nonlinear curves of q<sub>t</sub> varying with t<sup>1/2</sup> demonstrated that the adsorption process of Y<sub>2</sub>O<sub>3</sub>@BC600 for OTC consisted of multiple stages (Fig. 1b). These q<sub>t</sub> vs t<sup>1/2</sup> curves were divided into three linear segments for the model fitting. The b<sub>1</sub> values of phase 1 ranged of 2.00–12.96 mg/g (Table 1), that is, the curves did not go through the origin, implying the contribution of film diffusion (Pandiarajan et al., 2018). The phase 1 had greater rate constant (k<sub>11</sub>) than other two phases, suggesting faster adsorption of OTC by Y<sub>2</sub>O<sub>3</sub>@BC600 at the phase 1. For the beginning stage, OTC molecules were more easily trapped by the active sites of external surface of Y<sub>2</sub>O<sub>3</sub> coating layer, and also higher concentration facilitated the spread of organic molecules to the sorption sites (Zhang et al., 2019a). Following, OTC molecules diffused into mesopores and micropores of Y<sub>2</sub>O<sub>3</sub>@BC600, and were therewith adsorbed through pore filling and/or occupied the adsorption sites of internal surface inside the pores. The lower k<sub>12</sub> (5.13–20.71 mg/g) compared with k<sub>11</sub> (15.01–28.71 mg/g) could support the internal diffusion limitation in the sorption process of phase 2 (Yu et al., 2020). In addition, the as-prepared composite with more Y<sub>2</sub>O<sub>3</sub> coating had greater k<sub>11</sub> and k<sub>12</sub>, indicating that the interaction of Y<sub>2</sub>O<sub>3</sub> with OTC could accelerate the adsorption process. Lastly, the inner pore sites of Y<sub>2</sub>O<sub>3</sub>@BC600 were more difficult to utilize, and also the contact of OTC molecules reduced with active sites because of lower concentration, thus the sorption reached equilibrium stage. Overall, the process of OTC adsorption on Y<sub>2</sub>O<sub>3</sub>@BC600 composites was governed by film diffusion, pore diffusion, and the interaction on external/internal surfaces.

### 3.3. Adsorption isotherms

The adsorption amount of BC600 and Y<sub>2</sub>O<sub>3</sub>@BC600-1:4 for OTC increased gradually as OTC concentration increased (Fig. 2a). This implied that more sorption sites of the sorbents were occupied under higher OTC concentration. Besides, the increment may be closely associated with the usability of adsorption sites. For better understanding

Table 2

Isotherm parameters for OTC adsorption.

Kinetic models	Parameters	BC600	Y <sub>2</sub> O <sub>3</sub> @BC600-1:4
Langmuir	K <sub>L</sub> (L/mg)	0.067	0.096
	q <sub>m</sub> (mg/g)	21.25	223.46
	R <sup>2</sup>	0.9190	0.9929
Freundlich	K <sub>F</sub> [(mg/g)/(mg/L) <sup>1/n</sup> ]	3.19	46.88
	n	0.41	0.35
	R <sup>2</sup>	0.9680	0.9248
Temkin	K <sub>T</sub> (L/g)	0.90	1.01
	a (J/mol)	593.72	54.48
	R <sup>2</sup>	0.9324	0.9904

the adsorption characteristics, the Freundlich and Langmuir models were used to fit the isothermal data, whose fitting curves and parameters are shown in Fig. 2a and Table 2, respectively. The 1/n values were lower than 1, suggesting that the sorption occurred on heterogeneous surface and/or various binding sites (Al-Ghouti & Da'ana, 2020). The better fitting of Langmuir model on OTC adsorption of Y<sub>2</sub>O<sub>3</sub>@BC600-1:4 with high R<sup>2</sup> value of 0.9972 indicated that Y<sub>2</sub>O<sub>3</sub>-coating modification could increase specific sites for monolayered adsorption (Li et al., 2020). The Langmuir q<sub>m</sub> of OTC adsorption by Y<sub>2</sub>O<sub>3</sub>@BC600-1:4 was 223.46 mg/g, significantly greater than BC600 (21.25 mg/g) and the composites of biochar with other metallic oxides (Fe<sub>3</sub>O<sub>4</sub>, MgFe<sub>2</sub>O<sub>4</sub>, and Fe-Al oxides, etc.) for tetracyclines (24.69–184.50 mg/g) (Deng et al., 2022; Li et al., 2020; Luo et al., 2022; Tang et al., 2023). The isotherm of OTC on Y<sub>2</sub>O<sub>3</sub>@BC600-1:4 could be better described by nonlinear Temkin model (R<sup>2</sup> = 0.9904) relative to on BC600 (R<sup>2</sup> = 0.9324). The well fitting of Temkin model suggested that the interaction heat of the adsorbent with OTC linearly decreased with increasing adsorption (Guo et al., 2020). The K<sub>T</sub> value of Y<sub>2</sub>O<sub>3</sub>@BC600-1:4 was 1.01 L/g, greater than that of BC600 (0.90 L/g), meaning stronger binding force of the Y<sub>2</sub>O<sub>3</sub>-modified BC600 with OTC molecules than the pristine BC600.

The range of R<sub>L</sub> values at the given initial concentrations of OTC was

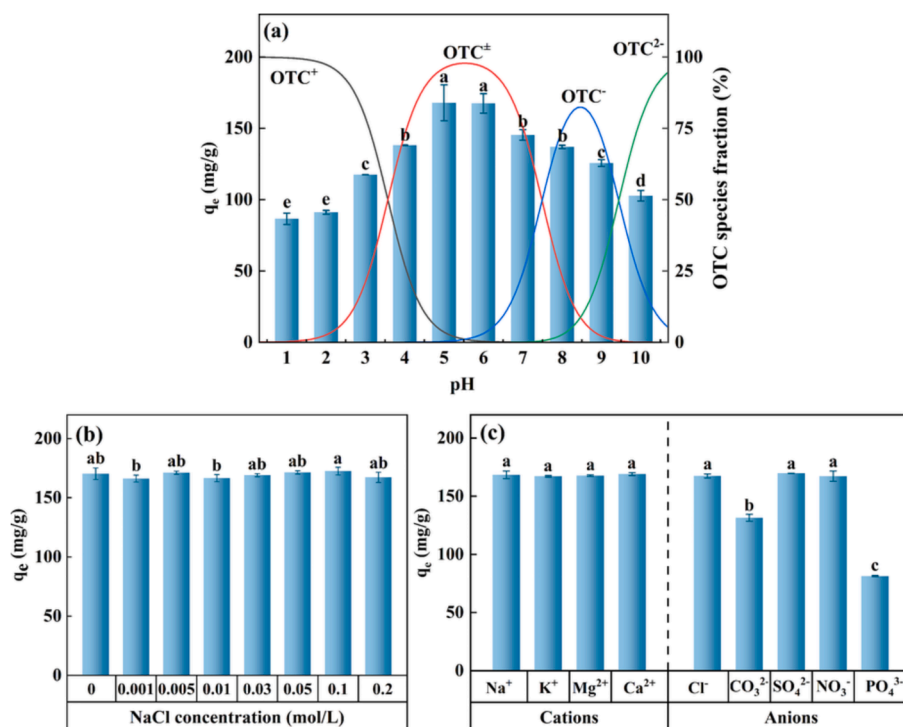


**Fig. 3.** The influence of solution pH (a), ionic strength (b), and coexisting ions (c) on OTC adsorption by  $Y_2O_3@BC600-1:4$ . Significant difference was marked with different lowercase letters ( $p < 0.05$ ).

0 to 1 (Fig. 2b), implying favorable adsorption of OTC on BC600 and  $Y_2O_3@BC600-1:4$ . For the same OTC concentrations, the lower  $R_L$  of  $Y_2O_3@BC600-1:4$  than that of BC600 declared that OTC adsorption became more favorable after  $Y_2O_3$  modification. The  $K_d$  curves drawn in Fig. 2c were used to comparatively analyze the adsorption affinity of BC600 before and after  $Y_2O_3$  coating for OTC. The decreased  $K_d$  varying with the increase of OTC concentration might be attributable to the nonlinear and heterogeneous adsorption. This was in accord with that the adsorbate molecules preferred to occupy strong binding sites (Vithanage et al., 2012). Importantly, all the  $K_d$  values of  $Y_2O_3@BC600-1:4$  were much higher than those of BC600, demonstrating that the coating of  $Y_2O_3$  onto BC600 dramatically enhanced the adsorption affinity toward OTC. Given the above,  $Y_2O_3@BC600$  composite had fine performance in capturing antibiotics in water.

### 3.4. Effect of solution pH and foreign ions

It was obviously noticed that the optimum pH occurred at pH 5 and 6. With increasing pH, the adsorptive amount of  $Y_2O_3@BC600-1:4$  for OTC continuously increased before pH 5, whereas decreased after pH above 6. The pH condition of adsorption system can affect the existing-form of adsorbate and surface charge of adsorbent, thus affecting their contact and interact. OTC molecule has three ionizable groups namely tricarbonyl amide, phenolic diketone, and dimethylamine, which undergo protonation or deprotonation at different pH conditions. The dominated species of OTC are  $OTC^+$  at  $pH < 3.57$ ,  $OTC^\pm$  at  $3.57 < pH < 7.49$ ,  $OTC^-$  at  $7.49 < pH < 9.44$ , and  $OTC^{2-}$  at  $pH > 9.44$  (Fig. 3a). It was obviously noticed that the OTC removal by  $Y_2O_3@BC600-1:4$  was pH-dependent, and the optimum pH occurred at pH 5 and 6. With increasing pH, the adsorptive amount of  $Y_2O_3@BC600-1:4$  for OTC continuously increased before pH 5, whereas decreased after pH above 6. Viewing the pH-regulated speciation of OTC and the zeta potential of  $Y_2O_3@BC600-1:4$  (see Supplementary material), the influence of pH condition on OTC adsorption was probably related to electrostatic interaction. Under more acidic condition, stronger repulsive force of positively charged surface of  $Y_2O_3@BC600-1:4$  with  $OTC^+$  inhibited the

adsorption more significantly. Also, the decreased sorption of OTC with increasing pHs above 7 was closely related with the electrostatic repulsive interaction between the negatively charged surface of  $Y_2O_3@BC600-1:4$  and  $OTC^-/OTC^{2-}$ . These facts were consistent with the experimental results obtained in other previous studies (Deng et al., 2022; Hamadeen & Elkhatib, 2022). Therefore, the underlying mechanisms for OTC removal could be inferred from the electrical properties of the adsorbent and adsorbent.

OTC adsorption on  $Y_2O_3@BC600-1:4$  at different NaCl concentrations were carried out to test the influence of ionic strength. With increasing NaCl concentration, there was almost no effect on the adsorption amounts (Fig. 3b). Commonly, the presence of mineral electrolytes may disturb the adsorption behavior of pollutants in natural waters and wastewater.  $Na^+$ ,  $K^+$ ,  $Mg^{2+}$ ,  $Ca^{2+}$ ,  $Cl^-$ ,  $CO_3^{2-}$ ,  $SO_4^{2-}$ ,  $NO_3^-$ , and  $PO_4^{3-}$  were therefore selected to inspect their influence on OTC adsorption in this study. As shown in Fig. 3c, it was found that these cations had little effect on the OTC removal. The anions ( $Cl^-$ ,  $SO_4^{2-}$ , and  $NO_3^-$ ) hardly affected OTC adsorption, but  $CO_3^{2-}$  and  $PO_4^{3-}$  exhibited significantly negative effect with the reduction of adsorption amount by 21.92% and 51.67%, respectively. Introducing  $CO_3^{2-}$  and  $PO_4^{3-}$  into adsorption system, low solubility salts (e.g.,  $Y_2(CO_3)_3$  and  $YPO_4$ ) may form (Djurdjevic et al., 2016; Liu & Byrne, 1997), thus shielding the surface sites of  $Y_2O_3$  particles and reducing OTC adsorption. Nevertheless, the adsorbing capacity of  $Y_2O_3@BC600-1:4$  still kept at high level, 131.48 and 81.38 mg/g under the presence of  $CO_3^{2-}$  and  $PO_4^{3-}$  respectively, under initial condition of pH 6 and 40 mg/L OTC. This result suggested that the as-prepared sorbent could be applied to eliminate antibiotics in the complicated wastewaters.

### 3.5. Proposed adsorption mechanisms

As well known, the adsorption of antibiotics onto biochars depended on complicated mechanisms, mainly electrostatic attraction,  $\pi-\pi$  interaction, H-bonding, and pore filling (Zhao et al., 2022). In this work, OTC sorption on  $Y_2O_3@BC600$  was also a complicated process and caused by synergistic mechanisms (see Supplementary material).



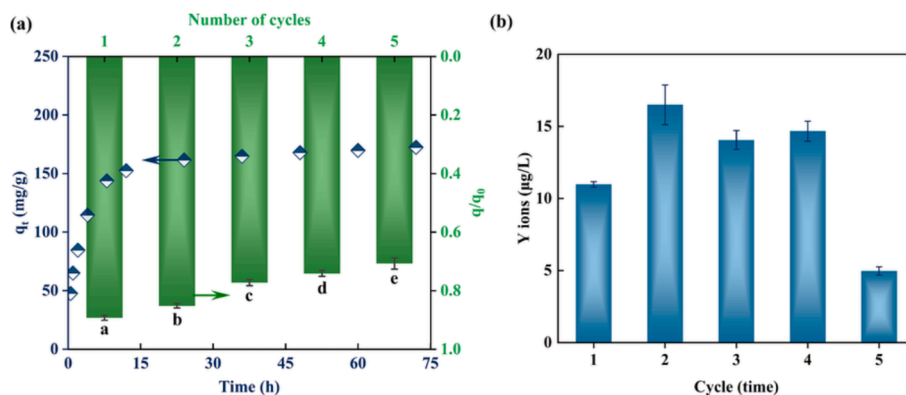


**Fig. 4.** The adsorption removal of OTC by  $Y_2O_3@BC600-1:4$  in wastewater and the recyclability for five cycles (a) and the leaching concentration of Y ions (b). Significant difference was marked with different lowercase letters ( $p < 0.05$ ).

The greater surface area of  $Y_2O_3@BC600$  supplied more exposed sites, and more micropores and mesopores increased the adsorption through pore diffusion and filling. The intraparticle diffusion model analysis implied the crucial role of pore diffusion in OTC adsorption. The suitable diameter range and greater volume of mesopores in  $Y_2O_3@BC600$  composite are more conducive to the entry of OTC molecules into pore channels and supply more available adsorptive surface. The coating of  $Y_2O_3$  nanoparticles definitely shielded carbon surface and even plugged mesopores and macropores of BC600, thus reducing the interaction of carbonaceous components (e.g.,  $-OH$ ,  $C=O$ , and  $C=C$  groups) with OTC. The increased adsorption at pH from 1 to 5 while decreased trend at raising pH above 6 demonstrated the participation of electrostatic interaction in the adsorptive removal of OTC, owing to  $Y_2O_3$ -resulting change of surface charge characteristics.  $Y_2O_3$  offers three hydrogen bond acceptors, and OTC molecule supplies seven hydrogen bond donors. Further, the hydroxylated surface of metal oxides  $Y_2O_3$  in aqueous solution can serve as the sites for ion exchange (Tamura et al., 1999). The normal H-bonding and ion exchange are prone to affect by coexisting ions. However, in this case, both  $Na^+$ ,  $K^+$ ,  $Mg^{2+}$ ,  $Ca^{2+}$  and  $Cl^-$ ,  $SO_4^{2-}$ ,  $NO_3^-$  had little impact on the adsorption of OTC by  $Y_2O_3@BC600-1:4$ , only  $CO_3^{2-}$  and  $PO_4^{3-}$  showed inhibiting effect because of the precipitation formation of  $Y_2(CO_3)_3$  and  $YPO_4$  on  $Y_2O_3$  surface, possibly shielding partial adsorption sites. These results suggest that a specific interaction of  $Y_2O_3$  with OTC molecule may occur.

The SR-FTIR mapping and spectra was used to more sensitively obtain the characteristic peaks of functional groups of the adsorbent after OTC sorption, which are given in the [Supplementary material](#).  $Y_2O_3@BC600-1:4$  had two SR-FTIR peaks at 1396 and 1527  $cm^{-1}$ , assigning to aliphatic and aromatic structure of BC600 and  $-OH$  of  $Y_2O_3$ . As expected, a new SR-FTIR peak at 2908  $cm^{-1}$  was detected in  $Y_2O_3@BC600-1:4$  adsorbed OTC, ascribing to N-H stretch of dimethylamine in OTC molecule (Cervini et al., 2016). The  $\mu$ -FTIR mapping image at 2908  $cm^{-1}$  was coincided with the distribution of  $Y_2O_3@BC600-1:4$  particles in the optical image, suggesting uniform adsorption of OTC. It is worth noting that there were obvious FTIR peak shift and intensity change at these absorption peaks (1396–1577  $cm^{-1}$ ) after OTC adsorption. Given the overlay of  $Y_2O_3$  particles on BC600 surface, the surface  $-OH$  may be crucial sites for bonding OTC molecules. (Blasioli et al., 2014) reported that medium-strong H-bonding occurred between neutral sulfamethoxazole molecule and silanol (Si-OH) of zeolite. Recently, direct spectroscopic evidence was also obtained for a type of strong hydrogen bond (charge-assisted hydrogen bonding, CAHB) between  $-OH$ ,  $-COOH$ , and  $-NH_2$  of adsorbents (e.g., nano  $SiO_2$ ) and ionizable pharmaceutical contaminants (Zhang et al., 2020; Zhang et al., 2022). Presumably, stronger hydrogen bonds (OTC- $H_2N^+ \cdots HO-Y_2O_3@BC600-1:4$ ) may form instead of normal hydrogen bond, which is an important one of the contributions for OTC adsorption. The appearance of new peak for N-H of OTC molecule,

upshifted FTIR peaks for surface hydroxyl site of  $Y_2O_3$ , and the well matching of their SR-FTIR mapping distribution after adsorption of OTC on  $Y_2O_3@BC600-1:4$  can be considered as possible evidence for this interaction. In addition, the proposed mechanism was consistent with the result from adsorption isotherms that  $Y_2O_3@BC600-1:4$  had greater adsorption affinity for OTC. Overall,  $Y_2O_3$  coating onto BC600 probably provided more specific active sites for adsorbing OTC.

### 3.6. Reusability of $Y_2O_3@BC600$ adsorbent

The recyclability of sorbent can reveal practical applicability for sustainable strategy of pollutant removal through adsorption technique. Here, the adsorption removal of OTC in wastewater by  $Y_2O_3@BC600-1:4$  was examined, and the exhausted sorbent was desorbed in 0.3 mol/L NaOH solution to evaluate regeneration performance. The wastewater was taken from secondary sedimentation tank of a sewage treatment plant, pH 6.68, COD 50.5 mg/L,  $NH_3-N$  5.17 mg/L,  $NO_3-N$  14.2 mg/L, and  $PO_4-P$  0.46 mg/L. As illustrated in Fig. 4a,  $Y_2O_3@BC600-1:4$  composite exhibited superior adsorption efficacy in eliminating OTC from the wastewater, with the equilibrium adsorption quantity reaching up to 164.81 mg/g. For the same initial OTC concentration, the equilibrium adsorption capacity of  $Y_2O_3@BC600-1:4$  was found to be nearly identical in both the background solution and the wastewater. That is,  $Y_2O_3@BC600$  composite showed relative selectivity for adsorbing OTC irrespective of coexistence of organic and inorganic dissolved substances in the wastewater.

Following five cycles, the NaOH-eluted adsorbent still retained 70.1% of the initial adsorption capacity, implying that  $Y_2O_3@BC600-1:4$  could be deemed as a durable adsorbent for OTC removal. Nevertheless, taking component complexity into consideration, the efficiency of  $Y_2O_3@BC600$  adsorbent in the removal of OTC and other contaminants needs to further examine in actual waters. The leaching concentration of Y ions during five cycles was  $<16.50 \mu g/L$  (Fig. 4b), and the mass loss of  $Y_2O_3@BC600$  was maintained below 16.97% before 1000  $^\circ C$  in the TGA measurement (see [Supplementary material](#)), suggesting that the synthesized composite showed better stability. Nevertheless, taking component complexity of actual polluted waters into consideration, the removal efficiency of OTC and other contaminants by  $Y_2O_3@BC600$  needs to be further examined. The future research efforts regarding the post-treatment of enriched or desorbed contaminants of the adsorbent need more concerns.

## 4. Conclusion

$Y_2O_3@BC600$  composite with outstanding sorption ability was prepared, its Langmuir adsorption capacity of OTC reached 223.46 mg/g, 10.52 times greater than BC600. The high dispersion of  $Y_2O_3$  nanoparticles, greater surface area, and more pores enhanced OTC

adsorption.  $Y_2O_3$  coating onto BC600 changed surface charge property, thus regulating the role of electrostatic interaction, and the mechanism of stronger H-bonding (CAHB,  $OTC-H_2N^+ \cdots HO-Y_2O_3@BC600$ ) was proposed.  $Y_2O_3@BC600-1:4$  could resist interference of cations and anions (except  $CO_3^{2-}$  and  $PO_4^{3-}$ ) and retain the ability of OTC removal in actual wastewater. The excellent stability and sustainability of  $Y_2O_3@BC600$  made it a promising sorbent for aqueous OTC.

### CRedit authorship contribution statement

**Jiaying Song:** Investigation, Methodology, Writing - original draft. **Lun Lu:** Manuscript review. **Jian Wang:** Investigation. **Li Xue:** Investigation. **Li Jinying:** Investigation. **Qianwen Wang:** Investigation, Data curation, Formal analysis. **Haiyan Du:** Data curation, Formal analysis. **Shuaishuai Xin:** Data curation, Formal analysis. **Lina Xu:** Manuscript review, Funding acquisition. **Qinghua Yan:** Data curation, Formal analysis. **Chengzhi Zhou:** Data curation, Formal analysis. **Guocheng Liu:** Writing - Review & Editing, Supervision, Funding acquisition. **YanJun Xin:** Supervision, Funding acquisition.

### Declaration of Competing Interest

The authors declare that they have no known competing financial interests or personal relationships that could have appeared to influence the work reported in this paper.

### Data availability

Data will be made available on request.

### Acknowledgements

This work was financially supported by National Natural Science Foundation of China (52170135, 52070107, 42207255), Shandong Provincial Natural Science Foundation (ZR2020MD112), Research Foundation for Talented Scholars of Qingdao Agricultural University (6651119010), and we thank the staffs from BL01B beamline of National Facility for Protein Science in Shanghai (NFPS) at Shanghai Synchrotron Radiation Facility.

### Appendix A. Supplementary data

Supplementary data to this article can be found online at <https://doi.org/10.1016/j.biortech.2023.129380>.

### References

- Aghazadeh, M., Nozad, A., Adelhani, H., Ghaemi, M., 2010. Synthesis of  $Y_2O_3$  nanospheres via heat-treatment of cathodically grown  $Y(OH)_3$  in chloride medium. *J. Electrochem. Soc.* 157 (10), 519–522.
- Ahsan, M.A., Islam, M.T., Hernandez, C., Kim, H., Lin, Y., Curry, M.L., Gardea-Torresdey, J., Noveron, J.C., 2018. Adsorptive removal of sulfamethoxazole and bisphenol A from contaminated water using functionalized carbonaceous material derived from tea leaves. *J. Environ. Chem. Eng.* 6 (4), 4215–4225.
- Al-Ghouti, M.A., Da'ana, D.A., 2020. Guidelines for the use and interpretation of adsorption isotherm models: A review. *J. Hazard. Mater.* 393, 122383.
- Biasioli, S., Martucci, A., Paul, G., Gigli, L., Cossi, M., Johnston, C.T., Marchese, L., Braschi, I., 2014. Removal of sulfamethoxazole sulfonamide antibiotic from water by high silica zeolites: a study of the involved host-guest interactions by a combined structural, spectroscopic, and computational approach. *J. Colloid Interface Sci.* 419, 148–159.
- Cervini, P., Machado, L.C.M., Ferreira, A.P.G., Ambrozini, B., Cavalheiro, J.T.G., 2016. Thermal decomposition of tetracycline and chlortetracycline. *J. Anal. Appl. Pyrolysis.* 118, 317–324.
- Charisiou, N.D., Siakavelas, G., Tzounis, L., Dou, B., Sebastian, V., Hinder, S.J., Baker, M. A., Polychronopoulou, K., Goula, M.A., 2020.  $Ni/Y_2O_3-ZrO_2$  catalyst for hydrogen production through the glycerol steam reforming reaction. *Int. J. Hydrogen Energy.* 45 (17), 10442–10460.
- Chen, J., Tang, C., Li, X., Sun, J., Liu, Y., Huang, W., Wang, A., Lu, Y., 2022. Preparation and modification of rape straw biochar and its adsorption characteristics for methylene blue in water. *Water.* 14 (22), 3761.

- Cheng, D., Ngo, H.H., Guo, W., Chang, S.W., Nguyen, D.D., Zhang, X., Varjani, S., Liu, Y., 2020. Feasibility study on a new pomelo peel derived biochar for tetracycline antibiotics removal in swine wastewater. *Sci. Total Environ.* 720, 137662.
- Deng, Y., Wang, M., Yang, Y., Li, X., Chen, W., Ao, T., 2022. Enhanced adsorption performance of sulfamethoxazole and tetracycline in aqueous solutions by  $MgFe_2O_4$ -magnetic biochar. *Water Sci. Technol.* 86 (3), 568–583.
- Djurđević, P., Jakovljević, I., Petrović, D., Cvijović, M., Joksović, L., 2016. Influence of yttrium(III) ion on calcium(II) and zinc(II) biospeciation in human blood plasma by computer simulation, pp. 93–105.
- Du, H., Yu, G., Guo, M., Xu, H., 2021. Investigation of carbon dynamics in rhizosphere by synchrotron radiation-based Fourier transform infrared combined with two dimensional correlation spectroscopy. *Sci. Total Environ.* 762, 143078.
- Guo, X., Liu, Y., Wang, J., 2020. Equilibrium, kinetics and molecular dynamic modeling of  $Sr^{2+}$  sorption onto microplastics. *J. Hazard. Mater.* 400, 123324.
- Guo, H., Zhang, W., Lou, L., Brioude, A., Mugnier, J., 2004. Structure and optical properties of rare earth doped  $Y_2O_3$  waveguide films derived by sol-gel process. *Thin Solid Films.* 458 (1), 274–280.
- Hamadeen, H.M., Elkhatib, E.A., 2022. New nanostructured activated biochar for effective removal of antibiotic ciprofloxacin from wastewater: Adsorption dynamics and mechanisms. *Environ. Res.* 210, 112929.
- Hasan, M.S., Geza, M., Vasquez, R., Chilkoor, G., Gadhamshetty, V., 2020. Enhanced heavy metal removal from synthetic stormwater using nanoscale zerovalent iron-modified biochar. *Water, Air, Soil Pollut.* 231 (5), 220.
- Ho, Y.S., McKay, G., 1999. Pseudo-second order model for sorption processes. *Process Biochem.* 34 (5), 451–465.
- Kaur Sodhi, K., Singh, C.K., 2022. Recent development in the sustainable remediation of antibiotics: a review. *Total Environ. Res. Themes.* 3–4, 100008.
- Khataee, A., Kayan, B., Gholami, P., Kalderis, D., Akay, S., Dinpazhoh, L., 2017. Sonocatalytic degradation of Reactive Yellow 39 using synthesized  $ZrO_2$  nanoparticles on biochar. *Ultrason. Sonochem.* 39, 540–549.
- Lamiri, L., Guerbois, L., Samah, M., Boukerika, A., Ouhenia, S., 2015. Structural, morphological and steady state photoluminescence spectroscopy studies of red  $Eu^{3+}$ -doped  $Y_2O_3$  nanophosphors prepared by the sol-gel method. *Luminescence.* 30 (8), 1336–1343.
- Leichtweis, J., Vieira, Y., Welter, N., Silvestri, S., Dotto, G.L., Carissimi, E., 2022. A review of the occurrence, disposal, determination, toxicity and remediation technologies of the tetracycline antibiotic. *Process Saf. Environ. Prot.* 160, 25–40.
- Li, J., Cai, X., Liu, Y., Gu, Y., Wang, H., Liu, S., Liu, S., Yin, Y., Liu, S., 2020. Design and synthesis of a biochar-supported nano manganese dioxide composite for antibiotics removal from aqueous solution. *Front. Environ. Sci.* 8, 62.
- Liu, X., Byrne, R.H., 1997. Rare earth and yttrium phosphate solubilities in aqueous solution. *Geochim. Cosmochim. Acta.* 61 (8), 1625–1633.
- Liu, G., Pan, X., Ma, X., Xin, S., Xin, Y., 2020. Effects of feedstock and inherent mineral components on oxidation resistance of biochars. *Sci. Total Environ.* 726, 138672.
- Liu, Z., Xu, Z., Xu, L., Buyong, F., Chay, T.C., Li, Z., Cai, Y., Hu, B., Zhu, Y., Wang, X., 2022. Modified biochar: synthesis and mechanism for removal of environmental heavy metals. *Carbon Res.* 1 (1).
- Lu, L., Yu, W., Wang, Y., Zhang, K., Chen, B., 2020. Application of biochar-based materials in environmental remediation: from multi-level structures to specific devices. *Biochar.* 2 (1), 1–31.
- Luo, S., Qin, J., Wu, Y., Feng, F., 2022. Tetracycline adsorption on magnetic sludge biochar: size effect of the  $Fe_3O_4$  nanoparticles. *R. Soc. Open Sci.* 9 (1), 210805.
- Okoye, C.O., Nyaruaba, R., Ita, R.E., Okon, S.U., Addey, C.I., Ebido, C.C., Opabunmi, A. O., Okeke, E.S., Chukwudozie, K.I., 2022. Antibiotic resistance in the aquatic environment: Analytical techniques and interactive impact of emerging contaminants. *Environ. Toxicol. Pharmacol.* 96, 103995.
- Pandiarajan, A., Kamaraj, R., Vasudevan, S., Vasudevan, S., 2018. OPAC (orange peel activated carbon) derived from waste orange peel for the adsorption of chlorophenoxyacetic acid herbicides from water: Adsorption isotherm, kinetic modelling and thermodynamic studies. *Bioresour. Technol.* 261, 329–341.
- Qiu, M., Liu, L., Ling, Q., Cai, Y., Yu, S., Wang, S., Fu, D., Hu, B., Wang, X., 2022. Biochar for the removal of contaminants from soil and water: a review. *Biochar.* 4 (19).
- Quaik, S., Embrandiri, A., Ravindran, B., Hossain, K., Al-Dhabi, N.A., Arasu, M.V., Ignacimuthu, S., Ismail, N., 2020. Veterinary antibiotics in animal manure and manure laden soil: scenario and challenges in Asian countries. *J. King Saud Univ., Sci.* 32 (2), 1300–1305.
- Shakya, A., Vithanage, M., Agarwal, T., 2022. Influence of pyrolysis temperature on biochar properties and Cr(VI) adsorption from water with groundnut shell biochars: mechanistic approach. *Environ. Res.* 215 (1), 114243.
- Shi, Q., Wang, W., Zhang, H., Bai, H., Liu, K., Zhang, J., Li, Z., Zhu, W., 2023. Porous biochar derived from walnut shell as an efficient adsorbent for tetracycline removal. *Bioresour. Technol.* 383, 129213.
- Tamura, H., Tanaka, A., Mita, K., Furuichi, R., 1999. Surface hydroxyl site densities on metal oxides as a measure for the ion-exchange capacity. *J. Colloid Interface Sci.* 209 (1), 225–231.
- Tang, J., Ma, Y., Zeng, C., Yang, L., Cui, S., Zhi, S., Yang, F., Ding, Y., Zhang, K., Zhang, Z., 2023. Fe-Al bimetallic oxides functionalized-biochar via ball milling for enhanced adsorption of tetracycline in water. *Bioresour. Technol.* 369, 128385.
- Verma, T., Aggarwal, A., Singh, S., Sharma, S., Sarma, S.J., 2022. Current challenges and advancements towards discovery and resistance of antibiotics. *J. Mol. Struct.* 1248, 131380.
- Vithanage, M., Jayarathna, L., Rajapaksha, A.U., Dissanayake, C.B., Bootharaju, M.S., Pradeep, T., 2012. Modeling sorption of fluoride on to iron rich laterite. *Colloids Surf A.* 398, 69–75.
- Wang, S.L., Tzou, Y.M., Lu, Y.H., Sheng, G., 2007. Removal of 3-chlorophenol from water using rice-straw-based carbon. *J. Hazard. Mater.* 147 (1–2), 313–318.

- Xiang, W., Zhang, X., Luo, J., Li, Y., Guo, T., Gao, B., 2022. Performance of lignin impregnated biochar on tetracycline hydrochloride adsorption: Governing factors and mechanisms. *Environ. Res.* 215 (2), 114339.
- Xie, J., Lin, R., Liang, Z., Zhao, Z., Yang, C., Cui, F., 2021. Effect of cations on the enhanced adsorption of cationic dye in Fe<sub>3</sub>O<sub>4</sub>-loaded biochar and mechanism. *J. Environ. Chem. Eng.* 9 (4), 105744.
- Xue, J., Lei, D., Zhao, X., Hu, Y., Yao, S., Lin, K., Wang, Z., Cui, C., 2022. Antibiotic residue and toxicity assessment of wastewater during the pharmaceutical production processes. *Chemosphere.* 291 (2), 132837.
- Yang, Y., Phuong Nguyen, T.M., Van, H.T., Nguyen, Q.T., Nguyen, T.H., Lien Nguyen, T. B., Hoang, L.P., Van Thanh, D., Nguyen, T.V., Nguyen, V.Q., Thang, P.Q., Yilmaz, M., Le, V.G., 2022. ZnO nanoparticles loaded rice husk biochar as an effective adsorbent for removing reactive red 24 from aqueous solution. *Mater. Sci. Semicond. Process.* 150, 106960.
- Yao, X., Ji, L., Guo, J., Ge, S., Lu, W., Chen, Y., Cai, L., Wang, Y., Song, W., 2020. An abundant porous biochar material derived from wakame (*Undaria pinnatifida*) with high adsorption performance for three organic dyes. *Bioresour. Technol.* 318, 124082.
- Yao, B., Luo, Z., Du, S., Yang, J., Zhi, D., Zhou, Y., 2021. Sustainable biochar/MgFe<sub>2</sub>O<sub>4</sub> adsorbent for levofloxacin removal: adsorption performances and mechanisms. *Bioresour. Technol.* 340, 125698.
- Yu, H., Gu, L., Chen, L., Wen, H., Zhang, D., Tao, H., 2020. Activation of grapefruit derived biochar by its peel extracts and its performance for tetracycline removal. *Bioresour. Technol.* 316, 123971.
- Zhang, J., Jiang, D., Lin, Q., Chen, Z., Huang, Z., 2013. Gelcasting and pressureless sintering of silicon carbide ceramics using Al<sub>2</sub>O<sub>3</sub>-Y<sub>2</sub>O<sub>3</sub> as the sintering additives. *J. Eur. Ceram. Soc.* 33 (10), 1695–1699.
- Zhang, P., Li, Y., Cao, Y., Han, L., 2019a. Characteristics of tetracycline adsorption by cow manure biochar prepared at different pyrolysis temperatures. *Bioresour. Technol.* 285, 121348.
- Zhang, W., Li, H., Tang, J., Lu, H., Liu, Y., 2019b. Ginger straw waste-derived porous carbons as effective adsorbents toward methylene blue. *Molecules* 24 (3), 469.
- Zhang, J., Zhai, J., Zheng, H., Li, X., Wang, Y., Li, X., Xing, B., 2020. Adsorption, desorption and coadsorption behaviors of sulfamerazine, Pb(II) and benzoic acid on carbon nanotubes and nano-silica. *Sci. Total Environ.* 738, 139685.
- Zhang, J., Zheng, H., Li, X., Li, N., Liu, Y., Li, T., Wang, Y., Xing, B., 2022. Direct spectroscopic evidence for charge-assisted hydrogen-bond formation between ionizable organic chemicals and carbonaceous materials. *Environ. Sci. Technol.* 56 (13), 9356–9366.
- Zhao, M., Ma, X., Liao, X., Cheng, S., Liu, Q., Wang, H., Zheng, H., Li, X., Luo, X., Zhao, J., Li, F., Xing, B., 2022. Characteristics of algae-derived biochars and their sorption and remediation performance for sulfamethoxazole in marine environment. *Chem. Eng. J.* 430 (4), 133092.

Contents lists available at [ScienceDirect](https://www.sciencedirect.com)

Chemosphere

journal homepage: [www.elsevier.com/locate/chemosphere](https://www.elsevier.com/locate/chemosphere)

## Fenton oxidation treatment of oxytetracycline fermentation residues: Harmless performance and bioresource properties

Wenqiang Jia<sup>a,b</sup>, Jiaying Song<sup>a</sup>, Jian Wang<sup>a,b</sup>, Jinying Li<sup>a</sup>, Xue Li<sup>a</sup>, Qianwen Wang<sup>c</sup>, Xiang Chen<sup>a</sup>, Guocheng Liu<sup>a,\*</sup>, Qinghua Yan<sup>a</sup>, Chengzhi Zhou<sup>a</sup>, Shuaishuai Xin<sup>a,\*\*</sup>, Yanjun Xin<sup>a</sup>

<sup>a</sup> Qingdao Engineering Research Center for Rural Environment, College of Resource and Environment, Qingdao Agricultural University, Qingdao, 266109, China

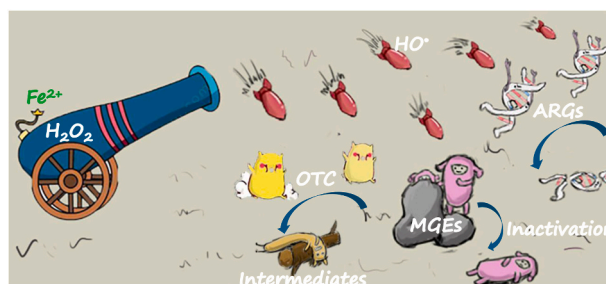
<sup>b</sup> State Key Laboratory of Urban Water Resource and Environment, School of Environment, Harbin Institute of Technology, Harbin, 150090, China

<sup>c</sup> Instrumental Analysis Center of Qingdao Agricultural University, Qingdao, 266109, China

### HIGHLIGHTS

- Oxytetracycline fermentation residues (OFRs) were treated by Fenton oxidation.
- Fenton oxidation treatment reduced oxytetracycline (OTC) in OFRs instantaneously.
- Degradation pathways of OTC in OFRs were clarified and the toxicity was evaluated.
- Inactivation of OTC resistant genes in OFRs was measured after Fenton oxidation.

### GRAPHICAL ABSTRACT



### ARTICLE INFO

Handling editor: Sergi Garcia-Segura

#### Keywords:

Antibiotic fermentation residues  
Residual antibiotic  
Antibiotic resistant genes  
Harmless treatment  
Degradation products  
Bioresource properties

### ABSTRACT

The pharmaceutical factories of oxytetracycline (OTC) massively produce OTC fermentation residues (OFRs). The high content of residual OTC and antibiotic resistance genes in OFRs must be considered and controlled at an acceptable level. This study therefore investigated the applicability of Fenton oxidation in OTC degradation and resistant gene inactivation of OFRs. The results revealed that  $\text{Fe}^{2+}$  as catalyzer could very rapidly activate  $\text{H}_2\text{O}_2$  to produce  $\text{HO}^\bullet$ , leading to instantaneous degradation of OTC. The optimum conditions for OTC removal were 60 mM  $\text{H}_2\text{O}_2$  and 140 mg/L  $\text{Fe}^{2+}$  under pH 7. After Fenton oxidation treatment, the release of water-soluble polysaccharides,  $\text{NO}_3\text{-N}$ , and  $\text{PO}_4\text{-P}$  was enhanced, whereas for proteins and  $\text{NH}_3\text{-N}$  were reduced. Three soluble fluorescence components (humic, tryptophan-like, and humic acid-like substances) were identified through fluorescence spectra with parallel factor analysis, and their reduction exceeded 50% after Fenton oxidation. There were twelve intermediates and three degradation pathways of OTC in OFRs during Fenton process. According to toxicity prediction, the comprehensive toxicity of OTC in OFRs was alleviated via Fenton oxidation treatment. In addition, Fenton oxidation showed the ability to reduce antibiotic resistance genes and mobile genetic elements, and even *tetO*, *tetG*, *int11*, and *int12* were eliminated completely. These results suggested that Fenton oxidation treatment could be an efficient strategy for removing OTC and resistance genes in OFRs.

\* Corresponding author.

\*\* Corresponding author.

E-mail addresses: [lg@qau.edu.cn](mailto:lg@qau.edu.cn) (G. Liu), [xinshuaishuai90@outlook.com](mailto:xinshuaishuai90@outlook.com) (S. Xin).

<https://doi.org/10.1016/j.chemosphere.2023.139201>

Received 27 April 2023; Received in revised form 30 May 2023; Accepted 11 June 2023

Available online 20 June 2023

0045-6535/© 2023 Elsevier Ltd. All rights reserved.

## 1. Introduction

Antibiotic fermentation residues (AFRs) are organic solid wastes from the manufacturing process of antibiotics, which can be produced in the amount of 147,000 tons each year in China and account for 70% of the world's total production (Cai et al., 2017; Hu et al., 2020). Oxytetracycline (OTC) as a veterinary antibiotic is extensively used to treat bacterial infections, and its fermentation residues (OFRs) contributes about 20% of the production of AFRs in China (Gong et al., 2021). OFRs contain high content of residual OTC (>1000 mg/kg) (Zhu et al., 2016), which pollution can inhibit microbial action, impose selective pressure on bacteria, even facilitate the proliferation of antibiotic resistance bacteria (Liu et al., 2022a). OFRs with high moisture content are particularly prone to corrupt, leading to the generation of antibiotic resistance genes (ARGs) (Cai et al., 2019). In addition, the ARGs were reported to spread through propagation and horizontal gene transfer of the host microbiota and enhance abundance (Jiang et al., 2022). The residual OTC in OFRs and the derived resistance bacteria and ARGs may cause great threats to ecological system and human health (Shen et al., 2019). OFRs had been listed in the *National Hazardous Waste List* of China since 2008 (Gong et al., 2020b). In most countries, AFRs are required to be harmlessly treated by high-temperature incineration to eliminate drug residues and ARGs (Chen et al., 2017a; Wang et al., 2021). The incineration treatment has high energy consumption, and also may cause secondary environmental pollution and the waste of OFR resource. Therefore, a simple and efficient method is sought to degrade residual antibiotic and inactivate ARGs in OFRs.

Current various treatment strategies mainly focused on removing residual antibiotics and improving the biodegradability of AFRs. Microwave irradiation could completely disintegrate residual antibiotic in cephalosporin mycelial dreg without any addition of chemicals (Cai et al., 2017). However, relatively high microwave power is bound to consume massive energy, limiting the large-scale application of microwave irradiation in disposing of AFRs. An alkaline-thermal pretreatment was used to reduce ARGs in spectinomycin mycelial residues and increase biodegradability (Song et al., 2020), but excess alkali addition was not beneficial to the subsequent resource utilization. The ionizing irradiation was developed for treating cephalosporin C fermentation residues, which removed cephalosporin C by 85.5% at 100 kGy (Chu et al., 2020). (Lu et al., 2021) reported that the carbonization could efficiently reduce the content of OTC and the abundance of ARGs in OFRs. However, this treatment required relatively high temperature and long retention time (>200 °C and >30 min), which increases the cost of harmless treatment. (Pan et al., 2023) developed low-temperature heating method (180 °C) to decompose doramectin, although high efficiency, the mycelial residues probably need to be pretreated via dewatering procedure. Hydrothermal treatment in the range of 120 °C–180 °C was effective in OFRs disintegration and OTC degradation, whereas high temperature tended to produce biodegradation-resistant substances and also high pressure was not beneficial for the cost and operability (Wang et al., 2020b). The AFRs could be composted into organic amendment, but OFR composting did not satisfactorily remove the high level of OTC and even increased the abundance of ARGs (Gong et al., 2021; Gong et al., 2020b). Considering the disadvantages of the above-mentioned treatments, therefore it has great significance to seek other green pollution-free and efficient pretreatment methods for the degradation of OTC and the inactivation of ARGs in OFRs.

Fenton oxidation treatment attracts attention in terms of wastewater treatment and sludge due to the reaction being mild and rapid, low cost, operational simplicity, and high efficiency of organic pollutant removal (Gamaralalage et al., 2019; Liu et al., 2013).  $\text{HO}^\bullet$  ( $E_0(\text{HO}^\bullet/\text{H}_2\text{O}) = +2.8 \text{ V}_{\text{NHE}}$ ) is produced when  $\text{H}_2\text{O}_2$  is catalyzed by Fe during the Fenton oxidation (Brillas and Garcia-Segura, 2020; Oturan et al., 2011), which is the second strongest oxidant known after fluorine (Brillas, 2022). Furthermore,  $\text{H}_2\text{O}_2$  can only be decomposed into  $\text{H}_2\text{O}$  and  $\text{O}_2$  compared to other oxidants and can not readily induce secondary pollution.

(Pulicharla et al., 2017) reported that Fenton reaction could well degrade chlortetracycline in wastewater sludge. In previous research, Fenton oxidation treatment was shown to be more effective at inactivating ARGs from excess sludge than microwave and alkaline treatment (Wang et al., 2020a). In addition, ARGs and antibiotic resistant bacteria on microplastics and in microplastic surrounding landfill leachate could be commendably removed by Fenton oxidation treatment (Shi et al., 2022b). However, there is little information about the treatment of AFRs using Fenton oxidation, despite the gratifying degradation rate can be obtained using Fenton method for most refractory organic contaminants, ARGs, and antibiotic resistant bacteria in terms of wastewaters, sludges, and microplastics. Therefore, Fenton oxidation may be hypothesized as a potential pretreatment method for degrading residual OTC and inactivating ARGs in OFRs.

In the present study, we carried out the practical treatment of Fenton oxidation to test the effectiveness in the elimination of residual OTC and ARGs in OFRs. Firstly, the effects of  $\text{H}_2\text{O}_2$  concentrations,  $\text{Fe}^{2+}$  dosages, and system pH condition on the degradation efficiency of OTC were investigated to determine the optimum condition for the treatment of OFRs. Secondly, the changes in the release of hydrophilic matters of OFRs before and after the Fenton oxidation were examined for analyzing bioresource properties. Then, the intermediate products of OTC produced from the Fenton oxidation treatment of OFRs were clarified, and the possible degradation pathways were proposed according to intermediates. Lastly, the inactivation of ARGs in OFRs was assessed during the oxidation process. The treatment effectiveness for residual OTC and ARGs showed the applicability of Fenton oxidation for disposing OFRs.

## 2. Materials and methods

### 2.1. Materials and chemicals

The raw OFRs was provided by a pharmaceutical manufacturer in Inner Mongolia, China, which was stored at  $-20^\circ\text{C}$  to prevent putrefaction. The OTC content of raw OFRs was 5060 mg/kg, and the physicochemical properties are shown in Table S1. OTC ( $\text{C}_{22}\text{H}_{24}\text{N}_2\text{O}_9$ , purity >98%) was purchased from Aladdin Chemical Reagent Co. Ltd. (China). Ferrous sulfate ( $\text{FeSO}_4 \cdot 7\text{H}_2\text{O}$ ), hydrogen peroxide ( $\text{H}_2\text{O}_2$ ), sodium hydroxide (NaOH), hydrochloric acid (HCl), methanol ( $\text{CH}_3\text{OH}$ ), sodium chloride (NaCl), acetic acid ( $\text{CH}_3\text{COOH}$ ), phosphoric acid ( $\text{H}_3\text{PO}_4$ ) and acetonitrile ( $\text{C}_2\text{H}_3\text{N}$ ) are analytic grade without further purification, and deionized water was used for all the experiments.

### 2.2. Experimental procedures

The 10 g OFRs and a certain amount of deionized water were mixed in 100 mL beaker to obtain the mixture with about 10% total solid content, and the suspension of OFRs was kept in a  $4^\circ\text{C}$  refrigerator for 12 h to make the solid matters fully absorb water. The obtained mixture were sonicated for 5 min and stirred for 1 min, and the operation was repeated to homogenize OFR suspension well. Subsequently,  $\text{H}_2\text{O}_2$  solution with initial concentrations of 5, 20, 40, 60, 80, 100 and 120 mM was added, the beaker was placed in a hexagonal stirrer, followed by adding a certain amount of  $\text{Fe}^{2+}$  with predetermined concentration of  $\text{Fe}^{2+}$ . Further, the degradation experiment was carried out at different pH levels of 1, 2.3, 3, 4, 5, 6, 7, 8, and 9 to reveal its influence on OTC removal. Finally, after 20 min of reaction, 5 mL sample was pipetted and immediately added into 16.5 mL methanol to quench the residual  $\text{H}_2\text{O}_2$ . The residual OTC of sample solution was extracted according to previous literature (Gong et al., 2020a). Triplicate was set up for the experiments.

### 2.3. Analytical methods

The concentration of OTC in the OFR suspensions was measured by a SIL-20AXR high-performance liquid chromatography with the

conditions of detection wavelength 355 nm, mobile phase acetonitrile/0.1% phosphoric acid (volume ratio of 15%/85%), and flow rate 1 mL/min (Gong et al., 2020a). The intermediates of OTC were analyzed using a triple series quadrupole mass spectrometer (Agilent 1290 Infinity/6460) described by Zhang (Zhang et al., 2022). The acute toxicity of OTC and its intermediates were analyzed by the Toxicity Estimation Software Tool (T.E.S.T). The concentration of water-soluble proteins, polysaccharides, NH<sub>3</sub>-N, NO<sub>3</sub>-N, and PO<sub>4</sub>-P released from OFRs were measured by the universal methods (Rice and Association, 2012). A F4700 fluorescence spectrometer (Hitachi, Japan) was used to record the fluorescence excitation-emission matrix spectra of the supernatant of OFR samples after Fenton treatment at optimum conditions ([Fe<sup>2+</sup>] = 140 mg/L, [H<sub>2</sub>O<sub>2</sub>] = 60 mM, pH = 7) for 0, 1, 3, 5, and 10 min with a scanning speed of 1200 nm/min. Prior to parallel factor analysis, the measured fluorescence spectra were ded Mili-Q water blank spectra to eliminate Raman scattering (Wen et al., 2003). The parallel factor analysis modeling was implemented by DOMFluor toolkit ([www.model.s.life.ku.dk](http://www.model.s.life.ku.dk)) in MATLAB 2010b, and the percentage of each component was calculated based on previous research (Bai et al., 2021; Stedmon and Bro, 2008).

The OFR sample treated by Fenton oxidation for 10 min was centrifugated at 4000 r/min for 5 min to produce supernatant and dreg. The DNA and ARGs in untreated OFRs and the supernatant and dreg of treated OFRs were respectively extracted and quantified according to the method descriptive by Gong (Gong et al., 2020b). Ten target ARGs related to OTC, two mobile genetic elements (MGEs) and 16S rRNA gene were amplified through a high-throughput qPCR (Thermo StepOne-Plus™). Primer sets used in this study were provided in Table S2. Heatmap for relative abundances of ARGs and integrons was generated in <https://hiplot-academic.com/>.

### 3. Results and discussion

#### 3.1. Optimizing degradation condition of OTC in OFRs by Fenton oxidation treatment

##### 3.1.1. OTC degradation kinetic in OFRs

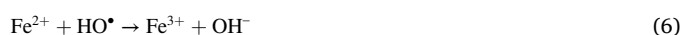
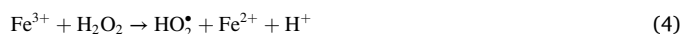
The degradation efficiency of OTC was investigated under different systems to estimate the performance of Fenton oxidation treatment within 60 min reaction time (Fig. S1). The OTC in OFRs could not realize self decomposition without the addition of reagents due to its high chemical stability. Besides, only 5.06% of OTC was removed in H<sub>2</sub>O<sub>2</sub> (60 mM) alone system, which could be explained by the limited oxidation activity of H<sub>2</sub>O<sub>2</sub>. Notably, the degradation efficiency of OTC significantly increased after the introduction of Fe<sup>2+</sup> compared with the H<sub>2</sub>O<sub>2</sub> alone system. Moreover, the reaction was completed instantaneously within 1 min and the degradation efficiency of OTC reached 63.5% when the concentration of H<sub>2</sub>O<sub>2</sub> and Fe<sup>2+</sup> was 60 mM and 140 mg/L, respectively, which greatly reduced the reaction time compared with other treatment methods to avoid consuming a lot of energy. The above phenomenon indicated that Fe<sup>2+</sup> as catalyzer could very rapidly activate H<sub>2</sub>O<sub>2</sub> to produce more HO• based on Haber-Weiss mechanism for the degradation of OTC (Tyagi et al., 2020). The Fenton oxidation process was divided in two reaction steps in this study. In a first step, OTC in OFRs was decomposed quickly within 1 min, ascribing to that H<sub>2</sub>O<sub>2</sub> could be activated to produce more HO• by a large number of Fe<sup>2+</sup>. As Fe<sup>2+</sup> ions were consumed in large quantities and rapidly, H<sub>2</sub>O<sub>2</sub> could not be activated in time to produce HO•. The reaction of second stage was much slower than the first one, and the degradation efficiency of OTC basically remained unchanged after the reaction time of 10 min. The above observation was similar to the report of the Fenton oxidation in the treatment of ciprofloxacin and landfill leachate (Aygun et al., 2012; Gupta and Garg, 2018). The reaction time was set as 10 min for the following discussion regarding the effect of different reaction conditions on the degradation efficiency of OTC in OFRs by Fenton oxidation treatment.

##### 3.1.2. Effects of H<sub>2</sub>O<sub>2</sub> concentration and Fe<sup>2+</sup> dosage

The production of HO• during the Fenton oxidation treatment is closely related to the H<sub>2</sub>O<sub>2</sub> concentration and Fe<sup>2+</sup> dosage. Therefore, it is necessary to explore the effects of H<sub>2</sub>O<sub>2</sub> concentration and Fe<sup>2+</sup> dosage on the degradation of OTC in OFRs. As shown in Fig. 1a, the degradation efficiency of OTC increased from 35.5% to 64.1% after 10 min with H<sub>2</sub>O<sub>2</sub> from 5 mM to 60 mM, suggesting that higher concentration of H<sub>2</sub>O<sub>2</sub> could provide more HO• and thus promote OTC degradation. Nevertheless, the degradation efficiency of OTC decreased from 64.1% to 54.8% when the concentration of H<sub>2</sub>O<sub>2</sub> continuously increased from 60 mM to 150 mM, which is attributed to the fact that the HO• radical could be scavenged by excess H<sub>2</sub>O<sub>2</sub> (Eq. (1) and (2)), producing HO<sub>2</sub>• or O<sub>2</sub> with lower oxidation potential (Wang et al., 2020b; Wu et al., 2022). Similar results were obtained in other studies (Wang et al., 2020b; Xin et al., 2021a; Zha et al., 2014).



The effect of Fe<sup>2+</sup> dosage from 80 mg/L to 210 mg/L on the degradation of OTC was investigated. As displayed in Fig. 1b, the degradation efficiency of OTC increased from 53.6% to 63.5% when Fe<sup>2+</sup> dosage ranged from 80 mg/L to 120 mg/L, which indicated that H<sub>2</sub>O<sub>2</sub> could be activated to produce more HO• via Eq. (3) with the increase of Fe<sup>2+</sup> dosage. Moreover, as shown in Eqs. (4) and (5), Fe<sup>3+</sup> reacts with H<sub>2</sub>O<sub>2</sub> and HO<sub>2</sub>• to form Fe<sup>2+</sup> although the reaction efficiency was low, leading to the depletion of Fe<sup>2+</sup> and the accumulation of Fe<sup>3+</sup> (Liu et al., 2022c; Zhu et al., 2019). However, the degradation efficiency of OTC decreased slightly with Fe<sup>2+</sup> dosage exceeding 140 mg/L. The above phenomenon can be explained as follows: (I) excess Fe<sup>2+</sup> could compete with OTC and act as HO• scavenger via Eq. (6), causing undesirable consumption of HO• and (II) more Fe(OH)<sub>3</sub> precipitates could be produced by excess Fe<sup>2+</sup> during the Fenton reaction process, which caused Fe<sup>2+</sup> could not rapidly activate H<sub>2</sub>O<sub>2</sub> to produce more HO• to effectively degrade OTC.



##### 3.1.3. Effects of operation pH

The pH of reaction system is usually considered as a significant factor in Fenton reaction, thus the effect of initial pH from 1.0 to 9.0 on degradation efficiency of OTC was investigated. As shown in Fig. 1c, the degradation efficiency of OTC increased from 60.7% at pH 1.0–69.6% at 3.0, which could be attributed to that H<sub>3</sub>O<sub>2</sub><sup>+</sup> as a stable form was generated under strong acidic conditions (pH < 3.0) via Eq. (7) and difficult to be activated to form HO• by catalyst (Ghanbari et al., 2020). Besides, excess H<sup>+</sup> could consumed HO• via Eq. (8) and inhibited the degradation of OTC. Previous studies have confirmed that the pH of 3.0 was identified as the optimal range for the degradation of organic pollutants by Fenton oxidation treatment (Nguyen et al., 2021; Zouanti et al., 2020). However, the result of the present work showed that the degradation efficiency of OTC further increased with the pH from 3.0 to 7.0, and the degradation efficiency of OTC reached 81.5% at pH 7.0. The degradation efficiency of OTC was intimately connected to the form of OTC species in the solution. Based on previous studies (Ramanayaka et al., 2020), the OTC species mainly exists as OTCH<sub>3</sub><sup>+</sup> at pH < 3.57, whereas the OTC species mainly exists as OTCH<sub>2</sub><sup>±</sup> at 3.57 < pH < 7.49 (Fig. S2). Generally, OTCH<sub>2</sub><sup>±</sup> has a higher electron density than OTCH<sub>3</sub><sup>+</sup>, which was more vulnerable to attack of HO• and lead to an increase the degradation efficiency of OTC with increasing pH from 3.0 to 7.0 (Chen et al., 2017b; Xin et al., 2021b). Although OTCH<sup>-</sup> or OTC<sup>2-</sup> as the

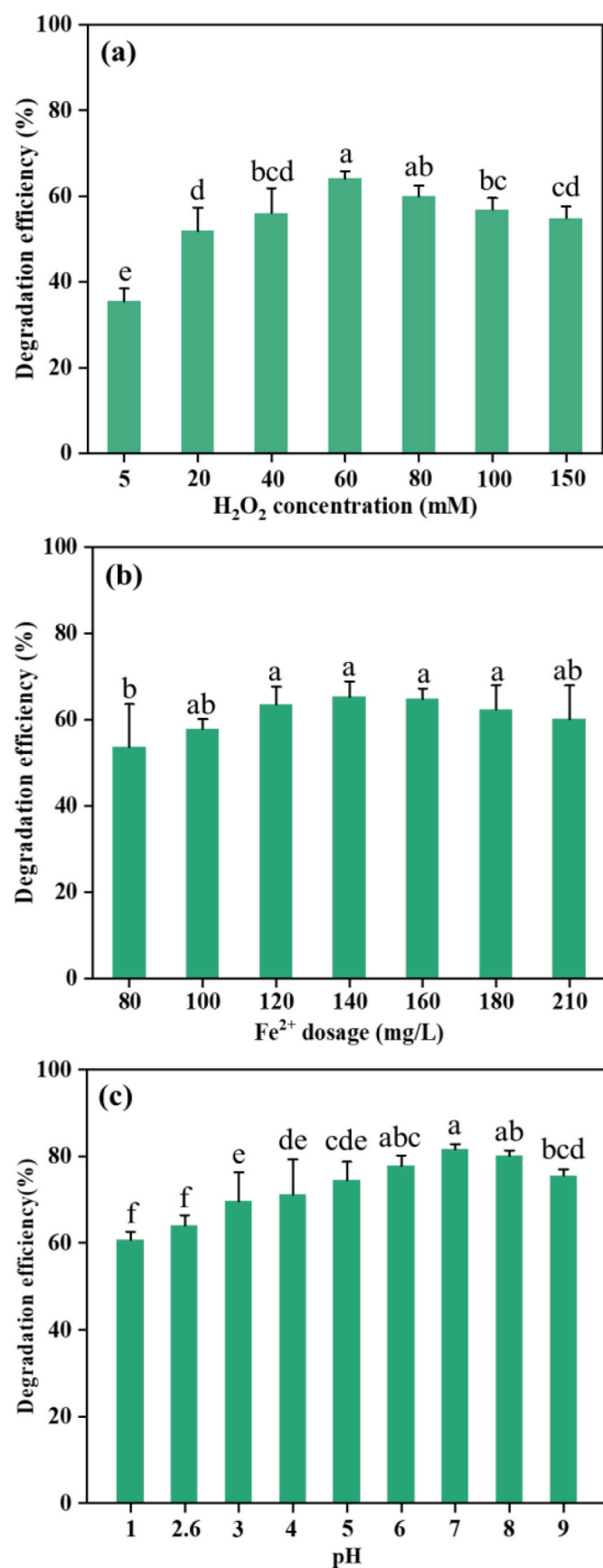
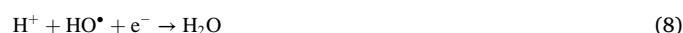


Fig. 1. Effects of H<sub>2</sub>O<sub>2</sub> concentration (a), Fe<sup>2+</sup> dosage (b) and solution pH (c) on OTC degradation in OFRs by Fenton treatment.

dominant existing form of OTC species at pH > 7.49 has a higher electron density than OTC $\text{H}_2^+$  (Ge et al., 2018), the degradation efficiency of OTC decreased to 75.5% with increasing pH to 9. The reduction of OTC degradation efficiency at pH > 7.0 could be attributed to two reasons: (I) the oxidation performance of HO $\cdot$  decreased under alkaline conditions (Zouanti et al., 2020) and (II) iron hydroxides may be produced via Eq. (9) under alkaline conditions (pH > 8.5) resulting in a decrease of Fe<sup>2+</sup>, which reduced the degradation efficiency of OTC.



### 3.2. The release of soluble biopolymers and nutrients

The release of water-soluble biopolymers (polysaccharides and proteins) from OFRs was investigated during the Fenton oxidation treatment. The concentration of soluble polysaccharides exhibited an increase trend within 1 min (Fig. 2a). Commonly, oxidation reactions have the effects of cell damage and sludge floc destruction (Zhang et al., 2021), thus this result could be attributed to that strong HO $\cdot$  of Fenton oxidation is capable of breaking the flocs and rupturing the mycelia cells in OFRs. Previous study found that heat-activated persulfate oxidation could also destroy the flocs of erythromycin fermentation residues and led to the solubilization of organics (Zhang et al., 2020). After the Fenton reaction of 1 min, the release of polysaccharides was nearly unchanged. The soluble polysaccharides may compete with mycelia cells for HO $\cdot$ , which inhibit the further increase of polysaccharide release (Chu et al., 2019). In normal case, the destruction of OFR flocs and mycelia due to Fenton oxidation should favor the release of soluble proteins. However, the concentration of soluble proteins showed a downward trend within 10 min Fenton reaction relative to 0 min (Fig. 2b). The decrease of protein release was primarily because the peptide bonds of protein molecules were easily attacked and destroyed by HO $\cdot$  with strong oxidation (Lund et al., 2011).

Fig. 2c–e gave the release of nitrogen and phosphorus nutrients when Fenton oxidation was applied to treat OFRs. As shown in Fig. 2c, the concentration of NH<sub>3</sub>-N showed a downward trend. The flocs disruption of OFRs by Fenton oxidation treatment could cause the dissolution of nitrogenous organics of mycelia into solution (Wang et al., 2018). Although the organic nitrogen could be converted into NH<sub>3</sub>-N by the strong oxidation performance of HO $\cdot$ , the generated NH<sub>3</sub>-N was liable to oxidize to NO<sub>3</sub>-N (Zhang et al., 2020). Moreover, (Shi et al., 2022a) validated the oxidation conversion of NH<sub>3</sub>-N into N<sub>2</sub>, NO<sub>3</sub>-N, or NO<sub>2</sub>-N by HO $\cdot$ . In this study, NH<sub>3</sub>-N would be released into the suspension, while at the same time it could be eliminated and transformed by HO $\cdot$ . For NO<sub>3</sub>-N, its release from the treated OFRs increased within 1 min (Fig. 2d), which could be attributed to the floc destruction and the cell rupture of residual microbe and the transformation of NH<sub>3</sub>-N to NO<sub>3</sub>-N.

The phosphorus nutrient is mainly derived from the cells of residual microbe in OFRs (Turner and Leytem, 2004). The concentration of PO<sub>4</sub>-P released from OFRs showed an upward trend within 0–3 min of Fenton reaction (Fig. 2e). Similar to the mechanism for the release of other water-soluble components, the floc destruction and cell rupture during Fenton reaction favor the release of phosphorus. Moreover, organophosphorus compounds and/or related phosphorus forms in OFRs can be transformed into PO<sub>4</sub>-P during the treatment of Fenton oxidation (Wang et al., 2022). However, the release of PO<sub>4</sub>-P exhibited the decreased pattern at the time range from 3 min to 10 min. (Zhang et al., 2020) reported the decreased release of PO<sub>4</sub>-P from erythromycin fermentation residues during the heat-activated persulfate oxidation, and they attributed the pattern to the adsorption of onto the solid particles of the residues. In this study, iron hydroxides may form during the Fenton oxidation (Eq. (9) and (10)) and accumulate with the increase of

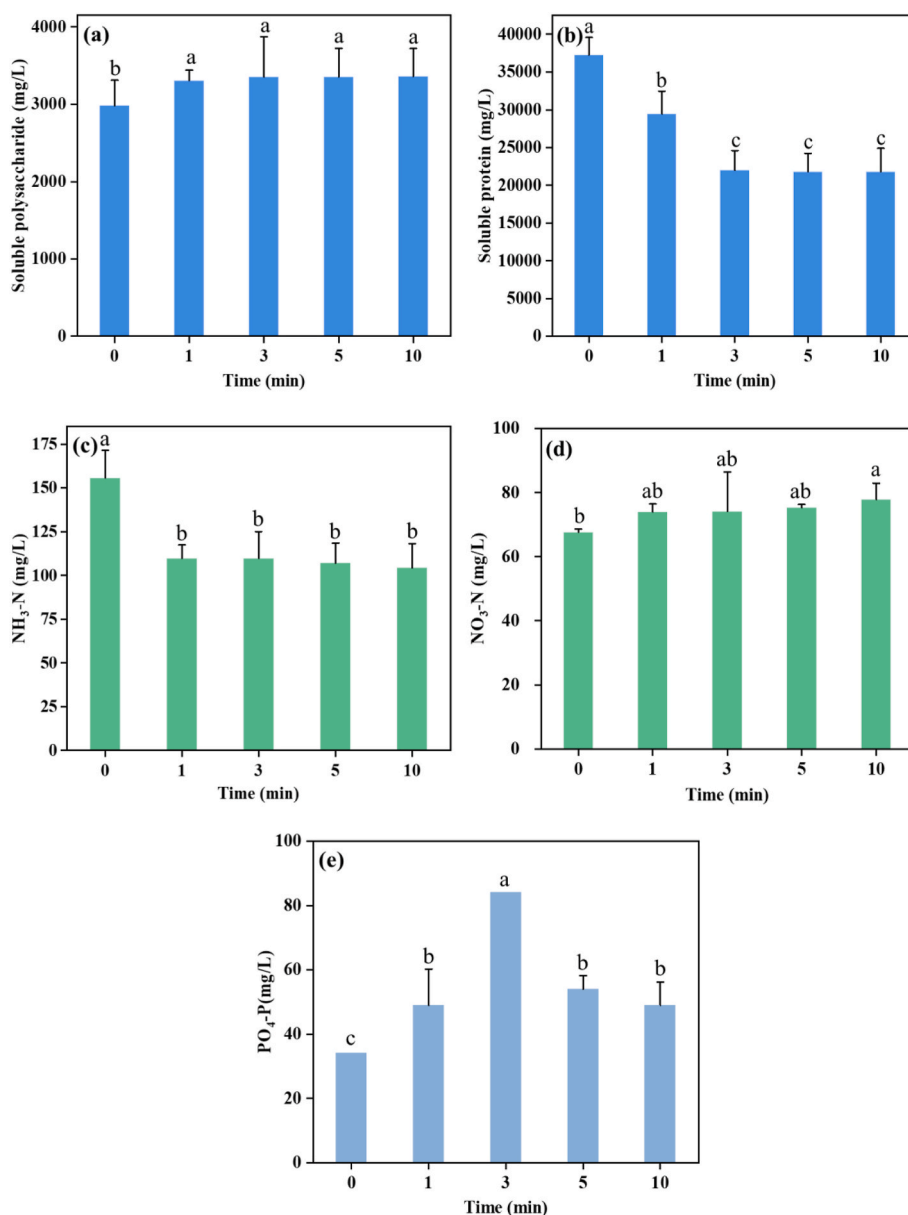


Fig. 2. The release of soluble polysaccharides (a), proteins (b), NH<sub>3</sub>-N (c), NO<sub>3</sub>-N (d), and PO<sub>4</sub>-P (e) from OFRs after Fenton treatment ([Fe<sup>2+</sup>] = 140 mg/L, [H<sub>2</sub>O<sub>2</sub>] = 60 mM, pH = 7).

reaction time. In solution, PO<sub>4</sub>-P could be greatly adsorbed by the iron hydroxides (Mochizuki et al., 2021). Moreover, the free metal ions (Fe<sup>2+</sup> and Fe<sup>3+</sup>) could combine with PO<sub>4</sub>-P into insoluble precipitates (Wang et al., 2022). These may be important reasons for the reduced release of PO<sub>4</sub>-P after Fenton reaction for 5–10 min. Overall, the release kinetic of PO<sub>4</sub>-P from OFRs under Fenton oxidation treatment may be governed complex mechanisms.

### 3.3. Fluorescence components identified by parallel factor analysis

Three components in OFR were determined based on residual analysis, split-half validation and random initialization analysis (Fig. 3). Excitation-emission matrix contours and wavelengths loadings of the three components in different OFR samples were eventually defined based on the excitation-emission matrix dataset. The component 1 (C1) was bimodal at Ex/Em of 320/430 nm and 250/430 nm (Fig. 3a and b), indicating the presence of humic substances (Qu et al., 2012). In Fig. 3c and d, the component 2 (C2) at Ex/Em of 280/340 nm was assigned to

tryptophan-like substances, which was related to biological production and microorganism activity (Her et al., 2004; Xu et al., 2013). The component 3 (C3) presented maxima peaks at Ex/Em of 400/490 nm and 270/490 nm (Fig. 3e and f), which were reported high polymer humic acid-like substances (Wen et al., 2003).

The fluorescence intensity distributions of three components in OFR samples by Fenton treatment at 0, 1, 3, 5 and 10 min were shown in Fig. 4. The fluorescence intensities of C1 and C2 were higher than that of C3, which indicated that C1 and C2 were the dominant components. The fluorescence intensity of three components in OFRs were immediately reduced by Fenton oxidation treatment within 1 min. During Fenton oxidation treatment process, the fluorescence intensity of humic, tryptophan-like, and humic acid-like substances reduced more than 52.3%, 52.7, and 53.8%, respectively. The reduction of fluorescence intensity for C1 could be attributed to two reasons: (I) the self-quenching of humic substances (Liu et al., 2022b) and (II) the highly electronegative carboxyl of humic substances could undergo the complexation with metal ions on the surfaces of the insoluble precipitates and form humic



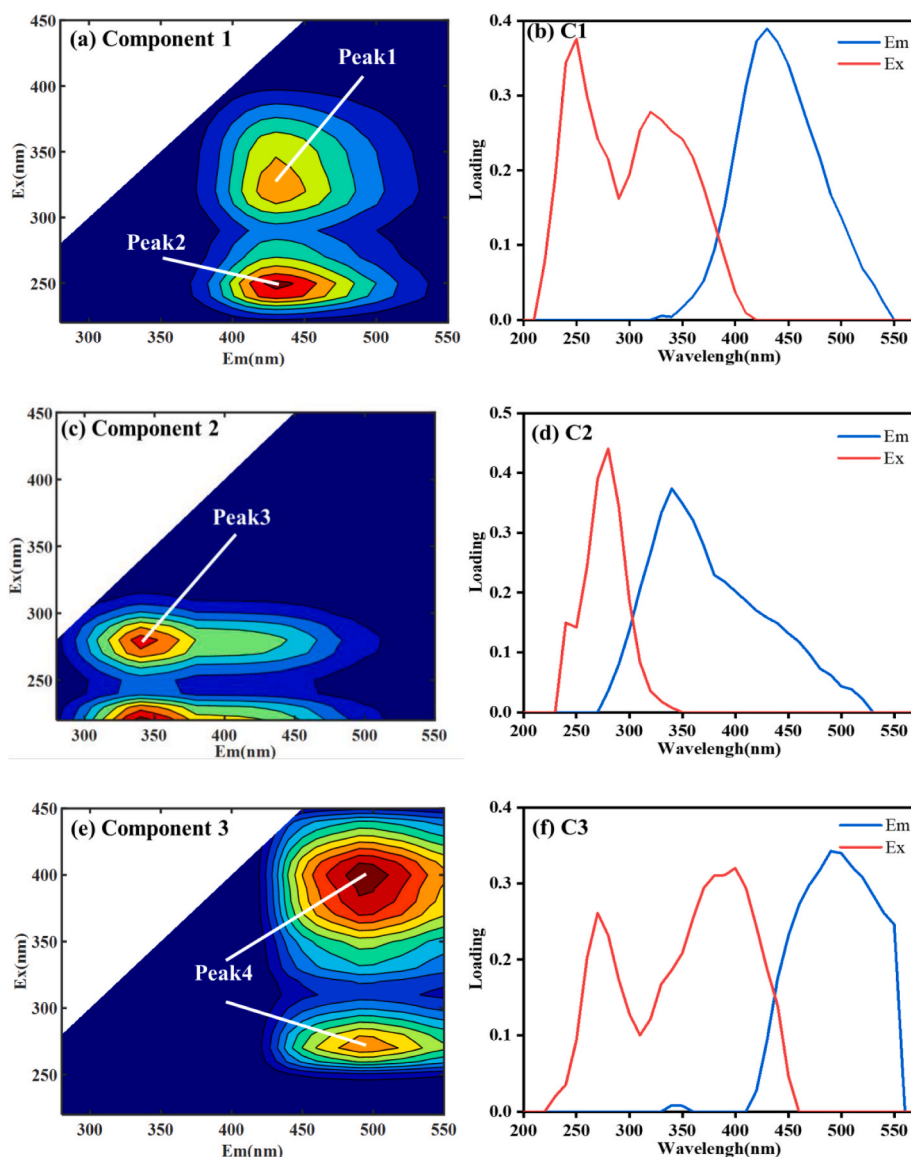


**Fig. 3.** Excitation-emission matrix contours and wavelengths loadings of the three components in OFR samples after Fenton treatment. (Component 1, C1 (a, b); Component 2, C2 (c, d); Component 3, C3 (e, f)).

substances-inorganic salt flocs (Wang et al., 2022). C2 was assigned to tryptophan-like protein substances, which the reduction of fluorescence intensity. The tryptophan-like proteins could be destroyed by  $\text{HO}^\bullet$  and converted into smaller organic fractions or inorganic matters without fluorescence characteristics. Similarly, (Chu et al., 2020) reported that the fluorescence intensity of tryptophan-like protein substances decreased considerably after ozonation. In addition, the introduction of iron ions could also denature tryptophan-like proteins leading to the fluorescence intensity decrease of C2 (Zhang et al., 2021). The fluorescence intensity of C3 immediately reduced during the oxidation, which could be explained by the chemical structure change of high polymer humic acid-like components under the action of  $\text{HO}^\bullet$  (Lu et al., 2020).

### 3.4. Degradation intermediates and toxicity estimation

To better investigate the degradation pathways of OTC in OFRs by Fenton oxidation treatment, the triple series quadrupole mass spectrometer was adopted to determine the possible intermediates under the optimum conditions ( $[\text{Fe}^{2+}] = 140 \text{ mg/L}$ ,  $[\text{H}_2\text{O}_2] = 60 \text{ mM}$ ,  $\text{pH} = 7$ ). The results of degradation intermediates and the possible degradation

pathways as shown in Fig. 5. In pathway I, OTC ( $m/z = 461.0$ ) was converted to P1 ( $m/z = 382.9$ ) through dehydration, deamidation and loss of hydroxyl groups (Yang et al., 2020). The formed P1 was further fragmented into P2 ( $m/z = 279.0$ ) and then resulted in the formation of P3 ( $m/z = 262.1$ ) through further the loss of hydroxyl group. Subsequently, the P3 was oxidized to generate P4 ( $m/z = 199.1$ ) and P5 ( $m/z = 143.1$ ) through open-ring reaction. In pathway II, the OTC was transformed into P6 ( $m/z = 476.4$ ), via hydroxylation and double carbon bonds breaking. Due to electron density augment of N in  $\text{NH}_2$  group, the acylamino on P6 by  $\text{HO}^\bullet$  attacked. Besides, the tertiary amine on P6 reacted with  $\text{HO}^\bullet$ . The formation of P7 ( $m/z = 389.0$ ) was ascribed to the above two reasons and the loss of hydroxyl group (Liu et al., 2016a; Tang et al., 2018). The further intermediates P8 ( $m/z = 274.2$ ) and P9 ( $m/z = 240.1$ ) were caused by dehydroxylation, deamidation, demethylation, decarbonylation and double carbon bonds breaking (Yang et al., 2020). For the pathway III, according to previous studies (Liu et al., 2016a; Liu et al., 2016b), the keto/enol sites of OTC were attacked through hydroxy addition reaction, leading to the open-ring reaction and formed multiple hydroxylated intermediate P10 ( $m/z = 525.1$ ). As a further degradation intermediates of P10, P11 ( $m/z = 349.2$ ) was generated as a result of the

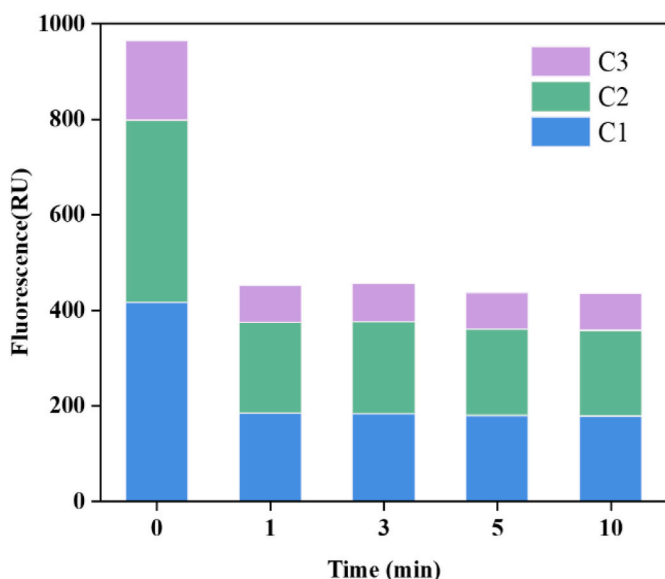


Fig. 4. The fluorescence intensity scores of the three components in OFR samples after Fenton treatment at 0, 1, 3, 5, and 10 min ( $[\text{Fe}^{2+}] = 140 \text{ mg/L}$ ,  $[\text{H}_2\text{O}_2] = 60 \text{ mM}$ ,  $\text{pH} = 7$ ).

removal of N-methyl, carboxyl, amino, carbonyl groups, and acylamide groups (Ma et al., 2021). Afterwards, P11 was converted into P12 ( $m/z = 305.1$ ) by dehydroxylation, oxidation of hydroxyl to carbonyl and the double carbon bonds breaking (Cao et al., 2016).

The half lethal concentrations of fathead minnow ( $\text{LC}_{50-96 \text{ h}}$ ) and daphnia magna ( $\text{LC}_{50-48 \text{ h}}$ ) were analyzed to assess the acute toxicity of OTC and its intermediates using Toxicity Estimation Software Tool. As shown in Fig. 6a, the  $\text{LC}_{50-96 \text{ h}}$  of OTC was  $1.12 \text{ mg/L}$ , which was defined as “toxic” for fathead minnow. The degradation intermediate P1 ( $0.12 \text{ mg/L}$ ), P8 ( $0.54 \text{ mg/L}$ ) and P9 ( $0.15 \text{ mg/L}$ ) were considered to be “very toxic” for fathead minnow due to the less than  $1 \text{ mg/L}$  of  $\text{LC}_{50-96 \text{ h}}$ . The  $\text{LC}_{50-96 \text{ h}}$  values of other intermediates were higher than that of OTC, which indicated that their acute toxicity for fathead minnow was lower than OTC. The acute toxicity of P4 ( $18.47 \text{ mg/L}$ ), P5 ( $27.21 \text{ mg/L}$ ), P6 ( $26.88 \text{ mg/L}$ ), P7 ( $19.25 \text{ mg/L}$ ), and P10 ( $17.77 \text{ mg/L}$ ) for fathead minnow even changed to “harmful” due to their  $\text{LC}_{50-96 \text{ h}}$  higher than  $10 \text{ mg/L}$  (Xin et al., 2021c; Zhou et al., 2020). Generally, the  $\text{LC}_{50-48 \text{ h}}$  in the range of  $0-12.7 \text{ mg/L}$  and higher than  $12.7 \text{ mg/L}$  are defined as “toxic” and “harmful” for daphnia magna, respectively (Yang et al., 2021). From the  $\text{LC}_{50-48 \text{ h}}$  result of OTC and its intermediates (Fig. 6b), the OTC was defined as “toxic” for daphnia magna due to that its  $\text{LC}_{50-48 \text{ h}}$  ( $4.29 \text{ mg/L}$ ) was lower than  $12.7 \text{ mg/L}$ . The acute toxicity of intermediates for daphnia magna, except for P8 ( $3.14 \text{ mg/L}$ ) and P9 ( $0.60 \text{ mg/L}$ ), was lower than that of OTC. Noteworthy, the  $\text{LC}_{50-96 \text{ h}}$  of P4 ( $50.81 \text{ mg/L}$ ), P5 ( $120.78 \text{ mg/L}$ ), P6 ( $16.44 \text{ mg/L}$ ), P7 ( $94.03 \text{ mg/L}$ ),

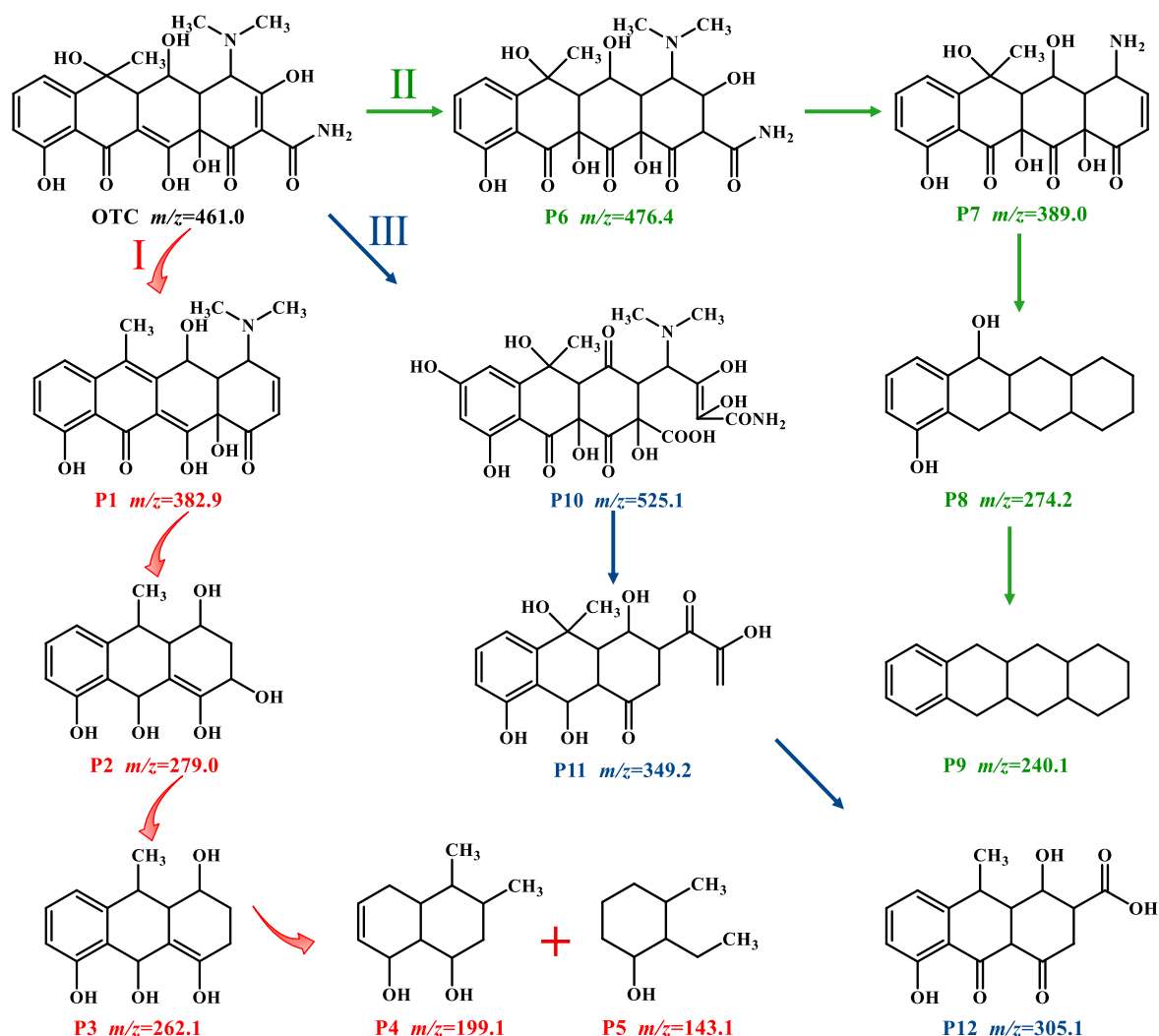


Fig. 5. Proposed degradation pathways of OTC in OFRs by Fenton treatment.

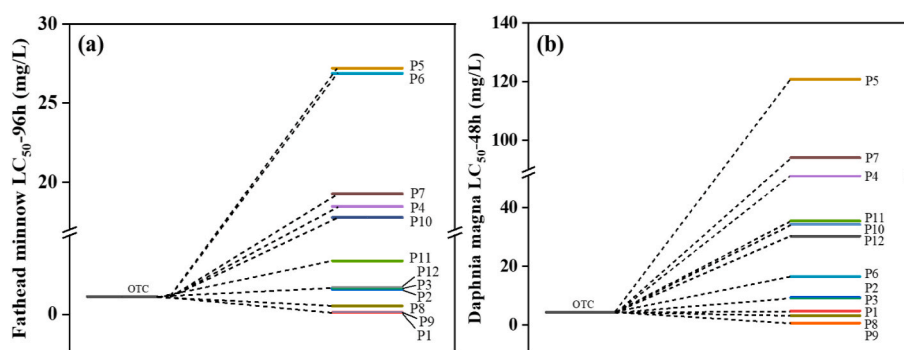


Fig. 6. The fathead minnow  $LC_{50-96}$  h (a) and daphnia magna  $LC_{50-48}$  h (b) of OTC and its intermediates.

P10 (34.21 mg/L), P11 (35.41 mg/L) and P12 (30.27 mg/L) was higher than 12.7 mg/L, thus the above intermediates became into “harmful” for daphnia magna. According to the toxicity prediction results, the overall environmental hazards of OFRs were effectively alleviated by Fenton oxidation treatment.

### 3.5. Abundances of ARGs and MGEs

Fenton oxidation has the unique characteristics of strong and rapid reaction, which made it attractive in ARGs emission reduction. The variations in the abundances of ARGs and MGEs in OFRs were investigated before and after Fenton oxidation treatment. As shown in Fig. 7, nine ARGs and MGEs (*int11* and *int12*) were detected in the raw OFRs. By contrast, the *tetG*, *tetO*, *tetX*, *tetW*, *tet32*, *tetQ*, *int11* and *int12* were not detected in the dreg of Fenton-treated OFRs, and also the *tetG*, *tetO*, *int11* and *int12* in the supernatant, suggesting the inactivation effect of Fenton oxidation treatment on ARGs and MGEs. The abundances of the tested ARGs (except *tetC* and *tetA*) and two MGEs in the treated OFRs showed a significant decline compared with raw OFRs, but few differences were observed for *tetC* and *tetA*. Previous study confirmed that reactive oxygen species may cause grave oxidative base lesions and modificate 2-deoxyribose respectively, resulting in genes destruction (Cadet et al., 2010).  $HO^{\bullet}$ ,  $^1O_2$ ,  $O_2^{\bullet-}$  and  $H_2O_2$  play outstanding role, among them  $HO^{\bullet}$  ( $E_0(HO^{\bullet}/H_2O) = +2.8 V_{NHE}$ ) was the most reactive (Chatterjee and Walker, 2017).  $HO^{\bullet}$  reacted with antibiotic resistant bacteria, resulting in cell death and DNA leakage (Ahmed et al., 2020).  $HO^{\bullet}$  further

attacked the DNA bases through I) adding to double bond, II) replacing hydrogen atom in methyl group, and III) attacking sugar residue in DNA bases immediate vicinity (Ahmed et al., 2021), resulting in DNA damage (Shi et al., 2022b; Vilela et al., 2021). Therefore, it is reasonable that the Fenton oxidation treatment can decrease the abundances of ARGs and MGEs in OFRs effectively.

## 4. Conclusion

This study attempted to explore the performance of OTC degradation and ARGs inactivation in OFRs by Fenton oxidation. The results suggested that Fenton oxidation treatment instantaneously and effectively removed OTC in OFRs under the conditions of 60 mM  $H_2O_2$ , 140 mg/L  $Fe^{2+}$ , and neutral pH 7. The method of Fenton oxidation boosted the release of polysaccharides,  $NO_3-N$  and  $PO_4-P$  into the suspension, whereas reduced the release of proteins and  $NH_3-N$ . Three water-soluble fluorescence components of OFRs were significantly degraded after the treatment of Fenton reaction. Twelve possible degradation intermediates of OTC in the Fenton-treated OFRs were identified, and correspondingly three degradation pathways were proposed. The predicted acute toxicities of major intermediates could be relieved effectively, lowering the environmental risks of OFRs. Notably, Fenton oxidation treatment could reduce the abundances of the most of ARGs and MGEs in OFRs. Therefore, Fenton oxidation method could be a promising approach for the removal of antibiotics and ARGs in antibiotic fermentation residues. Considering the huge production of antibiotic fermentation residues, large-scale practice of harmless treatment using Fenton oxidation requires in-depth study and assessment.

### Credit author statement

Wenqiang Jia: Data curation, Formal analysis, Investigation, Writing – original draft. Jian Wang: Data curation, Investigation. Jiaying Song: Data curation, Formal analysis, Investigation. Jinying Li and Xue Li: Investigation. Qianwen Wang: Methodology, Investigation. Xiang Chen: Formal analysis, Supervision. Guocheng Liu: Conceptualization, Writing – review & editing, Supervision, Funding acquisition. Qinghua Yan: Formal analysis, Supervision. Chengzhi Zhou: Software, Supervision. Shuaishuai Xin: Conceptualization, Writing – review & editing, Supervision. Yanjun Xin: Supervision, Funding acquisition. All authors read and approved the final manuscript.

### Declaration of competing interest

The authors declare that they have no known competing financial interests or personal relationships that could have appeared to influence the work reported in this paper.

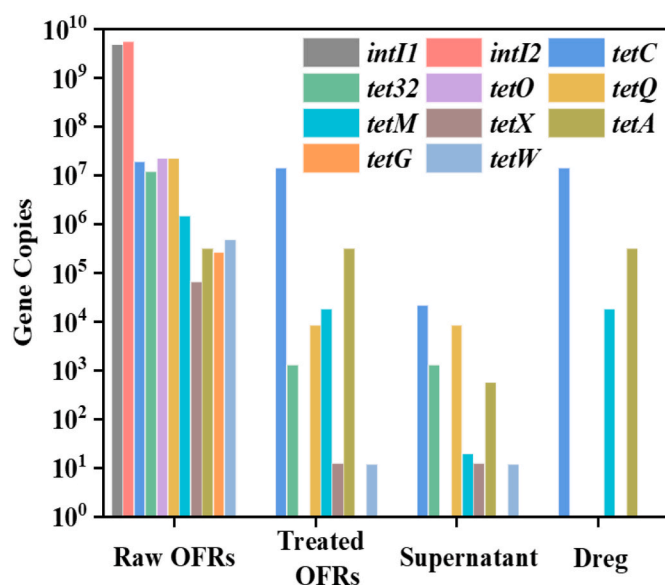


Fig. 7. Changes of the gene copies of ARGs and integrons in raw OFRs, treated OFRs, and the supernatant and dreg of treated OFRs.

## Data availability

Data will be made available on request.

## Acknowledgements

This work was financially supported by National Natural Science Foundation of China (52170135), and thanks for the supporting of sample testing by Instrumental Analysis Center of Qingdao Agricultural University.

## Appendix. ASupplementary data

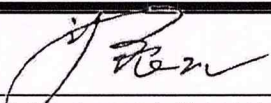
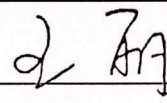
Supplementary data to this article can be found online at <https://doi.org/10.1016/j.chemosphere.2023.139201>.

## References

- Ahmed, Y., Lu, J., Yuan, Z., et al., 2020. Efficient inactivation of antibiotic resistant bacteria and antibiotic resistance genes by photo-Fenton process under visible LED light and neutral pH. *Water Res.* 179, 115878 <https://doi.org/10.1016/j.watres.2020.115878>.
- Ahmed, Y., Zhong, J., Yuan, Z., et al., 2021. Simultaneous removal of antibiotic resistant bacteria, antibiotic resistance genes, and micropollutants by a modified photo-Fenton process. *Water Res.* 197, 117075 <https://doi.org/10.1016/j.watres.2021.117075>.
- Aygun, A., Yilmaz, T., Nas, B., et al., 2012. Effect of temperature on fenton oxidation of young landfill leachate: kinetic assessment and sludge properties. *Globalst Int. J.* 14 (4), 487–495. <https://doi.org/10.1016/j.ecoleng.2012.09.001>.
- Bai, S., Xi, B., Li, X., et al., 2021. Anaerobic digestion of chicken manure: sequences of chemical structures in dissolved organic matter and its effect on acetic acid production. *J. Environ. Manag.* 296, 113245 <https://doi.org/10.1016/j.jenvman.2021.113245>.
- Brillas, E., 2022. Fenton, photo-Fenton, electro-Fenton, and their combined treatments for the removal of insecticides from waters and soils. A review. *Separ. Purific. Technol.* 284, 120290 <https://doi.org/10.1016/j.seppur.2021.120290>.
- Brillas, E., Garcia-Segura, S., 2020. Benchmarking recent advances and innovative technology approaches of Fenton, photo-Fenton, electro-Fenton, and related processes: a review on the relevance of phenol as model molecule. *Separ. Purific. Technol.* 237, 116337 <https://doi.org/10.1016/j.seppur.2019.116337>.
- Cadet, J., Douki, T., Ravanat, J., 2010. Oxidatively generated base damage to cellular DNA. *Free Radical Biol. Med.* 49 (1), 9–21. <https://doi.org/10.1016/j.freeradbiomed.2010.03.025>.
- Cai, C., Liu, H., Dai, X., et al., 2019. Multiple selection of resistance genes in arable soil amended with cephalosporin fermentation residue. *Soil Biol. Biochem.* 136, 107538 <https://doi.org/10.1016/j.soilbio.2019.107538>.
- Cai, C., Liu, H., Wang, B., 2017. Performance of microwave treatment for disintegration of cephalosporin mycelial dreg (CMD) and degradation of residual cephalosporin antibiotics. *J. Hazard Mater.* 331, 265–272. <https://doi.org/10.1016/j.jhazmat.2017.02.034>.
- Cao, M., Wang, P., Ao, Y., et al., 2016. Visible light activated photocatalytic degradation of tetracycline by a magnetically separable composite photocatalyst: graphene oxide/magnetite/cerium-doped titania. *J. Colloid Interface Sci.* 467, 129–139. <https://doi.org/10.1016/j.jcis.2016.01.005>.
- Chatterjee, N., Walker, G., 2017. Mechanisms of DNA damage, repair, and mutagenesis. *Environ. Mol. Mutagen.* 58, 235–263. <https://doi.org/10.1002/em.22087>.
- Chen, W., Geng, Y., Hong, J., et al., 2017a. Life cycle assessment of antibiotic mycelial residues management in China. *Renew. Sustain. Energy Rev.* 79, 830–838. <https://doi.org/10.1016/j.rser.2017.05.120>.
- Chen, Y., Ma, Y., Yang, J., et al., 2017b. Aqueous tetracycline degradation by H2O2 alone: removal and transformation pathway. *Chem. Eng. J.* 307, 15–23. <https://doi.org/10.1016/j.cej.2016.08.046>.
- Chu, L., Chen, D., Wang, J., et al., 2019. Degradation of antibiotics and antibiotic resistance genes in erythromycin fermentation residues using radiation coupled with peroxymonosulfate oxidation. *Waste Manag.* 96, 190–197. <https://doi.org/10.1016/j.wasman.2019.07.031>.
- Chu, L., Chen, D., Wang, J., et al., 2020. Degradation of antibiotics and inactivation of antibiotic resistance genes (ARGs) in Cephalosporin C fermentation residues using ionizing radiation, ozonation and thermal treatment. *J. Hazard Mater.* 382, 121058 <https://doi.org/10.1016/j.jhazmat.2019.121058>.
- Gamaralalage, D., Sawai, O., Nunoura, T., 2019. Degradation behavior of palm oil mill effluent in Fenton oxidation. *J. Hazard Mater.* 364, 791–799. <https://doi.org/10.1016/j.jhazmat.2018.07.023>.
- Ge, L., Dong, Q., Halsall, C., et al., 2018. Aqueous multivariate phototransformation kinetics of dissociated tetracycline: implications for the photochemical fate in surface waters. *Environ. Sci. Pollut. Control Ser.* 25 (16), 15726–15732. <https://doi.org/10.1007/s11356-018-1765-0>.
- Ghanbari, F., Riahi, M., Kakavandi, B., et al., 2020. Intensified peroxydisulfate/microparticles-zero valent iron process through aeration for degradation of organic pollutants: kinetic studies, mechanism and effect of anions. *J. Water Proc. Eng.* 36, 101321 <https://doi.org/10.1016/j.jwpe.2020.101321>.
- Gong, P., Liu, H., Wang, G., et al., 2021. Enhanced depletion of antibiotics and accelerated stabilization of dissolved organic matter by hydrothermal pretreatment during composting of oxytetracycline fermentation residue. *Bioresour. Technol.* 339, 125618 <https://doi.org/10.1016/j.biortech.2021.125618>.
- Gong, P., Liu, H., Wang, M., et al., 2020a. Characteristics of hydrothermal treatment for the disintegration of oxytetracycline fermentation residue and inactivation of residual antibiotics. *Chem. Eng. J.* 402, 126011 <https://doi.org/10.1016/j.cej.2020.126011>.
- Gong, P., Liu, H., Xin, Y., et al., 2020b. Composting of oxytetracycline fermentation residue in combination with hydrothermal pretreatment for reducing antibiotic resistance genes enrichment. *Bioresour. Technol.* 318, 124271 <https://doi.org/10.1016/j.biortech.2020.124271>.
- Gupta, A., Garg, A., 2018. Degradation of ciprofloxacin using Fenton's oxidation: effect of operating parameters, identification of oxidized by-products and toxicity assessment. *Chemosphere* 193, 1181–1188. <https://doi.org/10.1016/j.chemosphere.2017.11.046>.
- Her, N., Amy, G., Park, H., et al., 2004. Characterizing algogenic organic matter (AOM) and evaluating associated NF membrane fouling. *Water Res.* 38 (6), 1427–1438. <https://doi.org/10.1016/j.watres.2003.12.008>.
- Hu, J., Hong, C., Li, Z., et al., 2020. Nitrogen release of hydrothermal treatment of antibiotic fermentation residue and preparation of struvite from hydrolysate. *Sci. Total Environ.* 713, 135174 <https://doi.org/10.1016/j.scitotenv.2019.135174>.
- Jiang, M., Song, S., Liu, H., et al., 2022. Responses of methane production, microbial community and antibiotic resistance genes to the mixing ratio of gentamicin mycelial residues and wheat straw in anaerobic co-digestion process. *Sci. Total Environ.* 806 (2), 150488 <https://doi.org/10.1016/j.scitotenv.2021.150488>.
- Liu, H., Chen, Q., Yu, Y., et al., 2013. Influence of Fenton's reagent doses on the degradation and mineralization of H-acid. *J. Hazard Mater.* 263 (2), 593–599. <https://doi.org/10.1016/j.jhazmat.2013.10.021>.
- Liu, W., Li, J., Li, X., et al., 2022a. Increasing the removal efficiency of antibiotic resistance through anaerobic digestion with free nitrous acid pretreatment. *J. Hazard Mater.* 438, 129535 <https://doi.org/10.1016/j.jhazmat.2022.129535>.
- Liu, Y., Deng, S., Chen, L., et al., 2022b. Spectroscopic characterization of soil dissolved organic matter during dielectric barrier discharge (DBD) plasma treatment: effects of discharge power, atmosphere and soil moisture content. *Chemosphere* 297, 134145. <https://doi.org/10.1016/j.chemosphere.2022.134145>.
- Liu, Y., He, X., Fu, Y., et al., 2016a. Degradation kinetics and mechanism of oxytetracycline by hydroxyl radical-based advanced oxidation processes. *Chem. Eng. J.* 284, 1317–1327. <https://doi.org/10.1016/j.cej.2015.09.034>.
- Liu, Y., He, X., Fu, Y., et al., 2016b. Kinetics and mechanism investigation on the destruction of oxytetracycline by UV-254nm activation of persulfate. *J. Hazard Mater.* 305, 229–239. <https://doi.org/10.1016/j.jhazmat.2015.11.043>.
- Liu, Y., Wang, X., Sun, Q., et al., 2022c. Enhanced visible light photo-Fenton-like degradation of tetracyclines by expanded perlite supported FeMo(3)O(x)/g-C(3)N(4) floating Z-scheme catalyst. *J. Hazard Mater.* 424 (A), 127387 <https://doi.org/10.1016/j.jhazmat.2021.127387>.
- Lu, Q., Dai, L., Li, L., et al., 2021. Valorization of oxytetracycline fermentation residue through torrefaction into a versatile and recyclable adsorbent for water pollution control. *J. Environ. Chem. Eng.* 9 (4), 105397 <https://doi.org/10.1016/j.jece.2021.105397>.
- Lu, W., Chen, N., Feng, C., et al., 2020. Treatment of polluted river sediment by electrochemical oxidation: changes of hydrophilicity and acute cytotoxicity of dissolved organic matter. *Chemosphere* 243, 125283. <https://doi.org/10.1016/j.chemosphere.2019.125283>.
- Lund, M., Heinonen, M., Baron, C., et al., 2011. Protein oxidation in muscle foods: a review. *Mol. Nutr. Food Res.* 55 (1), 83–95. <https://doi.org/10.1002/mnfr.201000453>.
- Ma, W., Yao, B., Zhang, W., et al., 2021. Fabrication of PVDF-based piezocatalytic active membrane with enhanced oxytetracycline degradation efficiency through embedding few-layer E-MoS2 nanosheets. *Chem. Eng. J.* 415, 129000 <https://doi.org/10.1016/j.cej.2021.129000>.
- Mochizuki, Y., Bud, J., Liu, J., et al., 2021. Adsorption of phosphate from aqueous using iron hydroxides prepared by various methods. *J. Environ. Chem. Eng.* 9 (1), 104645 <https://doi.org/10.1016/j.jece.2020.104645>.
- Nguyen, C., Tran, M., Van, T., et al., 2021. Efficient removal of antibiotic oxytetracycline from water by Fenton-like reactions using reduced graphene oxide-supported bimetallic Pd/nZVI nanocomposites. *J. Taiwan Inst. Chem. Eng.* 119, 80–89. <https://doi.org/10.1016/j.tice.2021.02.001>.
- Oturán, M., Oturan, N., Edelahe, M., et al., 2011. Oxidative degradation of herbicide diuron in aqueous medium by Fenton's reaction based advanced oxidation processes. *Chem. Eng. J.* 171 (1), 127–135. <https://doi.org/10.1016/j.cej.2011.03.072>.
- Pan, M., Xin, Y., Wang, Z., et al., 2023. Benign treatment and resource utilization characteristics of doramectin fermentation residues. *J. Clean. Prod.* 401, 136777 <https://doi.org/10.1016/j.jclepro.2023.136777>.
- Pulicharla, R., Brar, S., Rouissi, T., et al., 2017. Degradation of chlortetracycline in wastewater sludge by ultrasonication, Fenton oxidation, and ferro-sonication. *Ultrason. Sonochem.* 34, 332–342. <https://doi.org/10.1016/j.ultsonch.2016.05.042>.
- Qu, F., Liang, H., Wang, Z., et al., 2012. Ultrafiltration membrane fouling by extracellular organic matters (EOM) of *Microcystis aeruginosa* in stationary phase: influences of interfacial characteristics of foulants and fouling mechanisms. *Water Res.* 46 (5), 1490–1500. <https://doi.org/10.1016/j.watres.2011.11.051>.
- Ramanayaka, S., Sarkar, B., Cooray, A., et al., 2020. Halloysite nanoclay supported adsorptive removal of oxytetracycline antibiotic from aqueous media. *J. Hazard. Mater.* 384, 121301 <https://doi.org/10.1016/j.jhazmat.2019.121301>.
- Rice, E., Association, A., 2012. *Standard Methods for the Examination of Water and Wastewater*. China Architecture & Building Press.

- Shen, Y., Zhuan, R., Chu, L., et al., 2019. Inactivation of antibiotic resistance genes in antibiotic fermentation residues by ionizing radiation: exploring the development of recycling economy in antibiotic pharmaceutical factory. *Waste Manag.* 84, 141–146. <https://doi.org/10.1016/j.wasman.2018.11.039>.
- Shi, H., Li, C., Wang, L., et al., 2022a. In-situ synthesis of ZnSe nanoparticles onto monoclinic BiVO<sub>4</sub> for boosted photocatalytic decomposition of ammonia nitrogen in water. *J. Environ. Chem. Eng.* 10 (6), 108881 <https://doi.org/10.1016/j.jece.2022.108881>.
- Shi, J., Wang, B., Li, X., et al., 2022b. Distinguishing removal and regrowth potential of antibiotic resistance genes and antibiotic resistant bacteria on microplastics and in leachate after chlorination or Fenton oxidation. *J. Hazard Mater.* 430, 128432 <https://doi.org/10.1016/j.jhazmat.2022.128432>.
- Song, S., Jiang, M., Yao, J., et al., 2020. Alkaline-thermal pretreatment of spectinomycin mycelial residues: insights on anaerobic biodegradability and the fate of antibiotic resistance genes. *Chemosphere* 261, 127821. <https://doi.org/10.1016/j.chemosphere.2020.127821>.
- Stedmon, C.A., Bro, R., 2008. Characterizing dissolved organic matter fluorescence with parallel factor analysis: a tutorial. *Limnol. Oceanogr. Methods* 6 (11), 572–579. <https://doi.org/10.4319/lom.2008.6.572>.
- Tang, S., Yuan, D., Rao, Y., et al., 2018. Evaluation of antibiotic oxytetracycline removal in water using a gas phase dielectric barrier discharge plasma. *J. Environ. Manag.* 226, 22–29. <https://doi.org/10.1016/j.jenvman.2018.08.022>.
- Turner, B., Leytem, A., 2004. Phosphorus compounds in sequential extracts of animal manures: chemical speciation and a novel fractionation procedure. *Environ. Sci. Technol.* 38 (22), 6101–6108. <https://doi.org/10.1021/es0493042>.
- Tyagi, M., Kumari, N., Jagadevan, S., 2020. A holistic Fenton oxidation-biodegradation system for treatment of phenol from coke oven wastewater: optimization, toxicity analysis and phylogenetic analysis. *J. Water Proc. Eng.* 37, 101475 <https://doi.org/10.1016/j.jwpe.2020.101475>.
- Vilela, P., Mendonca, R., Starling, M., et al., 2021. Metagenomic analysis of MWWTP effluent treated via solar photo-Fenton at neutral pH: effects upon microbial community, priority pathogens, and antibiotic resistance genes. *Sci. Total Environ.* 801, 149599 <https://doi.org/10.1016/j.scitotenv.2021.149599>.
- Wang, G., Deng, D., Hu, C., et al., 2020a. More effective removal of antibiotic resistance genes from excess sludge by microwave integrated fenton treatment. *Int. Biodeterior. Biodegrad.* 149, 104920 <https://doi.org/10.1016/j.ibiod.2020.104920>.
- Wang, J., Liu, C., Feng, J., et al., 2020b. MOFs derived Co/Cu bimetallic nanoparticles embedded in graphitized carbon nanocubes as efficient Fenton catalysts. *J. Hazard Mater.* 394, 122567 <https://doi.org/10.1016/j.jhazmat.2020.122567>.
- Wang, M., Zhang, B., Cai, C., et al., 2018. Acidic hydrothermal treatment: characteristics of organic, nitrogen and phosphorus releasing and process optimization on lincomycin removal from lincomycin mycelial residues. *Chem. Eng. J.* 336, 436–444. <https://doi.org/10.1016/j.cej.2017.12.041>.
- Wang, Q., Zhang, Z., Xu, G., et al., 2021. Pyrolysis of penicillin fermentation residue and sludge to produce biochar: antibiotic resistance genes destruction and biochar application in the adsorption of penicillin in water. *J. Hazard Mater.* 413, 125385 <https://doi.org/10.1016/j.jhazmat.2021.125385>.
- Wang, R., Zhu, W., Zhao, S., et al., 2022. Hydrothermal oxidation-precipitation method for recovering phosphorus from dewatered sludge and the mechanisms involved. *Separ. Purif. Technol.* 298, 121580 <https://doi.org/10.1016/j.seppur.2022.121580>.
- Wen, C., Paul, W., Leenheer, J., et al., 2003. Fluorescence excitation-emission matrix regional integration to quantify spectra for dissolved organic matter. *Environ. Sci. Technol.* 37 (24), 5701–5710.
- Wu, Z., Gu, Y., Xin, S., et al., 2022. CuxNiyCo-LDH nanosheets on graphene oxide: an efficient and stable Fenton-like catalyst for dual-mechanism degradation of tetracycline. *Chem. Eng. J.* 434, 134574 <https://doi.org/10.1016/j.cej.2022.134574>.
- Xin, S., Liu, G., Ma, X., et al., 2021a. High efficiency heterogeneous Fenton-like catalyst biochar modified CuFeO<sub>2</sub> for the degradation of tetracycline: economical synthesis, catalytic performance and mechanism. *Appl. Catal. B Environ.* 280, 119386 <https://doi.org/10.1016/j.apcatb.2020.119386>.
- Xin, S., Ma, B., Liu, G., et al., 2021b. Enhanced heterogeneous photo-Fenton-like degradation of tetracycline over CuFeO<sub>2</sub>/biochar catalyst through accelerating electron transfer under visible light. *J. Environ. Manag.* 285, 112093 <https://doi.org/10.1016/j.jenvman.2021.112093>.
- Xin, S., Ma, B., Zhang, C., et al., 2021c. Catalytic activation of peroxydisulfate by alfalfa-derived nitrogen self-doped porous carbon supported CuFeO<sub>2</sub> for nimesulide degradation: performance, mechanism and DFT calculation. *Appl. Catal. B Environ.* 294, 120247 <https://doi.org/10.1016/j.apcatb.2021.120247>.
- Xu, H., Cai, H., Yu, G., et al., 2013. Insights into extracellular polymeric substances of cyanobacterium *Microcystis aeruginosa* using fractionation procedure and parallel factor analysis. *Water Res.* 47 (6), 2005–2014. <https://doi.org/10.1016/j.watres.2013.01.019>.
- Yang, G., Liang, Y., Xiong, Z., et al., 2021. Molten salt-assisted synthesis of Ce4O7/Bi4MoO9 heterojunction photocatalysts for Photo-Fenton degradation of tetracycline: enhanced mechanism, degradation pathway and products toxicity assessment. *Chem. Eng. J.* 425, 130689 <https://doi.org/10.1016/j.cej.2021.130689>.
- Yang, Y., Zeng, G., Huang, D., et al., 2020. Molecular engineering of polymeric carbon nitride for highly efficient photocatalytic oxytetracycline degradation and H<sub>2</sub>O<sub>2</sub> production. *Appl. Catal. B Environ.* 272, 118970 <https://doi.org/10.1016/j.apcatb.2020.118970>.
- Zha, S., Cheng, Y., Gao, Y., et al., 2014. Nanoscale zero-valent iron as a catalyst for heterogeneous Fenton oxidation of amoxicillin. *Chem. Eng. J.* 255, 141–148. <https://doi.org/10.1016/j.cej.2014.06.057>.
- Zhang, B., He, X., Yu, C., et al., 2022. Degradation of tetracycline hydrochloride by ultrafine TiO<sub>2</sub> nanoparticles modified g-C<sub>3</sub>N<sub>4</sub> heterojunction photocatalyst: influencing factors, products and mechanism insight. *Chin. Chem. Lett.* 33 (3), 1337–1342. <https://doi.org/10.1016/j.ccllet.2021.08.008>.
- Zhang, Y., Liu, H., Dai, X., et al., 2020. The release of organic matter, nitrogen, phosphorus and heavy metals from erythromycin fermentation residue under heat-activated persulfate oxidation conditioning. *Sci. Total Environ.* 724, 138349 <https://doi.org/10.1016/j.scitotenv.2020.138349>.
- Zhang, Y., Meng, C., He, Y., et al., 2021. Influence of cell lysis by Fenton oxidation on cryptic growth in sequencing batch reactor (SBR): implication of reducing sludge source discharge. *Sci. Total Environ.* 789, 148042 <https://doi.org/10.1016/j.scitotenv.2021.148042>.
- Zhou, Y., He, J., Lu, J., et al., 2020. Enhanced removal of bisphenol A by cyclodextrin in photocatalytic systems: degradation intermediates and toxicity evaluation. *Chin. Chem. Lett.* 31 (10), 2623–2626. <https://doi.org/10.1016/j.ccllet.2020.02.008>.
- Zhu, G., Yu, X., Xie, F., et al., 2019. Ultraviolet light assisted heterogeneous Fenton degradation of tetracycline based on polyhedral Fe<sub>3</sub>O<sub>4</sub> nanoparticles with exposed high-energy {110} facets. *Appl. Surf. Sci.* 485, 496–505. <https://doi.org/10.1016/j.apsusc.2019.04.239>.
- Zhu, X., Yang, S., Wang, L., et al., 2016. Tracking the conversion of nitrogen during pyrolysis of antibiotic mycelial fermentation residues using XPS and TG-FTIR-MS technology. *Environ. Pollut.* 211, 20–27. <https://doi.org/10.1016/j.envpol.2015.12.032>.
- Zouanti, M., Bezzina, M., Dhib, R., 2020. Experimental study of degradation and biodegradability of oxytetracycline antibiotic in aqueous solution using Fenton process. *Environ. Eng. Res.* 25 (3), 316–323.

## 教育部武汉理工大学科技查新工作站 检索证明

委托单位	青岛农业大学			
委托人	刘国成			
检索要求	指定检索刘国成 2021 年发表论文 “Investigating the effects of biochar colloids and nanoparticles on cucumber early seedlings” 被 SCI 数据库收录以及最新中科院 JCR 期刊影响因子与分区信息			
<b>检索结果</b>				
数据库	收录篇数			
SCI	1 篇（第 1 作者）			
<b>中科院 JCR 期刊影响因子与分区信息</b>				
刊名	ISSN	IF	分区（大类）	分区（小类）
SCIENCE OF THE TOTAL ENVIRONMENT	0048-9697	7.963	环境科学与生态学 1 区	ENVIRONMENTAL SCIENCES 环境科学 1 区
声明	委托人接受本证明，视为已对本证明所列论文检索信息核对，确认无误，若有不实，由委托人承担全部责任。			
检索人			审核人	
<p>注：1. 期刊分区及影响因子信息来自 2020 年版中国科学院文献情报中心期刊分区表；</p> <p>2. 目前 web of science 数据库中已不再区分 SCI 与 SCIE, 统一称 SCI, 特此说明；</p> <p>3. 论文详情详见附件。</p>				

检索附件：SCI 、其他 

教育部科技查新工作站（G09）

2021 年 11 月 19 日

G09  
数据库收录论文

## Investigating the effects of biochar colloids and nanoparticles on cucumber early seedlings

作者: Liu, GC (Liu, Guocheng)<sup>[1]</sup>; Pan, MQ (Pan, Meiqi)<sup>[1]</sup>; Song, JY (Song, Jiaying)<sup>[1]</sup>; Guo, MY (Guo, Mengyao)<sup>[1]</sup>; Xu, LN (Xu, Lina)<sup>[2]</sup>; Xin, YJ (Xin, Yanjun)<sup>[1]</sup>

SCIENCE OF THE TOTAL ENVIRONMENT

卷: 804

文献号: 150233

DOI: 10.1016/j.scitotenv.2021.150233

出版年: JAN 15 2022

文献类型: Article

查看期刊影响力

### 摘要

Understanding about the influence of biochar colloidal and nanoscale particles on plant is limited. We therefore extracted the colloids and nanoparticles from hot pepper stalk biochar (CB600 and NB600), and examined physiological responses of cucumber early seedlings through hydroponic culture and pot experiment. CB600 had no significant effect on shoot at 500 mg/L, while it decreased root biomass and inhibited lateral root development. The biomass and root length, area, and tip number dramatically reduced after 500 mg/L NB600 treatment. Water content of NB600exposed shoot was lower, suggesting water uptake and transfer might be hindered. For resisting exposure stress, root hair number and length increased. Even, the study observed swelling and hyperplasia of root hairs after direct exposure of CB600 and NB600. These adverse effects might be associated with the contact and adhesion of CB600 and NB600 with sharp edges to root surface. For a low concentration of 50 mg/L, NB600 did not influence cucumber early seedlings. In soil, CB600 and NB600 did not cause inhibitory effect at relatively high contents of 500 mg/kg and 2000 mg/kg. This study provides useful information for understanding phytotoxicity and environmental risk of biochar colloids and nanoparticles, which has significant implications with regard to biochar application safety. (c) 2021 Published by Elsevier B.V.

### 关键词

作者关键词: Biochar; Colloids; Nanoparticles; Seedling; Root morphology

KeyWords Plus: DISSOLVED BLACK CARBON; PYROLYSIS TEMPERATURE; PLANT-GROWTH; HEAVY-METALS; HUMIC-ACID; SOIL; TRANSPORT; AGGREGATION; STABILITY; TOXICITY

### 作者信息

#### 通讯作者地址:

Qingdao Agricultural University Qingdao Agr Univ, Coll Resource & Environm, Qingdao Engr Res Ctr Rural Environm, Qingdao 266109, Peoples R China.

通讯作者地址: Liu, GC; Xin, YJ (通讯作者)

Qingdao Agr Univ, Coll Resource & Environm, Qingdao Engr Res Ctr Rural Environm, Qingdao 266109, Peoples R China.

#### 地址:

[ 1 ] Qingdao Agr Univ, Coll Resource & Environm, Qingdao Engr Res Ctr Rural Environm, Qingdao 266109, Peoples R China

[ 2 ] Qingdao Agr Univ, Coll Landscape Architecture & Forestry, Qingdao 266109, Peoples R China

电子邮件地址: lg@qau.edu.cn; xintom2000@126.com

### 基金资助致谢

基金资助机构	显示详情	授权号
Natural Science Foundation of Shandong Province		ZR2020MD112
National Natural Science Foundation of China (NSFC)		52070107
Support Plan on Youth Innovation Science and Technology for Higher Education of Shandong Province		2019JKD014
Research Foundation for Talented Scholars of Qingdao Agricultural University		6651119010

查看基金资助信息

### 出版商

ELSEVIER, RADARWEG 29, 1043 NX AMSTERDAM, NETHERLANDS

### 期刊信息

Impact Factor (影响因子): Journal Citation Reports

### 类别 / 分类

研究方向: Environmental Sciences & Ecology

Web of Science 类别: Environmental Sciences

### 文献信息

语言: English

入藏号: WOS:000704389800013

PubMed ID: 34520920

ISSN: 0048-9697

eISSN: 1879-1026

### 其他信息

IDS 号: WC6TZ

Web of Science 核心合集中的 "引用的参考文献": 60

Web of Science 核心合集中的 "被引频次": 0

### 引文网络

在 Web of Science 核心合集中

0

被引频次

创建引文跟踪

60

引用的参考文献

查看相关记录

### 新增功能! 您可能也喜欢... BETA

Eco-friendly carboxymethyl cellulose hydrogels filled with nanocellulose or nanoclays for agriculture applications as soil conditioning and nutrient carrier and their impact on cucumber growing. COLLOIDS AND SURFACES A-PHYSICO-CHEMICAL AND ENGINEERING ASPECTS (2021)

Phosphorus uptake, distribution and transformation with *Chlorella vulgaris* under different trophic modes. CHEMOSPHERE (2021)

Adsorption and catalytic degradation of preservative parabens by graphene-family nanomaterials. SCIENCE OF THE TOTAL ENVIRONMENT (2022)

Effects of biochar nanoparticles as a soil amendment on the structure and hydraulic characteristics of a sandy loam soil. SOIL USE AND MANAGEMENT (2021)

Controlling the Structural Robustness of Zirconium-Based Metal Organic Frameworks for Efficient Adsorption on Tetracycline Antibiotics. WATER (2021)

查看所有建议

### 用于 Web of Science 中

在 Web of Science 中使用次数

11

11

最近 180 天

2013 年至今

进一步了解

### 此记录来自:

Web of Science 核心合集  
- Science Citation Index Expanded

### 建议修正

如果希望提高此记录中数据的质量, 请提供修正建议。



## Investigating the effects of biochar colloids and nanoparticles on cucumber early seedlings



Guocheng Liu<sup>a,\*</sup>, Meiqi Pan<sup>a</sup>, Jiaying Song<sup>a</sup>, Mengyao Guo<sup>a</sup>, Lina Xu<sup>b</sup>, Yanjun Xin<sup>a,\*</sup>

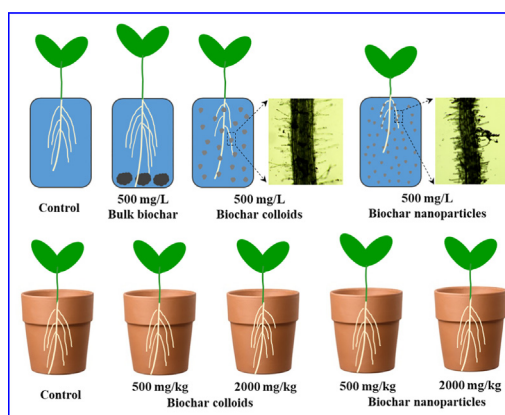
<sup>a</sup> Qingdao Engineering Research Center for Rural Environment, College of Resource and Environment, Qingdao Agricultural University, Qingdao 266109, China

<sup>b</sup> College of Landscape Architecture and Forestry, Qingdao Agricultural University, Qingdao 266109, China

### HIGHLIGHTS

- Effects of biochar colloids/nanoparticles on cucumber seedlings were examined.
- Hydroponic exposure of biochar colloids/nanoparticles inhibited root development.
- Hyperplasia and deformation of root hairs occurred after direct exposure treatment.
- Biochar colloids/nanoparticles had no negative impact on cucumber seedlings in soil.

### GRAPHICAL ABSTRACT



### ARTICLE INFO

#### Article history:

Received 9 July 2021

Received in revised form 24 August 2021

Accepted 5 September 2021

Available online xxxx

Editor: Baoliang Chen

#### Keywords:

Biochar

Colloids

Nanoparticles

Seedling

Root morphology

### ABSTRACT

Understanding about the influence of biochar colloidal and nanoscale particles on plant is limited. We therefore extracted the colloids and nanoparticles from hot pepper stalk biochar (CB600 and NB600), and examined physiological responses of cucumber early seedlings through hydroponic culture and pot experiment. CB600 had no significant effect on shoot at 500 mg/L, while it decreased root biomass and inhibited lateral root development. The biomass and root length, area, and tip number dramatically reduced after 500 mg/L NB600 treatment. Water content of NB600-exposed shoot was lower, suggesting water uptake and transfer might be hindered. For resisting exposure stress, root hair number and length increased. Even, the study observed swelling and hyperplasia of root hairs after direct exposure of CB600 and NB600. These adverse effects might be associated with the contact and adhesion of CB600 and NB600 with sharp edges to root surface. For a low concentration of 50 mg/L, NB600 did not influence cucumber early seedlings. In soil, CB600 and NB600 did not cause inhibitory effect at relatively high contents of 500 mg/kg and 2000 mg/kg. This study provides useful information for understanding phytotoxicity and environmental risk of biochar colloids and nanoparticles, which has significant implications with regard to biochar application safety.

© 2021 Published by Elsevier B.V.

### 1. Introduction

Biochar is considered to have tremendous potential at carbon sequestration (Lehmann et al., 2006), soil improvement (Agegnehu et al., 2017), and pollutant remediation (Lian and Xing, 2017) owing to its superior properties. In practical application, particle size is a key

\* Corresponding authors.

E-mail addresses: [lg@qau.edu.cn](mailto:lg@qau.edu.cn) (G. Liu), [xintom2000@126.com](mailto:xintom2000@126.com) (Y. Xin).



index of biochar products, which can affect agronomic and environmental benefits greatly (Lim et al., 2016; Lu et al., 2020; Major, 2010). Recently, a number of studies reported physical disintegration of biochars, leading to the formation of microparticles and even nanoparticles (Braadbaart et al., 2009; Liu et al., 2018a; Spokas et al., 2014). Besides the degradation in particle size, physicochemical characteristics (e.g., surface area, functional groups, and aromaticity, etc.) of biochar ultrafines had been demonstrated to differ from those of bulky biochar (Oleszczuk et al., 2016; Qu et al., 2016; Song et al., 2019). Therefore, it is reasonable to infer that biochar micro/nanoparticles will exhibit unique biogeochemical processes in natural environment.

To date, the environmental behavior of ultrafine biochar has attracted increasing attention. Several previous articles found that biochar nanoparticles had great mobility in the column of quartz sand or soil (Chen et al., 2017; Wang et al., 2013a; Wang et al., 2013b), and aging process could increase the transportability of biochar colloids (Wang et al., 2019). Chen et al. (2018) reported that the wood chip biochar nanoparticles facilitated phosphorus (P) retention in acidic soils, whereas caused more release of Fe/Al oxides-associated P in alkaline soils. In salt-affected soils, nano-biochar could be used as enhancer for P adsorption (Mahmoud et al., 2020). Biochar nanoparticles are also able to reduce runoff and nitrate loss in sandy soils (Chen et al., 2020). Biochar colloids and nanoparticles had strong colloidal stability (Song et al., 2019; Yang et al., 2019) and consistently remained high dispersion in natural freshwaters (Liu et al., 2018a; Xu et al., 2017). In addition, colloidal biochars showed excellent adsorption performance for heavy metals (e.g.,  $\text{Cd}^{2+}$  and  $\text{Pb}^{2+}$ ) (Qian et al., 2016; Xu et al., 2020), phthalate esters (Ma et al., 2019), tetracycline (Ma et al., 2020), and antibiotic resistance genes (Lian et al., 2020). Also, the heteroaggregation of biochar nanoparticles with goethite could influence the adsorption of organic pollutants (e.g., phenanthrene) greatly (Lian et al., 2019). It is noteworthy that the current studies primarily focus on physicochemical processes of biochar micro/nanoparticles. Comparatively, our understanding regarding biological responses to biochar colloids and nanoparticles is rather scarce.

In general, dissolved hazardous substances can be detected in biochars, such as heavy metals, polycyclic aromatic hydrocarbons (PAHs), polychlorinated dioxins/furans (PCDDs/DFs) and persistent free radicals, and these chemicals may cause environmental stress to organisms (Lieke et al., 2018; Luo et al., 2020; Lyu et al., 2016). Not only that, there were numerous reports about complicated responses of microorganisms, invertebrates, and plants to biochar particles with different size range from hundreds of micrometers to several millimeters (Billah et al., 2019; Prodana et al., 2019; Sarfraz et al., 2020). The studies of Yue et al. (2019) and Shen et al. (2020) reported the detoxification of biochar nanoparticles on rice growth under the treatments of Cd and ferulic acid, respectively. The specific fraction (pass through 0.45- $\mu\text{m}$  membrane) of biochar also could facilitate photoreduction of Hg(II) to Hg(0) and reduce Hg uptake by lettuce (*Lactuca sativa* L.) (Li et al., 2020). However, there is limited information regarding the influence of direct exposure to biochar micro/nanoparticles on plants. Zhang et al. (2020a) prepared six types of nanoparticles from rice straw/wood sawdust-derived biochars and tested their impacts on seed germination and growth of rice, tomato, and reed. Zhang's work filled in the gap of the study about plant response to the exposure of biochar ultrafine particles. But notably, the yield of colloidal particle release from bulk biochar was much greater than that of nanoparticle formation (Liu et al., 2018a; Song et al., 2019). Thus, it is imperative to examine the influence of biochar colloids and nanoparticles on plants to ensure biochar application safety.

Under the above backgrounds, this study prepared a bulky biochar from the stalks of hot pepper (*Capsicum frutescens* L.) and extracted corresponding colloids and nanoparticles through a procedure of sonication, sedimentation, and centrifugation. Further, hydroponic and pot experiments were carried out to explore the impacts of biochar colloids and nanoparticles on plant seedlings. The findings will offer helpful information for cognizing the biological response of plants to the stress

of ultrafine biochar and reveal potential environmental risk of the physical degradation of biochar bulk particles.

## 2. Materials and methods

### 2.1. Preparation of bulky, colloidal, and nano biochars

The hot pepper stalks were collected from a plastic greenhouse in Shouguang, Shandong, China. The feedstock was washed by tap water and then dried at 80 °C for 24 h before pyrolysis. The biochar was produced at 600 °C for 2 h under  $\text{N}_2$  condition (Xin et al., 2021). The biochar was lightly crushed to pass a 60-mesh sieve, soaked in distilled water to remove soluble matters, and dried at 80 °C in a vacuum drying oven. The biochar particles were regarded as bulk sample and named as BB600.

The biochar colloids and nanoparticles were obtained as described by Liu et al. (2018a). Briefly, 8 g BB600 was added in a beaker with 400 mL distilled water, stirred for 5 min, and then sonicated in water/ice bath for 30 min (50% duty cycle, 300 W) (JY99-IIDN, Scientz, China). After 24 h settling to remove >1- $\mu\text{m}$  particles, the suspension was sucked out by a syringe and centrifuged at 4200g for 30 min to separate the colloids (>100 nm) and the supernatant containing biochar nanoparticles (<100 nm). The extraction operation was repeated five times. The settling particles, colloids, and nanoparticles of biochar were labelled as RB600, CB600, and NB600, respectively. All the biochar fractions were freezing-dried into powder form at -80 °C (10N, Scientz, China) and stored in airtight bags.

### 2.2. Characterization of biochar samples

Transmission electron microscopy (TEM) (H-7650, Hitachi, Japan) was employed for morphological observation of CB600 and NB600. Fourier transform infrared spectroscopy (FTIR) was obtained by an IRTracer-100 (Shimadzu, Japan). Each of the biochars was scanned for 30 times with a range of 500  $\text{cm}^{-1}$  to 4000  $\text{cm}^{-1}$ . The biochar samples were scanned by a DXR Raman microscope (Thermo Scientific, USA) to collect Raman spectra. A 532 nm laser was used as excitation source. Raman spectrum deconvolution was performed to analyze the hidden species of carbon structures with Gaussian-Lorentzian curve-fitting formulas (Yu et al., 2020).

### 2.3. Seed germination and hydroponic treatment

Seeds of cucumber were obtained from Institute of Vegetable and Flower, Chinese Academy of Agricultural Sciences. The cucumber seeds were sterilized in 10%  $\text{H}_2\text{O}_2$  solution for 10 min and thoroughly washed with deionized water. BB600 and RB600 were wetted and stirred in deionized water for 2 h, respectively, and the suspensions of CB600 and NB600 were prepared and dispersed by sonicating for 5 min. For the germination, the seeds were exposed to biochar suspension in glass Petri dishes. Briefly, 10-mL of biochar suspension was added into each dish with one piece of filter paper, and following 20 grains of sterile seeds were put onto the filter paper. The concentration of biochar suspension is 500 mg/L. Taking possible nanotoxicity of biochar nanoparticles on plants (Zhang et al., 2020a), a relatively lower concentration (50 mg/L) was used for NB600 exposure in this study. The treatments were run in quintuplicate along with a blank without biochar (Control), and all the dishes were placed in dark at 25 °C randomly. After 3 days, the germination of seeds was examined and counted.

To examine root development in the presence of biochar particles, the roots were exposed in biochar suspensions directly. The cucumber seeds were placed on wet filter paper until radicle broke through seed coat, wrapped with soft sponge gently, then transferred and vertically fixed into a perforated foam board. The foam board (10 seeds/board) was put into a cubic glass container with biochar suspension and kept water submerge the radicles. The above procedure is shown in Fig. S1.

For this testing, the concentrations of biochar suspensions are consistent with those of seed germination experiment. Each treatment was conducted in triplicates, and the suspensions of biochars were replaced every 24 h. After 3-day culturing, half of the early seedlings were sampled to measure fresh and dry weight of shoot and root. Other half was used to analyze root morphology (length, diameter, tip number,

area, and volume) using an Epson scanner (Expression 12000XL, Epson, Japan) and WinRHIZO soft (Pro 2005, Regent instruments Inc., Canada) (Wang et al., 2017). The roots and root hairs were further observed using a Leica DM500 microscope (Germany) and analyzed with the Leica Application Suite software, and the number and length of root hairs were counted and measured by the Image J software.

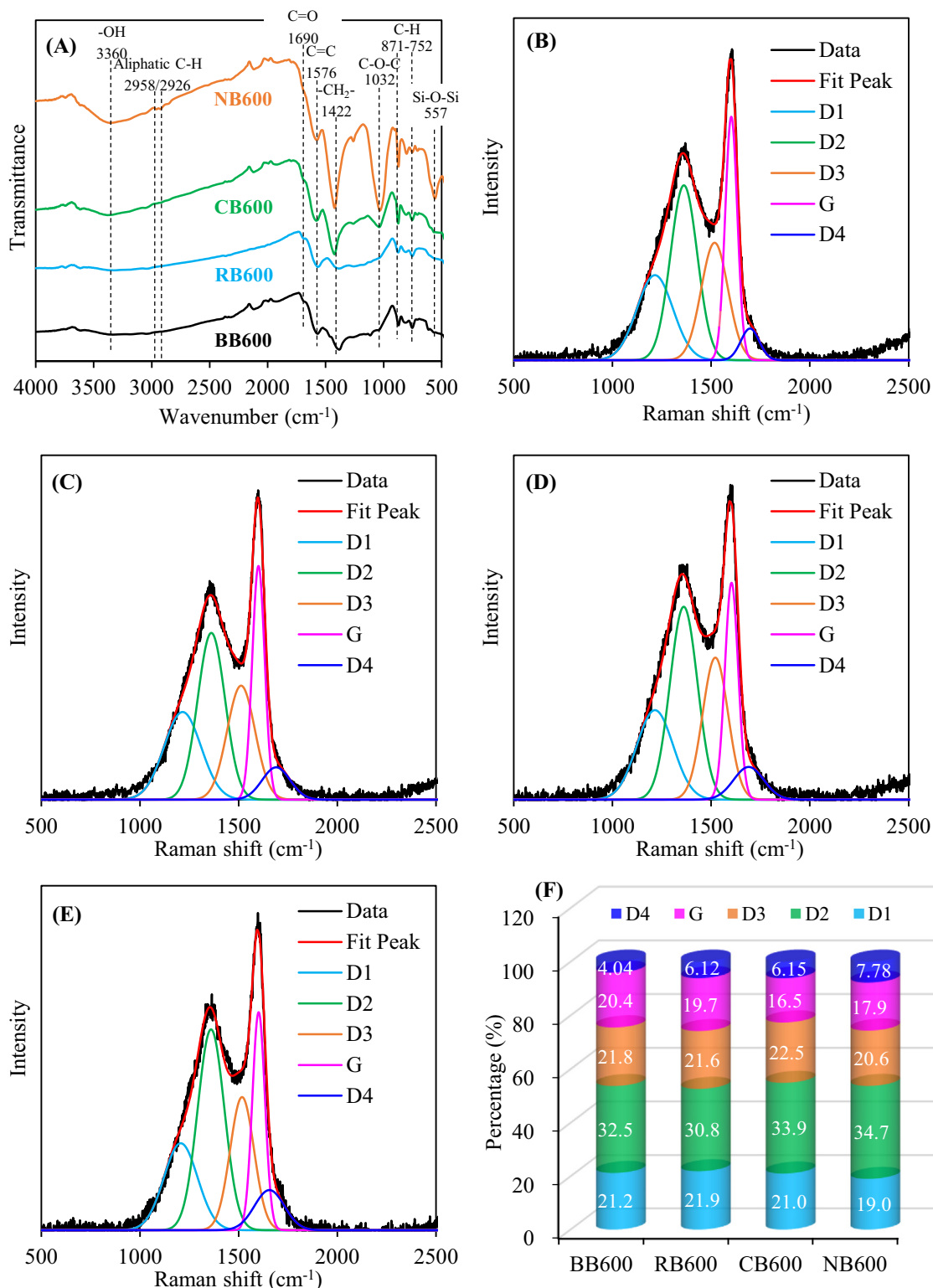


**Fig. 1.** FTIR spectra (A) of biochars and fitted-curves for Raman spectra of BB600 (B), RB600 (C), CB600 (D), and NB600 (E). (F) indicates the percentage of fitting peak area to total area of all the peaks.

## 2.4. Pot experiment

Surface samples (0–20 cm) of lime concretion black soil were collected from a cropland in Qingdao, Shandong, China (36°89'N, 120°52' E). The soil was air-dried, passed through a 2-mm sieve, and homogenized. The soil properties were: pH 7.41, bulk density 1.46 g/cm<sup>3</sup>, soil organic matter 12.6 g/kg, cation exchange capacity 23.3 cmol/kg, total nitrogen 0.68 g/kg, total phosphorus 0.72 g/kg, available nitrogen 160 mg/kg, available phosphorus 42.8 mg/kg, available potassium 143 mg/kg, sand 30.7%, silt 38.8%, and clay 30.5%. The suspensions of CB600 and NB600 were added into soil and incubated at 60% of water holding capacity and (28 ± 2) °C for 7 days. The adding contents of biochar into soil were 500 mg/kg and 2000 mg/kg, respectively, which was converted basing on a commonly used application rate of bulk biochar (5%) and the yield of biochar colloids and nanoparticles (1%–4%) (Liu et al., 2018a; Zhang et al., 2020a). The treated soils were air-dried, homogenized, and incubated again before sowing. Five cucumber seeds were sowed in 100 g soil per pot, and thinned to the best two for further experiment. After 7 days of incubation, the shoots and roots of cucumber seedlings were separately harvested to obtain the data of plant height, fresh weight, dry weight, and root morphological parameters. The pot experiment was run in quintuplicates.

## 2.5. Statistical analysis

The experimental data were expressed as mean values with standard deviation. A one-way analysis of variance (ANOVA) was employed to analyze statistical significance by the Least Significant Difference (LSD) test ( $p < 0.05$ ) using SPSS 20.0.

## 3. Results and discussion

### 3.1. Properties of biochar samples

The morphological images of CB600 and NB600 from TEM observation are shown in Fig. S2. Both CB600 and NB600 in the TEM graphs

are solid particles with diverse appearance, which were similar with the micromorphology of peanut shell biochar colloids and nanoparticles in our previous study (Liu et al., 2018a). Also, Wang et al. (2019) reported an irregular shape of pinewood chip-derived biochar nanoparticles, and Ma et al. (2019) observed various shapes of biochar colloids from corn straw and rice husk using scanning electron microscopy. Inconsistently, the biochar colloids and nanoparticles existed as smooth spheres under TEM observation in some articles (Hameed et al., 2020; Zhang et al., 2020a). In accordance to TEM images, the particle diameter of CB600 and NB600 was measured and analyzed. The particle size of CB600 and NB600 was in the range of (0.2–4.0) μm and (20–150) nm, respectively, and their average diameter was (1.47 ± 0.82) μm and (59.0 ± 28.1) nm. The particles with bin center diameter of 1.0 μm and 40 nm had maximum size distribution frequency, accounting for 31.8% and 37.5%, respectively. Once the particle size of CB600 and NB600 exceeds 1.0 μm and 40 nm, the size distribution frequency decreased with increasing diameter.

FTIR and Raman spectra were used to obtain qualitative information about structural properties of biochar samples. All the biochars possessed FTIR characteristic peaks at 3360 cm<sup>-1</sup>, (2926–2958) cm<sup>-1</sup>, 1690 cm<sup>-1</sup>, 1576 cm<sup>-1</sup>, 1422 cm<sup>-1</sup>, 1032 cm<sup>-1</sup>, and (752–871) cm<sup>-1</sup> (Fig. 1A). These peaks indicate O–H of hydroxyl, aliphatic C–H, C=O of carboxyl, aromatic C=C, –CH<sub>2</sub>, C–O–C, and aromatic C–H, respectively (Chen et al., 2014; Wang et al., 2019). The peak intensity of aliphatic groups (–CH<sub>2</sub> and C–O–C) followed an order: NB600 > CB600 > BB600 > RB600. Further, NB600 had a clear peak at 557 cm<sup>-1</sup> that attributed to Si–O–Si deformation vibration, but this peak was much weaker for BB600, RB600, and CB600. The results suggested that aliphatic carbon and Si-containing minerals were primarily enriched in the fraction of nanoscale biochar after the preparation procedure, which was well agreed with the previous studies by Qu et al. (2016) and Liu et al. (2018a).

There were two characteristic bands of carbon structures in the biochars, i.e., D band at ~1360 cm<sup>-1</sup> and G band at ~1595 cm<sup>-1</sup>, in Raman measurement (Fig. 1B–E). These two bands are attributed to disordered structure and graphitic crystallite, respectively. To gain loss and hidden

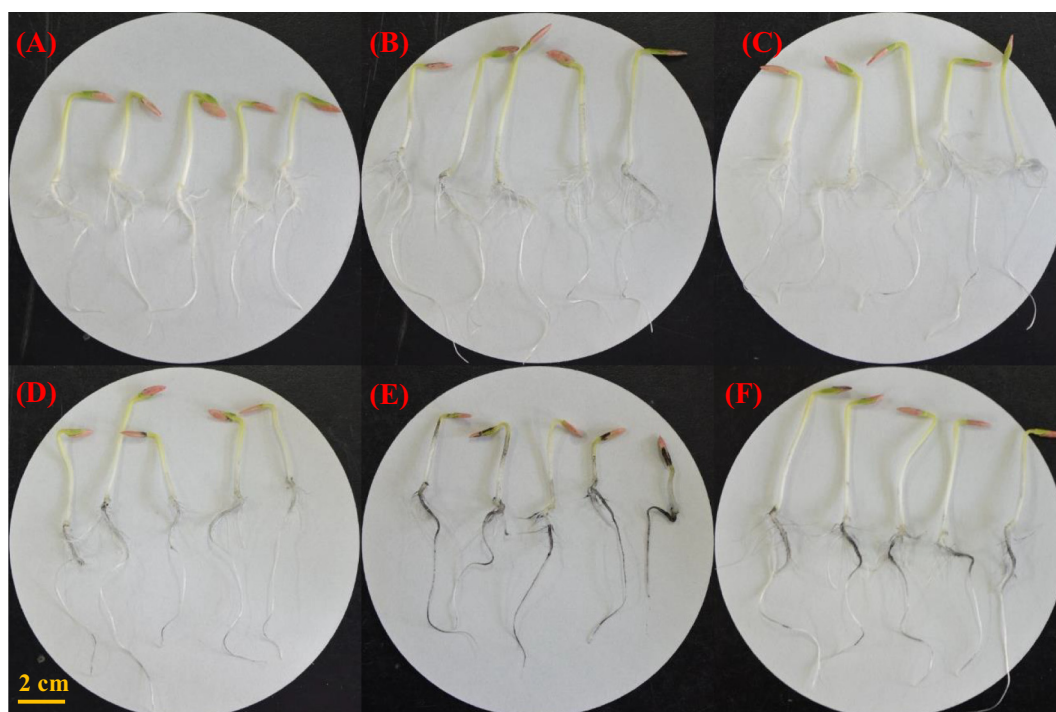


Fig. 2. The cucumber seedlings from hydroponic treatments of Control (A), 500 mg/L BB600 (B), 500 mg/L RB600 (C), 500 mg/L CB600 (D), 500 mg/L NB600 (E), and 50 mg/L NB600 (F).

information due to overlap between D band and G band, the peaks were divided into D1, D2, D3, G, and D4 bands at about  $1210\text{ cm}^{-1}$ ,  $1360\text{ cm}^{-1}$ ,  $1520\text{ cm}^{-1}$ ,  $1600\text{ cm}^{-1}$ , and  $1650\text{ cm}^{-1}$  using Gaussian-Lorentzian curve-fitting formulas (Sadezky et al., 2005; Yu et al., 2020). The peaks of D1, D2, and D4 are generally considered to originate from disordered graphitic structures, and the D3 band indicates amorphous carbon, while the G peak corresponds to perfect graphite lattice. For CB600 and NB600, the sum of percentage of D1, D2, and D4 peak area to total area of all the peaks was greater than that of BB600, and they had lower percentage value of G band (Fig. 1F), indicating more less-ordered carbon structures and less graphitic crystallites. Overall, the results of FTIR and Raman demonstrated greater amount of nonaromatic carbon and defect structures in biochar colloids and nanoparticles.

### 3.2. Effects of hydroponic exposure of biochars on cucumber seedlings

The influence of biochars on germination rate of cucumber seeds is shown in Fig. S3. The hydroponic treatments of BB600, RB600, CB600, and NB600 had no effect on the germination rate of cucumber seeds relative to the control. Consistently, Zhang et al. (2020a) reported that six kinds of biochar nanoparticles did not influence the germination rate of tomato seeds. But, one type of biochar nanoparticles reduced the germination rate of rice seeds at  $50\text{ mg/L}$ . By contrast, the treatments of CB600 and NB600 at much higher concentration ( $500\text{ mg/L}$ ) did not affect the germination rate of cucumber seeds in our study.

The cucumber early seedlings after the hydroponic exposure of BB600, RB600, CB600, and NB600 were imaged with a digital camera in detail, as shown in Fig. 2. It could be observed evidently that BB600 adding increased the biomass of cucumber shoot and root comparing with the control. The plant height of BB600-treated cucumber seedlings was 22.2% higher than that of untreated one (Fig. 3A). In comparison with the control, the fresh weight of shoot and root of cucumber seedlings were increased by 10.5% and 5.83% under presence of  $500\text{ mg/L}$  BB600 (Fig. 3B), though the increase was not statistically significant. Correspondingly, there was also a slight improvement on the dry weight after BB600 addition (Fig. 3C). Beneficial effects of biochars on cucumber had been extensively reported by many studies (Jaiswal et al., 2014; Zhou et al., 2021). The release of available nutrients (e.g., N and P) and hormone (e.g., ethylene) was the possible mechanism for plant growth promotion by bulk biochars (Piash et al., 2021; Zheng et al., 2013).

Dissimilarly, the growth of cucumber germination stage was retarded after the hydroponic exposure to NB600 at  $500\text{ mg/L}$  (Figs. 2E and 3B–C). The fresh and dry weight of shoot of  $500\text{ mg/L}$  NB600-exposed seedlings were only 69.2% and 80.6% of those of unexposed control. Even, the inhibition ratios of  $500\text{ mg/L}$  NB600 to the fresh and dry root biomass were 57.6% and 59.5%, respectively. The early seedling growth was also tested with a lower concentration of NB600 ( $50\text{ mg/L}$ ), but no significant influence was observed. For CB600, we also found the stress effect on cucumber roots at  $500\text{ mg/L}$ , whereas its difference with

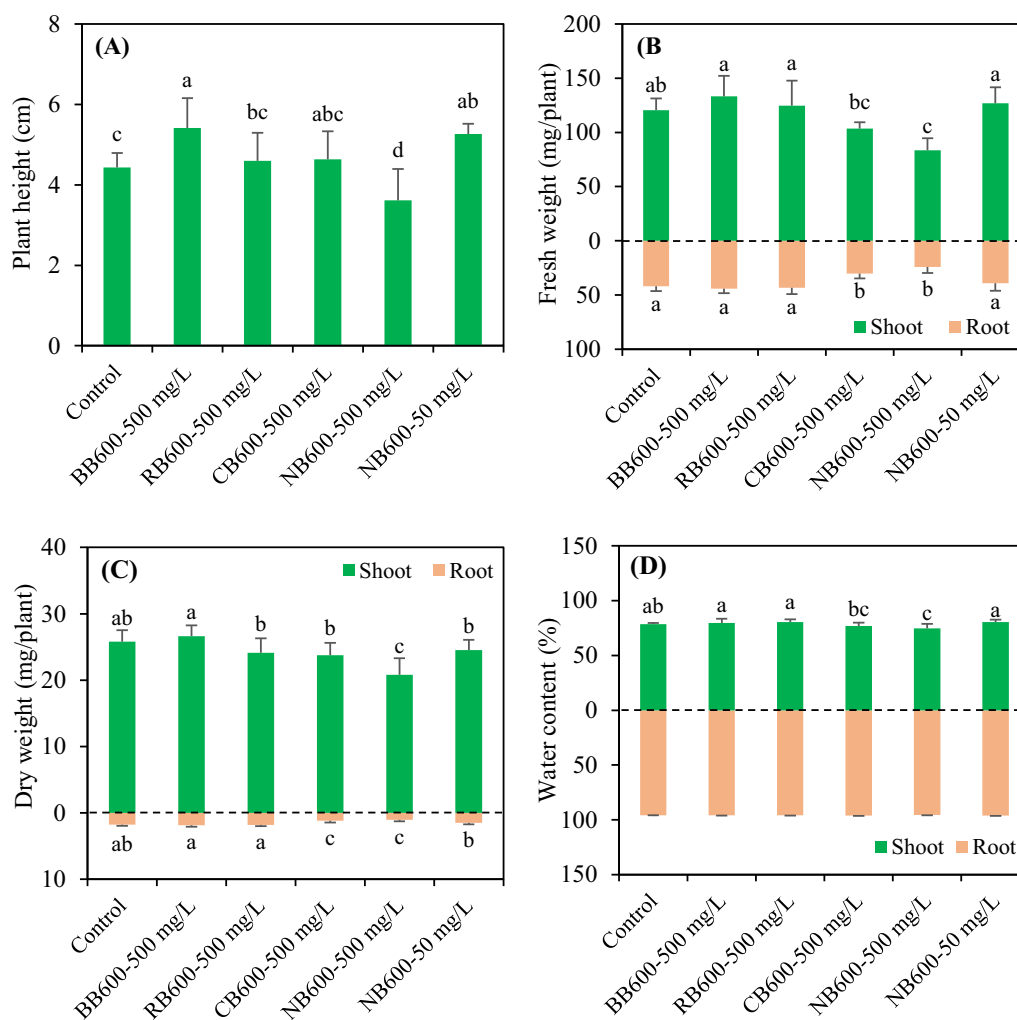


**Fig. 3.** The plant height (A), fresh weight (B), dry weight (C), and water content (D) of cucumber seedlings after hydroponic exposure to biochars. Significant difference was marked with different lowercase letters ( $p < 0.05$ ).

**Table 1**  
Root morphology of cucumber seedlings after hydroponic exposure to biochars.

Treatments	Root parameters				
	Length (cm)	Diameter (mm)	Tip number	Area (cm <sup>2</sup> )	Volume (cm <sup>3</sup> )
Control	17.6 ± 2.5abc	0.43 ± 0.03a	43.6 ± 9.7abc	2.35 ± 0.36abc	0.025 ± 0.004abc
BB600-500 mg/L	21.3 ± 1.9a	0.41 ± 0.08a	57.2 ± 11.3a	2.78 ± 0.60ab	0.030 ± 0.012ab
RB600-500 mg/L	20.6 ± 2.2ab	0.45 ± 0.07a	52.6 ± 10.0ab	2.90 ± 0.57a	0.033 ± 0.011a
CB600-500 mg/L	14.5 ± 2.4 cd	0.44 ± 0.08a	29.0 ± 7.7 cd	1.97 ± 0.36 cd	0.022 ± 0.007bc
NB600-500 mg/L	10.8 ± 2.8d	0.47 ± 0.05a	22.4 ± 14.2d	1.55 ± 0.41d	0.017 ± 0.006c
NB600-50 mg/L	16.7 ± 4.8bc	0.45 ± 0.08a	42.2 ± 13.5bc	2.28 ± 0.36bc	0.025 ± 0.005abc

the control was not significant in shoot biomass. By comparison, the hydroponic treatment with NB600 had greater inhibiting effect on cucumber early seedlings than CB600 exposure. It could be clearly observed that a large amount of NB600 adhered to the primary and lateral roots (Fig. 2E and F). Consistently, Zhang et al. (2020a) reported the adhesion of biochar nanoparticles to plant root surfaces. But, few CB600 particles were attached to the roots, significantly less than NB600. In addition, many previous reports found the aggregation of other nanomaterials (e.g., graphene and carbon nanotubes) onto the surface of plant roots, subsequently affecting seedling growth (Begum et al., 2011; Cañas et al., 2008; Zhang et al., 2015). The contact between carbon nanoparticles and roots may be an important factor for phytotoxicity (Begum et al., 2011; Zhao et al., 2014). Therefore, the root sensitivity will be extremely high to the direct exposure of biochar nanoparticles. The morphology changes of cucumber root system after the hydroponic treatments of CB600 and NB600 were analyzed in the next section further.

### 3.3. Morphology of cucumber roots under hydroponic exposure to biochars

The information of root length, diameter, tip number, area, and volume are listed in Table 1. These parameters (except diameter) of

root morphology of the hydroponic culture with 500 mg/L BB600 were better than those of the control, although less significantly. This implies the beneficial effect of BB600 on the root development of cucumber early seedlings. RB600 also caused similar impacts in the hydroponic experiment. The root length, area, and tip number were significantly reduced ( $p < 0.05$ ) after the exposure to 500 mg/L NB600. But, the treatment of 50 mg/L NB600 did not affect the elongation of cucumber roots. The total root length of 500 mg/L CB600-exposed cucumber seedlings was lower than that of unexposed ones. Notably, the taproot length of cucumber seedlings under the presence of CB600 was obviously longer than that of the control (Fig. 2A and D). This means that CB600 exposure primarily inhibited the development of lateral roots, which is in agreement with fewer number of root tips (Table 1).

Further observation of lateral roots and root hairs was performed by the microscope imaging. There was no significant difference in the diameter of lateral roots between the unexposed and exposed treatments (Fig. 4). But, the length and/or amount of root hairs after all the treatments were visually increased comparing with the control. Using statistics, the number, average length, and length distribution of root hairs were analyzed in depth, as shown in Fig. 5. The hydroponic culture with the bulk biochars (BB600 and RB600) did not

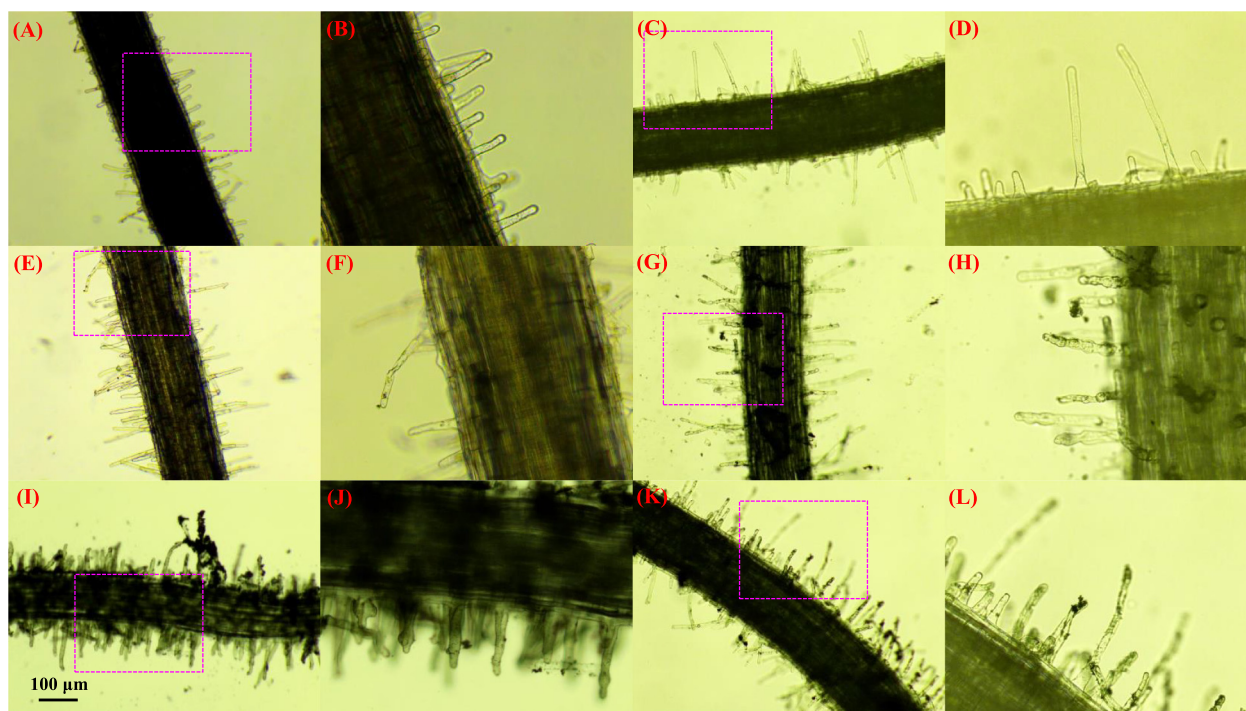


**Fig. 4.** The root hair morphology of cucumber seedlings under hydroponic treatments of Control (A, B), 500 mg/L BB600 (C, D), 500 mg/L RB600 (E, F), 500 mg/L CB600 (G, H), 500 mg/L NB600 (I, J), and 50 mg/L NB600 (K, L). The images of B, D, F, H, J, and L were enlarged from the square region of panels A, C, E, G, I, and K, respectively.

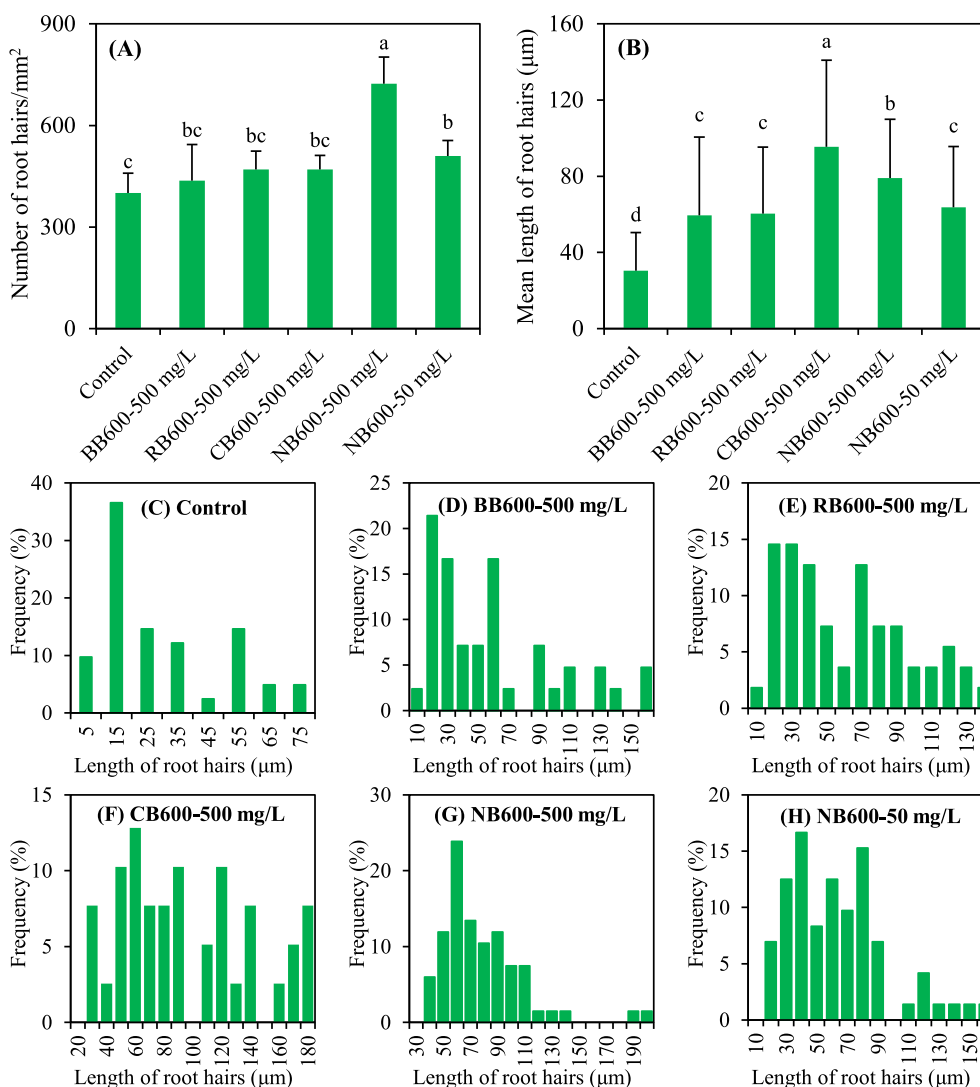


**Fig. 5.** The number (A) and length (B) of root hairs of cucumber seedlings after hydroponic exposure to biochars. (C–H) indicate length distribution of root hairs under different treatments. Significant difference was marked with different lowercase letters ( $p < 0.05$ ,  $n$  of lateral roots = 5,  $n$  of root hairs > 50).

influence the number of root hairs significantly, whereas the average length increased by 95.5% and 98.8% (Fig. 5A–B), respectively. Even, the increasing proportion of root hairs reached up to 214.2% by 500 mg/L CB600. After NB600 exposure (both 50 mg/L and 500 mg/L), the number and average length of root hairs increased remarkably, and greater increase occurred at higher concentration. The length of root hairs ranged from 5 µm to 75 µm in the unexposed treatment, and the bin center length value with the most frequency was 15 µm (Fig. 5C). By comparison, the range of root hair length was broadened after the introducing of biochar samples, and the length values of most root hairs were greater (Fig. 5D–H). For instance, the length of 500 mg/L NB600-exposed root hairs was in the range of 40 µm to 200 µm, and the length value with the most frequency was 60 µm (Fig. 5G).

It is well known that root hair is main site of plants for absorbing water and inorganic nutrients. For the germination stage, the biochar-resulted changes of root hairs might be closely associated with water uptake of cucumber seedlings. Via testing, we found that the water content of cucumber seedling shoot under the treatment of 500 mg/L NB600 was significantly lower than that of the control (Fig. 3D). There were also large amounts of NB600 aggregates attached onto the surface and surrounding of root hairs (Fig. 4I).

Similarly, Zhang et al. (2020a) reported that biochar nanoparticle adhesion caused epidermal openings clogging and hindered water transfer of tomato and reed. For resisting the exposure stress of NB600 and its induced suppression on water absorption, therefore, more root hairs of cucumber seedlings were developed. Furthermore, swelling and bump hyperplasia of many root hairs were obviously observed after the treatments of CB600 and NB600 at 500 mg/L (Fig. 4H and J). Partial particles of CB600 and NB600 exhibited sharp shapes in the TEM images (Fig. S2). Penetration and cut of graphene with sharp edges in the plant and algae cells had been reported previously (Zhang et al., 2015; Zhao et al., 2017). The sharp edges and corners of biochar micro/nanoparticles directly contacted with root hairs, which would result in physical damage. This is a possible reason for the aberrant morphology of root hairs. For the lower concentration of 50 mg/L, few amounts of NB600 particles deposited on the root hair surface (Fig. 4K). The increase and lengthening of root hairs could be a response to the stress of NB600 exposure at 50 mg/L, but this treatment did not result in atypical morphology of root hairs.

Overall, the present study found the tight attachment of biochar colloids/nanoparticles-roots and the resulting adverse responses of taproot, lateral roots and root hairs. Taking contact toxicity of nano

materials into consideration, the toxicity of biochar colloids and nanoparticles on root cells (e.g., membrane damage, uptake and transport) and possible toxic mechanisms (e.g., oxidative stress and physical penetration) needs further investigation.

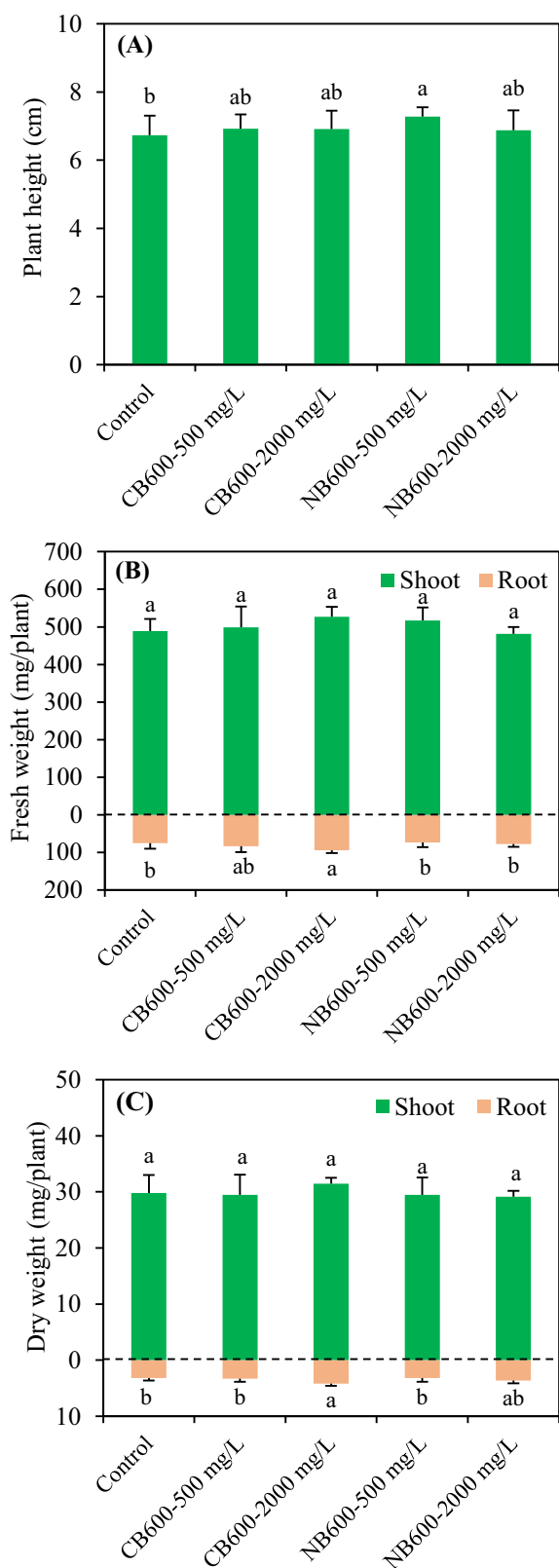


**Fig. 6.** The plant height (A), fresh weight (B), and dry weight (C) of cucumber seedlings in pot experiments with CB600 and NB600. Significant difference was marked with different lowercase letters ( $p < 0.05$ ).

#### 3.4. Growth of cucumber seedlings in soil with CB600 and NB600 addition

The early seedling growth of cucumber was studied in the soils containing CB600 or NB600 using pot experiment. The phenotype and growth responses of cucumber seedlings to CB600 and NB600 in the lime concretion black soil were photographed and shown in Fig. S5A–E. For 2000 mg/kg (biochar/soil) treatment, there were a number of black particles on root surfaces (Fig. S5F), implying the adhesion of NB600. However, the addition of NB600 in the tested soil did not cause significant adverse effects on the plant height, fresh weight, and dry weight of cucumber seedlings (Fig. 6). Even, there was a slight improvement of cucumber seedling growth in the soil with NB600. The plant height increased by 8.05% after NB600 exposure at 500 mg/kg. For CB600, no significant influence was observed on the plant height and biomass of shoot and root at 500 mg/kg. CB600 addition at the rate of 2000 mg/kg caused 25.5% and 31.8% increase in the fresh and dry weight of cucumber seedling roots (Fig. 6B and C), respectively. The analyses of root morphology suggested that CB600 primarily improved root length at the dosage of 2000 mg/kg (Table 2). Both CB600 and NB600 in the soil had no significant effect on other root parameters (i.e., tip number, diameter, area, and volume) at the two tested concentrations. These results suggested that biochar colloids and nanoparticles did not trigger toxicological effects on early seedling growth of plants in soil, even at relatively high exposure concentration (e.g., 2000 mg/kg).

In natural soils, the biochar microscale and nanoscale particles with more oxygenic groups are liable to interact with soil minerals (e.g., goethite and hematite) and also could form homoaggregates in soil solution (Gui et al., 2021; Lian et al., 2019; Liu et al., 2018b; Spokas et al., 2014; Yang et al., 2021; Zhang et al., 2020b). This close interaction could decrease the probability of direct contact between plant roots and biochar colloids and nanoparticles, thus reducing exposure risk. Furthermore, the biochar-mineral association could enhance stability of soil aggregates (Lin et al., 2012; Pituello et al., 2018), and subsequently improve soil structure and water retention (Fu et al., 2019; Mao et al., 2019). This is the possible reason for the beneficial effects of CB600 and NB600 on the early seedling growth of cucumber in the tested soil.

#### 4. Conclusions

This study demonstrated negative effects of hydroponic exposure with CB600 and NB600 on cucumber early seedlings. The exposure of CB600 could reduce root biomass at 500 mg/L, mainly inhibiting lateral root development, while CB600 did not affect the shoot. By contrast, NB600-caused phytotoxicity was more significant. After treating with NB600, both shoot and root growth decreased greatly. Moreover, the water absorption and transfer might be hindered. For resisting exposure stress, root hairs increased and lengthened. Even, we observed swelling and hyperplasia of root hairs under the exposure. To our best knowledge, this is the first observation on the atypical hyperplasia of root hairs under direct exposure of biochar colloids and nanoparticles. These adverse responses were largely related with the contact and adhesion of CB600 and NB600 with sharp edges and corners to root surface. But for a low concentration of 50 mg/L, no significant influence of NB600 was observed on cucumber seedlings. Our pot experiment revealed that the existing of CB600 and NB600 did not have negative impacts on plant seedlings in soil. In actual waters and soils, the behaviors of ultrafine biochar such as colloidal process, transformation, weathering and aging highly depend on the complicated and diversified conditions. Therefore, the physiological responses of plants to biochar colloids and nanoparticles in natural environments need further investigation.

#### CRedit authorship contribution statement

**Guocheng Liu:** Investigation, Writing – review & editing, Formal analysis, Funding acquisition. **Meiqi Pan:** Investigation, Methodology,

**Table 2**  
Root morphology of cucumber seedlings in pot experiments with biochar addition.

Treatments	Root parameters				
	Length (cm)	Diameter (mm)	Tip number	Area (cm <sup>2</sup> )	Volume (cm <sup>3</sup> )
Control	44.7 ± 6.20b	0.44 ± 0.03a	73.9 ± 13.2ab	6.06 ± 1.10a	0.066 ± 0.015a
CB600-500 mg/kg	49.4 ± 12.8ab	0.46 ± 0.04a	77.4 ± 11.8ab	7.54 ± 2.51a	0.080 ± 0.031a
CB600-2000 mg/kg	57.7 ± 8.28a	0.46 ± 0.08a	91.2 ± 16.9a	7.73 ± 3.03a	0.078 ± 0.012a
NB600-500 mg/kg	43.6 ± 3.48b	0.43 ± 0.01a	73.9 ± 8.69ab	5.73 ± 0.66a	0.061 ± 0.009a
NB600-2000 mg/kg	50.2 ± 10.4ab	0.42 ± 0.02a	71.1 ± 18.5b	7.53 ± 1.03a	0.081 ± 0.033a

Data curation, Formal analysis. **Jiaying Song**: Data curation, Formal analysis. **Mengyao Guo**: Data curation, Formal analysis. **Lina Xu**: Data curation, Formal analysis. **Yanjun Xin**: Writing – review & editing, Supervision.

### Declaration of competing interest

The authors declare that they have no known competing financial interests or personal relationships that could have appeared to influence the work reported in this paper.

### Acknowledgements

This work was financially supported by Shandong Provincial Natural Science Foundation (ZR2020MD112), National Natural Science Foundation of China (52070107), Support Plan on Youth Innovation Science and Technology for Higher Education of Shandong Province (2019KJD014), and Research Foundation for Talented Scholars of Qingdao Agricultural University (6651119010).

### Appendix A. Supplementary data

Supplementary data to this article can be found online at <https://doi.org/10.1016/j.scitotenv.2021.150233>.

### References

Agegnehu, G., Srivastava, A.K., Bird, M.L., 2017. The role of biochar and biochar-compost in improving soil quality and crop performance: a review. *Appl. Soil Ecol.* 119, 156–170.

Begum, P., Ikhtiar, R., Fugetsu, B., 2011. Graphene phytotoxicity in the seedling stage of cabbage, tomato, red spinach, and lettuce. *Carbon* 49, 3907–3919.

Billah, M.M., Ahmad, W., Ali, M., 2019. Biochar particle size and rhizobia strains effect on the uptake and efficiency of nitrogen in lentils. *J. Plant Nutr.* 42, 1709–1725.

Braadbaart, F., Poole, I., van Brussel, A.A., 2009. Preservation potential of charcoal in alkaline environments: an experimental approach and implications for the archaeological record. *J. Archaeol. Sci.* 36, 1672–1679.

Cañas, J.E., Long, M., Nations, S., Vadan, R., Dai, L., Luo, M., Ambikapathi, R., Lee, E.H., Olszyk, D., 2008. Effects of functionalized and nonfunctionalized single-walled carbon nanotubes on root elongation of select crop species. *Environ. Toxicol. Chem.* 27, 1922–1931.

Chen, M., Alim, N., Zhang, Y., Xu, N., Cao, X., 2018. Contrasting effects of biochar nanoparticles on the retention and transport of phosphorus in acidic and alkaline soils. *Environ. Pollut.* 239, 562–570.

Chen, M., Wang, D., Yang, F., Xu, X., Xu, N., Cao, X., 2017. Transport and retention of biochar nanoparticles in a paddy soil under environmentally-relevant solution chemistry conditions. *Environ. Pollut.* 230, 540–549.

Chen, T., Zhang, Y., Wang, H., Lu, W., Zhou, Z., Zhang, Y., Ren, L., 2014. Influence of pyrolysis temperature on characteristics and heavy metal adsorptive performance of biochar derived from municipal sewage sludge. *Bioresour. Technol.* 164, 47–54.

Chen, X., Zhou, B., Wang, Q., Tao, W., Lin, H., 2020. Nano-biochar reduced soil erosion and nitrate loss in sloping fields on the loess plateau of China. *Catena* 187, 104346.

Fu, Q., Zhao, H., Li, H., Li, T., Hou, R., Liu, D., Ji, Y., Gao, Y., Yu, P., 2019. Effects of biochar application during different periods on soil structures and water retention in seasonally frozen soil areas. *Sci. Total Environ.* 694, 133732.

Hameed, R., Lei, C., Lin, D., 2020. Adsorption of organic contaminants on biochar colloids: effects of pyrolysis temperature and particle size. *Environ. Sci. Pollut. Res. Int.* 27, 18412–18422.

Gui, X., Song, B., Chen, M., Xu, X., Ren, Z., Li, X., Cao, X., 2021. Soil colloids affect the aggregation and stability of biochar colloids. *Sci. Total Environ.* 771, 145414.

Jaiswal, A.K., Elad, Y., Graber, E.R., Frenkel, O., 2014. Rhizoctonia solani suppression and plant growth promotion in cucumber as affected by biochar pyrolysis temperature, feedstock and concentration. *Soil Biol. Biochem.* 69, 110–118.

Lehmann, J., Gaunt, J., Rondon, M., 2006. Bio-char sequestration in terrestrial ecosystems—a review. *Mitig. Adapt. Strateg. Glob. Chang.* 11, 403–427.

Li, L., Wang, X., Fu, H., Qu, X., Chen, J., Tao, S., Zhu, D., 2020. Dissolved black carbon facilitates photoreduction of Hg(II) to Hg(0) and reduces mercury uptake by lettuce (*Lactuca sativa* L.). *Environ. Sci. Technol.* 54, 11137–11145.

Lian, F., Xing, B., 2017. Black carbon (Biochar) in water/soil environments: molecular structure, sorption, stability, and potential risk. *Environ. Sci. Technol.* 51, 13517–13532.

Lian, F., Yu, W., Zhou, Q., Gu, S., Wang, Z., Xing, B., 2020. Size matters: Nano-biochar triggers decomposition and transformation inhibition of antibiotic resistance genes in aqueous environments. *Environ. Sci. Technol.* 54, 8821–8829.

Lian, F., Yu, W.C., Wang, Z.Y., Xing, B.S., 2019. New insights into black carbon nanoparticle-induced dispersibility of goethite colloids and configuration-dependent sorption for phenanthrene. *Environ. Sci. Technol.* 53, 661–670.

Lieke, T., Zhang, X., Steinberg, C.E.W., Pan, B., 2018. Overlooked risks of biochars: persistent free radicals trigger neurotoxicity in *Caenorhabditis elegans*. *Environ. Sci. Technol.* 52, 7981–7987.

Lim, T., Spokas, K., Feyereisen, G., Novak, J., 2016. Predicting the impact of biochar additions on soil hydraulic properties. *Chemosphere* 142, 136–144.

Lin, Y., Munroe, P., Joseph, S., Kimber, S., Van Zwieten, L., 2012. Nanoscale organo-mineral reactions of biochars in ferrosol: an investigation using microscopy. *Plant Soil* 357, 369–380.

Liu, G., Zheng, H., Jiang, Z., Zhao, J., Wang, Z., Pan, B., Xing, B., 2018a. Formation and physicochemical characteristics of nano biochar: insight into chemical and colloidal stability. *Environ. Sci. Technol.* 52, 10369–10379.

Liu, G., Zheng, H., Jiang, Z., Wang, Z., 2018b. Effects of biochar input on the properties of soil nanoparticles and dispersion/sedimentation of natural mineral nanoparticles in aqueous phase. *Sci. Total Environ.* 634, 595–605.

Lu, L., Yu, W., Wang, Y., Zhang, K., Zhu, X., Zhang, Y., Wu, Y., Ullah, H., Xiao, X., Chen, B., 2020. Application of biochar-based materials in environmental remediation: from multi-level structures to specific devices. *Biochar* 2, 1–31.

Luo, J., Lin, L., Liu, C., Jia, C., Chen, T., Yang, Y., Shen, M., Shang, H., Zhou, S., Huang, M., Wang, Y., Zhou, D., Fan, J., Clark, J.H., Zhang, S., Zhu, X., 2020. Reveal a hidden highly toxic substance in biochar to support its effective elimination strategy. *J. Hazard. Mater.* 399, 123055.

Lyu, H., He, Y., Tang, J., Hecker, M., Liu, Q., Jones, P.D., Codling, G., Giesy, J.P., 2016. Effect of pyrolysis temperature on potential toxicity of biochar if applied to the environment. *Environ. Pollut.* 218, 1–7.

Ma, S., Jing, F., Sohi, S.P., Chen, J., 2019. New insights into contrasting mechanisms for PAE adsorption on millimeter, micron- and nano-scale biochar. *Environ. Sci. Pollut. Res.* 26, 18636–18650.

Ma, X., Xin, Y., Yan, Q., Pan, X., Xin, S., Huang, X., Chen, Q., Liu, G., 2020. Adsorption characteristics of tetracycline onto biochars as affected by solution chemistry conditions and ball milling treatment. *Water Air Soil Pollut.* 231, 387.

Mahmoud, E., El Baroudy, A., Ali, N., Sleem, M., 2020. Spectroscopic studies on the phosphorus adsorption in salt-affected soils with or without nano-biochar additions. *Environ. Res.* 184, 109277.

Major, J., 2010. Guidelines on practical aspects of biochar application to field soil in various soil management systems. *Int. Biochar Initiative* 1–23.

Mao, J., Zhang, K., Chen, B., 2019. Linking hydrophobicity of biochar to the water repellency and water holding capacity of biochar-amended soil. *Environ. Pollut.* 253, 779–789.

Oleszczuk, P., Cwikla-Bundyra, W., Bogusz, A., Skwarek, E., Ok, Y.S., 2016. Characterization of nanoparticles of biochars from different biomass. *J. Anal. Appl. Pyrol.* 121, 165–172.

Piash, M.I., Iwabuchi, K., Itoh, T., Uemura, K., 2021. Release of essential plant nutrients from manure- and wood-based biochars. *Geoderma* 397, 115100.

Pituello, C., Dal Ferro, N., Francioso, O., Simonetti, G., Berti, A., Piccoli, I., Pisi, A., Morari, F., 2018. Effects of biochar on the dynamics of aggregate stability in clay and sandy loam soils. *Eur. J. Soil Sci.* 69, 827–842.

Prodana, M., Silva, C., Gravato, C., Verheijen, F.G.A., Keizer, J.J., Soares, A., Loureiro, S., Bastos, A.C., 2019. Influence of biochar particle size on biota responses. *Ecotoxicol. Environ. Saf.* 174, 120–128.

Qian, L., Zhang, W., Yan, J., Han, L., Gao, W., Liu, R., Chen, M., 2016. Effective removal of heavy metal by biochar colloids under different pyrolysis temperatures. *Bioresour. Technol.* 206, 217–224.

Qu, X., Fu, H., Mao, J., Ran, Y., Zhang, D., Zhu, D., 2016. Chemical and structural properties of dissolved black carbon released from biochars. *Carbon* 96, 759–767.

Sadezky, A., Muckenhuber, H., Grothe, H., Niessner, R., Pöschl, U., 2005. Raman microspectroscopy of soot and related carbonaceous materials: spectral analysis and structural information. *Carbon* 43, 1731–1742.

Sarfaraz, R., Yang, W., Wang, S., Zhou, B., Xing, S., 2020. Short term effects of biochar with different particle sizes on phosphorous availability and microbial communities. *Chemosphere* 256, 126862.



- Shen, Y., Tang, H., Wu, W., Shang, H., Zhang, D., Zhan, X., Xing, B., 2020. Role of nano-biochar in attenuating the allelopathic effect from *Imperata cylindrica* on rice seedlings. *Environ. Sci. Nano* 7, 116–126.
- Song, B., Chen, M., Zhao, L., Qiu, H., Cao, X., 2019. Physicochemical property and colloidal stability of micron- and nano-particle biochar derived from a variety of feedstock sources. *Sci. Total Environ.* 661, 685–695.
- Spokas, K.A., Novak, J.M., Masiello, C.A., Johnson, M.G., Colosky, E.C., Ippolito, J.A., Trigo, C., 2014. Physical disintegration of biochar: an overlooked process. *Environ. Sci. Technol. Lett.* 1, 326–332.
- Wang, D., Zhang, W., Hao, X., Zhou, D., 2013a. Transport of biochar particles in saturated granular media: effects of pyrolysis temperature and particle size. *Environ. Sci. Technol.* 47 (2), 821–828.
- Wang, D., Zhang, W., Zhou, D., 2013b. Antagonistic effects of humic acid and iron oxyhydroxide grain-coating on biochar nanoparticle transport in saturated sand. *Environ. Sci. Technol.* 47, 5154–5161.
- Wang, H., Zheng, H., Jiang, Z., Dai, Y., Liu, G., Chen, L., Luo, X., Liu, M., Wang, Z., 2017. Efficacies of biochar and biochar-based amendment on vegetable yield and nitrogen utilization in four consecutive planting seasons. *Sci. Total Environ.* 593–594, 124–133.
- Wang, Y., Zhang, W., Shang, J., Shen, C., Joseph, S.D., 2019. Chemical aging changed aggregation kinetics and transport of biochar colloids. *Environ. Sci. Technol.* 53, 8136–8146.
- Xin, S., Liu, G., Ma, X., Gong, J., Ma, B., Yan, Q., Chen, Q., Ma, D., Zhang, G., Gao, M., Xin, Y., 2021. High efficiency heterogeneous Fenton-like catalyst biochar modified CuFeO<sub>2</sub> for the degradation of tetracycline: economical synthesis, catalytic performance and mechanism. *Appl. Catal. B Environ.* 280, 119386.
- Xu, F., Wei, C., Zeng, Q., Li, X., Alvarez, P.J.J., Li, Q., Qu, X., Zhu, D., 2017. Aggregation behavior of dissolved black carbon: implications for vertical mass flux and fractionation in aquatic systems. *Environ. Sci. Technol.* 51, 13723–13732.
- Xu, Y., Ou, Q., Liu, C., Zhou, X., He, Q., Wu, Z., Huang, R., Ma, J., Lu, D., Huangfu, X., 2020. Aggregation and deposition behaviors of dissolved black carbon with coexisting heavy metals in aquatic solution. *Environ. Sci. Nano* 7, 2773–2784.
- Yang, F., Xu, Z., Huang, Y., Tsang, D.C.W., Ok, Y.S., Zhao, L., Qiu, H., Xu, X., Cao, X., 2021. Stabilization of dissolvable biochar by soil minerals: release reduction and organo-mineral complexes formation. *J. Hazard. Mater.* 412, 125213.
- Yang, W., Shang, J., Sharma, P., Li, B., Liu, K., Flury, M., 2019. Colloidal stability and aggregation kinetics of biochar colloids: effects of pyrolysis temperature, cation type, and humic acid concentrations. *Sci. Total Environ.* 658, 1306–1315.
- Yu, J., Guo, Q., Ding, L., Gong, Y., Yu, G., 2020. Studying effects of solid structure evolution on gasification reactivity of coal chars by in-situ raman spectroscopy. *Fuel* 270, 117603.
- Yue, L., Lian, F., Han, Y., Bao, Q., Wang, Z., Xing, B., 2019. The effect of biochar nanoparticles on rice plant growth and the uptake of heavy metals: implications for agronomic benefits and potential risk. *Sci. Total Environ.* 656, 9–18.
- Zhang, K., Wang, Y., Mao, J., Chen, B., 2020a. Effects of biochar nanoparticles on seed germination and seedling growth. *Environ. Pollut.* 256, 113409.
- Zhang, M., Gao, B., Chen, J., Li, Y., 2015. Effects of graphene on seed germination and seedling growth. *J. Nanopart. Res.* 17, 78.
- Zhang, P., Liu, A., Huang, P., Min, L., Sun, H., 2020b. Sorption and molecular fractionation of biochar-derived dissolved organic matter on ferrihydrite. *J. Hazard. Mater.* 392, 122260.
- Zhao, J., Cao, X., Wang, Z., Dai, Y., Xing, B., 2017. Mechanistic understanding toward the toxicity of graphene-family materials to freshwater algae. *Water Res.* 111, 18–27.
- Zhao, J., Wang, Z., White, J.C., Xing, B., 2014. Graphene in the aquatic environment: adsorption, dispersion, toxicity and transformation. *Environ. Sci. Technol.* 48, 9995–10009.
- Zheng, H., Wang, Z., Deng, X., Zhao, J., Luo, Y., Novak, J., Herbert, S., Xing, B., 2013. Characteristics and nutrient values of biochars produced from giant reed at different temperatures. *Bioresour. Technol.* 130, 463–471.
- Zhou, R., Wang, Y., Tian, M., Shah Jahan, M., Shu, S., Sun, J., Li, P., Ahammed, G.J., Guo, S., 2021. Mixing of biochar, vinegar and mushroom residues regulates soil microbial community and increases cucumber yield under continuous cropping regime. *Appl. Soil Ecol.* 161, 103883.



第十五届山东省大学生科技节

# 荣誉证书

## 山东省大学生环保创意大赛

### 三等奖

专业赛道：山东省大学生环保创意大赛

作品名称：Y203改性生物炭高效纳米复合材料去除水中土霉素

参赛学生：宋佳颖, 孙伟凯, 王舰, 李金莹, 李雪

所在学校：青岛农业大学

指导老师：刘国成



证书编号：SDUC202339-3-0057

二〇二三年九月



通知公告

首页 > 导航栏目 > 通知公告

### 关于公布第五届青岛农业大学节能减排社会实践与科技竞赛获奖名单的通知

2023-06-06 12:31:49 浏览数: 301

节能减排是深入贯彻落实科学发展观，助力伟大中国梦的实现，构建社会主义和谐社会的重大举措。5月10日，由创新创业学院主办，机电工程学院、资源与环境学院、建筑工程学院承办的《第五届青岛农业大学节能减排社会实践与科技竞赛暨2023年“建行杯”第十六届全国大学生节能减排社会实践与科技竞赛选拔赛》汇报答辩在线上顺利举行。资源与环境学院、机电工程学院、建筑工程学院、化学与药学院、巴蒂斯未来农业科技学院等6个学院多支队伍参加了现场汇报答辩。

在校赛汇报答辩环节，选手充分利用PPT、视频、动画等方式对参赛作品进行了全方位讲解。专家评委们从作品科学性、创新性、节能性、环保性和应用效果等方面对作品申报材料进行了严格审阅和现场打分。经专家评委综合评议后，评选出一等奖6项、二等奖9项、三等奖10项。拟推荐一等奖、二等奖获奖作品参加“建行杯”第十六届全国大学生节能减排社会实践与科技竞赛国赛角逐。

具体获奖名单公布如下：

序号	团队或作品名称	团队队长	获奖等级
1	阳光小队	董雅楠	一等奖
2	电驱助农—面向丘陵山区的新能源动力装备	吕延士	一等奖
3	“热电节能”—微环境制冷调温新势力	杨鑫航	一等奖
4	尾菜高温堆肥化处理技术与装置设计	许淑妮	一等奖
5	浮萍碳微球多功能水处理吸附剂“环萍”小队	王玉婷	一等奖
6	蓝天卫士小分队	王爱斌	一等奖
7	姜姜特攻队	姜立坤	二等奖
8	“环保俊树”队	李晓芬	二等奖
9	万众“猪”目小分队	李宗明	二等奖
10	三维电极耦合氯离子高效去除阿力甜的电催化氧化方法	刘婷婷	二等奖
11	贝精助福泥团队	任洪政	二等奖
12	智能水肥机队	徐文虎	二等奖
13	基于光伏的家用直流微电网	潘王杰	二等奖
14	全铁循环—基于生物质还原的绿铁能源技术	崔文婧	二等奖
15	普瑞赛思	闫吉顺	二等奖
16	三十五万扬沙	闫宗钰	三等奖
17	小天才队	顾顿	三等奖
18	源梦社会实践队	孔孜涵	三等奖
19	源源不断队	潘美琦	三等奖
20	石半功贝团队	曲玉馨	三等奖
21	高铁酸盐的原位合成及应用	苏芷卉	三等奖
22	“清暖人间”：北方地区自建房农户清洁取暖现状及影响因素——基于青岛市的调查研究报告调研小队	于宇	三等奖
23	无线充电智能车	郭建升	三等奖
24	基于Arduino的低油耗生姜精量播种机	张春蕾	三等奖
25	“芯”材料——一种智能混凝土裂缝修复剂	于子豪	三等奖

编辑:相涵月

责任编辑:林鑫

上一篇: 学术交流预告 “農谈科技论文写作与发表”

下一篇: 关于举办资源与环境学院第四届大学生学术论坛的通知



序号: \_\_\_\_\_

编码: \_\_\_\_\_

# 第十六届全国大学生节能减排 社会实践与科技竞赛作品申报书

【科技作品类（含实物制作、软件、设计等）】

作品名称: 新肥兴农——多拉菌素菌渣高效资源化利用

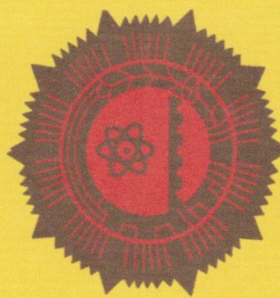
学校全称: 青岛农业大学

申报者姓名: 潘美琦, 宋佳颖, 王志琳, 路红丽

指导教师: 辛言君, 刘国成

团队类型: 研究生团队

三等奖



三等奖



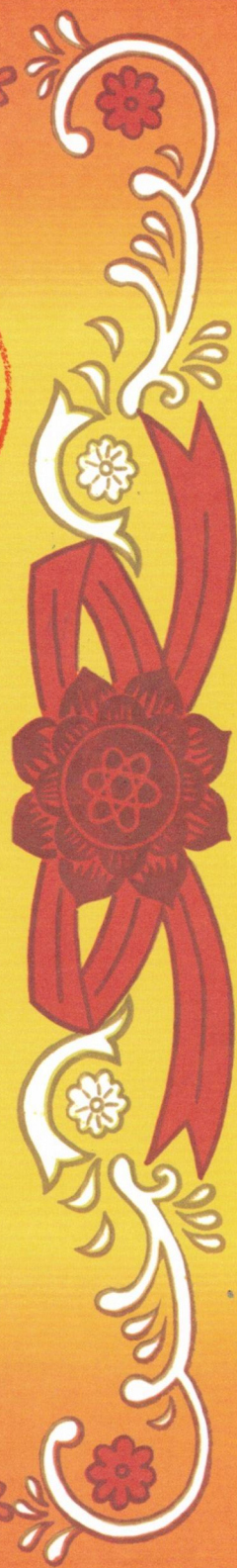
王志琳、潘美琦、李晓芬、宋佳颖、王东 同学：

在第四届青岛农业大学节能减排社会实践与科技竞赛中  
获得 三 等奖，特发此证，以示表彰。

指导教师：辛言君



二〇一二年十月



## 证明材料

兹证明资源与环境学院学生宋佳颖，参与项目“吸附协同类芬顿功能型 XFemOn/生物炭构筑及无害化处理抗生素菌渣效能与机制”，该学生在在主持人指导下认真收集资料，积极撰写论文，与课题组成员一起做了大量有效工作，为课题做出了一定贡献。

特此证明。

项目负责人签字：刘国成

2023年9月26日

## 第三届可持续固体废物处理与管理国际会议通知 (SWTM-2023)

### 各有关单位、专家：

为深入贯彻可持续发展战略，推进有机固体废物处理与资源化利用协同发展，助力深入打好污染防治攻坚战，受国际生物过程协会（International Bioprocessing Association, IBA）和中国农学会委托，西北农林科技大学联合中国农业大学、南京农业大学拟在陕西杨凌举办第三届可持续固体废物处理与管理国际会议（3<sup>rd</sup>SWTM）。此次会议主要关注固体废物处理与资源化利用的前沿生物技术，邀请国内外专家学者、工程师和其他管理人员，全面交流固体废物处理和管理方面的新理论、新技术、新模式和新产品等重要成果，以推动固体废物资源循环利用相关产业的发展。

### 一、会议议题

有机废弃物制备生物能源、燃料和化学品/生物化学品  
矿业固体废物的生物处理和资源回收  
固体废弃物好氧堆肥及污染控制  
有机废弃物制备生物炭及其应用  
城市固体废物的资源化处理  
纳米技术及其在固体废物处理中的应用

### 二、组织机构

**主办单位：**西北农林科技大学  
**协办单位：**中国农业大学  
南京农业大学  
能源与环境可持续性中心  
印度生物技术研究协会  
**指导单位：**国际生物过程协会（IBA）  
中国农学会

### 三、会议时间地点

**时间：**2023年7月28日—7月31日  
**地点：**杨凌示范区  
**重要日程安排：**  
**注册时间：**2023年7月28日  
**学术会议：**2023年7月29日、30日全天及31日上午

## 四、会议论文及海报征集

欢迎大家积极参加会议并提交摘要及海报，摘要格式参见模板 (<http://2023swtm.aconf.org/zh-cn/news/4899.html>)，海报模板为 80 cm(宽)× 180 cm (高)，提交截止时间为 2023 年 6 月 30 日，提交网站 <http://2023swtm.aconf.org/zh-cn/index.html>。

## 五、会议注册费及缴纳方式

国内参会代表注册费

项目	4月30日之前注册 (人民币)	5月1日-7月27日注册 (人民币)	会议现场注册 (人民币)
学生 (IBA 会员)	1000	1200	1400
学生 (非 IBA 会员)	1200	1400	1600
参会代表 (IBA 会员)	1400	1600	1800
参会代表 (非 IBA 会员)	1800	2000	2200
随行人员	800	1000	1200

国际参会代表注册费

项目	4月30日之前注册 (美元)	5月1日-7月27日注册 (美元)	会议现场注册 (美元)
学生 (IBA 会员)	100	150	200
学生 (非 IBA 会员)	150	200	250
参会代表 (IBA 会员)	150	175	275
参会代表 (非 IBA 会员)	200	250	300
随行人员	100	150	200

会议注册费可通过会议网站提供的汇款方式缴纳，食宿自理。

## 六、会务组联系方式

Mukesh Kumar Awasthi, 副教授, +86-18392197328

王权, 副教授, +86-15891723940

电子邮件: [swtm2023@163.com](mailto:swtm2023@163.com); [swtm2023@nwsuaf.edu.cn](mailto:swtm2023@nwsuaf.edu.cn)

西北农林科技大学, 陕西, 杨凌示范区 712100





	<p>aerobic fermentation processes and analysis of factors affecting their GI, Shuwen Du Zhejiang University, China</p> <p>Effects of functional membrane coverings on carbon and nitrogen evolution during aerobic composting: Insight into the succession of bacterial and fungal communities, Jimpeng Xiong, China Agricultural University, China</p> <p>Undervalued Humin Components in Humus:</p>			<p>Microorganisms in MEC-AD, Xueting Wang, Harbin Institute of Technology, China</p> <p>Development mechanism of flexible biogas production in regionally distributed microgrids: based on evolutionary game theory, Yiyun Liu, Anhui University of Technology, China</p>		<p>Utilization, Xiuxiu Ruan, Shanghai University, China</p> <p>Effects of Fenton oxidation treated oxytetracycline fermentation residues as soil amendment: Soil properties and antibiotic resistance, Jiaying Song, Qingdao Agricultural University, China</p>		<p>Co-fermentation of Waste Activated Sludge and Food Waste into Volatile Fatty Acids, Gang Guo, Huazhong University of Science and Technology, China</p> <p>Progress on the efficient grease synthesis by organic waste bioconversion employing black soldier fly, Mengyao Dong, Huazhong Agricultural University, China</p> <p>Links between carbon/nitrogen ratio, synergy and microbial characteristics of</p>
14:45~15:00		14:45~15:00	14:45~15:00	14:45~15:00	14:45~15:00	14:45~15:00	14:45~15:00	14:45~15:00
15:00~15:15		15:00~15:15	15:00~15:15	15:00~15:15	15:00~15:15	15:00~15:15	15:00~15:15	15:00~15:15

N 13

**Effects of Fenton oxidation treated oxytetracycline fermentation residues as soil amendment: Soil properties and antibiotic resistance**

Jiaying Song, Wenqiang Jia, Jinying Li, Guocheng Liu

*Qingdao Agricultural University, Qingdao 266109, China*

Oxytetracycline (OTC) fermentation residue (OFR) is biosolid waste of OTC production process. To date, the main treatment of OFR is incineration, and the study regarding its other harmless disposal and resource utilization attracts increasing attention. In this study, soil incubation was performed to investigate the influence of Fenton oxidation treated OFR (FOFR) on soil physicochemical properties, enzymatic activity, and microbial community. Further, antibiotic residue, antibiotic resistance genes (ARGs), and mobile genetic elements (MGEs) were determined and analyzed in the OFR-amended soil. After adding FOFR, soil pH increased firstly before 20 days and then decreased. The contents of soil organic matters, nitrogen, phosphorus, and potassium of FOFR addition treatment were higher than those of OFR one indicating that Fenton oxidation could promote the availability of these nutrients in OFR. The enzyme activity was not inhibited throughout the incubation stage of FOFR-amended soil. In the soils, OTC concentration decreased quickly, below the detection limit of LC/MS/MS after 60 days, and Fenton oxidation could significantly eliminate residual OTC of OFR. Bacterial community structure of FOFR-amended soil was converged to be similar with the control soil after 90 days. Our results suggested that Fenton oxidation might be in favor of limiting the spread of OTC resistance genes and MGEs of OFR in soil reclamation.

**Keywords:** Oxytetracycline fermentation residue; Fenton oxidation; Soil amendment; Antibiotic resistance genes; Soil bacterial communities.





青岛农业大学资源与环境学院  
QINGDAO AGRICULTURAL UNIVERSITY SCHOOL OF RESOURCES AND ENVIRONMENT

第三届中国固体废物  
处理与管理国际会议



## Fenton 氧化处理土霉素菌渣 作为土壤改良剂的影响

Effect of Fenton oxidation treated oxytetracycline fermentation residues as soil amendment

汇报人：宋佳颖  
2023年7月30日

### 参加学术会议——第 18 届中欧膜产业技术创新合作大会



参会名单	
1. 王强	21. 李强
2. 张明	22. 刘伟
3. 陈伟	23. 赵刚
4. 孙磊	24. 周敏
5. 吴昊	25. 郑宇
6. 李华	26. 王磊
7. 张强	27. 陈伟
8. 孙磊	28. 周敏
9. 吴昊	29. 郑宇
10. 李华	30. 王磊
11. 张强	31. 陈伟
12. 孙磊	32. 周敏
13. 吴昊	33. 郑宇
14. 李华	34. 王磊
15. 张强	35. 陈伟
16. 孙磊	36. 周敏
17. 吴昊	37. 郑宇
18. 李华	38. 王磊
19. 张强	39. 陈伟
20. 孙磊	40. 周敏
21. 吴昊	41. 郑宇
22. 李华	42. 王磊
23. 张强	43. 陈伟
24. 孙磊	44. 周敏
25. 吴昊	45. 郑宇
26. 李华	46. 王磊
27. 张强	47. 陈伟
28. 孙磊	48. 周敏
29. 吴昊	49. 郑宇
30. 李华	50. 王磊
31. 张强	51. 陈伟
32. 孙磊	52. 周敏
33. 吴昊	53. 郑宇
34. 李华	54. 王磊
35. 张强	55. 陈伟
36. 孙磊	56. 周敏
37. 吴昊	57. 郑宇
38. 李华	58. 王磊
39. 张强	59. 陈伟
40. 孙磊	60. 周敏
41. 吴昊	61. 郑宇
42. 李华	62. 王磊
43. 张强	63. 陈伟
44. 孙磊	64. 周敏
45. 吴昊	65. 郑宇
46. 李华	66. 王磊
47. 张强	67. 陈伟
48. 孙磊	68. 周敏
49. 吴昊	69. 郑宇
50. 李华	70. 王磊
51. 张强	71. 陈伟
52. 孙磊	72. 周敏
53. 吴昊	73. 郑宇
54. 李华	74. 王磊
55. 张强	75. 陈伟
56. 孙磊	76. 周敏
57. 吴昊	77. 郑宇
58. 李华	78. 王磊
59. 张强	79. 陈伟
60. 孙磊	80. 周敏
61. 吴昊	81. 郑宇
62. 李华	82. 王磊
63. 张强	83. 陈伟
64. 孙磊	84. 周敏
65. 吴昊	85. 郑宇
66. 李华	86. 王磊
67. 张强	87. 陈伟
68. 孙磊	88. 周敏
69. 吴昊	89. 郑宇
70. 李华	90. 王磊
71. 张强	91. 陈伟
72. 孙磊	92. 周敏
73. 吴昊	93. 郑宇
74. 李华	94. 王磊
75. 张强	95. 陈伟
76. 孙磊	96. 周敏
77. 吴昊	97. 郑宇
78. 李华	98. 王磊
79. 张强	99. 陈伟
80. 孙磊	100. 周敏

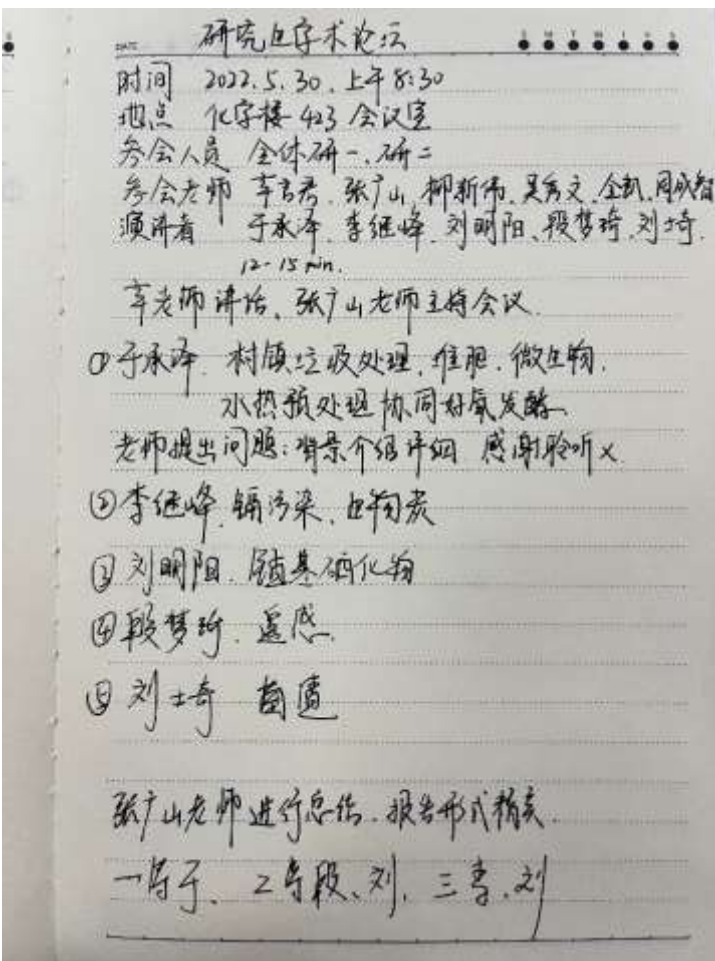
### 参加学术会议——漫谈科技论文写作与发表



参加学术会议——热水解强化土霉素菌渣好氧堆肥及肥料安全性研究



参加学术会议——青岛农业大学第十一届研究生学术论坛会议



# 证 书

宋佳颖同学被评为2021-2022学年青岛农业大学优秀  
研究生干部，特发此证，以资鼓励。



二〇二三年四月

## 资源与环境学院

## 2022-2023 届研究生会换届名单公示

根据研究生处《关于做好 2022 年各学院研究生会换届工作的通知》，严格按照竞岗条件及说明，经综合考察各位候选人具体情况，参考个人竞岗志愿，综合评议决定我院 2022-2023 届院研究生会换届名单如下：

序号	部门	职位	姓名	性别	备注
1	主席团	主席	宋佳颖	女	
2		主席	张哲宁	男	
3		主席	陈孟欣	女	
4	秘书处	副秘书长	牛云梦	女	
5		副秘书长	丁魏	男	
6	权益部	部长	赵庆斌	男	
7		部长	冯晓璐	女	
8	宣传部	部长	王海兵	女	
9		部长	朱慧娴	女	
10	学术部	部长	卢士旭	男	
11		部长	王欣洁	女	
12	文体部	部长	旺承飞	男	
13	实践与乡村振兴部	部长	周培福	男	

注：试用期为三个月。

共青团青岛农业大学资源与环境学院委员会

2022 年 11 月 10 日

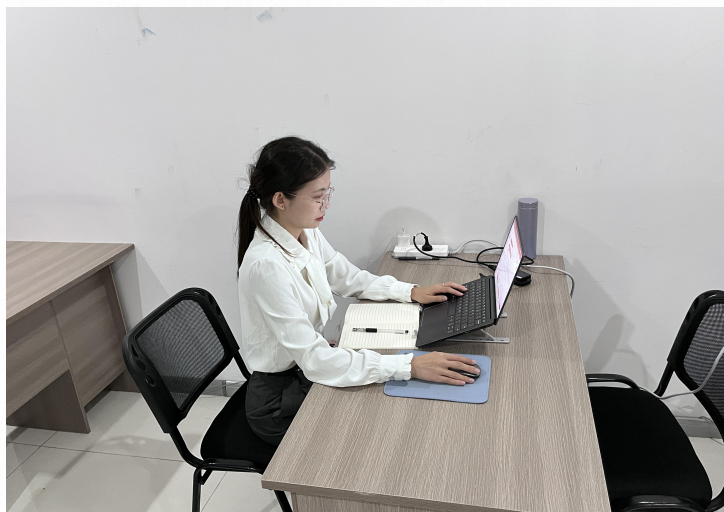
## 社会实践证明

兹证明：

宋佳颖，女，身份证号：370782199909223685，青岛农业大学，资源与环境学院，农业资源与环境专业2021级硕士研究生，该生于2023年7月3日至2023年7月7日在青岛市城阳区流亭街道团工委进行“青春向阳”大学生社会实践活动。

该生在社会实践期间表现积极，能严格遵守我部门的各项规章制度，工作认真负责，获得大家的一致好评。

特此证明！





# 聘 书

LETTER OF APPOINTMENT

宋佳颖 同志:

聘请您为流亭街道东蓝家庄社区团支部兼职

副书记

聘期一年，特发此证。

共青团青岛市城阳区委员会

2023年5月6日

# 荣誉证书

宋佳颖同学：

在2022年“知网杯”信息检索技能大赛中，成绩优秀，荣获三等奖。

特发此证，以资鼓励。



二〇二二年二月



# 荣誉证书

HONORARY CREDENTIAL



宋佳磊 同学：

在山东省产教融合研究生联合培养示范基地（建设）暨科技

小院 2021 年度学术报告会中成绩突出，荣获：

## 二等奖



山东省产教融合研究生联合培养示范基地（建设）  
青岛农业大学资源与环境学院  
二〇二一年十一月十一日

# 荣誉证书

HONORARY CREDENTIAL



潘祥瑞、贾文强、宋佳颖、王亚文、秦琦琦：

在青岛农业大学第一届研究生乡村振兴科技强农+创新大赛  
科技作品竞赛中荣获 三等奖。

作品名称：基于农村生活用水的氯化含碘酚类副产物的生成规律  
研究

指导教师：刘国成



青岛农业大学

二〇二二年十月八日

## 张憬怡评选材料清单

附件 1：中科院 1 区 SCI 一作

附件 2：中科院 1 区 SCI 二作

附件 3：资源与环境学院“2022-2023 年度优秀共青团员”

附件 4：参与导师项目

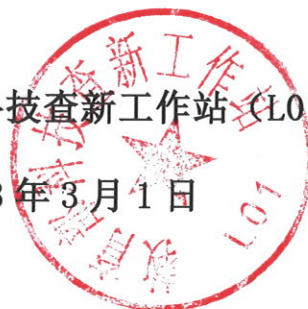
## 论文收录引用检索报告

检索项目	检索青岛农业大学李鹏 (Li Peng) 2022 年发表的论文被 SCI 网络数据库收录情况
检索工具	Web of Science
检索方式	题目 (作者提供文章列表)
检索结果	期刊 Science of the Total Environment, 环境科学与生态学 SCI 一区, 2022 影响因子 10.753
检索结论	检索青岛农业大学李鹏 (Li Peng) 2022 年发表的论文被 SCI 网络数据库收录情况:  共有 1 篇被 SCI 收录, 详情见附件。

特此证明。

教育部科技查新工作站 (L01)

2023 年 3 月 1 日



# Web of Science™

1 record(s) printed from Clarivate Web of Science

## 第 1 条, 共 1 条

**标题:** Atmospheric Pb induced hormesis in the accumulator plant *Tillandsia usneoides*

**作者:** Li, P (Li, Peng); Zhang, JY (Zhang, Jingyi); Sun, XY (Sun, Xingyue); Agathokleous, E (Agathokleous, Evgenios); Zheng, GL (Zheng, Guiling)

**来源出版物:** SCIENCE OF THE TOTAL ENVIRONMENT 卷: 811 文献号: 152384 DOI: 10.1016/j.scitotenv.2021.152384 出版年: MAR 10 2022

**Web of Science 核心合集中的 "被引频次":** 7

**被引频次合计:** 7

**使用次数 (最近 180 天):** 5

**使用次数 (2013 年至今):** 20

**引用的参考文献数:** 52

**摘要:** While numerous studies reported hormesis in plants exposed to heavy metals, metals were commonly added in the growth substrate (e.g. soil or solution). The potential of heavy metals in the atmosphere to induce hormesis in plants, however, remains unknown. In this study, we exposed the widely-used accumulator plant *Tillandsia usneoides* to 10 atmospheric Pb concentrations (0-25.6  $\mu\text{g center dot m}^{-3}$ ) for 6 or 12 h. Three types of dose-response relationships between different response endpoints (biomarkers) and Pb concentrations were found for *T. usneoides*. The first was a monophasic dose response, in which the response increased linearly with increasing Pb concentrations, as seen for metallothionein (MT) content after a 6-h exposure. The second and dominating type was a biphasic-hormetic dose response, exhibited by malondialdehyde (MDA), superoxide anion radical ( $\text{O}_2\text{ center dot}^-$ ), and superoxide dismutase (SOD) after 6 or 12 h of exposure and by glutathione (GSH) and MT content after 12 h of treatment. The third type was a triphasic dose response, as seen for leaf electric conductivity after 6 or 12 h of exposure and GSH after 6 h of exposure. This finding suggests that Pb inhibited the response of *T. usneoides* at very low concentrations, stimulated it at low-to-moderate concentrations, and inhibited it at higher concentrations. Our results demonstrate diverse adaptation mechanisms of plants to stress, in the framework of which alternating between up- and down-regulation of biomarkers is at play when responding to different levels of toxicants. The emergence of the triphasic dose response will further enhance the understanding of time-dependent hormesis.

**入藏号:** WOS:000755044400011

**PubMed ID:** 34923012

**语言:** English

**文献类型:** Article

**作者关键词:** Air pollution; Biomarker; Atmospheric heavy metals; Triphasic dose response

**KeyWords Plus:** ZEBRAFISH EMBRYOS; OXIDATIVE STRESS; SPANISH MOSS; POLLUTION; FOLIAR; RESPONSES; EXPOSURE; RISK; L.; CD

**地址:** [Li, Peng; Zhang, Jingyi; Sun, Xingyue; Zheng, Guiling] Qingdao Agr Univ, Sch

Resources & Environm, Qingdao 266109, Shandong, Peoples R China.  
[Agathokleous, Evgenios] Nanjing Univ Informat Sci & Technol NUIST, Sch Appl Meteorol,  
Dept Ecol, Nanjing 21044, Jiangsu, Peoples R China.

**通讯作者地址:** Zheng, GL (通讯作者), Qingdao Agr Univ, Sch Resources & Environm,  
Qingdao 266109, Shandong, Peoples R China.

**电子邮件地址:** zgl@qau.edu.cn

**Affiliations:** Qingdao Agricultural University

**作者识别号:**

作者	Web of Science ResearcherID	ORCID 号
Agathokleous, Evgenios	D-2838-2016	0000-0002-0058-4857

**出版商:** ELSEVIER

**出版商地址:** RADARWEG 29, 1043 NX AMSTERDAM, NETHERLANDS

**Web of Science Index:** Science Citation Index Expanded (SCI-EXPANDED)

**Web of Science 类别:** Environmental Sciences

**研究方向:** Environmental Sciences & Ecology

**IDS 号:** YY8OG

**ISSN:** 0048-9697

**eISSN:** 1879-1026

**29 字符的来源出版物名称缩写:** SCI TOTAL ENVIRON

**ISO 来源出版物缩写:** Sci. Total Environ.

**来源出版物页码计数:** 9

**基金资助致谢:**

基金资助机构	授权号
National Natural Science Foundation of China	41475132 41571472

This study was funded by the National Natural Science Foundation of China (41475132, 41571472).

**输出日期:** 2023-03-01

---

End of File

107





Contents lists available at ScienceDirect

## Science of the Total Environment

journal homepage: [www.elsevier.com/locate/scitotenv](http://www.elsevier.com/locate/scitotenv)

## Hormesis in the heavy metal accumulator plant *Tillandsia ionantha* under Cd exposure: Frequency and function of different biomarkers



Jingyi Zhang<sup>a,1</sup>, Zhen Tang<sup>a,1</sup>, Evgenios Agathokleous<sup>b</sup>, Guiling Zheng<sup>a</sup>, Liang Xu<sup>a</sup>, Peng Li<sup>a,\*</sup>

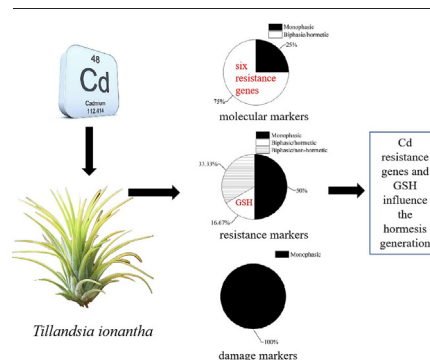
<sup>a</sup> School of Resources and Environment, Qingdao Agricultural University, Qingdao, Shandong 266109, China

<sup>b</sup> Department of Ecology, School of Applied Meteorology, Nanjing University of Information Science and Technology (NUIST), Nanjing, Jiangsu 21044, China

## HIGHLIGHTS

- Cd can generate hormesis in *Tillandsia ionantha*.
- The frequencies of hormesis occurrence in Cd resistance genes are high.
- Cd resistance genes and GSH play an important role in the generation of hormesis.

## GRAPHICAL ABSTRACT



## ARTICLE INFO

Editor: Paola Verlicchi

**Keywords:**

Cadmium  
Dose-response relationship  
Occurrence frequency  
Resistance gene  
Stress biomarkers  
Time-dependent hormesis

## ABSTRACT

Cadmium is one of the most biotoxic substances among all heavy metals, but an increasing number of studies indicate that low-dose Cd can induce hormesis in some plants. However, the frequency of hormesis in various biomarkers (molecular, resistance, and damage markers) and their associated function in hormesis-generation are poorly understood. In this study, the heavy metal accumulator plant *Tillandsia ionantha* Planch. was exposed to 5 mM CdCl<sub>2</sub> with 6 different time periods. The trends of 18 biomarkers after Cd exposure were detected. The percentage for all non-monophasic responses based on dose-response modeling was higher (50%), in which seven (38.89%) biomarkers showed hormesis, indicating that hormesis effect can commonly occur in this plant. However, the occurrence frequency of hormesis in different types of biomarkers was different. Six Cd resistance genes, glutathione (GSH) among 6 resistance markers, and 0 damage markers showed hormesis. Factor analysis further showed that the 6 Cd resistance genes and GSH were positively intercorrelated in the first principal component. Therefore, heavy metal resistance genes and GSH may play an important role in the generation of hormesis. Our experiment shows that time-dependent non-monophasic responses, including hormesis, are activated by considerably high concentrations of Cd, presenting a strategy to cope with and potentially reduce the anticipated damage as the dose of stress increases over time.

### 1. Introduction

It is now widely understood that the response of organisms to stress are commonly not monophasic (linear) but non-monophasic and non-linear (Agathokleous et al., 2022). Hormesis refers to a non-linear, biphasic dose response that occurs when organisms are exposed to toxic substances with increasing of exposure or dose level, that is, stimulation or beneficial reactions are caused by low doses and inhibition or toxicity is caused by

\* Corresponding author.

E-mail address: [pengleep@qau.edu.cn](mailto:pengleep@qau.edu.cn) (P. Li).

<sup>1</sup> Jingyi Zhang and Zhen Tang are the co-first authors and made equal contributions to this work.

<http://dx.doi.org/10.1016/j.scitotenv.2023.164328>

Received 7 February 2023; Received in revised form 16 May 2023; Accepted 17 May 2023

Available online 19 May 2023

0048-9697/© 2023 Elsevier B.V. All rights reserved.

high doses (Calabrese et al., 2016). Although the recognition of hormesis has a long and controversial history (Calabrese, 2018), an increasing number of plants, animals and microorganisms show this feature when they are stressed by toxins at different concentrations or doses, indicating that the hormesis effect is a quite common phenomenon (Mushak, 2013; Sthijns et al., 2016; Sun et al., 2018; Agathokleous et al., 2020). In recognition of the accumulating evidence of hormetic responses, international regulatory authorities also formally consider the hormesis effect in environmental management decisions (Agathokleous et al., 2022).

Cadmium (Cd) is one of the most biotoxic substances among all heavy metals (Kushwaha et al., 2015), but an increasing number of studies have shown that low-dose Cd can induce some plants to produce hormesis (Carvalho et al., 2020). For example, low-concentration Cd treatment resulted in different degrees of biomass enhancement in *Lonicera japonica* (Jia et al., 2015), *Brassica napus* (Durenne et al., 2018), *Dianthus carthusianorum* (Muszynska et al., 2018), and *Polygonatum sibiricum* (Xie et al., 2021). Low-level Cd also induced an increase in catalase (CAT) and peroxidase (POD) content in *P. sibiricum* and an increase in superoxide dismutase (SOD) content in *Bletilla striata*, which ranged between 206 and 277 % (Yang et al., 2022). In the Cd-enriched plant *Celosia argentea*, three metal transport genes (HMA3, ABC15 and ATPase 4) are upregulated under Cd stress (Yu et al., 2023). Hence, various types of biomarkers, including damage, resistance and molecular biomarkers, can be used to reflect the hormesis effect of Cd (Carvalho et al., 2020).

To date, the generation mechanism of hormesis has not been uniformly explained (Muszynska and Labudda, 2019; Carvalho et al., 2020; Calabrese and Agathokleous, 2021; Erofeeva, 2022). Different theories such as overcompensation, overcorrection, DNA damage repair, receptor mechanisms and oxidative stress mechanisms have been used to explain the hormesis effect (Calabrese et al., 2016; Calabrese, 2018; Shahid et al., 2020; Chakrabarti and Mukherjee, 2022). Substances that can scavenge reactive oxygen species (ROS) or effectively chelate toxins, such as antioxidants, metal binding proteins, and their related functional genes have also been considered to play an important role in the generation of hormesis (Poschenrieder et al., 2013; Agathokleous et al., 2019).

Importantly, the frequency difference of stimulation or inhibition effects of different biomarkers is often closely related to the up- or down-regulation of the adaptive mechanism of the hormesis effect (Calabrese and Agathokleous, 2021). Therefore, it is a feasible method to explore the influence factors of the hormesis effect by analyzing the frequency difference of the hormesis effect in different types of biomarkers. Moreover, there are only a few studies evaluating the frequency of non-linear dose responses including hormesis in different types of biomarkers (Erofeeva, 2014, 2020; Belz and Sinkkonen, 2021).

*Tillandsia* spp. (Bromeliaceae) are epiphytic plants with the special property of growing in the air without needing soil (Benzing, 2000). They mainly use their leaves to absorb water and nutrients from the atmosphere, thus their leaves have a strong absorption capacity (Benz and Martin, 2006). A large number of studies have confirmed that different kinds of *Tillandsia* spp. can rapidly absorb and accumulate a variety of air pollutants, especially heavy metals (e.g. Hg, Cd, Pb, Ni, Cu, Cr, Zn), thus becoming a widely used accumulating indicator plant for monitoring changes in heavy metals (Calasans and Malm, 1997; Pignata et al., 2002; Vianna et al., 2011; Schreck et al., 2020; Sun et al., 2021a; Li et al., 2022).

*Tillandsia* spp. have shown different responses to heavy metal stress. After treatment with 2  $\mu\text{M}$   $\text{Cd}^{2+}$  solution for one month, four kinds of *Tillandsia* spp. did not exhibit obvious morphological damage and an increase in the content of glutathione (GSH), but the content of ROS and POD increased significantly (Kováčik et al., 2014). Studies of the changes in 8 biomarkers of *T. usneoides* treated with 10 concentrations of Hg and Pb revealed that with Hg concentrations varying from low to high, SOD activity first decreased and then increased, while the content of metallothionein (MT) first increased and then decreased (Sun et al., 2021b). With Pb concentrations ranging from low to high, the change trend of superoxide anion free radical ( $\text{O}_2^-$ ), SOD, and malondialdehyde (MDA) also conformed to the biphasic hormesis effect (Li et al., 2022). These results

confirmed that the hormesis effect exists in *Tillandsia* spp., which also indicates that heavy metals commonly affect accumulator plants to produce hormesis, and has important implications for remediation practices (Calabrese and Agathokleous, 2021; Agathokleous et al., 2023). However, whether Cd can induce hormesis in *Tillandsia* spp. as well as the frequency and function difference of different biomarkers in the hormesis effect have not been deeply explored.

In addition, in an adaptive hormetic response, not only the concentration but also the time/dose should be considered (Sthijns et al., 2016). It is known that chemically induced hormesis exhibits significant temporal variation, with an initial increase in the maximum stimulation followed by a significant decline but maintained at biologically beneficial enhanced levels (Agathokleous et al., 2020). Sthijns et al. (2016) consider that the quickest adaptive response to oxidative stress is direct enzyme modification, increasing GSH levels or activating GSH-dependent protective enzymes. However, a mechanistic understanding of time-dependent hormesis in plants is lacking.

In this study, *Tillandsia ionantha* Planch. plants were treated with Cd for different durations to analyze the frequency and function of various biomarkers in the hormesis effect. We hypothesized that a specific concentration of the heavy metal Cd can generate hormesis in *Tillandsia* spp. over time, and different types of biomarkers express different hormesis frequencies. Moreover, we assumed that related genes may play an important role in the generation of hormesis. Considering the known relative tolerance of *T. ionantha*, we became interested in examining whether this plant can respond non-linearly and hormetically to increasing doses of Cd exposures that are considerably higher than the current environmental ones. If such responses occur at increasing exposures that are considerably higher than the environmental, one may assume that non-linear and hormetic responses can widely occur at low exposures that are within the current environmental ranges.

## 2. Material and methods

### 2.1. Material

*Tillandsia ionantha* (Fig. 1) with a fresh weight of 25–30 g was selected as the material. Before each experiment, *T. ionantha* was cleaned, soaked in deionized water for 20 min, and then dried for 30 min at room temperature to achieve a similar initial status of the research material.

### 2.2. Cd treatment

As accumulative indicator plants of heavy metals, *Tillandsia* spp. have strong resistance to various heavy metals. Wannaz et al. (2011) placed *T. capillaris* plants into solutions of 10 mM  $\text{Ni}^{2+}$ ,  $\text{Cu}^{2+}$ ,  $\text{Pb}^{2+}$  and  $\text{Zn}^{2+}$  for 45 min, and the plants showed no symptoms of dying. Therefore, to determine the low Cd dose range for *T. ionantha*, one preliminary experiment was performed. With a 5 mM  $\text{CdCl}_2$  solution as the fixed stress concentration, *T. ionantha* was immersed in  $\text{CdCl}_2$  solution for 2 h per day, and the plant lasted for 15 days before it died. Therefore, 6 time periods were set in the formal experiments: 0, 1, 2, 3, 4 and 5 days. This one-day interval was selected based on the understanding that physiological hormesis is maximized within hours to one week and considering the lack of studies covering hormesis at this resolution of time responses (Moustakas et al., 2022a, 2022b). Identification of hormetic-like responses to such dose increase over time may imply the possibility that dose-response evaluations with several doses (including considerably smaller ones) covering the full dose-response continuum are expected to induce hormetic effects on identified hormesis-showing biomarkers. For each treatment, 3 *T. ionantha* plants were selected as 3 replicates. According to the daily watering method of *Tillandsia* spp., *T. ionantha* was soaked in Cd solution for 2 h at the same time every day. As the *Tillandsia* spp. belongs to the crassulacean acid metabolism (CAM) type of plants, and its stomata open at night (Benzing, 2000). The stress started at 18:00 pm and ended at 20:00 pm.

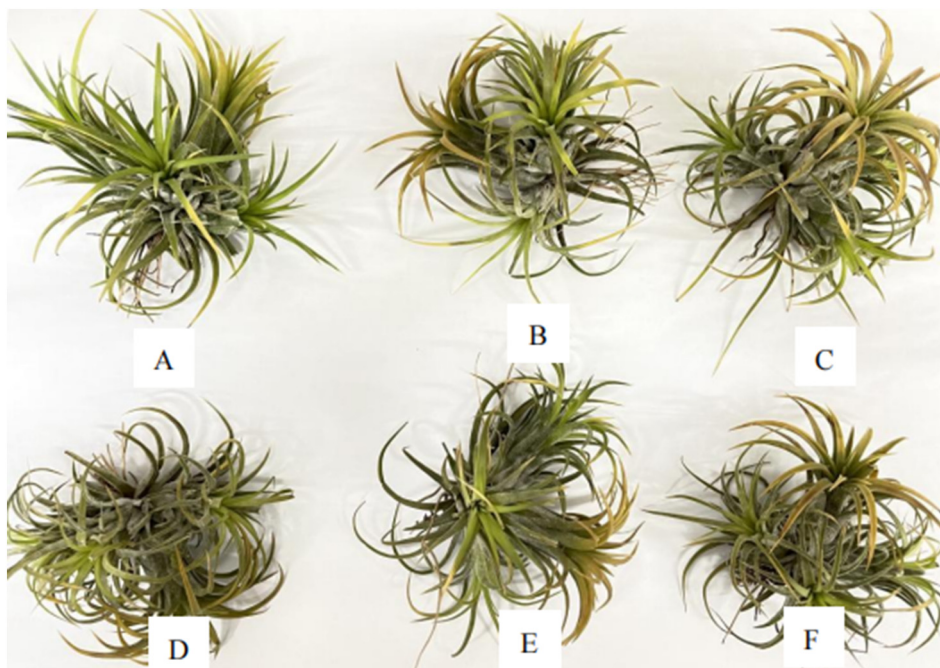


Fig. 1. *Tillandsia ionantha* treated with Cd for different duration.

Notes: A, without Cd treatment; B, after 1 day treatment; C, after 2 days treatment; D, after 3 days treatment; E, after 4 days treatment; F, after 5 days treatment.

### 2.3. Determination of Cd content in leaves

Cd extraction from plant leaves was performed according to the method exploited by Xie et al. (2021), and an ICP series (Optima 8000, PerkinElmer, USA) was utilized to measure the Cd content.

### 2.4. Determination of damage markers of *T. ionantha*

Biomass, MDA, relative electric conductivity and  $O_2^-$  were used as four indices of damage markers. The biomass is based on plant fresh weight. With reference to the methods of Li (2000), the relative electric conductivity was measured with a conductivity meter (DDS-307A, INESA, China), the MDA content was measured with the thiobarbituric acid (TBA) method, and the  $O_2^-$  content was measured with reference to Li et al. (2022).

### 2.5. Determination of resistance markers of *T. ionantha*

Six indices, i.e., SOD, POD, CAT, GSH, nonprotein sulfhydryl peptide (NPT), and phytochelatins (PCs) were used as resistance markers. The leaf SOD activity was determined by the nitrogen blue tetrazole method, the CAT activity was determined by the ultraviolet absorption method, and the POD activity was determined by the guaiacol method (Li, 2000). The content of GSH was determined with reference to Li et al. (2022).

The content of NPT was determined by DTNB colorimetry. One gram of fresh plant sample was weighed and placed in a mortar. Six milliliters of precooled ( $4^\circ\text{C}$ ) 5% sulfosalicylic acid solution was added, and the solution was ground to the homogenate in an ice bath, and then centrifuged at 10000 rpm at  $4^\circ\text{C}$  for 20 min. The supernatant was used for NPT determination. DTNB was the developer, and the same amount of solution without DTNB was used as the control. The light absorption value (A<sub>412</sub>) was measured at 412 nm and expressed in  $\text{mmol}\cdot\text{g}^{-1}\text{FW}$  (FW is the fresh weight).

The difference method is adopted for the content of PCs. The PC content was calculated as the total amount of NPT - the content of GSH.

### 2.6. Expression analysis of genes related to Cd resistance

After being treated with Cd, *T. ionantha* was sequenced according to the gene sequencing results of the related plant (in the same family)

*Ananas comosus* (L.) Merr. (Ming et al., 2015). All 9 genes related to Cd resistance in pineapple (Table 1) were selected to analyze their expression in *T. ionantha* leaves. These genes are associated with proteins containing PLAC8 motifs, which are rich in cystine and have various functions in promoting growth, antioxidants and detoxification. The reference gene was 18S. The RNA of leaves was extracted by the TRIzol method, and the cDNA was synthesized by using the full gold TransScriptR II All in One First Strand cDNA Synthesis SuperMix for PCR kit. Quantitative PCR primers were designed using the Primer Blast function of the NCBI website. Using cDNA as a template, each gene was detected by fluorescence quantitative PCR. The results were calculated by the  $2^{-\Delta\Delta Ct}$  method. The control sample was corrected to 1 as the relative expression amount, and the processed material data were its relative multiple.

### 2.7. Statistical analysis

All the above experiments were repeated 3 times, and the data were statistically analyzed using SPSS 23.0 (IBM, USA). Normal distribution and variance homogeneity of the data were first checked. One-way ANOVA followed by Tukey's HSD post hoc test was used to test for significant differences among groups treated with different doses of Cd, and  $p < 0.05$  indicated that there was a significant difference. A correlation analysis was carried out for all markers after Cd stress, expressed by the Pearson correlation coefficient, and a correlation heatmap was made using Origin software. Then, a factor analysis was carried out with 14 resistance indices and molecular indices.

Different responses to Cd treatment were expressed as a percent increase or decrease relative to the control exposure. Each dose-response relationship was classified following the model-fitting Dr-Fit software (Di Veroli et al., 2015). The best model is selected according to the Akaike information criterion (AIC). The lower the AIC value is, the higher the model fitness is. The model includes four types: 1) monophasic inhibition effect; 2) biphasic effect (two inhibition effects); 3) biphasic hormesis effect (one inhibition effect + one stimulation effect); 4) multiphasic effect (2 inhibition effects + 1 stimulation effect or 1 inhibition effect + 2 stimulation effects or multiple inhibition or stimulation effects).

**Table 1**  
Cd resistance related genes and primer sequences.

Target gene	Primer sequence	Fragment length (bp)	Annealing temperature (°C)
Aco013305.1 (G1)	F:5'GGTGTGCGCACTCGGTCTA3' R:5'TCCGCTGGTGGCTCATAG 3'	19	58.8
Aco014425.1 (G2)	F:5' AAACCATGCTTCTTCCA 3' R:5' ATTGCCGACCCCTCATAGA 3'	18	53.3
Aco018130.1 (G3)	F:5'GTAAGACCACAGCAGCAC 3' R:5' TCTATGTACGCAATCAG 3'	18	47.9
Aco000249.1 (G4)	F:5'ATTGTATGCTTGTGGCTAG 3' R:5'CCGTCACGCAGAGTATCA 3'	20	50.7
Aco005063.1 (G5)	F:5'TTGCCACTGCTTCTGTAC 3' R:5'AGACTCCTTCTGTTTCG 3'	18	48.8
Aco001065.1 (G6)	F:5' TGCGTTGTATCAGGTTGT 3' R:5'CAGAGCAGCCTTCATTAC 3'	18	49.0
Aco003013.1 (G7)	F:5' TTCGACCCAAACTCATC 3' R:5'GGCACCAGCAAGTCAAGC 3'	18	53.0
Aco002708.1 (G8)	F:5' TGTATCTGCTCCTCCTC 3' R:5'TTCCCACTTCGTTTATTTC 3'	18	49.3
Aco001066.1 (G9)	F:5'AAAAGACGCTGAACGATA 3' R:5'TGCCACCCTACAAATACA 3'	18	48.4

### 3. Results

#### 3.1. Cd content in *T. ionantha* leaves

The Cd content in *T. ionantha* leaves increased linearly with increasing duration of Cd stress (Fig. 2A). The leaf Cd content of the control *T. ionantha* plants was as low as  $2.11 \pm 0.34 \mu\text{g}\cdot\text{g}^{-1}$ . After one day of Cd treatment, the Cd content in the leaves increased significantly to  $269.34 \pm 7.76 \mu\text{g}\cdot\text{g}^{-1}$ . With the increase in treatment days, the Cd content in *T. ionantha* leaves continued to increase and significantly reached  $674.44 \pm 87.41 \mu\text{g}\cdot\text{g}^{-1}$  after 5 days of treatment.

#### 3.2. Effect of cd on the damage markers of *T. ionantha*

There was no obvious visible injury (symptoms) on *T. ionantha* leaves after treatment with Cd, and thus, there was no observable difference in morphology among Cd dose treatments (Fig. 1).

##### 3.2.1. Biomass

The biomass of *T. ionantha* without Cd treatment was  $4.54 \pm 0.81 \text{ g}$ . After one day of Cd treatment, the biomass increased to  $5.40 \pm 0.93 \text{ g}$ . Then, it decreased, reaching the lowest value ( $3.22 \pm 0.71 \text{ g}$ ) on the fourth day of treatment (Fig. 2B), and then increased to  $4.04 \pm 0.74 \text{ g}$  on the fifth day. However, statistical analysis showed that there was no significant difference in biomass content after different Cd treatments (Fig. 2B). The fitting of the dose-response curve showed that the biomass of *T. ionantha* was more consistent with the monophasic dose-response model (AIC = 6.61, Table S1).

##### 3.2.2. MDA content

The MDA content in the leaves of control *T. ionantha* plants was  $1.07 \pm 0.18 \text{ mmol}\cdot\text{g}^{-1}$ . Although Cd stress tended to decrease the content of MDA in leaves (Fig. 2C), there were no significant differences ( $p < 0.05$ ). The dose-response relationship of the MDA content was more consistent with the monophasic dose-response model (AIC = 27.92, Table S1).

##### 3.2.3. Relative electrical conductivity

The relative electrical conductivity of *T. ionantha* leaves after Cd treatment was significantly increased after 4 days of exposure to Cd compared to the control (Fig. 2D). Moreover, it was significantly higher after 3, 4, and 5 days of treatment than after 2 days of exposure. The dose-response fitting shows that the relative conductivity of *T. ionantha* is more consistent with the monophasic dose-response model (AIC = 33.6), although the

biphasic hormetic model also showed a relatively good fit (AIC = 36.7) (Table S1).

#### 3.2.4. $\text{O}_2^-$ content

The content of  $\text{O}_2^-$  tended to vary; however, there was no statistically significant difference among Cd treatments (Fig. 2E). The dose-response curve of the  $\text{O}_2^-$  content is more consistent with the monophasic model (AIC = 34.8), albeit the biphasic hormetic also showed a similar performance (AIC = 36.2) (Table S1).

### 3.3. Effect of Cd on the resistance index of *T. ionantha* leaves

#### 3.3.1. SOD activity

The SOD activity in *T. ionantha* leaves did not differ significantly between the control and the different Cd treatments (Fig. 3A). However, it was significantly lower after 4 days of treatment than after 1 day of treatment. The dose-response curve was more consistent with the monophasic model (AIC = 30.2), although the biphasic hormetic model also displayed a similar performance (AIC = 32.0) (Table S1).

#### 3.3.2. CAT activity

The CAT activity in *T. ionantha* leaves did not differ significantly among Cd treatment conditions (Fig. 3B). The model fitting dose-response curve was more consistent with the monophasic model (AIC = 28.03, Table S1).

#### 3.3.3. POD activity

The POD activity in *T. ionantha* significantly decreased after one day of treatment and then significantly increased to levels similar to the control on Day 3 (Fig. 3C). The dose-response model was more consistent with the biphasic model (AIC = 33.6), and the monophasic model ranked second in terms of fitting (AIC = 36.5) (Table S1). There was nowhere an increase over the control and, while this is a biphasic response (rightly captured by the modeling) mathematically, based on the definition (biologically) and current understanding of hormesis the dose response is not considered hormetic in this study. However, it should be noted that such molecules display highly pleiotropic responses over time, and a denser dose/time component might be needed to reveal whether a significant increase would be yielded.

#### 3.3.4. GSH content

The GSH content in *T. ionantha* leaves tended to increase after Cd treatments, and the increase was statistically significant on Days 1 and 5 compared to the control (Fig. 3D). The biphasic hormesis model displayed the best fit to the GSH content dose-response data (AIC = 34.90, Table S1).

#### 3.3.5. NPT content

The content of NPT decreased significantly after 1–4 days of Cd treatment relative to the control and increased again to levels similar to the control after 5 days of Cd treatment (Fig. 3E). The fitting of the dose-response curve shows that the biphasic model best fits the NPT dose-response data (AIC = 33.61, Table S1). Similar to the changing trend in POD, there was nowhere an increase over the control. So the dose response of NPT is not considered hormetic in this study.

#### 3.3.6. PC content

The PC content in *T. ionantha* was significantly decreased after 1–5 days of Cd exposure compared to the control (Fig. 3F). The fitting of the dose-response curve indicated that the relationship between PC content and Cd dose was best described by the monophasic model (AIC = 30.4); the biphasic hormetic model showed the second best fit (AIC = 32.0) (Table S1).

### 3.4. Expression of cd-related resistance genes

Among all 9 Cd resistance genes screened from *A. comosus*, 8 could be expressed in *T. ionantha*, namely G1–G8 (Fig. 4). With the increase

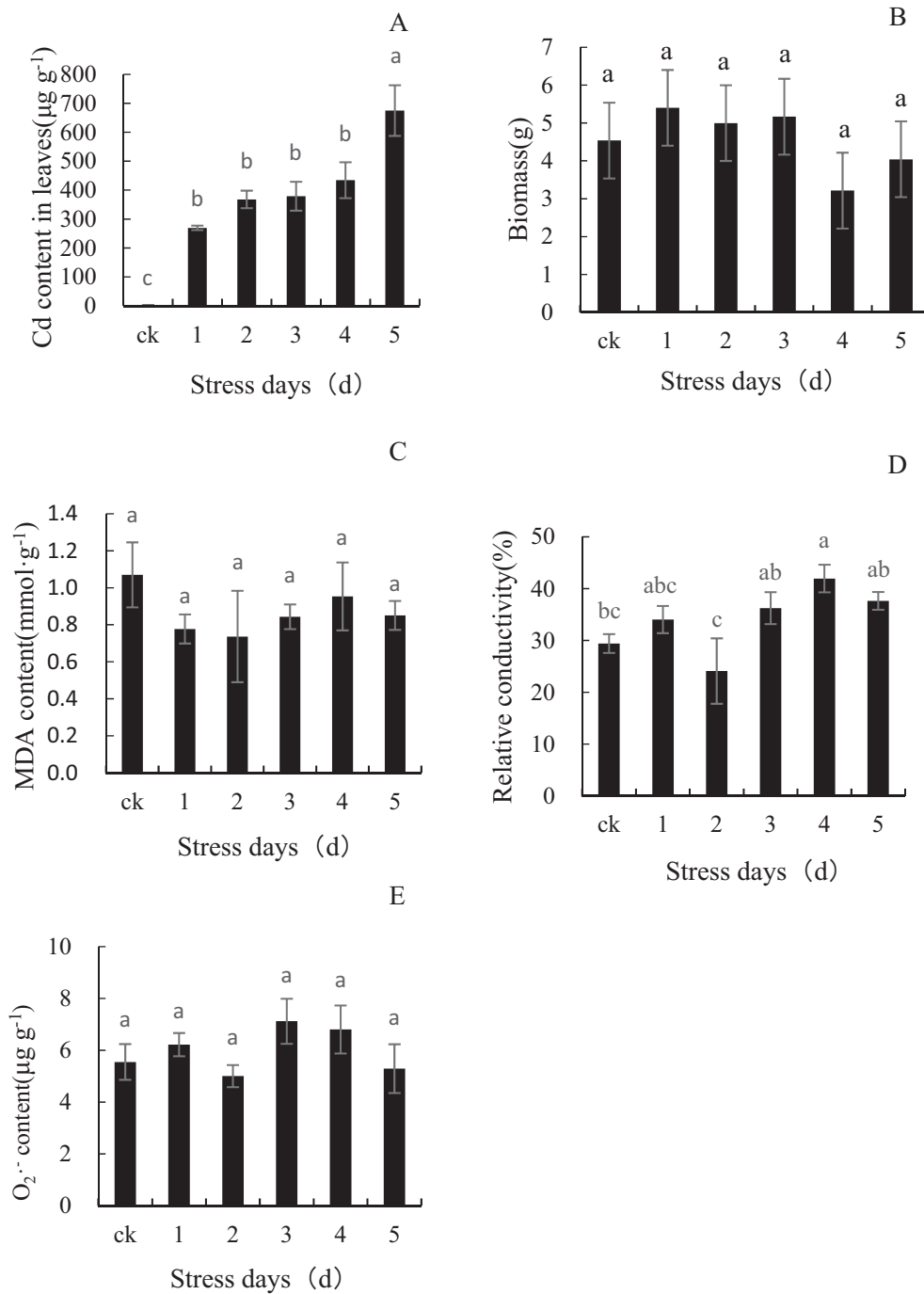


**Fig. 2.** Changes of Cd content and four damage markers in *Tillandsia ionantha* after Cd treatment.

Notes: MDA, malondialdehyde; O<sub>2</sub><sup>·-</sup>, superoxide anion radical. The data are means ± SD (n = 3). Different small letters indicate a significant difference between different times for treatment with the same Cd concentration at the level of 0.05, whereas same small letters indicate no significant difference.

in Cd dosage, the change trend of the expression amount of seven genes (all genes except for G3) was similar, but the change amplitude was different. Commonly, the expression of these seven genes increased significantly after 2–4 days of stress, depending on the gene, and then decreased to levels similar to or lower than the control on the fifth day of stress (Fig. 4). The dose-response curve fitting shows that the response of the genes G1, G2, G3, G4, G6 and G7 is best described by the biphasic hormesis model while the relationships of genes G5 and G8 are more consistent with the monophasic model (Table S1).

### 3.5. Frequency analysis of hormesis effect in different types of markers

Dr-Fit analysis showed that among the four dose-response types, only two types of dose-response models showed the best fit, namely, the monophasic and biphasic models (Table S1). But based on the definition and current understanding of hormesis, the biphasic dose response of POD and NPT is not considered hormetic in this study. So for all 18 markers (Fig. S1), the occurrence rate of biphasic response as the best fit model was 50 % and hormesis was 38.89 %. However, the rate was different for different types of markers. Among the 8 Cd-related resistance genes, 6 showed hormesis

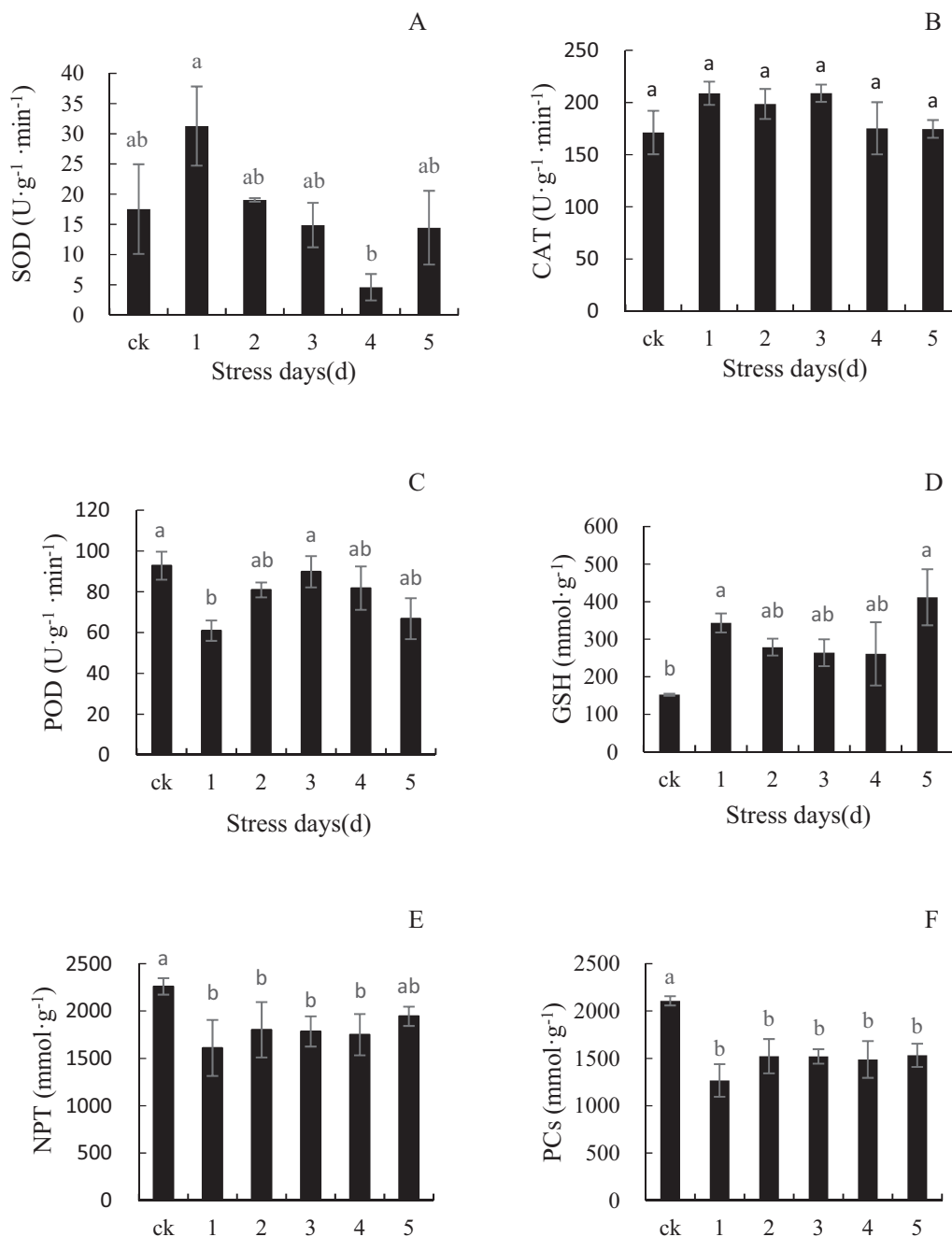


**Fig. 3.** Changes of resistance markers of *Tillandsia ionantha* after Cd stress.

Note: SOD, superoxide dismutase; CAT, catalase; POD, peroxidase; GSH, glutathione; NPT, non-protein sulphhydryl peptide; PCs, phytochelatins. The data are means  $\pm$  SD ( $n = 3$ ). Different small letters indicate a significant difference between different times for treatment with the same Cd concentration at the level of 0.05, whereas same small letters indicate no significant difference.

effects, accounting for 75 %. Among the resistance indices (SOD, CAT, POD, PCs, GSH, NPT), there was only GSH showing a hormesis effect, accounting for 16.67 %. Among the four damage markers of biomass,  $O_2^-$ , MDA and electrical conductivity, no hormesis effect was observed.

### 3.6. Sensitivity analysis of different markers to hormesis effect

#### 3.6.1. Correlation analysis

The correlation among the biomarkers of *T. ionantha* is shown in Fig. 5. Overall, the proportion of markers with a significant correlation is small. Except for G3 and G6, the other six genes were positively intercorrelated. In addition to G6, GSH was also positively correlated with 7 genes, while

biomass and POD were negatively correlated with all 8 genes, and the correlation was statistically significant for G7 and G8.

#### 3.6.2. Factor analysis

Factor analysis showed that three principal components could be extracted from 14 markers, and the cumulative proportion to the total variance was 88.49 %, meaning that these three principal components could retain most of the information of the original indicators. Table 2 shows that the contribution rate of the first principal component is 46.25 %, mainly consisting of GSH (0.902) and 6 genes, which have a high positive load, while POD (-0.819) has a high negative load. The contribution rate of the second component was 28.88 %, mainly consisting of NPT,

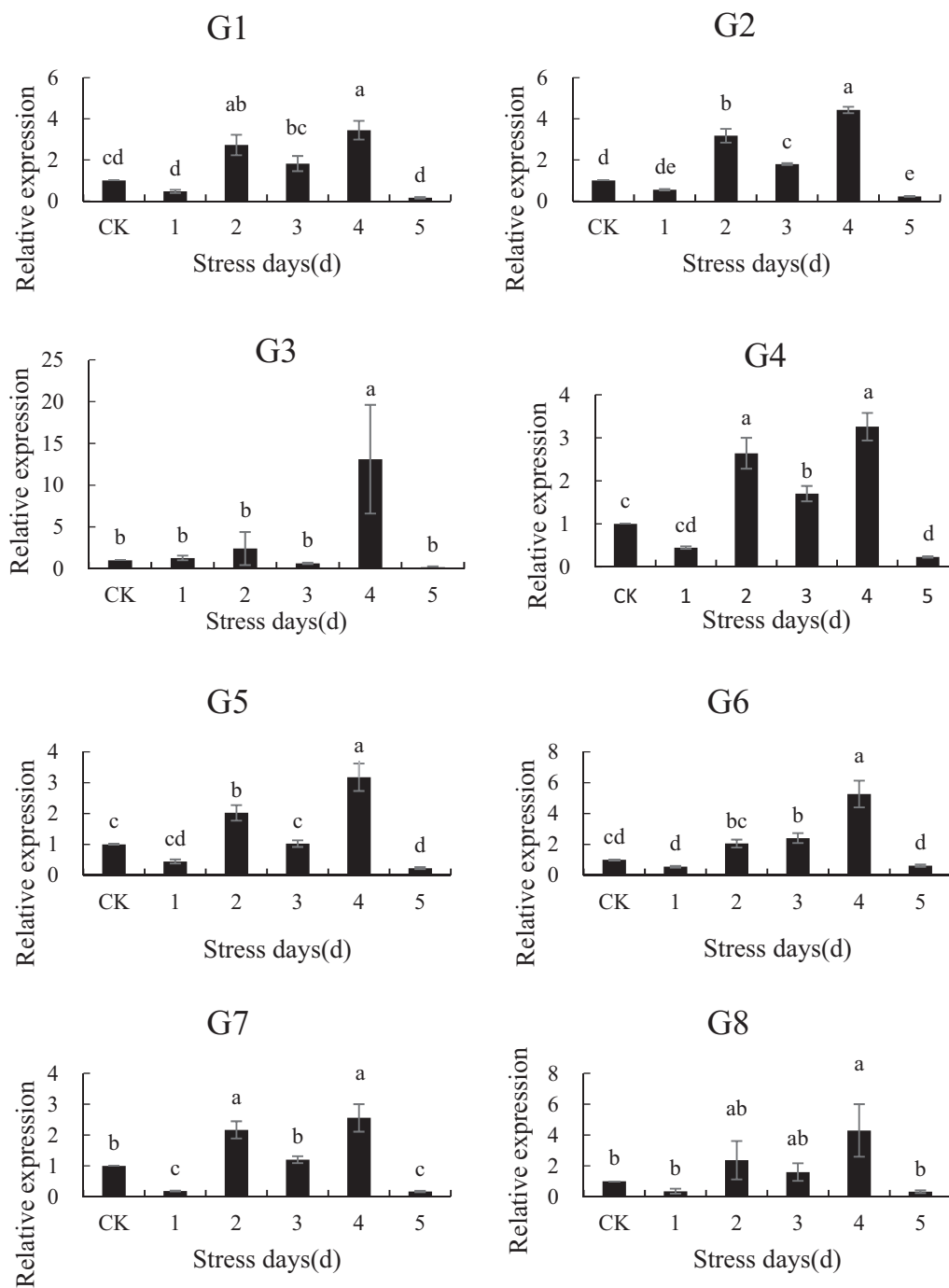


**Fig. 4.** Expression analysis of Cd related resistance genes in *Tillandsia ionantha* after Cd stress.

Notes: G1, Aco013305.1; G2, Aco014425.1; G3, Aco018130.1; G4, Aco000249.1; G5, Aco005063.1; G6, Aco001065.1; G7, Aco003013.1; G8, Aco002708.1. The data are means  $\pm$  SD (n = 3). Different small letters indicate a significant difference between different times for treatment with the same Cd concentration at the level of 0.05, whereas same small letters indicate no significant difference.

PCs (0.722), CAT ( $-0.896$ ) and SOD ( $-0.697$ ). However, NPT and PCs had a large positive load, while CAT and SOD had a negative load. The third major component included G3 and G6 genes. G6 had a higher positive load, while G3 had a negative load.

#### 4. Discussion

##### 4.1. The resistance and response styles of *Tillandsia* spp. to Cd

As heavy metal-accumulating indicator plants, *Tillandsia* spp. can rapidly accumulate heavy metals, such as Hg, Ni, Cu, Pb, and Zn (Calasans

and Malm, 1997; Pignata et al., 2002; Vianna et al., 2011; Schreck et al., 2020; Sun et al., 2021a). Kováčik et al. (2012) showed that the Cd content exceeded  $400 \mu\text{g}\cdot\text{g}^{-1}$  after 2 months of treatment of *T. albida* with  $10 \mu\text{M}$  CdCl<sub>2</sub> and reached  $200 \mu\text{g}\cdot\text{g}^{-1}$  after 30 days of treatment of *T. capillaris* with  $2 \mu\text{M}$  CdCl<sub>2</sub> (Kováčik et al., 2014). In this study, the concentration of Cd was considerably higher ( $5 \text{ mM}$ ; 500–2500-fold), but the treatment time was shorter (5 days). With the extension of Cd treatment time, the Cd content in *T. ionantha* leaves increased, basically linearly, reaching  $674.44 \mu\text{g}\cdot\text{g}^{-1}$  after 5 days, which indicated that *Tillandsia* spp. could accumulate Cd rapidly and effectively. It is worth noting that under such a high concentration treatment, *T. ionantha* had no obvious damage symptoms

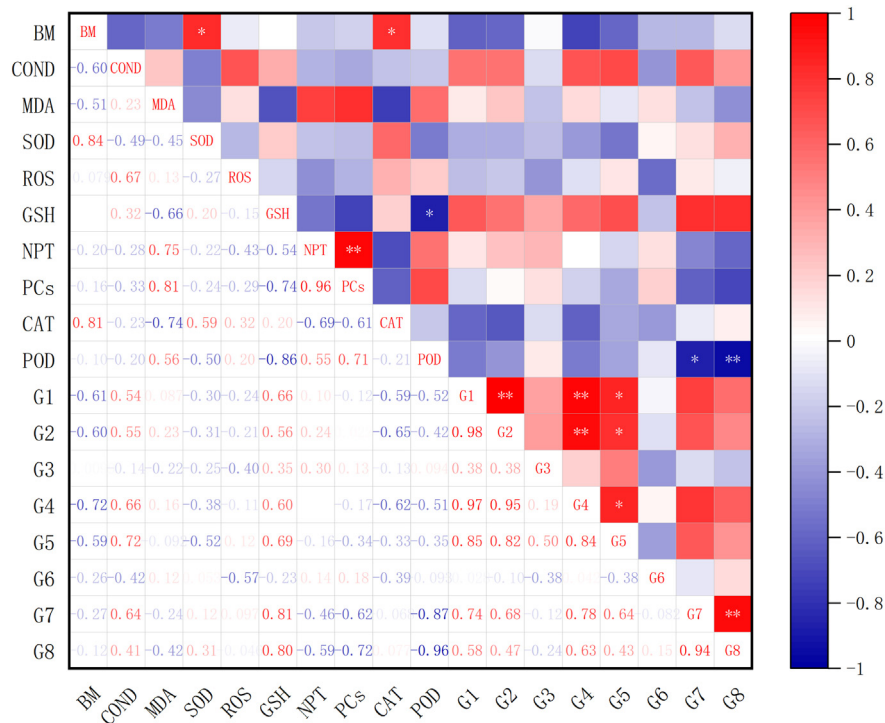


**Fig. 5.** Correlation analysis of different biomarkers of *Tillandsia ionantha* after Cd treatment for 1–5 days. Notes: BM, biomass; COND, conductivity; MDA, malondialdehyde; SOD, superoxide dismutase; O<sub>2</sub><sup>-•</sup>, superoxide anion radical; CAT, catalase; POD, peroxidase; GSH, glutathione; NPT, non-protein sulfhydryl peptide; PCs, phytochelatins; G1, Aco013305.1; G2, Aco014425.1; G3, Aco018130.1; G4, Aco000249.1; G5, Aco005063.1; G6, Aco001065.1; G7, Aco003013.1; G8, Aco002708.1. Red represents positive correlation, blue represents negative correlation, color depth represents the strength of correlation, lower left corner value is Pearson correlation coefficient, upper right corner \* represents significant correlation at 0.05 level, and \*\* represents significant correlation at 0.01 level.

(Fig. 1), indicating that *Tillandsia* spp. have strong resistance to the heavy metal Cd, which is also similar to the results of Kováčik et al. (2012, 2014). However, it should be mentioned that the exposure lasted 2 h per day, which allowed plants to undergo a postconditioning process and thus potentially promoted a more effective alleviation of stress compared to continuous exposure (Calabrese et al., 2020).

The response of organisms to oxidative stress is very complex. Recent studies have shown that not only biphasic but also even polyphasic effects occur in some plants, animals and microorganisms (Choi et al., 2012; Erofeeva, 2018; Fan et al., 2021; Kong et al., 2016; Li et al., 2022; Wang et al., 2021), although such evidence is sporadic due in part to the high requirements of an increased number of doses. Such nonmonophasic effects were characterized as a paradox (Erofeeva, 2018). Currently, there are three widely recognized ways by which organisms respond to stressors,

**Table 2**  
Factor analysis with 14 resistance and molecular biomarkers in *Tillandsia ionantha* after Cd stress.

Biomarkers	Component 1	Component 2	Component 3
ACO003013 (G7)	0.944	-0.165	0.174
Glutathione (GSH)	0.902	-0.26	-0.225
ACO000249.1 (G4)	0.865	0.459	0.161
ACO002708 (G8)	0.864	-0.382	0.326
ACO013305.1 (G1)	0.864	0.492	0.056
Peroxidase (POD)	-0.819	0.457	-0.236
ACO005063.1 (G5)	0.815	0.382	-0.383
ACO014425.1 (G2)	0.787	0.583	0.04
Catalase (CAT)	-0.154	-0.896	-0.408
Non-protein sulfhydryl peptide (NPT)	-0.388	0.803	0.159
Phytochelatin (PCs)	-0.59	0.722	0.197
Superoxide dismutase (SOD)	-0.036	-0.697	0.224
ACO001065 (G6)	-0.114	0.052	0.848
ACO018130.1 (G3)	0.184	0.445	-0.672

namely a linear-no-threshold (LNT) response, a linear response with threshold, and hormesis, a biphasic response (Agathokleous et al., 2019, 2020; Costantini and Borremans, 2019). Although most hormetic responses are observed based on different toxin concentrations (Agathokleous et al., 2019, 2020), time-dependent hormesis is found in several dose-response relationships (Sthijns et al., 2016; Moustakas et al., 2022a, 2022b). Our experiment also shows that time-dependent hormetic mechanisms are activated by considerably high concentrations of Cd, presenting an ecological strategy to reduce the anticipated damage as the dose of stress increases over time. Although there were four patterns in the dose-effect model, there were two main dose-response patterns in various biomarkers of *T. ionantha* after Cd stress treatment at different times, monophasic and biphasic (Table S1).

Erofeeva (2020) used multiple indices to detect the frequency of different types of dose effects in five different forms of plants (*Betula pendula*, *Tilia cordata*, *Taraxacum officinale*, *Triticum aestivum*, *Pisum sativum*) under heavy metal, herbicide, formaldehyde and salt stress and found that the frequency of nonmonophasic responses was higher than that of monophasic dose effects. However, Erofeeva (2020) found that in nonsingle-phase dose effects, the hormesis effect did not dominate, but other tri- or multiphasic “paradoxical effects” dominated. In contrast, in our results, the hormesis effect dominated in the nonmonophasic effect (Fig. S1), which further hints at the high occurrence and superiority of the hormesis effect. However, it should be noted that is required multiple dose effect fitting to form a curve to determine whether there are multiple effects between organisms and toxins (Katsnelson et al., 2021).

**4.2. The frequency of hormesis and the associated function of different types of biomarkers**

This study further revealed that the frequency of hormesis in different types of markers considerably differed. Molecular or resistance markers



promote the generation of hormesis and indicate the existence of hormesis (Agathokleous et al., 2020; Ma et al., 2022). In this study, Cd resistance genes had the highest frequency of hormetic response occurrence, followed by resistance substances (Fig. S1), indicating that both genes and antioxidants, especially the genes, may play a greater role in the process of producing hormetic effect. However, due to hormetic trade-offs, stress does not always cause synchronous improvement of different plant parameters (Erofeeva, 2022). The nonsignificant changes in damage markers compared to the control (Fig. 2) are consistent with hormetic trade-off 2 (hormesis of some plant traits with invariability in others), which is observed more often than hormetic trade-off 1 (hormesis accompanied by the deterioration of some plant traits) (Erofeeva, 2022).

Some scholars believe that although the potential mechanisms of toxic stimulation are diverse, they are all based on changes at the molecular level, regardless of the cellular or individual levels (Carvalho et al., 2020). Therefore, this leads to the DNA damage repair theory that explains the hormesis effect (Mägdefrau et al., 2019). Some studies have shown that some biological stimulators maintain homeostasis by activating gene expression in plants as a way to adapt to stress (Vargas-Hernandez et al., 2017; Dong et al., 2020). Overexpressing GSH1 and AsPCS1 increases the tolerance and accumulation of Cd in *Arabidopsis thaliana* (Guo et al., 2008). In this experiment, there were 9 Cd resistance genes in the related species of *A. comosus* (Ming et al., 2015), 8 of which were successfully amplified in *T. ionantha*, and 6 genes showed obvious hormesis effects (Table S1). In the factor analysis (Table 2), six genes also belonged to the first principal component. Therefore, the Cd resistance genes are principal sensitive markers of the hormesis effect and the main induction for the hormesis effect.

Some resistant substances also play an important role in the production of hormesis (Poschenrieder et al., 2013; Carvalho et al., 2020). Antioxidant enzymes such as SOD, CAT and POD, as defense mechanisms in plants, can effectively eliminate ROS produced by plants (Gill and Tuteja, 2010). GSH and PCs, as nonprotein sulfhydryl compounds in plants, can chelate with Cd<sup>2+</sup> and form complexes that exist in the cytoplasm or are transported to vacuoles, thus slowing the toxicity of Cd to plants or enhancing the tolerance of plants to Cd (Adamis et al., 2007). In this experiment, GSH in *T. ionantha* showed obvious hormesis effect after Cd treatment, indicating that GSH was sensitive marker of the hormesis effects among the six resistance markers tested, which also suggested that its changes promoted the occurrence of hormesis effects to some extent.

In the face of Cd stress, plants have evolved various defense mechanisms, in which GSH is considered to play a central role (Jozefczak et al., 2012). As a widely distributed tripeptide compound, GSH is composed of glutamic acid, cysteine and glycine, and several GSH molecules are polymerized to form phytochelatin (PCs). The sulfhydryl group (-SH) in GSH and PC cysteine has a high affinity for metals, so it becomes a key chelating agent for removing heavy metals (Ma et al., 2022). GSH is rich in cysteine, and the six selected genes (Table 1) are also rich in cysteine (Ming et al., 2015). Therefore, the synergistic relationship between GSH and Cd resistance genes in the production of hormesis deserves further study.

This study included a range of increasing Cd exposures that are well above the current environmental exposures (but selected based on a preliminary assay; see methods). A limitation of this approach is that the plants, while showing non-linear and hormetic responses, they could be under severe oxidative stress, where the adaptive hormetic capacity of the plants was considerably lowered. This might mean a considerably lower potential for expression of dynamic, non-linear and especially hormetic responses, relative to what might have been observed if several environmental and sub-environmental exposures were studied. Therefore, the percentages of the non-linear responses, and particularly the hormetic responses, might have been underestimated in this study. Nevertheless, these results provide an important basis to design and execute new studies with considerably lower doses of Cd administered to this plant than those applied in this study. The results suggest that further research with a range of smaller concentrations and exposure durations is warranted for a more critical and comprehensive analysis of the actual hormetic responses of this plant.

Finally, this study showcases a discrepancy in the classification of hormesis between mathematical dose-response modeling (using classic dose-response analysis software) and based on the biological definition of hormesis. Specifically, this study indicates that a biphasic dose response with one inhibition and one stimulation, classified based on dose-response modeling, is not necessarily a hormetic response based on the definition and current understanding of hormesis in the biology literature. Therefore, caution should be exercised to comply with the definition and understanding in biology when characterizing a dose response as hormesis based on mathematic dose-response model.

## 5. Conclusion

The non-linear response, and especially the hormesis effect, helps plants adapt to various stressors, which is expected to provide new perspectives for improving phytoremediation capabilities in the future. After Cd stress of different durations, 7 of the 18 biomarkers of *T. ionantha* showed the hormesis effect, which further explained the common occurrence of the time-dependent hormesis effect induced by Cd. However, there are obvious differences in the frequency of the hormesis effect among the three types of biomarkers. The hormesis frequency of molecular markers is higher than that of resistance markers, and no damage markers show hormesis. On the one hand, the hormesis frequency of molecular markers reflects the different sensitivity of different markers to the hormesis effect, and on the other hand, it also suggests that changes at the molecular level may more likely influence the generation of the hormesis effect. Nevertheless, the low-dose excitatory effect of a toxicant may be the result of multiple mechanisms. Further research on how different mechanisms are expressed sequentially and interactively will be of great significance to reveal the influence factors of the hormesis effect.

## CRedit authorship contribution statement

Jingyi Zhang and Zhen Tang performed the experiments, Evgenios Agathokleous and Guiling Zheng analyzed the results, Peng Li designed the experiments and analyzed the results. All authors write, review and edit the manuscript.

## Data availability

Data will be made available on request.

## Declaration of competing interest

The authors declare that they have no known competing financial interests or personal relationships that could have appeared to influence the work reported in this paper.

## Acknowledgements

This study was funded by the National Natural Science Foundation of China (No. 32271699).

## Appendix A. Supplementary data

Supplementary data to this article can be found online at <https://doi.org/10.1016/j.scitotenv.2023.164328>.

## References

- Adamis, P.D.B., Panek, A.D., Eleutherio, E.C.A., 2007. Vacuolar compartmentation of the cadmium glutathione complex protects *Saccharomyces cerevisiae* from mutagenesis. *Toxicol. Lett.* 173 (1), 1–7.
- Agathokleous, E., Kitao, M., Calabrese, E.J., 2019. Hormesis: a compelling platform for sophisticated plant science. *Trends Plant Sci.* 24 (4), 318–327.
- Agathokleous, E., Kitao, M., Calabrese, E.J., 2020. Hormesis: highly generalizable and beyond laboratory. *Trends Plant Sci.* 25 (11), 1076–1086.

- Agathokleous, E., Barcelo, D., Aschner, M., Azevedo, R.A., Bhattacharya, P., Costantini, D., et al., 2022. Rethinking subthreshold effects in regulatory chemical risk assessments. *Environ. Sci. Technol.* 56, 11095–11099.
- Agathokleous, E., Liu, C.J., Calabrese, E.J., 2023. Applications of the hormesis concept in soil and environmental health research. *Soil Environ. Health* 1 (1), 100003.
- Belz, R.G., Sinkkonen, A., 2021. Low glyphosate doses change reproduction and produce tolerant offspring in dense populations of *Hordeum vulgare*. *Pest Manag. Sci.* 77, 4770–4784.
- Benz, B.W., Martin, C.E., 2006. Foliar trichomes, boundary layers, and gas exchange in 12 species of epiphytic *Tillandsia* (Bromeliaceae). *J. Plant Physiol.* 163 (6), 648–656.
- Benzing, D.H., 2000. Bromeliaceae: Profile of an Adaptive Radiation. Cambridge University Press.
- Calabrese, E.J., 2018. Hormesis: path and progression to significance. *Int. J. Mol. Sci.* 19 (10), 2871.
- Calabrese, E.J., Agathokleous, E., 2021. Accumulator plants and hormesis. *Environ. Pollut.* 274, 116526.
- Calabrese, E.J., Dhawan, G., Kapoor, R., Iavicoli, I., Calabrese, V., 2016. Hormesis: a fundamental concept with widespread biological and biomedical applications. *Gerontology* 62 (5), 530–535.
- Calabrese, E.J., Mattson, M.P., Dhawan, G., Kapoor, R., Calabrese, V., Giordano, J., 2020. Hormesis: a potential strategic approach to the treatment of neurodegenerative disease. *Int. Rev. Neurobiol.* 155, 271–301.
- Calasans, C.F., Malm, O., 1997. Elemental mercury contamination survey in a chlor-alkali plant by the use of transplanted Spanish moss, *Tillandsia usneoides* (L.). *Sci. Total Environ.* 208 (3), 165–177.
- Carvalho, M.E.A., Castro, P.R.C., Azevedo, R.A., 2020. Hormesis in plants under Cd exposure: from toxic to beneficial element? *J. Hazard. Mater.* 384, 121434.
- Chakrabarti, M., Mukherjee, A., 2022. Metallo-adaptive response: a unique survival strategy of plants under genotoxic stress. *Nucleus* 65, 99–106.
- Choi, V.W.Y., Yum, E.H.W., Konishi, T., Oikawa, M., Cheng, S.H., Yu, K.N., 2012. Triphasic low-dose response in zebrafish embryos irradiated by microbeam protons. *J. Radiat. Res.* 53 (3), 475–481.
- Costantini, D., Borremans, B., 2019. The linear no-threshold model is less realistic than threshold or hormesis-based models: an evolutionary perspective. *Chem. Biol. Interact.* 301, 26–33.
- Di Veroli, G.Y., Fornari, C., Goldlust, I., Mills, G., Koh, S.B., Bramhall, J.L., Richards, F.M., Jodrell, D.I., 2015. An automated fitting procedure and software for dose-response curves with multiphasic features. *Sci. Rep.* 5, 14701.
- Dong, C., Wang, G., Du, M., Niu, C., Zhang, P., Zhang, X., 2020. Biostimulants promote plant vigor of tomato and strawberry after transplanting. *Sci. Hortic.* 267, 109355.
- Durenne, B., Druart, P., Blondel, A., Fauconnier, M.L., 2018. How cadmium affects the fitness and the glucosinolate content of oilseed rape plantlets. *Environ. Exp. Bot.* 155, 185–194.
- Erofeeva, E.A., 2014. Hormesis and paradoxical effects of wheat seedling (*Triticum aestivum* L.) parameters upon exposure to different pollutants in a wide range of doses. *Dose-Response* 12 (1), 121–135.
- Erofeeva, E.A., 2018. Hormesis and paradoxical effects of pea (*Pisum sativum* L.) parameters upon exposure to formaldehyde in a wide range of doses. *Ecotoxicology* 27 (5), 569–577.
- Erofeeva, E.A., 2020. Estimating the frequency of hormesis and other non-monotonic responses in plants experiencing road traffic pollution in urban areas and experimental pollutant exposure. *Environ. Monit. Assess.* 192 (7), 1–17.
- Erofeeva, E.A., 2022. Environmental hormesis of non-specific and specific adaptive mechanisms in plants. *Sci. Total Environ.* 804, 150059.
- Fan, D., Sun, J., Liu, C., Wang, S., Han, J., Agathokleous, E., 2021. Measurement and modeling of hormesis in soil bacteria and fungi under single and combined treatments of Cd and Pb. *Sci. Total Environ.* 783, 147494.
- Gill, S.S., Tuteja, N., 2010. Reactive oxygen species and antioxidant machinery in abiotic stress tolerance in crop plants. *Plant Physiol. Biochem.* 48 (12), 909–930.
- Guo, J., Dai, X., Xu, W., Ma, M., 2008. Overexpressing GSH1 and AsPCS1 simultaneously increases the tolerance and accumulation of cadmium and arsenic in *Arabidopsis thaliana*. *Chemosphere* 72, 1020–1026.
- Jia, L., Liu, Z., Chen, W., Ye, Y., Yu, S., He, X., 2015. Hormesis effects induced by cadmium on growth and photosynthetic performance in a hyperaccumulator, *Lonicera japonica* Thunb. *J. Plant Growth Regul.* 34, 13–21.
- Jozefczak, M., Remans, T., Vangronsveld, J., Cuypers, A., 2012. Glutathione is a key player in metal-induced oxidative stress defenses. *Int. J. Mol. Sci.* 13 (3), 3145–3175.
- Katsnelson, B.A., Panov, V.G., Minigaliev, I.A., Bushueva, T.V., Gurvich, V.B., Privalova, L.I., 2021. On an extended understanding of the term “hormesis” for denoting alternating directions of the organism’s response to increasing adverse exposures. *Toxicology* 447, 152629.
- Kong, E.Y., Cheng, S.H., Yu, K.N., 2016. Biphasic and triphasic dose responses in zebrafish embryos to low-dose 150 kV X-rays with different levels of hardness. *J. Radiat. Res.* 57 (4), 363–369.
- Kováčik, J., Klejdus, B., Štork, F., Hedbavny, J., 2012. Physiological responses of *Tillandsia albida* (Bromeliaceae) to long-term foliar metal application. *J. Hazard. Mater.* 239, 175–182.
- Kováčik, J., Babula, P., Bořivoj, K., Hedbavny, J., 2014. Comparison of oxidative stress in four *Tillandsia* species exposed to cadmium. *Plant Physiol. Biochem.* 80, 33–40.
- Kushwaha, A., Rani, R., Kumar, S., Gautam, A., 2015. Heavy metal detoxification and tolerance mechanisms in plants: implications for phytoremediation. *Environ. Rev.* 23, 1–13.
- Li, H.S., 2000. Principles and Techniques of Plant Physiological and Biochemical Experiment. Higher Education Press, Beijing, China.
- Li, P., Zhang, J., Sun, X., Agathokleous, E., Zheng, G., 2022. Atmospheric Pb induced hormesis in the accumulator plant *Tillandsia usneoides*. *Sci. Total Environ.* 811, 152384.
- Ma, X., Zhao, X., Zhang, Q., Zhou, Z., Dou, Y., Ji, W., Li, J., 2022. Comparative transcriptome analysis of broccoli seedlings under different Cd exposure levels revealed possible pathways involved in hormesis. *Sci. Hortic.* 304, 111330.
- Mägdefrau, A.S., Ludwig, K., Weigel, C., Köse, N., Guerra, G.M., Dakhovnik, A., Kusan, C., 2019. DNA-Damage-induced Hormetic Responses. The Science of Hormesis in Health and Longevity. Academic Press, pp. 149–159.
- Ming, R., VanBuren, R., Wai, C.M., Tang, H., Schatz, M.C., Bowers, J.E., 2015. The pineapple genome and the evolution of CAM photosynthesis. *Nat. Genet.* 47 (12), 1435–1442.
- Moustakas, M., Dobrikova, A., Sperdoulis, I., Han, C., Adamakis, I.D.S., Moustaka, J., Apostolova, E.A., 2022a. Hormetic spatiotemporal photosystem II response mechanism of *Salvia* to excess zinc exposure. *Int. J. Mol. Sci.* 23, 11232.
- Moustakas, M., Moustaka, J., Sperdoulis, I., 2022b. Hormesis in photosystem II: a mechanistic understanding. *Curr. Opin. Toxicol.* 29, 57–64.
- Mushak, P., 2013. How prevalent is chemical hormesis in the natural and experimental worlds? *Sci. Total Environ.* 443, 573–581.
- Muszynska, E., Labudda, M., 2019. Dual role of metallic trace elements in stress biology—from negative to beneficial impact on plants. *Int. J. Mol. Sci.* 20, 3117.
- Muszynska, E., Hanus-Fajerska, E., Ciarkowska, K., 2018. Studies on lead and cadmium toxicity in *Dianthus carthusianorum* calamine ecotype cultivated in vitro. *Plant Biol.* 20, 474–482.
- Pignata, M.L., Gudiño, G.L., Wannaz, E.D., Plá, R.R., González, C.M., Carreras, H.A., Orellana, L., 2002. Atmospheric quality and distribution of heavy metals in Argentina employing *Tillandsia capillaris* as a biomonitor. *Environ. Pollut.* 120 (1), 59–68.
- Poschenrieder, C., Cabot, C., Martos, S., Gallego, B., Barceló, J., 2013. Do toxic ions induce hormesis in plants? *Plant Sci.* 212, 15–25.
- Schreck, E., Viers, J., Blondel, I., Auda, Y., Macouin, M., Zouiten, C., Freydier, R., Dufrechou, G., Chmeleff, J., Darrozes, J., 2020. *Tillandsia usneoides* as biomonitors of trace elements contents in the atmosphere of the mining district of Cartagena-La Unión (Spain): new insights for element transfer and pollution source tracing. *Chemosphere* 241, 124955.
- Shahid, M., Niazi, N.K., Rinklebe, J., Bundschuh, J.B., Dumat, C., Pinelli, E., 2020. Trace elements-induced phytohormesis: a critical review and mechanistic interpretation. *Crit. Rev. Environ. Sci. Technol.* 50 (19), 1984–2015.
- Sthijns, M.M., Weseler, A.R., Bast, A., Haenen, G.R., 2016. Time in redox adaptation processes: from evolution to hormesis. *Int. J. Mol. Sci.* 17 (10), 1649.
- Sun, H., Calabrese, E.J., Zheng, M., Wang, D., Pan, Y., Lin, Z., Liu, Y., 2018. A swinging seesaw as a novel model mechanism for time-dependent hormesis under dose-dependent stimulatory and inhibitory effects: a case study on the toxicity of antibacterial chemicals to *Aliivibrio fischeri*. *Chemosphere* 205, 15–23.
- Sun, X., Li, P., Zheng, G., 2021a. Cellular and subcellular distribution and factors influencing the accumulation of atmospheric Hg in *Tillandsia usneoides* leaves. *J. Hazard. Mater.* 414, 125529.
- Sun, X., Li, P., Zheng, G., 2021b. Biomarker responses of Spanish moss *Tillandsia usneoides* to atmospheric Hg and hormesis in this species. *Front. Plant Sci.* 12, 625799.
- Vargas-Hernandez, M., Macias-Bobadilla, I., Guevara-Gonzalez, R.G., Romero-Gomez, S.D.J., Rico-García, E., Ocampo-Velazquez, R.V., 2017. Plant hormesis management with biostimulants of biotic origin in agriculture. *Front. Plant Sci.* 8, 1762.
- Vianna, N.A., Gonçalves, D., Brandão, F., de Barros, R.P., Meire, R.O., Torres, J.P.M., 2011. Assessment of heavy metals in the particulate matter of two Brazilian metropolitan areas by using *Tillandsia usneoides* as atmospheric biomonitor. *Environ. Sci. Pollut. Res.* 18 (3), 416–427.
- Wang, S., Huang, B., Fan, D., Agathokleous, E., Guo, Y., Zhu, Y., Han, J., 2021. Hormetic responses of soil microbiota to exogenous Cd: a step toward linking community-level hormesis to ecological risk assessment. *J. Hazard. Mater.* 416, 125760.
- Wannaz, E.D., Carreras, H.A., Abril, G.A., Pignata, M.L., 2011. Maximum values of Ni<sup>2+</sup>, Cu<sup>2+</sup>, Pb<sup>2+</sup> and Zn<sup>2+</sup> in the biomonitor *Tillandsia capillaris* (Bromeliaceae): relationship with cell membrane damage. *Environ. Exp. Bot.* 74, 296–301.
- Xie, M., Chen, W., Dai, H., Wang, X., Li, Y., Yu, C.K., Sun, H., Wang, L., 2021. Cadmium-induced hormesis effect in medicinal herbs improves the efficiency of safe utilization for low cadmium-contaminated farmland soil. *Ecotoxicol. Environ. Saf.* 225, 112724.
- Yang, L., Kang, Y., Dai, H., Wang, X., Xie, M., Liu, J., 2022. Differential responses of polysaccharides and antioxidant enzymes in alleviating cadmium toxicity of tuber traditional Chinese medicinal materials. *Environ. Sci. Pollut. Res.* 29, 60832–60842.
- Yu, G., Ullah, H., Wang, X., Liu, J., Chen, B., Jiang, P., 2023. Integrated transcriptome and metabolome analysis reveals the mechanism of tolerance to manganese and cadmium toxicity in the Mn/Cd hyperaccumulator *Celosia argentea* Linn. *J. Hazard. Mater.* 443, 130206.

## 论文收录引用检索报告

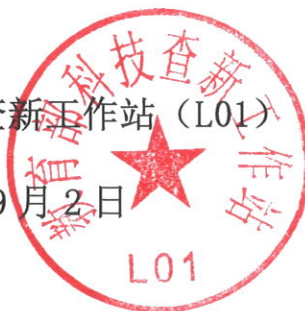
检索项目	检索青岛农业大学李鹏 (Li Peng) 2023 年发表的论文被 SCI 网络数据库收录情况
检索工具	Web of Science
检索方式	题目 (作者提供文章列表)
检索结果	期刊 Science of the Total Environment, 环境科学与生态学 SCI 一区, 2023 影响因子 9.8
检索结论	检索青岛农业大学李鹏 (Li Peng) 2023 年发表的论文被 SCI 网络数据库收录情况:  共有 1 篇被 SCI 收录, 详情见附件。



特此证明。

教育部科技查新工作站 (L01)

2023 年 9 月 2 日



## Record 1 of 1

**Title:** Hormesis in the heavy metal accumulator plant *Tillandsia ionantha* under Cd exposure: Frequency and function of different biomarkers

**Author(s):** Zhang, JY (Zhang, Jingyi); Tang, Z (Tang, Zhen); Agathokleous, E (Agathokleous, Evgenios); Zheng, GL (Zheng, Guiling); Xu, L (Xu, Liang); Li, P (Li, Peng)

**Source:** SCIENCE OF THE TOTAL ENVIRONMENT **Volume:** 889 **Article Number:** 164328 **DOI:** 10.1016/j.scitotenv.2023.164328 **Early Access Date:** MAY 2023 **Published:** SEP 1 2023

**Times Cited in Web of Science Core Collection:** 1

**Total Times Cited:** 1

**Usage Count (Last 180 days):** 12

**Usage Count (Since 2013):** 12

**Cited Reference Count:** 59

**Abstract:** Cadmium is one of the most biotoxic substances among all heavy metals, but an increasing number of studies indicate that low-dose Cd can induce hormesis in some plants. However, the frequency of hormesis in various biomarkers (molecular, resistance, and damage markers) and their associated function in hormesis-generation are poorly understood. In this study, the heavy metal accumulator plant *Tillandsia ionantha* Planch. was exposed to 5 mM CdCl<sub>2</sub> with 6 different time periods. The trends of 18 biomarkers after Cd exposure were detected. The percentage for all non-monophasic responses based on dose-response modeling was higher (50 %), in which seven (38.89 %) biomarkers showed hormesis, indicating that hormesis effect can commonly occur in this plant. However, the occurrence frequency of hormesis in different types of biomarkers was different. Six Cd resistance genes, glutathione (GSH) among 6 resistance markers, and 0 damage markers showed hormesis. Factor analysis further showed that the 6 Cd resistance genes and GSH were positively intercorrelated in the first principal component. Therefore, heavy metal resistance genes and GSH may play an important role in the generation of hormesis. Our experiment shows that time-dependent nonmonophasic responses, including hormesis, are activated by considerably high concentrations of Cd, presenting a strategy to cope with and potentially reduce the anticipated damage as the dose of stress increases over time.

**Accession Number:** WOS:001008191200001

**PubMed ID:** 37211113

**Language:** English

**Document Type:** Article

**Author Keywords:** Cadmium; Dose-response relationship; Occurrence frequency; Resistance gene; Stress biomarkers; Time-dependent hormesis

**KeyWords Plus:** ZEBRAFISH EMBRYOS; OXIDATIVE STRESS; CADMIUM; BROMELIACEAE; GLUTATHIONE; CAPILLARIS; TOLERANCE; USNEOIDES; RESPONSES



**Addresses:** [Zhang, Jingyi; Tang, Zhen; Zheng, Guiling; Xu, Liang; Li, Peng] Qingdao Agr Univ, Sch Resources & Environm, Qingdao 266109, Shandong, Peoples R China.

[Agathokleous, Evgenios] Nanjing Univ Informat Sci & Technol NUIST, Sch Appl Meteorol, Dept Ecol, Nanjing, Jiangsu, Peoples R China.

**Corresponding Address:** Li, P (corresponding author), Qingdao Agr Univ, Sch Resources & Environm, Qingdao 266109, Shandong, Peoples R China.

**E-mail Addresses:** pengleep@qau.edu.cn

**Affiliations:** Qingdao Agricultural University; Nanjing University of Information Science & Technology

**Publisher:** ELSEVIER

**Publisher Address:** RADARWEG 29, 1043 NX AMSTERDAM, NETHERLANDS

**Web of Science Index:** Science Citation Index Expanded (SCI-EXPANDED)

**Web of Science Categories:** Environmental Sciences

**Research Areas:** Environmental Sciences & Ecology

**IDS Number:** J2TR5

**ISSN:** 0048-9697

**eISSN:** 1879-1026

**29-char Source Abbrev.:** SCI TOTAL ENVIRON

**ISO Source Abbrev.:** Sci. Total Environ.

**Source Item Page Count:** 10

**Funding:**

Funding Agency	Grant Number
National Natural Science Foundation of China	32271699

**Acknowledgements** This study was funded by the National Natural Science Foundation of China (No. 32271699) .

**Output Date:** 2023-09-02

---

End of File



Contents lists available at ScienceDirect

## Science of the Total Environment

journal homepage: [www.elsevier.com/locate/scitotenv](http://www.elsevier.com/locate/scitotenv)

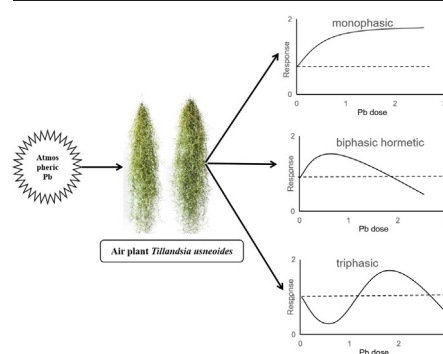
## Atmospheric Pb induced hormesis in the accumulator plant *Tillandsia usneoides*

Peng Li<sup>a</sup>, Jingyi Zhang<sup>a</sup>, Xingyue Sun<sup>a</sup>, Evgenios Agathokleous<sup>b</sup>, Guiling Zheng<sup>a,\*</sup><sup>a</sup> School of Resources and Environment, Qingdao Agricultural University, Qingdao, Shandong 266109, China<sup>b</sup> Department of Ecology, School of Applied Meteorology, Nanjing University of Information Science and Technology (NUIST), Nanjing, Jiangsu 21044, China

## HIGHLIGHTS

- The nature of the relationship between air Pb and the air plant was studied.
- Three types of dose-response relationships were found, indicating dynamic responses.
- Atmospheric Pb induced biphasic-hormetic dose response in *T. usneoides*.
- Triphasic dose response was also revealed.
- The mechanisms are discussed, providing an opportunity for improving risk assessment.

## GRAPHICAL ABSTRACT



## ARTICLE INFO

## Article history:

Received 2 October 2021

Received in revised form 21 November 2021

Accepted 10 December 2021

Available online 16 December 2021

Editor: Michael Norman Moore

## Keywords:

Air pollution

Biomarker

Atmospheric heavy metals

Triphasic dose response

## ABSTRACT

While numerous studies reported hormesis in plants exposed to heavy metals, metals were commonly added in the growth substrate (e.g. soil or solution). The potential of heavy metals in the atmosphere to induce hormesis in plants, however, remains unknown. In this study, we exposed the widely-used accumulator plant *Tillandsia usneoides* to 10 atmospheric Pb concentrations (0–25.6  $\mu\text{g}\cdot\text{m}^{-3}$ ) for 6 or 12 h. Three types of dose-response relationships between different response endpoints (biomarkers) and Pb concentrations were found for *T. usneoides*. The first was a monophasic dose response, in which the response increased linearly with increasing Pb concentrations, as seen for metallothionein (MT) content after a 6-h exposure. The second and dominating type was a biphasic-hormetic dose response, exhibited by malondialdehyde (MDA), superoxide anion radical ( $\text{O}_2^{\cdot-}$ ), and superoxide dismutase (SOD) after 6 or 12 h of exposure and by glutathione (GSH) and MT content after 12 h of treatment. The third type was a triphasic dose response, as seen for leaf electric conductivity after 6 or 12 h of exposure and GSH after 6 h of exposure. This finding suggests that Pb inhibited the response of *T. usneoides* at very low concentrations, stimulated it at low-to-moderate concentrations, and inhibited it at higher concentrations. Our results demonstrate diverse adaptation mechanisms of plants to stress, in the framework of which alternating between up- and down-regulation of biomarkers is at play when responding to different levels of toxicants. The emergence of the triphasic dose response will further enhance the understanding of time-dependent hormesis.

## 1. Introduction

Atmospheric contamination by heavy metals is a widespread global issue due to the complex origination (such as mining, manufacturing, and

fossil fuel burning), wide distribution, high bioaccumulation, and toxicity (Li et al., 2018; Dinake et al., 2021). Some investigations have revealed that heavy metals can enter plants through foliage (Uzu et al., 2010; Xiong et al., 2017; Natasha and Khalid, 2020). Despite considerable

\* Corresponding author.

E-mail address: [zgl@qau.edu.cn](mailto:zgl@qau.edu.cn) (G. Zheng).

progress in recent years, however, data regarding foliar metal uptake and associated phytotoxicity remain extremely limited compared to phytotoxicity as a result of root exposure and uptake (Shahid et al., 2017).

Organisms respond to environmental challenges in various ways. Among them, the linear dose response with no toxicological threshold (LNT) has been extensively studied in toxicological studies, especially because most previous studies primarily focused on high doses of pollutants (Costantini and Borremans, 2019). A different kind of dose response is hormesis, in the framework of which a toxicant has a stimulating effect at low doses and a toxic effect at high doses, thus forming a biphasic dose-response relationship considering also the effects of sub-threshold doses of toxicants (Agathokleous et al., 2019a, 2019b, 2020). Although hormesis had undergone a long-lasting controversial history (Calabrese, 2018), an increasing number of plants, animals, and microorganisms are found to exhibit hormesis when subjected to different environmental stresses, including heavy metals, suggesting hormesis is a common phenomenon (Muszynska and Labudda, 2019; Shahid et al., 2019; Agathokleous et al., 2020; Salinitro et al., 2021). Various biomarkers, including biomass, enzyme activity, chlorophyll fluorescence traits, photosynthesis and photosynthetic pigment concentrations, and other oxidative stress indicators, can be used to investigate hormesis in plants (Carvalho et al., 2020).

*Tillandsia* spp. (Bromeliaceae) are perennial flowering plants known as “air plants” because they do not need soil substrate for their growth; they thrive on “air” by clinging to branches, wires, rocks, and any other materials or structures that provide a suitable habitat for their growth and development (Benzing, 2000). *Tillandsia* spp. are native to Central and South America, with over 600 species, and are easy to cultivate and have high ornamental value, thus being widely introduced worldwide (Benzing, 2000). Most *Tillandsia* species are epiphytes, absorbing water and nutrients from the air via leaves; therefore, the leaves have a high capacity to also absorb air pollutants, such as heavy metals. Hence, *Tillandsia* spp. has become an accumulative indicator plant that can sensitively monitor heavy-metal pollution of the air. Numerous studies have shown that various atmospheric heavy metals, including Hg, Co, Cu, Fe, Ni, Mn, Pb, Cd, Pb, V, Cs, and Zn, can be effectively accumulated in different species of *Tillandsia* (Calasans and Malm, 1997; Figueiredo et al., 2007; Wannaz et al., 2011; Sánchez-Chardi, 2016; Schreck et al., 2020; Sun et al., 2021a).

*Tillandsia* spp. produces different physiological responses after heavy-metal stress. After treating *T. capillaris* with different concentrations (0.5–10 mM) of Ni, Cu, Zn, or Pb solutions for 45 min, the malondialdehyde (MDA) content was increased by Pb treatment but was not significantly changed by Ni, Cu, and Zn treatments (Wannaz et al., 2011). Treatment of four *Tillandsia* spp. species with 2  $\mu\text{M}$   $\text{Cd}^{2+}$  for one month did not cause significant morphological damage and elevation in the glutathione (GSH) level, but caused a significant elevation in the reactive oxygen species (ROS) and peroxidase (POD) levels (Kováčik et al., 2014). The prevalence of hormesis in the widely-used accumulative indicator *Tillandsia* spp., however, remains to be elucidated, although it is now understood that heavy metals cause hormesis in (hyper)accumulator plants (Calabrese and Agathokleous, 2021). Importantly, bioindication outcomes and pollution status assessments based on an LNT or threshold dose-response perspective could be incorrect if *Tillandsia* spp. exhibits non-considered hormetic responses to heavy metals (or other pollutants). Hence, hormetic responses of *Tillandsia* spp. to heavy metals should be studied.

Changes in the levels of various biomarkers in *Tillandsia usneoides* were previously studied after atmospheric Hg treatment. The dose-response curves between Hg concentrations and the content of superoxide dismutase (SOD), GSH, and metallothionein (MT) were in agreement with hormesis (Sun et al., 2021b), suggesting that other heavy metals may also induce hormesis in *Tillandsia* spp. Here, we exposed *T. usneoides* to Pb concentration gradients ranging from very low to high, for 6 or 12 h, to evaluate the response of main biomarkers and construct dose-response curves. We were interested in exploring the various characteristics and mechanisms of the occurrence of Pb-induced hormesis in *Tillandsia* spp. for the first time, considering also the potential temporal variation in hormetic

responses (Agathokleous et al., 2020). We hypothesized that *T. usneoides* displays diverse physiological responses to Pb stress, with common occurrence of hormesis; however, with the same biomarkers displaying dose-response relationships that vary in their nature depending on exposure duration. Such adjustments in key biomarkers within a hormetic dose-response framework would allow *T. usneoides* to enhance its coping potential and protect itself against damage induced by accumulated stress.

## 2. Material and methods

### 2.1. Material

*T. usneoides* is known as Spanish moss because of its moss-like shape (Benzing, 2000). *T. usneoides* has weak roots and slender stems with thin, curved leaves that form a chain-like hanging structure (Fig. 1). In this study, healthy *T. usneoides* plants of similar size were selected as experimental materials. First, they were thoroughly washed with deionized water and soaked for 30 min to saturate them with water. Then, they were dried uniformly for 30 min at 25 °C.

### 2.2. Atmospheric Pb treatment

The experiment was conducted in an airtight exposure chamber made of polymethyl methacrylate (PMMA) with a volume of 0.08 m<sup>3</sup>. The chamber was connected to an air pump and an atomizer. The air pump provided continuous air power for the atomization system, and the atomizer produced a fine mist of the heavy-metal solution in an external syringe to create an aerosol atomized environment. There was a fan rotating in the middle of the chamber to quickly and evenly mix the gaseous heavy metals.

A 1/1000 balance was used to accurately weigh a fresh weight of 40 g of *T. usneoides* plant material for each treatment. The plants were divided into five groups and five replicates of 8 g each were created, and the grouped *T. usneoides* were suspended on a thin rope inside the chamber. The annual limit for the atmospheric lead concentration set is 0.5  $\mu\text{g}\cdot\text{m}^{-3}$  in China (Ministry of Environmental Protection, 2012). So ten Pb concentration values (0, 0.1, 0.2, 0.4, 0.8, 1.6, 3.2, 6.4, 12.8, and 25.6  $\mu\text{g}\cdot\text{m}^{-3}$ ) below and above the Pb limitation value and two exposure durations (6 h and 12 h) were studied, resulting in 20 dose treatments. As *T. usneoides* demonstrates crassulacean acid metabolism and open stomata at night (Benzing, 2000), the 6-h atomization experiment was carried out at night between 18:00 and 24:00, whereas the 12-h atomization experiment was conducted between 18:00 and 06:00 the next day. The amount of Pb standard solution required was measured according to the set Pb concentration and the volume of the atomization box. To reduce the impact of the injection time, the amount of Pb solution in the syringe was uniformly set to 30 mL and the injection rate was set to 15 mL·h<sup>-1</sup>.

### 2.3. Pb-induced visible injury

Immediately after the treatment with different doses of Pb, the *T. usneoides* plants were removed and visually observed for visible injuries.

### 2.4. Determination of the damage markers in leaf

The leaf relative conductivity and MDA and  $\text{O}_2\cdot^-$  levels were used to assess the damage after the treatments. Referring to the method proposed by Li (2000), the relative conductivity was determined using a DDS-307A conductivity meter; the MDA content was determined using the thiobarbituric acid method.

The  $\text{O}_2\cdot^-$  content was determined using the method suggested by Lei et al. (2006). Briefly, 1 g of *T. usneoides* samples were ground in 65 mol·L<sup>-1</sup> phosphate buffer (pH 7.8) with quartz sand using a mortar on ice. The ground samples were transferred to centrifuge tubes, and brought up to a volume of 10 mL with phosphate buffer. After filtering, the samples were centrifuged at 10,000 rpm for 10 min, and the supernatant was collected as the extract for further experiments. Two milliliters of the extract



Fig. 1. *Tillandsia usneoides* before and after Pb treatment. A, Before Pb stress; B, After exposure to  $6.4 \mu\text{g}\cdot\text{m}^{-3}$  Pb for 6 h; C, After exposure to  $25.6 \mu\text{g}\cdot\text{m}^{-3}$  Pb for 12 h.

(1.5 mL of phosphate buffer and 0.5 mL of hydroxylamine hydrochloride) were added, followed by incubation in a thermostatic water bath at  $25^\circ\text{C}$  for 20 min after mixing. Next, 2 mL of the reaction solution aspirated from each of those tubes were added to three individual new tubes containing 2 mL of  $17 \text{ mmol}\cdot\text{L}^{-1}$  *p*-aminobenzene sulfonic acid and 2 mL of  $7 \text{ mmol}\cdot\text{L}^{-1}$   $\alpha$ -naphthylamine. The samples were incubated in a thermostatic water bath at  $30^\circ\text{C}$  for 30 min to react. Finally, absorbance was measured at 530 nm to calculate the  $\text{O}_2^-$  content.

### 2.5. Determination of the resistance markers

SOD, GSH, and MT contents were used to assess the resistance. The SOD activity was determined using the nitrogen blue tetrazolium method proposed by Li (2000).

The GSH content was determined following the method suggested by Qian et al. (2013). Briefly, 0.5 g of fresh samples were weighed and ground in 5 mL of 5% trichloroacetic acid, and the supernatant was collected after centrifuging at 1500 rpm for 10 min. One milliliter of distilled water, 1 mL of  $0.1 \text{ mol}\cdot\text{L}^{-1}$  phosphate buffer, and 0.5 mL of  $4 \text{ mmol}\cdot\text{L}^{-1}$  DTNB solution were added in a new tube and mixed. Two additional tubes were prepared. First, 1 mL of the supernatant and 1 mL of  $0.1 \text{ mol}\cdot\text{L}^{-1}$  phosphate buffer (pH 7.7) were added in each tube. Then, 0.5 mL of  $4 \text{ mmol}\cdot\text{L}^{-1}$  DTNB solution were added to one tube, and 0.5 mL of  $0.1 \text{ mol}\cdot\text{L}^{-1}$  phosphate buffer (pH 6.8) was added to the other tube. The two tubes were incubated at  $25^\circ\text{C}$  for 10 min. Absorbance of the chromo-developing solution was measured immediately at 412 nm. Absorbance values of the mixtures in the sample tube (ODs) and blank control tube (ODc) were recorded. GSH content was calculated according to the difference in absorbance values per leaf fresh mass ( $\mu\text{mol}\cdot\text{g}^{-1}$  FW).

The MT content was determined by adopting the metal-binding method: 1.0 g of a fresh plant sample was weighed into a mortar, and 6 mL of pre-chilled  $0.1 \text{ mol}\cdot\text{L}^{-1}$  Tris-HCl buffer (pH 8.6) were added. The sample was ground in an ice bath until homogenization and extracted overnight in a refrigerator. To collect the supernatant, the sample was heated in a water bath at  $90^\circ\text{C}$  for 3 min, brought to  $25^\circ\text{C}$ , and centrifuged at 10,000 rpm for 10 min. Then, pre-chilled anhydrous ethanol (a volume three times the volume of the supernatant) was added, precipitated overnight at  $-20^\circ\text{C}$ , and centrifuged at 10,000 rpm for 10 min. The precipitate was retained, and then 5 mL of  $0.1 \text{ mol}\cdot\text{L}^{-1}$  Tris-HCl buffer were added to the precipitate, dissolved for 3 h, and centrifuged at 10,000 rpm for 10 min to collect the supernatant. The MT content was calculated after determining the Pb content using the atomic fluorescence method.

### 2.6. Data analysis

#### 2.6.1. Assessment of exposure-response relationships

Physiological responses to Pb exposure were expressed as a percent increase or decrease relative to the control exposure. Each exposure-response relationship was classified following the model-fitting method of Di Veroli et al. (2015). Four kinds of models were evaluated for goodness of fit to the

exposure-response data: i) monophasic without agonist effect, ii) biphasic with 2 points of inhibition, iii) biphasic with one stimulatory effect, and iv) triphasic with stimulatory effect and 2 points of inhibition. The best-fitting model was chosen based on the small-sample corrected Akaike Information Criterion (AIC), where a lower AIC score indicates a better fit.

#### 2.6.2. Standard hypothesis testing of treatment effect

Average values corresponding to each Pb level were used as statistical units. Differences between the data obtained from the various doses of Pb were identified using a one-way ANOVA followed by the Tukey-HSD post hoc test. For ANOVAs, all variables were checked for normality of variance using the Shapiro-Wilk test and homogeneity using Levene's test. Differences were considered significant if  $p < 0.05$ . Data were analyzed using SPSS 23.0 (IBM, USA).

## 3. Results

### 3.1. Pb-induced visible injuries

*T. usneoides* remained green after treatment with  $0\text{--}3.2 \mu\text{g}\cdot\text{m}^{-3}$  Pb (Fig. 1A). When the Pb dose was increased to  $6.4 \mu\text{g}\cdot\text{m}^{-3}$  for 6 h, the leaves began to develop yellowing at the tips (Fig. 1B). Visual observations indicated that the yellowing area of the leaves increased as the Pb dose continued to increase; however, no plants showed obvious deterioration, including those treated with the largest Pb dose (Fig. 1C).

### 3.2. Relative conductivity

The relative conductivity of *T. usneoides* leaves before the Pb treatment of 6 and 12 h was  $30.55 \pm 1.54\%$  (Table 1) and  $30.75 \pm 1.81\%$  (Table 2), with no statistically significant difference between the means ( $p > 0.05$ ). After exposed to  $0.1 \mu\text{g}\cdot\text{m}^{-3}$  Pb, the conductivity value increased significantly. Then, it decreased after exposure to  $0.2 \mu\text{g}\cdot\text{m}^{-3}$ , and increased again at  $0.4$  (6 h) or  $0.8$  (12 h)  $\mu\text{g}\cdot\text{m}^{-3}$  Pb (Fig. 2A). Generally, significant differences existed among different treatments for 6 h ( $F = 138.545$ ,  $p < 0.001$ ) and 12 h ( $F = 693.396$ ,  $p < 0.001$ ). The relationship between Pb concentrations and relative conductivity after 6 or 12 h of treatment was best described by a triphasic model (Table 3).

### 3.3. MDA content

After 6 or 12 h of Pb treatment, the MDA content in *T. usneoides* leaves exhibited a similar triphasic trend, i.e. first increased, then decreased, and finally increased again (Fig. 2B). The MDA content was highest when Pb was applied at a concentration of  $25.6 \mu\text{g}\cdot\text{m}^{-3}$ , reaching  $4.54 \pm 0.07 \text{ nmol}\cdot\text{g}^{-1}$  and  $4.70 \pm 0.09 \text{ nmol}\cdot\text{g}^{-1}$  after 6 (Table 1) and 12 h (Table 2); it was significantly higher than the means of the other treatments. The first peak of MDA content was different between 6 and 12 h of Pb treatment, respectively. The first peak was  $2.86 \pm 0.46 \text{ nmol}\cdot\text{g}^{-1}$  after 6 h of Pb treatment at the concentration of  $1.6 \mu\text{g}\cdot\text{m}^{-3}$ , while it was



**Table 1**Changes in six biomarkers in *Tillandsia usneoides* after a 6-h exposure to different Pb concentrations. Values shown are means  $\pm$  SEs ( $n = 5$ ).

Pb concentration ( $\mu\text{g}\cdot\text{m}^{-3}$ )	REC (%)	MDA ( $\text{nmol}\cdot\text{g}^{-1}$ )	$\text{O}_2^{\cdot-}$ ( $\mu\text{g}\cdot\text{g}^{-1}$ )	SOD ( $\text{U}\cdot\text{g}^{-1}\cdot\text{min}^{-1}$ )	GSH ( $\mu\text{mol}\cdot\text{g}^{-1}$ )	MT ( $\mu\text{g}\cdot\text{L}^{-1}$ )
0.0	30.55 $\pm$ 1.54b	1.74 $\pm$ 0.2c	363.82 $\pm$ 4.54b	143.80 $\pm$ 31.49c	166.57 $\pm$ 17.57a	78.95 $\pm$ 9.73a
0.1	75.91 $\pm$ 1.2a	2.22 $\pm$ 0.12bc	371.09 $\pm$ 2.82ab	151.00 $\pm$ 25.77bc	153.00 $\pm$ 11.91ab	81.53 $\pm$ 23.95a
0.2	28.45 $\pm$ 2.91b	2.11 $\pm$ 0.33bc	374.37 $\pm$ 0.31a	155.00 $\pm$ 19.75bc	138.62 $\pm$ 14.13ab	80.38 $\pm$ 15.21a
0.4	34.55 $\pm$ 5.77b	2.30 $\pm$ 0.4bc	367.82 $\pm$ 6.05ab	160.42 $\pm$ 11.57bc	156.92 $\pm$ 12.99a	80.62 $\pm$ 17.8a
0.8	20.36 $\pm$ 0.3c	2.67 $\pm$ 0.32b	377.75 $\pm$ 2.52a	143.86 $\pm$ 15.78c	167.57 $\pm$ 3.95a	80.39 $\pm$ 9.07a
1.6	19.29 $\pm$ 1.57c	2.86 $\pm$ 0.46b	371.22 $\pm$ 5.97ab	120.57 $\pm$ 40.5c	103.25 $\pm$ 4.45bc	80.43 $\pm$ 14.14a
3.2	22.89 $\pm$ 2.36bc	2.31 $\pm$ 0.25bc	374.47 $\pm$ 2.41a	200.67 $\pm$ 25.9b	124.46 $\pm$ 8.29b	82.52 $\pm$ 9.77a
6.4	25.29 $\pm$ 4.38bc	2.07 $\pm$ 0.73bc	370.36 $\pm$ 4.1ab	211.43 $\pm$ 21.0b	124.12 $\pm$ 4.87b	80.09 $\pm$ 11.86a
12.8	30.88 $\pm$ 1.55b	2.64 $\pm$ 0.14b	321.98 $\pm$ 0.62c	260.32 $\pm$ 3.48ab	91.69 $\pm$ 12.11bc	80.48 $\pm$ 2.41a
25.6	33.49 $\pm$ 0.97b	4.54 $\pm$ 0.07a	370.85 $\pm$ 1.12a	305.00 $\pm$ 18.71a	111.62 $\pm$ 37.63bc	80.39 $\pm$ 16.59a

REC, relative electric conductivity; MDA, malondialdehyde;  $\text{O}_2^{\cdot-}$ , superoxide anion radical; SOD, superoxide dismutase; GSH, glutathione; MT, metallothionein. Different small letters indicate a significant difference among different treatments for the same parameter at the level of 0.05. Data were tested with ANOVA followed by Tukey-HSD post hoc test.

$3.65 \pm 0.06 \text{ nmol}\cdot\text{g}^{-1}$  after 12 h of treatment with  $6.4 \mu\text{g Pb}\cdot\text{m}^{-3}$ . The best model explaining the relationship between Pb concentrations and MDA content after 6 or 12 h of treatment was the biphasic (Table 3).

### 3.4. $\text{O}_2^{\cdot-}$ content

The  $\text{O}_2^{\cdot-}$  content in *T. usneoides* leaves varied between 321.98 and  $377.75 \mu\text{g}\cdot\text{g}^{-1}$  (Table 1) and between 296.74 and  $379.98 \mu\text{g}\cdot\text{g}^{-1}$  (Table 2) after 6 and 12 h of Pb treatment, respectively. No significant differences were found between these ranges, except that the  $\text{O}_2^{\cdot-}$  content at  $12.8 \mu\text{g}\cdot\text{m}^{-3}$  Pb was significantly lower than that in other treatments. Nevertheless, the analysis of the fitting curves showed a clear trend between the  $\text{O}_2^{\cdot-}$  content and the Pb dose. As the Pb concentration increased, the  $\text{O}_2^{\cdot-}$  content increased, decreased, and then increased again in the form of a flat S shape (Fig. 2C). A biphasic model displayed the best fit to the relationship between Pb concentrations and  $\text{O}_2^{\cdot-}$  content after 6 or 12 h of treatment (Table 3).

### 3.5. SOD activity

SOD activity of *T. usneoides* leaves continued to increase with an increasing Pb concentration from 0 to  $0.4 \mu\text{g}\cdot\text{m}^{-3}$ , whether after 6 or 12 h of treatment (Fig. 3A). When the Pb concentration was increased to  $0.8 \mu\text{g}\cdot\text{m}^{-3}$ , SOD activity decreased, but the difference was not significant (Tables 1, 2). SOD activity was the highest at the largest Pb concentration, reaching  $305.00 \pm 18.71$  and  $440.00 \pm 53.85 \text{ U}\cdot\text{g}^{-1}\cdot\text{min}^{-1}$  at 6 and 12 h respectively, which were significantly higher than those at lower Pb concentrations (Tables 1, 2). The best model between Pb concentrations and SOD content after 6 or 12 h of treatment was biphasic (Table 3).

### 3.6. GSH content

When *T. usneoides* was exposed to different Pb concentrations in the range of  $0\text{--}0.8 \mu\text{g}\cdot\text{m}^{-3}$  for 6 h, the GSH content did not change significantly

(Table 1). With an increasing Pb concentration, the GSH content decreased significantly (Fig. 3B) to reach a minimum value of  $91.69 \pm 12.11 \mu\text{mol}\cdot\text{g}^{-1}$  at a Pb concentration of  $12.8 \mu\text{g}\cdot\text{m}^{-3}$ , a value that was significantly smaller than that of the control group ( $166.6 \pm 19.7 \mu\text{mol}\cdot\text{g}^{-1}$ ).

At 12 h, the GSH content first increased with Pb concentration increasing to 0.1 and  $0.2 \mu\text{g}\cdot\text{m}^{-3}$  (Fig. 3B); however, the difference among them was not significant (Table 2). After this, the GSH content decreased significantly in the Pb concentration range of 0.4 to  $1.6 \mu\text{g}\cdot\text{m}^{-3}$  (Table 2), reaching a minimum of  $94.8 \pm 22.6 \mu\text{mol}\cdot\text{g}^{-1}$  at  $1.6 \mu\text{g Pb}\cdot\text{m}^{-3}$ . When the Pb concentration was larger ( $3.2\text{--}25.6 \mu\text{g}\cdot\text{m}^{-3}$ ), the GSH content increased again to become closer to the control value. The best model describing the relationship between Pb concentrations and GSH content for the 6-h treatment was triphasic, while for the 12-h treatment was biphasic (Table 3).

### 3.7. MT content

Generally, no significant differences of MT contents existed among different treatments for 6 h ( $F = 0.008$ ,  $p > 0.05$ ) and 12 h ( $F = 1.426$ ,  $p > 0.05$ ). After 6 h of Pb treatment, the MT content in *T. usneoides* showed an increasing trend with an increase in Pb concentration (Fig. 3C). A maximum of  $3.567 \mu\text{g}\cdot\text{L}^{-1}$  was reached at a Pb concentration of  $3.2 \mu\text{g}\cdot\text{m}^{-3}$ , but the MT content did not differ significantly between the various Pb treatment groups (Table 1). At 12 h, under treatment with different concentrations of Pb, the MT content in *T. usneoides* leaves first increased and then decreased with the increase in Pb concentration (Fig. 3C). The MT content in *T. usneoides* leaves did not change significantly at low Pb concentrations ( $0.1\text{--}0.4 \mu\text{g}\cdot\text{m}^{-3}$ ). At the two highest Pb concentrations applied ( $12.8$  and  $25.6 \mu\text{g}\cdot\text{m}^{-3}$ ), the MT content in *T. usneoides* leaves sharply increased (Table 2). The best model fit to the relationship between Pb concentrations and MT content after 6 h of treatment was monophasic but turned into biphasic at 12 h (Table 3).

**Table 2**Changes in six biomarkers in *Tillandsia usneoides* after a 12-h exposure to different Pb concentrations. Values are means  $\pm$  SEs ( $n = 5$ ).

Pb concentration ( $\mu\text{g}\cdot\text{m}^{-3}$ )	REC (%)	MDA ( $\text{nmol}\cdot\text{g}^{-1}$ )	$\text{O}_2^{\cdot-}$ ( $\mu\text{g}\cdot\text{g}^{-1}$ )	SOD ( $\text{U}\cdot\text{g}^{-1}\cdot\text{min}^{-1}$ )	GSH ( $\mu\text{mol}\cdot\text{g}^{-1}$ )	MT ( $\mu\text{g}\cdot\text{L}^{-1}$ )
0.0	30.75 $\pm$ 1.81c	2.46 $\pm$ 0.06 cd	357.30 $\pm$ 5.65a	134.52 $\pm$ 8.55c	177.88 $\pm$ 29.56a	55.56 $\pm$ 13.65a
0.1	69.99 $\pm$ 1.39b	2.03 $\pm$ 0.23d	379.98 $\pm$ 2.64a	150.38 $\pm$ 13.32d	198.45 $\pm$ 8.89a	62.19 $\pm$ 27.25a
0.2	66.48 $\pm$ 1.51b	2.35 $\pm$ 0.26d	373.74 $\pm$ 6.16a	150.67 $\pm$ 28.93d	181.42 $\pm$ 11.28a	65.56 $\pm$ 18.35a
0.4	24.38 $\pm$ 1.32d	2.37 $\pm$ 0.52d	373.59 $\pm$ 1.51a	174.55 $\pm$ 38.74 cd	130.09 $\pm$ 2.30bc	57.56 $\pm$ 6.36a
0.8	75.17 $\pm$ 0.06a	2.78 $\pm$ 0.06 cd	371.95 $\pm$ 3.96a	148.33 $\pm$ 36.67d	105.64 $\pm$ 13.06 cd	83.59 $\pm$ 27.53a
1.6	19.82 $\pm$ 1.11e	2.73 $\pm$ 0.16 cd	378.18 $\pm$ 2.89a	152.00 $\pm$ 22.72d	94.76 $\pm$ 22.58d	62.64 $\pm$ 10.40a
3.2	23.55 $\pm$ 0.13de	3.19 $\pm$ 0.57bc	358.41 $\pm$ 6.19a	223.33 $\pm$ 22.51 cd	118.36 $\pm$ 12.99 cd	63.56 $\pm$ 11.19a
6.4	26.01 $\pm$ 1.61d	3.65 $\pm$ 0.5b	361.40 $\pm$ 3.23a	325.00 $\pm$ 38.01b	99.50 $\pm$ 7.71 cd	64.51 $\pm$ 29.40a
12.8	31.44 $\pm$ 0.09c	2.29 $\pm$ 0.26d	296.74 $\pm$ 35.56b	347.89 $\pm$ 31.79b	125.44 $\pm$ 0.94bc	91.31 $\pm$ 5.49a
25.6	34.34 $\pm$ 3.07c	4.70 $\pm$ 0.08a	378.45 $\pm$ 0.82a	440.00 $\pm$ 53.85a	162.05 $\pm$ 29.29ab	100.09 $\pm$ 9.77a

REC, relative electric conductivity; MDA, malondialdehyde;  $\text{O}_2^{\cdot-}$ , superoxide anion radical; SOD, superoxide dismutase; GSH, glutathione; MT, metallothionein. Different small letters indicate a significant difference among different treatments for the same parameter at the level of 0.05. Data were tested with ANOVA followed by Tukey-HSD post hoc test.

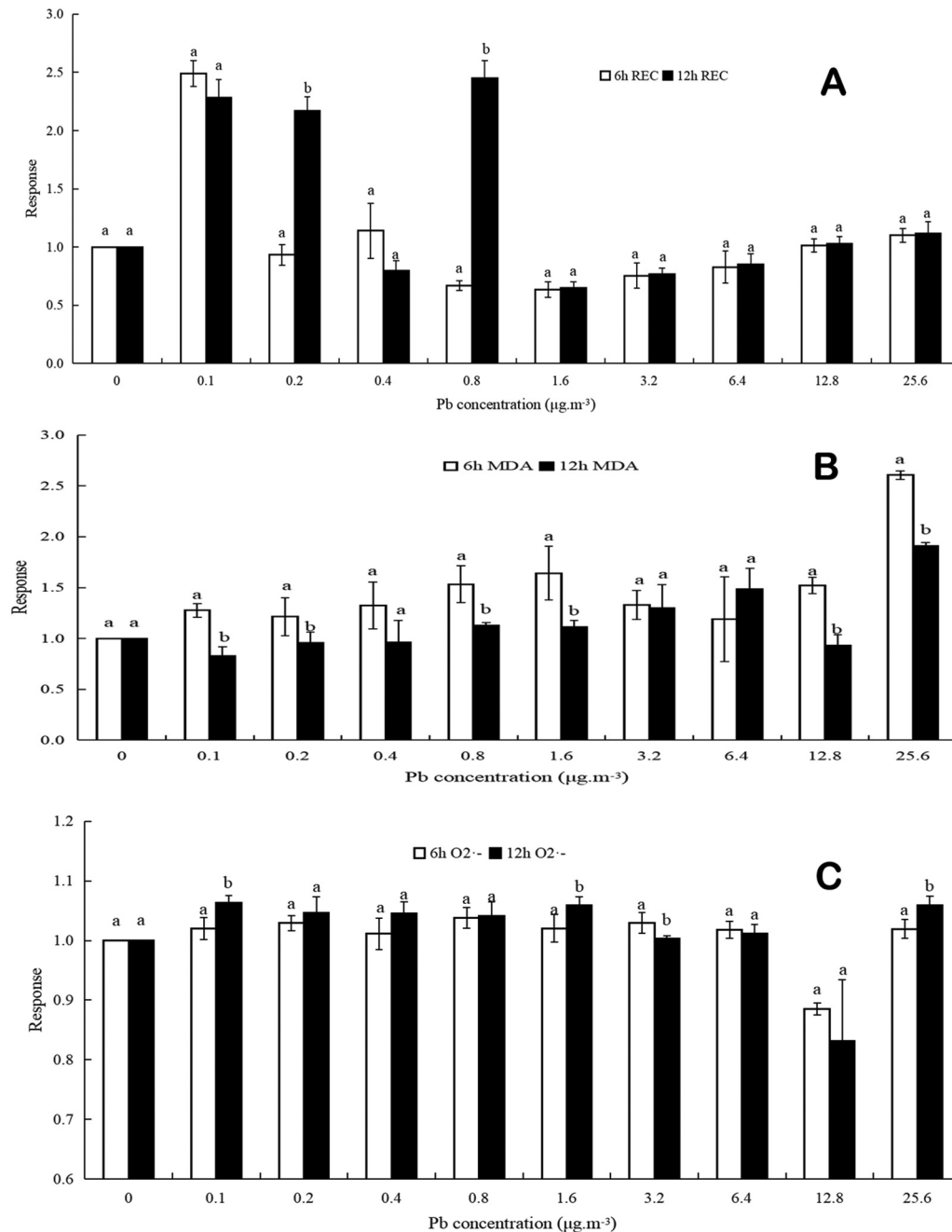


**Fig. 2.** Effects of Pb on damage markers of the leaf in *Tillandsia usneoides* after 6 h and 12 h exposure. A, REC, relative electric conductivity; B, MDA, malondialdehyde; C,  $\text{O}_2^{\cdot-}$ , superoxide anion radical; The response to Pb exposure was expressed as a percent increase or decrease relative to the control exposure where Pb concentration is zero and the response index is 1. The data are means  $\pm$  SEs ( $n = 5$ ). Different small letters indicate a significant difference between different times for treatment with the same Pb concentration at the level of 0.05, whereas same small letters indicate no significant difference.

#### 4. Discussion

Among the atmospheric heavy metals, lead, as a non-essential element, can easily accumulate in organisms, destroy cell structure, and cause serious harm to the ecological environment (Natasha and Khalid, 2020; Dinake et al., 2021). The natural background value of lead in the atmosphere is very low, with only about  $5 \times 10^{-5} \mu\text{g}\cdot\text{m}^{-3}$  (Elsom, 1996), and the annual limit is  $0.5 \mu\text{g}\cdot\text{m}^{-3}$  in China (Ministry of Environmental Protection, 2012). In this experiment, 10 Pb concentrations (from 0 to  $25.6 \mu\text{g}\cdot\text{m}^{-3}$ ) and two exposure durations were set, resulting in a total of 20 treatment conditions applied to stress *T. usneoides*. After 12 h of treatment with the maximum Pb concentration of  $25.6 \mu\text{g}\cdot\text{m}^{-3}$ , *T. usneoides* only showed yellowing of the leaves without obvious deterioration

(Fig. 1C), yet the Pb concentration in the atomization box was 51-fold the annual average atmospheric Pb concentration limit ( $0.5 \mu\text{g}\cdot\text{m}^{-3}$ ). This result indicates that *T. usneoides* is resistant to atmospheric Pb stress, extending previous findings that accumulator plants are resistant to a wide range of biotic or abiotic stresses (Barbosa et al., 2015). This may be the reason why *Tillandsia* spp. has become a widely used indicator to reflect the levels of atmospheric pollutants based on the contents of retained pollutants (Wannaz et al., 2011; Li et al., 2019).

The response of different biomarkers in *T. usneoides* to Pb was diverse, and there were three main types of fitting types. The first was a monophasic, linear dose response observed for the MT content after 6 h of treatment. The second was a biphasic dose response with one inhibition and one stimulation, i.e. a hormetic dose response (Agathokleous et al., 2020), found for

**Table 3**

Akaike Information Criterion (AIC) for the four fitting types corresponding to Pb exposure-response relationships for six biomarkers in *Tillandsia usneoides*.

Response trait	Exposure time	Fitting type	AIC
REC	6 h	Hill/monophasic (1 inhib.)	1969.57
		Biphasic (2 inhib.)	1979.53
		Biphasic (1 inhib. + 1 stim.)	278.28
REC	12 h	Triphasic (1 inhib. + 2 stim.)	256.82
		Hill/monophasic (1 inhib.)	2376.05
		Biphasic (2 inhib.)	2371.18
MDA	6 h	Biphasic (1 inhib. + 1 stim.)	1574.70
		Triphasic (1 inhib. + 2 stim.)	821.31
		Hill/monophasic (1 inhib.)	3186.52
MDA	12 h	Biphasic (2 inhib.)	9499.59
		Biphasic (1 inhib. + 1 stim.)	149.57
		Triphasic (1 inhib. + 2 stim.)	155.52
O <sub>2</sub> <sup>-•</sup>	6 h	Hill/monophasic (1 inhib.)	520.25
		Biphasic (2 inhib.)	4026.63
		Biphasic (1 inhib. + 1 stim.)	219.18
O <sub>2</sub> <sup>-•</sup>	12 h	Triphasic (1 inhib. + 2 stim.)	223.22
		Hill/monophasic (1 inhib.)	638.17
		Biphasic (2 inhib.)	630.12
SOD	6 h	Biphasic (1 inhib. + 1 stim.)	182.74
		Triphasic (1 inhib. + 2 stim.)	506.26
		Hill/monophasic (1 inhib.)	221.44
SOD	12 h	Biphasic (2 inhib.)	224.38
		Biphasic (1 inhib. + 1 stim.)	121.42
		Triphasic (1 inhib. + 2 stim.)	323.16
GSH	6 h	Hill/monophasic (1 inhib.)	124.33
		Biphasic (2 inhib.)	230.57
		Biphasic (1 inhib. + 1 stim.)	102.64
GSH	12 h	Triphasic (1 inhib. + 2 stim.)	108.22
		Hill/monophasic (1 inhib.)	333.29
		Biphasic (2 inhib.)	732.79
MT	6 h	Biphasic (1 inhib. + 1 stim.)	106.31
		Triphasic (1 inhib. + 2 stim.)	119.85
		Hill/monophasic (1 inhib.)	177.01
MT	12 h	Biphasic (2 inhib.)	144.45
		Biphasic (1 inhib. + 1 stim.)	182.48
		Triphasic (1 inhib. + 2 stim.)	105.58
MT	6 h	Hill/monophasic (1 inhib.)	101.81
		Biphasic (2 inhib.)	107.76
		Biphasic (1 inhib. + 1 stim.)	90.91
MT	12 h	Triphasic (1 inhib. + 2 stim.)	108.02
		Hill/monophasic (1 inhib.)	42.23
		Biphasic (2 inhib.)	49.50
MT	6 h	Biphasic (1 inhib. + 1 stim.)	48.15
		Triphasic (1 inhib. + 2 stim.)	54.14
		Hill/monophasic (1 inhib.)	51.56
MT	12 h	Biphasic (2 inhib.)	85.45
		Biphasic (1 inhib. + 1 stim.)	49.67
		Triphasic (1 inhib. + 2 stim.)	54.92

REC, relative electric conductivity; MDA, malondialdehyde; O<sub>2</sub><sup>-•</sup>, superoxide anion radical; SOD, superoxide dismutase; GSH, glutathione; MT, metallothionein; inhib., inhibition; stim., stimulation.

MDA, O<sub>2</sub><sup>-•</sup>, SOD, and GSH after 6 or 12 h of exposure and for MT after 12 h of exposure. The third was a triphasic dose response in the leaf relative electrical conductivity after 6 or 12 h of treatment and for GSH after 6 h of treatment. These results indicate the complexity of studying dose-response relationships as a result of exposures to environmental pollutants.

The monophasic linear (LNT) model between the toxicant dose and the biological response has been widely studied (Costantini and Borremans, 2019), and the changes in MT content after 6 h exposure activity in the present experiment agreed with this model. MT is a metal-binding protein, which is effective in mitigating heavy-metal damage in plants (Natasha and Khalid, 2020). The MT activity in *T. usneoides* increased with increasing Pb concentrations in both the 6-h and 12-h treatments. However, the dose-response relationship became biphasic within 12 h, suggesting that the linear dose response may only depict an initial disruption of the homeostasis at the very early stages of stress, i.e. a transient state preceding more complex non-monotonic responses (Agathokleous, 2018; Muszynska and Labudda, 2019; Carvalho et al., 2020). The responses of MT activity found in this study suggest that *T. usneoides* tried to protect itself from the

Pb-induced oxidative damage, which may also account for its high resistance to Pb stress.

It is worth noting that the leaf relative electrical conductivity, and GSH dose-response curves after 6 h of treatment were triphasic. Increasing Pb doses induced an increase, followed by a decrease and then a second increase in the conductivity contents, whether at 6 h or 12 h of treatment. In contrast, Pb induced a decrease, then an increase, and finally a decrease in GSH contents at 6 h of treatment. GSH is an antioxidant substance, which is also effective in mitigating heavy metal-induced damage in plants (Natasha and Khalid, 2020). It means that *T. usneoides* is inhibited by a very low concentration of Pb, stimulated by a low-to-medium concentration, and inhibited again after treatment at a higher concentration, resulting in a triphasic dose response involving hormesis. Similar triphasic responses have been observed in a number of studies, such as with (i) zebrafish embryos exposed to proton microbeam and X-rays (Choi et al., 2012; Kong et al., 2016), (ii) microorganisms exposed to Cd and Pb (Fan et al., 2021; Wang et al., 2021), and (iii) higher plants exposed to formaldehyde and other air pollutants (Calabrese and Agathokleous, 2021; Erofeeva, 2020; Erofeeva, 2018). A recent review by Katsnelson et al. (2021) indicates that alternating between upregulation and downregulation of any response is possible when living organisms respond to different levels of toxicants, while specific and non-specific adaptive responses may reflect an inducible adaptive capacity of plants challenged with stress to acclimate to random, unpredictable environmental changes (Erofeeva, 2022). Furthermore, Erofeeva (2018) suggested that Shelford's curve and hormesis complemented each other, with hormesis be localized in the stress zone of the Shelford's curve in situations where "adaptive mechanisms are disabled within the ecological optimum". An increasing number of studies documents the occurrence of triphasic responses of various organisms to atmospheric and soil pollutants (Calabrese and Agathokleous, 2021), suggesting that ultra-low doses that are much below the traditional toxicological thresholds can produce negative effects. These findings indicate the need for more studies covering the entire dose-response spectrum to enlighten ecological risk assessments.

Response mechanisms of various organisms to adversity, including hormesis, are essentially defense, adaptation, or repair mechanisms when facing an adverse attack, and are the result of natural selection in the process of evolution in nature (Costantini and Borremans, 2019; Calabrese and Agathokleous, 2020). In contrast with the fixed physical and chemical laws followed by inanimate matter, organisms are inherently dynamic, and the mechanisms and rates of adaptation to adversity are even more variable. Different toxicants cause varying biological mechanisms of hormesis, and the mechanisms of hormesis caused by the same toxicant on different organisms are complex and diverse (Agathokleous et al., 2020; Jalal et al., 2021; Erofeeva, 2022). Mechanisms that can theoretically explain hormesis include overcompensation, overcorrection, and DNA damage repair (Calabrese, 2018). Substances that scavenge ROS or can effectively chelate toxicants, such as antioxidants and metal-binding proteins and their associated functional genes are thought to play a major role in hormesis (Agathokleous and Calabrese, 2019; Kim et al., 2018). SOD activity in *Hordeum vulgare* increases before decreasing as the concentration of Cd increases (Kaciene et al., 2015). Furthermore, stress induced by heavy metals, such as Cu, Zn, Ni, and Cd, caused a significant elevation in the expression of MT and phytochelatin genes in three *Azolla* spp. (Talebi et al., 2019). The triphasic dose response involving hormesis found in this study may be a response mechanism of this taxon of *Tillandsia* spp. to stress or may be a more general mechanism of numerous taxa that is currently non-recognized.

The changes in the MDA, O<sub>2</sub><sup>-•</sup>, SOD, and GSH content after 12 h of treatment in the present experiment also revealed the above-mentioned mechanisms, which were consistent with the type for hormesis (Agathokleous et al., 2019b, 2020). However, differing from common hormesis, i.e., stimulation at low concentrations and inhibition at high concentrations, very low Pb concentrations induced a decrease in the GSH and SOD content, whereas high Pb concentrations induced an increase in the GSH and SOD content in *T. usneoides* leaves. SOD, which is mainly found

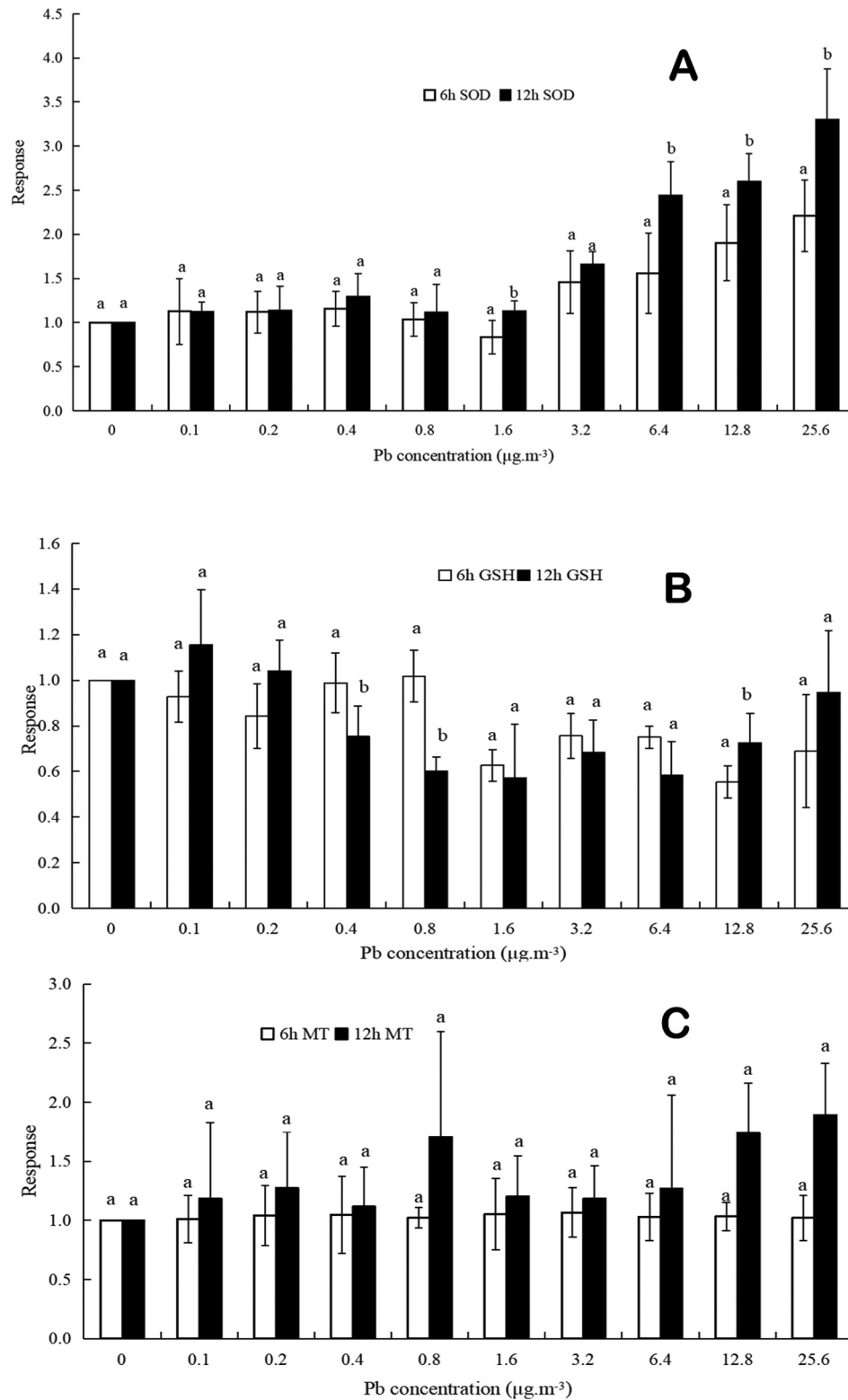


**Fig. 3.** Effects of Pb on the resistance markers in *Tillandsia usneoides* after 6 h and 12 h exposure. A, SOD, superoxide dismutase; B, GSH, glutathione; C, MT, metallothionein. The response to Pb exposure was expressed as a percent increase or decrease relative to the control exposure where Pb concentration is zero and the response index is 1. The data are means  $\pm$  SEs ( $n = 5$ ). Different small letters indicate a significant difference between different times for treatment with the same Pb concentration at the level of 0.05, whereas same small letters indicate no significant difference.

in the cytoplasm and between the inner and outer mitochondrial membranes, is the first enzyme to interact with ROS radicals, controlling the steady-state level of  $\text{O}_2^{\cdot-}$  in plant cells and protecting the organism from oxidative damage (Lscher et al., 2002). The fact that the levels of GSH and

SOD decreased before increasing implies that the effect of Pb on *T. usneoides* might be inhibitory at first and then stimulating. The beneficial stimulating effect of the toxicant, Pb, on organisms cannot always be maintained, and the inhibitory effect is bound to occur only after a certain concentration is

reached. Therefore, a “high concentration” of GSH and SOD at this threshold value may only be a “moderate concentration” of  $O_2^{\cdot-}$  and MDA. Hormesis-like stimulatory effects can occur because accumulator plants are resistant to various toxicants (Barbosa et al., 2015; Calabrese and Agathokleous, 2021). The difference in the response to Pb between the GSH, SOD,  $O_2^{\cdot-}$ , and MDA contents may be mainly because of their differential sensitivity to Pb, which has long been recognized for different biomarkers (Bartell, 2006).

## 5. Conclusion

The dose-response relationship between the changes in the SOD,  $O_2^{\cdot-}$ , and MDA contents and Pb in *T. usneoides* leaves suggests that Pb can induce hormesis in *T. usneoides*. Following a recent study demonstrating that atmospheric Hg induces hormesis in *T. usneoides* (Sun et al., 2021b), this study further suggests that hormesis may also be quite common in the accumulative indicator plant *Tillandsia* spp. The hypothesis of hormesis was further enriched by the triphasic dose response to Pb, reflected in the changes in the leaf relative electrical conductivity and GSH contents; however, whether this triphasic dose response is widespread needs to be further studied. Since various air pollutants, including Hg, Pb,  $O_3$ , formaldehyde, can induce hormesis in plants (Agathokleous et al., 2019a; Pan et al., 2020; Conte et al., 2021; Sun et al., 2021b), further studies designed to evaluate hormetic responses to air pollutants are needed to feed ecological risk assessments and enlighten critical levels setting.

## CRedit authorship contribution statement

Peng Li performed the experiments and analyzed the results, Jingyi Zhang and Xingyue Sun performed the experiments, Evgenios Agathokleous analyzed the results, Guiling Zheng designed the experiments and analyzed the results. All authors write, review and edit the manuscript.

## Declaration of competing interest

The authors declare that they have no known competing financial interests or personal relationships that could have appeared to influence the work reported in this paper.

## Acknowledgement

This study was funded by the National Natural Science Foundation of China (41475132, 41571472).

## References

Agathokleous, E., Calabrese, E.J., 2019. Hormesis can enhance agricultural sustainability in a changing world. *Glob. Food Sec.* 20, 150–155.

Agathokleous, E., Kitao, M., Calabrese, E.J., 2019a. Hormesis: a compelling platform for sophisticated plant science. *Trends Plant Sci.* 24 (4), 318–327.

Agathokleous, E., 2018. Environmental hormesis, a fundamental non-monotonic biological phenomenon with implications in ecotoxicology and environmental safety. *Ecotoxicol. Environ. Saf.* 148, 1042–1053.

Agathokleous, E., Araminien, V., Belz, R.G., Calatayud, V., Calabrese, E.J., 2019b. A quantitative assessment of hormetic responses of plants to ozone. *Environ. Res.* 176, 108527.

Agathokleous, E., Kitao, M., Calabrese, E.J., 2020. Hormesis: highly generalizable and beyond laboratory. *Trends Plant Sci.* 25 (11), 1076–1086.

Barbosa, B., Boleo, S., Sidella, S., Costa, J., Duarte, M.P., Mendes, B., Cosentino, S.L., Fernando, A.L., 2015. Phytoremediation of heavy metal-contaminated soils using the perennial energy crops *Miscanthus* spp. and *Arundo donax* L. *Bioenergy Res.* 8, 1500–1511.

Bartell, Steven M., 2006. Biomarkers, bioindicators, and ecological risk assessment—a brief review and evaluation. *Environ. Bioindic.* 1 (1), 60–73.

Benzing, D.H., 2000. Bromeliaceae: Profile of an Adaptive Radiation. Cambridge University Press.

Calabrese, E.J., 2018. Hormesis: path and progression to significance. *Int. J. Mol. Sci.* 19, 2871.

Calabrese, E.J., Agathokleous, E., 2020. Theodosius Dobzhansky's view on biology and evolution vol 2.0: “Nothing in biology makes sense except in light of evolution and evolution's dependence on hormesis-mediated acquired resilience that optimizes biological performance and numerous diverse short and longer term protective strategies”. *Environ. Res.* 186, 109559.

Calabrese, E.J., Agathokleous, E., 2021. Accumulator plants and hormesis. *Environ. Pollut.* 274, 116526.

Calasans, C.F., Malm, O., 1997. Elemental mercury contamination survey in chlor-alkali plant by the use of transplanted Spanish moss, *Tillandsia usneoides* (L.). *Sci. Total Environ.* 208 (3), 165–177.

Carvalho, M.E.A., Castro, P.R.C., Azevedo, R.A., 2020. Hormesis in plants under Cd exposure: from toxic to beneficial element? *J. Hazard. Mater.* 384, 121434.

Choi, V.W.Y., Yum, E.H.W., Konishi, T., Oikawa, M., Cheng, S.H., Yu, K.N., 2012. Triphasic low-dose response in zebrafish embryos irradiated by microbeam protons. *J. Radiat. Res.* 53, 475–481.

Conte, A., Otu-Larbi, F., Alivernini, A., Hoshika, Y., Fares, S., 2021. Exploring new strategies for ozone-risk assessment: a dynamic-threshold case study. *Environ. Pollut.* 287 (9), 117620.

Costantini, D., Borremans, B., 2019. The linear no-threshold model is less realistic than threshold or hormesis-based models: an evolutionary perspective. *Chem. Biol. Interact.* 301, 26–33.

Di Veroli, G.Y., Fornari, C., Goldlust, I., Mills, G., Koh, S.B., Bramhall, J.L., Richards, F.M., Jodrell, D.I., 2015. An automated fitting procedure and software for dose-response curves with multiphasic features. *Sci. Rep.* 5, 14701.

Dinake, P., Mokgosi, S.M., Kelebemang, R., Kereeditse, T.T., Motswetla, O., 2021. Pollution risk from Pb towards vegetation growing in and around shooting ranges—a review. *Environ. Pollut. Bioavail.* 33 (1), 88–103.

Elsom, D., 1996. Smog Alert: Managing Urban Air Quality. Earthscan Publications Ltd, UK.

Erofeeva, E.A., 2018. Hormesis and paradoxical effects of pea (*Pisum sativum* L.) parameters upon exposure to formaldehyde in a wide range of doses. *Ecotoxicology* 27, 569–577.

Erofeeva, E.A., 2020. Estimating the frequency of hormesis and other non-monotonic responses in plants experiencing road traffic pollution in urban areas and experimental pollutant exposure. *Environ. Monit. Assess.* 192, 460.

Erofeeva, E.A., 2022. Environmental hormesis of non-specific and specific adaptive mechanisms in plants. *Sci. Total Environ.* 804, 150059.

Fan, D.W., Sun, J., Liu, C., Wang, S.Y., Han, J.G., Agathokleous, E., Zhu, Y.L., 2021. Measurement and modeling of hormesis in soil bacteria and fungi under single and combined treatments of Cd and Pb. *Sci. Total Environ.* 783, 147494.

Figueiredo, A.M.G., Nogueira, C.A., Saiki, M., Milian, F.M., Domingos, M., 2007. Assessment of atmospheric metallic pollution in the metropolitan region of Sao Paulo, Brazil, employing *Tillandsia usneoides* L. as biomonitor. *Environ. Pollut.* 145, 279–292.

Jalal, A., Junior, J.C., Ribeiro, J.S., Fernandes, G.C., Mariano, G.G., Trindade, V.D.R., Reis, A.R., 2021. Hormesis in plants: physiological and biochemical responses. *Ecotoxicol. Environ. Saf.* 207, 111225.

Kaciene, G., Zaltauskaite, J., Milce, E., Juknys, R., 2015. Role of oxidative stress on growth responses of spring barley exposed to different environmental stressors. *J. Plant Ecol.* 8 (6), 605–616.

Katsnelson, B.A., Panov, V.G., Minigaliev, I.A., Bushueva, T.V., Gurvich, V.B., Privalova, L.L., Klinova, S.V., Sutunkova, M.P., 2021. On an extended understanding of the term “hormesis” for denoting alternating directions of the organism's response to increasing adverse exposures. *Toxicology* 447, 152629.

Kim, S.A., Lee, Y.M., Choi, J.Y., DRJ, Jr, Lee, D.H., 2018. Evolutionarily adapted hormesis-inducing stressors can be a practical solution to mitigate harmful effects of chronic exposure to low dose chemical mixtures. *Environmental Pollution* 233, 725–734.

Kong, E.Y., Cheng, S.H., Yu, K.N., 2016. Biphasic and triphasic dose responses in zebrafish embryos to low-dose 150 kV X-rays with different levels of hardness. *J. Radiat. Res.* 57 (4), 363–369.

Kováčik, J., Babula, P., Klejdus, B., Hedbavny, J., 2014. Comparison of oxidative stress in four *Tillandsia* species exposed to cadmium. *Plant Physiol. Biochem.* 80, 33–40.

Lei, Y., Yin, C., Li, C., 2006. Differences in some morphological, physiological, and biochemical responses to drought stress in two contrasting populations of *Populus przewalskii*. *Physiol. Plant.* 127 (2), 182–191.

Li, H.S., 2000. Principles and Techniques of Plant Physiological and Biochemical Experiment. Higher Education Press, Beijing, China.

Li, P., Sun, X.Y., Cheng, J., Zheng, G.L., 2019. Absorption of the natural radioactive gas  $^{222}Rn$  and its progeny  $^{210}Pb$  by Spanish moss *Tillandsia usneoides* and its response to radiation. *Environ. Exp. Bot.* 158, 22–27.

Li, X., Li, Z., Lin, C.-J., Bi, X., Liu, J., Feng, X., Zhang, H., Chen, J., Wu, T., 2018. Health risks of heavy metal exposure through vegetable consumption near a large-scale Pb/Zn smelter in Central China. *Ecotoxicol. Environ. Saf.* 161, 99–110.

Lescher, R.G., Erturk, N., Heath, L.S., 2002. Role of superoxide dismutases (SODs) in controlling oxidative stress in plants. *J. Exp. Bot.* 53 (372), 1331–1341.

<collab>Ministry of Environmental Protection, China<collab>, 2012. Ambient Air Quality Standards (GB 3095-2012). China Environmental Science Press, Beijing.

Muszynska, E., Labudda, M., 2019. Dual role of metallic trace elements in stress biology—from negative to beneficial impact on plants. *Int. J. Mol. Sci.* 20 (13), 3117–3144.

Natasha, Shahid M., Khalid, S., 2020. Foliar application of lead and arsenic solutions to *Spinacia oleracea*: biophysicochemical analysis and risk assessment. *Environ. Sci. Pollut. Res.* 23 (15), 1–11.

Pan, L., Zou, X.J., Lie, G.W., Xue, L., Chen, H.Y., 2020. Ozone-induced changes in physiological and biochemical traits in *Elaeocarpus sylvestris* and *Michelia chapensis* in south China. *Atmos. Pollut. Res.* 11 (5), 973–980.

Qian, C.L., He, Z.P., Zhao, Y.Y., Mi, H.B., Chen, X.H., Mao, L.C., 2013. Maturity-dependent chilling tolerance regulated by the antioxidant capacity in postharvest cucumber (*Cucumis sativus* L.). *J. Sci. Food Agric.* 93, 626–633.

Salinitro, M., Mattarello, G., Guardigli, G., Odajiu, M., Tassoni, A., 2021. Induction of hormesis in plants by urban trace metal pollution. *Sci. Rep.* 11, 20329.

Sánchez-Chardi, A., 2016. Biomonitoring potential of five sympatric *Tillandsia* species for evaluating urban metal pollution (Cd, Hg and Pb). *Atmos. Environ.* 131, 352–359.

Schreck, E., Viers, J., Blondet, I., Auda, Y., Macouin, M., Zouiten, C., Freyrier, R., Dufrechoux, G., Chmeleff, J., Darrozes, J., 2020. *Tillandsia usneoides* as biomonitors of trace elements

- contents in the atmosphere of the mining district of Cartagena-La Unión (Spain): new insights for element transfer and pollution source tracing. *Chemosphere* 241, 124955.
- Shahid, M., Dumat, C., Khalid, S., Schreck, E., Xiong, T., Niazi, N.K., 2017. Foliar heavy metal uptake, toxicity and detoxification in plants: a comparison of foliar and root metal uptake. *J. Hazard. Mater.* 325, 36–58.
- Shahid, M., Shamshad, S., Farooq, A.B.U., Rafiq, M., Khalid, S., Dumat, C., Zhang, Y., Hussain, I., Niazi, N.K., 2019. Comparative effect of organic amendments on physio-biochemical traits of young and old bean leaves grown under cadmium stress: a multivariate analysis. *Environ. Sci. Pollut. Res.* 26, 11579–11590.
- Sun, X.Y., Li, P., Zheng, G.L., 2021a. Cellular and subcellular distribution and factors influencing the accumulation of atmospheric Hg in *Tillandsia usneoides* leaves. *J. Hazard. Mater.* 414, 125529.
- Sun, X.Y., Li, P., Zheng, G.L., 2021b. Biomarker responses of Spanish moss *Tillandsia usneoides* to atmospheric Hg and hormesis in this species. *Front. Plant Sci.* 12, 625799.
- Talebi, M., Tabatabaei, B.E.S., Akbarzadeh, H., 2019. Hyperaccumulation of Cu, Zn, Ni, and Cd in azolla species inducing expression of metallothionein and phytochelatin synthase genes. *Chemosphere* 230, 488–497.
- Uzu, G., Sobanska, S., Sarret, G., Munoz, M., Dumat, C., 2010. Foliar lead uptake by lettuce exposed to atmospheric fallouts. *Environ. Sci. Technol.* 44, 1036–1042.
- Xiong, T., Dumat, C., Dappe, V., Vezin, H., Schreck, E., Shahid, M., Pierart, A., Sobanska, S., 2017. Copper oxide nanoparticle foliar uptake, phytotoxicity, and consequences for sustainable urban agriculture. *Environ. Sci. Technol.* 51, 5242–5251.
- Wang, S.Y., Huang, B., Fan, D.W., Agathokleous, E., Guo, Y.H., Zhu, Y.L., Han, J.G., 2021. Hormetic responses of soil microbiota to exogenous Cd: a step toward linking community-level hormesis to ecological risk assessment. *J. Hazard. Mater.* 416, 125760.
- Wannaz, E.D., Carreras, H.A., Abril, G.A., Pignata, M.L., 2011. Maximum values of Ni<sup>2+</sup>, Cu<sup>2+</sup>, Pb<sup>2+</sup> and Zn<sup>2+</sup> in the biomonitor *Tillandsia capillaris* (Bromeliaceae): relationship with cell membrane damage. *Environ. Exp. Bot.* 74, 296–301.

## 附件3：资源与环境学院“2022-2023年度优秀共青团员”

# 资源与环境学院 2022 年度优秀共青团员、五四青年 标兵公示名单

### 优秀共青团员：

刘晓霖	高永臻	林晓彤	王 晨	丁 豪	傅晨熙	韩佳文	闫辰宇
安娜	张 宇	赵 敏	翟奇奇	王嘉玉	牛 玉	王亚宁	何海燕
马振伟	张志翔	刘春亮	邢锦豪	张弘健	郭晴雯	泮 彤	纪理赫
刘孟琪	陈诗瑶	崔玉娇	张浩然	殷子蝶	王明扬	李智颖	王梦超
贾广慧	温浩杰	任效申	吴沂东	赵 云	付凯楠	李思奇	张立旭
张振鑫	杨玉品	张 昊	王军伟	吴 涵	冯茹冰	董洪敏	梁继杰
孙秀鹏	韩腾腾	夏培润	张钊瑞	桑晓莹	马玉翠	陈冉冉	胡文杰
张康宁	姜龙龙	尹 硕	刘 伟	姜向阳	魏可明	赵子瀛	刘晓丽
黄长培	赵文婷	穆 然	刘弘一	朱秋晨	陈 晗	张铭沁	杜永琪
高存晓	梅梦瑶	姚悦涵	王紫月	程 悦	魏淑慧	孙小茜	郝梦玥
聂嘉岐	刘 雯	潘道洁	徐小昕	阎 茹	陈雅楠	刘 莉	胡亚楠
孙佳林	林 睿	王昕月	李淑月	周音悦	李伟明	刘 飞	姚亚雯
杨 月	邢璐凡	李龙骧	陈 秀	侯云凤	庄旭龙	李雅婧	姬保函
胥鑫颖	丁一凡	庄晓悦	林子坤	梁 冰	牛茹怡	田 亮	车朝跃
张薪鲁	张 娜	许馨钰	甄 峰	董婧婧	张文静	张 豪	孙新茹
谢梦雪	赵丽婷	韩晓敏	刘文禹	刘 朔	陈若宁	刘小荷	张智雅
黄晓雨	赵茗芳	邓贞静	李 静	蒋清会	陈亚宏	曲玉馨	孙传艳
高 玥	王秀茹	孙申奥	李灿灿	于鑫蕾	赵国芹	刘亚军	李超媛
胡 冰	董雅宁	张梦媛	王盛典	郭昕宇	丁玉明	王沐然	商梦舟
许子涵	安芙瑶	王晓楠	高之琳	邢若昞	宋祥霄	何姝静	刘占彬
赵晨聪	初於翰	段惠敏	赵荣森	邱宝娴	滕悦宏	滕书宇	佟琪琪
孙政博	陆常旭	杨春伟	刘雯燕	刘昱彤	郑 琪	唐宪坤	王佳怡
徐梦鸽	刘宇晖	陈亦卿	刘佳琦	李英第	张成龙	姜晓芹	朱 彤
亓凯霞	高枫舒	金岩松	邓文迪	张憬怡	程 奔	杨小春	王国霖
于 泉	李 雪	刘思琪	王 真	唐 震	赵庆斌	陈 阳	刘悦萱
孙志豪	冯晓璐	朱慧娴	石 璐	谢涛鸿	滕 跃	王梓洋	王 冉
李佳慧	王泽玮	赵金冉	陈 宇	王文文	赵洪倩	李 茜	潘永芳
张心雨	燕浩闻						

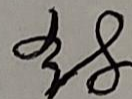
五四青年标兵：社会工作与实践标兵 姜晓芹

## 青岛农业大学科研项目参与证明

兹证明，学生张憬怡，学号 20212108026，参与由李鹏主持的项目，项目名称为：大气重金属指示植物松萝中多相剂量效应的产生及谷胱甘肽的动态变化；项目批准号：32271699；项目状态为：进行中。该学生在该项目进行过程中表现优异。

特此证明。

课题负责人签字：



2023 年 10 月 7 日